University of Southampton

Faculty of Engineering and the Environment

Fluid Structure Interactions research group

Analysis of downwind sail structures using non-linear shell finite elements

wrinkle development and fluid interaction effects

by

Daniele Trimarchi

Thesis for the degree of Doctor of Philosophy

June 1, 2012

Declaration of authorship

I, Daniele Trimarchi, declare that the thesis entitled *Analysis of downwind sail structures using non-linear shells finite elements, wrinkle development and fluid interaction effects* and the work presented in the thesis are both my own, and have been generated by me as the result of my original research. I confirm that:

- This work was done wholly or mainly while in candidature for a research degree at this University;
- Where any part of this thesis has previously been submitted for a degree or any other qualification at this University or any other institution, this has been clearly stated;
- Where I have consulted the published work of others, this is always clearly attributed;
- Where I have quoted from the work of others, the source is always given. With the exception of such quotations, this thesis is entirely my own work;
- I have acknowledged all main sources of help;
- Where the thesis is based on work done by myself jointly with others, I have made clear exactly what was done by others and what I have contributed myself;
- Parts of this work have been published in [1], [2] and [3].

Signed: .....

Date : .....

Abstract

Downwind yacht sails are subjected to fluid structure interaction effects which can slightly change the initial design shape, with a direct impact on the overall performances. The turbulent flow acting on downwind sails is separated for the larger part of the device, with large vortices and recirculating regions. The sail is made of a thin fabric, the deformation of which is affected by *wrinkling*, which produces out-of-plane oscillations of the surface of the fabric, and locally changes the stress/strain distribution. Because of the interactions of these fluid and structural phenomena, the detailed analysis of downwind sails requires sophisticated approaches able to capture the structural deformations, the generation of the wrinkles and the unsteady fluid structure interactions. This is not achieved in conventional sail analysis, the state of the art of which consist, for the most advanced applications, in steady fluid structure analysis adopting membrane structural elements, which are unable to reproduce the wrinkling.

The turbulent flow is here analysed with a Reynolds Averaged Navier Stokes method implemented in the finite volume solver OpenFOAM, and case studies are presented regarding the detailed description of the flow/wrinkle interactions, as well as the flow generation on full 3D sail-type devices. This approach is a good compromise between accuracy and computational expense, allowing the investigation of unsteady fluid structure interactions. The work presented here in fact primarily concentrates on the structural response and its influence on the fluid flow rather than the analysis of the fine details of an isolated unsteady flow.

Shell finite elements of the M*ixed* I*nterpolation* T*ensorial* C*omponents* (MITC) family are used for simulating the fabric. The use of these sophisticated Finite Elements allows for capturing the greater detail of the structural behaviour and the generation of the wrinkles. Comparisons are presented between the results obtained with the shells and the membrane finite elements, traditionally adopted for the structural analysis of fabrics. The performances of the method are demonstrated with simplified validation test cases and applications are

shown for realistic 3D devices.

Unsteady fluid structure interaction analysis is performed using the Arbitrary Lagrangian Eulerian (ALE) framework, providing a conservative environment. Validation test cases are compared with reference solutions and the inflation of a sail-type device is analysed.

The flow development is accurately captured, and the presence of wrinkles on the cross-flow determine a substantial decrease of the lift and an increase in the drag. Inducing unsteadiness in the flow produces a general increase of the performances of the device.

Using shell elements the wrinkling can be directly reproduced, while using membrane models require additional *wrinkling* models. The prediction performances of the MITC shells are substantially higher than those of the Constant Strain Triangles (CST) membranes, traditionally adopted for simulating the sail fabric.

Unsteady fluid structure interaction analysis are validated against reference solutions with good agreement. When applying the method to yacht-sail type geometries, results are coherent and consistent with the sailing practise.

Acknowledgements

Many people contributed to this thesis in many ways. Thanks to my supervisors prof. Turnock and Dr. Taunton for giving me the opportunity of doing this research. Thanks to Matteo Scarponi for making possible this adventure and for his precious support.

I would like to thank in particular Dr. Chapelle and Dr. Vidrascu, INRIA Rocquencourt, for accepting to co-supervise this work and for teaching me the details of the continuum mechanics, the finite elements and the implementation of a scientific computational code. Working with them has been day after day a pleasure and a honour.

Thanks to all the people who contribute to the long and often useful discussions on the various subjects. In particular, thanks Asven Gariah for all the good time in the office, to Andreas Feymark, Christophe Kassiotis and Matteo Lombardi for the discussion on the Fluid Structure Interactions in OpenFOAM, to Annabelle Colin for the help with the shell model. Thanks to Andrea Bucchi and Jean-Michel Forestier for all the support they gave me, especially in the beginning of this adventure. Thanks to Cesare Rizzo for being always supportive and helpful and to Cesare Corrado for being very often right. Thanks to all the people of "batiment 16" for sharing time, experiences and ideas. Thanks to Tom Lloyd and Simon Lewis for reading, advising and the correcting this work.

Nomenclature

General nomenclature:

A	$[m^2]$	area
$\mathcal{E}$		the three-dimensional *physical space*
$\mathbb{R}^3$		the three-dimensional *mathematical space*
V, dV	$[m^3]$	volume and differential volume
ξ^1, ξ^2, ξ^3		real valued numbers
$\vec{\imath}_1$, $\vec{\imath}_2$, $\vec{\imath}_3$		independent vectors forming a basis
$O\vec{M}$		vector
$\mathbf{T}$		tensor
$\otimes$		tensor product
∇		gradient operator
$\nabla\cdot$		divergence operator
Δ		Laplacian operator

Fluid nomenclature:

S	$[m^2]$	surface
ϵ	$[m^2/s^3]$	dissipation of the turbulent kinetic energy
k	$[m^2/s^2]$	turbulent kinetic energy
C_d, C_l, C_x, C_y		drag, lift, $x-$force and $y-$force coefficients
Co		Courant number
D	$[m]$	Diameter
Δx, Δy, Δt	$[m]$, $[s]$	space and time increments
δ_2	$[mm]$	momentum thickness
ℓ	$[m]$	length scale
m	$[Kg]$	mass

μ	$[Kg/ms]$	dynamic viscosity of the fluid
ν	$[m^2/s]$	kinematic viscosity of the fluid
ν_{T}	$[m^2/s]$	turbulent eddy viscosity
p, p', $p*$	$[N/m^2]$	pressure, pressure corrections
Re		Reynolds number
t	$[s]$	time
u^+, y^+		adimensional velocity and wall distance
u', v', w'	$[m/s]$	turbulent velocity oscillations; velocity corrections
$u*$, $v*$, $w*$	$[m/s]$	velocity corrections
u_∞	$[m/s]$	reference velocity
q	$[m/s]$	velocity scale
τ_w	$[Kg/ms^2]$	wall shear stress
ρ, ρ_f	$[Kg/m^3]$	density of the fluid
T	$[s]$	time period
ω	$[1/s]$	specific rate of dissipation of the turbulence kinetic energy
$\vec{f}, \vec{F}$	$[N]$	infinitesimal and integral force
$\vec{M}$	$[N\,m]$	moment
$\vec{q}, \vec{Q}$,	$[Kg\,m/s]$	infinitesimal and integral momentum
$\vec{v}$	$[m/s]$	velocity
$\mathbf{D}$	$[1/s]$	strain velocity tensor
$\mathbf{I}$		Identity tensor
$\mathbf{S}$, $\mathbf{W}$	$[1/s]$	symmetric and anti-symmetric parts of the strain velocity tensor
$\vec{t}$, $\mathbf{T}$	$[n/m^2]$	infinitesimal tension, stress tensor
$\mathbf{T}^{turb}$	$[Kg/ms^2]$	Reynolds stress tensor

Structural nomenclature:

c_1, c_2		Rayleigh damping coefficients
E	$[N/mm^2]$	Young modulus
$e_{ij}(\vec{U})$		components of the linearised Green−Lagrange strain tensor
H^{ikkl}, $C^{\alpha\beta\lambda\mu}$, $D^{\alpha\lambda}$	$[N/mm^2]$	components of the constitutive tensor
I	$[m^4]$	moment of inertia
I_w		wrinkling index
J		Jacobian

λ_i		$i-th$ eigen-value
$\lambda_k(r,s)$		shape function value in the local reference
λ, μ		Lamé constants
L_w	$[mm]$	wrinkle wavelength
n_w		number of wrinkles
ν, ν_s		Poisson ratio
ξ		damping coefficient
p	$[N/m]$	distributed load
ρ, ρ_s	$[Kg/mm^3]$	density of the structure
S		Shell midsurface
T_n	$[s]$	period of oscillation corresponding
		to the natural frequency
t, $t(\xi^1,\xi^2)$	$[mm]$	thickness of the shell
$\sigma_{ij}(\vec{U})$	$[N/m^2]$	components of the stress tensor
σ_w		standard deviation of a wrinkled section
		with respect to a regression curve
V, dV	$[mm^3]$	infinitesimal and integral volume
W^{int}, W^{ext}	$[Nm]$	internal and external work
ω_i, ω_n	$[s]$	ith oscillation frequency, natural frequency
Z_c		zero crossing of the wrinkled section
$\underline{\alpha}$		rotations
$\vec{a}_\alpha$		local basis tangent to the shell midsurface
$\mathbf{C}$	$[N/mm^2]$	linearised constitutive relationship
$\vec{F}$	$[N]$	force vector
$(\vec{g}_1,\vec{g}_2,\vec{g}_3)$		covariant basis
$(\vec{g}^1,\vec{g}^2,\vec{g}^3)$		contravariant basis
$\vec{\Phi}$, $\vec{\phi}$		charts (Section 4.1.3)
$\vec{\phi}$		position vector (Section 4.1.7)
$\vec{\phi}$		eigen-vectors (Section 4.1.9
θ_λ, $\vec{a}^\lambda$		nodal displacement vector:
		rotation and rotation components
$\vec{u}=(u,v,w)$	$[m]$	nodal displacement vector: translations

$\vec{U}$, $\Delta\vec{U}$	$[m]$	displacement vector and
		incremental displacement vector
$\vec{V}, \vec{v}$		test (shape) functions
$\mathbf{Y}$	$[m]$	displacement vector
$\mathbf{M}$	$[Kg]$	mass matrix
$\mathbf{K}$	$[N/m]$	stiffness matrix
$\mathbf{C}$	$[Ns/m]$	damping matrix
$\mathbf{B}$		matrix of the derivatives
$\mathbf{C}$	$[N/mm^2]$	Constitutive matrix

Contents

List of Tables

List of Figures

Mathematical Preliminaries

Some general notations and operators commonly used for continuum mechanics are here introduced. These basic concepts will be recalled in the later chapters, and in particular when reviewing the theoretical part of the fluid and the structural mechanics.

0.1 Vectors and tensors: definitions and operations

Let us define:

- $\mathcal{E}$ the three-dimensional *physical space*, also called *Euclidean* space;
- $\mathbb{R}^3$ the three-dimensional *mathematical space*, defined as a set of all triples of real numbers, i.e. quantities of the type (ξ^1, ξ^2, ξ^3), where ξ^1, ξ^2, ξ^3 are real valued numbers.

It is assumed that an origin O is given in $\mathcal{E}$, so that it is possible to identify points and vectors. A vector is denoted with the symbol: $\vec{}$. Then, by choosing a basis in $\mathcal{E}$, i.e. three independent vectors $\vec{\imath}_1$, $\vec{\imath}_2$, $\vec{\imath}_3$ that are attached to O, we obtain a natural (canonical) *one-to-one* mapping from $\mathbb{R}^3$ to $\mathcal{E}$ defined by:

$$(\xi^1, \xi^2, \xi^3) \rightarrow \xi^1\vec{\imath}_1 + \xi^2\vec{\imath}_2 + \xi^3\vec{\imath}_3 \tag{1}$$

(ξ^1, ξ^2, ξ^3) are then called the *components* of the vector $\xi^1\vec{\imath}_1 + \xi^2\vec{\imath}_2 + \xi^3\vec{\imath}_3$ in the basis ($\vec{\imath}_1$, $\vec{\imath}_2$, $\vec{\imath}_3$). A point is now identified by this vector such that:

$$O\vec{M} = \xi^1\vec{\imath}_1 + \xi^2\vec{\imath}_2 + \xi^3\vec{\imath}_3 \tag{2}$$

Then (ξ^1, ξ^2, ξ^3) are also the *coordinates* of M in the coordinate system defined by O and $(\vec{\imath}_1, \vec{\imath}_2, \vec{\imath}_3)$ [1]. In the rest of this introductory discussion $(\vec{\imath}_1, \vec{\imath}_2, \vec{\imath}_3)$ is assumed to be orthonormal.

[1] The meaning of superscript (ξ^i) in curvilinear reference systems will be made clear when treating curvilinear coordinate systems in Chapter 4.

A *tensor* is an object that generalizes vectors to a higher dimension. For example, we can consider the family of couples of base vectors, that we write:

$$\vec{\imath}_m \otimes \vec{\imath}_n, \quad m, n = 1, 2, 3 \tag{3}$$

where $\otimes$ is the tensor product. This is an operator between tensors, an example of which is given below for two vectors (in this case the tensor product is called *outer* product, in contrast to the *inner* product detailed in Equation 6):

$$\vec{a} \otimes \vec{b} = \sum_{k,l} a_k b_l \, \vec{\imath}_k \otimes \vec{\imath}_l \tag{4}$$

Such an operator is also valid for higher order tensors. Using couples of base vectors (as in equation (4)) for higher order vector space we get the space of second order tensors, denoted by $\mathcal{E} \otimes \mathcal{E}$. Similarly, it is possible to consider tensors of any order.

Given a tensor of any order (in this case: 2), it is possible to use the tensor product for decomposing the tensor on a specific base of the form given in equation (3), thus:

$$\mathbf{T} = \sum_{m=1}^{3} \sum_{n=1}^{3} T_{mn} \, \vec{\imath}_m \otimes \vec{\imath}_n \tag{5}$$

The Dot product on tensors generalizes the classical concept on vectors (which is also called *inner* product). It takes the last order of the first argument and the first order of the second argument. The dot product between a tensor of order n and a tensor of order m is a tensor of order n+m-2. In the case of second order tensors, the result will also be a $2 + 2 - 2 = 2^{nd}$ order tensor:

$$\mathbf{U} \cdot \mathbf{T} = \sum_{m=1}^{3} \sum_{n=1}^{3} \sum_{k=1}^{3} \sum_{l=1}^{3} U_{mn} \, T_{kl} \, (\vec{\imath}_n \cdot \vec{\imath}_k) \, \vec{\imath}_m \otimes \vec{\imath}_l = \sum_{m,l} \Big(\sum_{n} U_{mn} \, T_{nl} \Big) \vec{\imath}_m \otimes \vec{\imath}_l \tag{6}$$

where the last equality holds because $\vec{\imath}_n \cdot \vec{\imath}_k = \delta_{nk}$. This can be easily rewritten in components as: $(\vec{\vec{U}} \cdot \vec{\vec{T}})_{ij} = \sum_k U_{ik} T_{kj}$. In the case of vectors, the dot product assumes the shape in equation (7): the scalar is a $1 + 1 - 2 = 0^{th}$ order tensor.

$$\vec{u} \cdot \vec{v} = \sum_i u_i v_i \tag{7}$$

The Double-dot product on tensors combines the last order of the first tensor with the first order of the second tensor as the dot product. In addition, it also combines the last but one of the first tensor with the second of the second tensor:

$$\mathbf{U} : \mathbf{T} = \sum_{m=1}^{3} \sum_{n=1}^{3} \sum_{k=1}^{3} \sum_{l=1}^{3} U_{mn} \, T_{kl} \, (\vec{\imath}_n \cdot \vec{\imath}_k) \, (\vec{\imath}_m \cdot \vec{\imath}_l) = \sum_{m,n} U_{mn} \, T_{nm} \tag{8}$$

0.2 Gradient

The gradient of a scalar function $f(x_1, x_2, ..., x_n)$ is a differential operator, denoted with the symbol ∇, which defines a vector field whose components are the partial derivatives of f. In a Cartesian reference system then:

$$\nabla f = \frac{\partial f}{\partial x_1}\vec{\imath}_1 + \frac{\partial f}{\partial x_2}\vec{\imath}_2 + \frac{\partial f}{\partial x_3}\vec{\imath}_3 = \sum_i f_{,i}\,\vec{\imath}_i \tag{9}$$

The gradient of a scalar field is a vector field that points in the direction of the greatest rate of increase of the scalar field, and whose magnitude represents the greatest rate of change.

0.3 Divergence

The divergence $\nabla\cdot$ is a differential operator which associates a scalar to a vector $\vec{v}$ such that, in an orthonormal reference system:

$$\nabla \cdot \vec{v} = \frac{\partial v_1}{\partial x_1} + \frac{\partial v_2}{\partial x_2} + \frac{\partial v_3}{\partial x_3} = \sum_{i,k} \delta_{ik} v_{i,k} \tag{10}$$

0.4 Laplacian

The Laplacian Δ is a differential operator which associates to a twice-differentiable real-valued scalar function $f(x_1, x_2, ..., x_n)$ the scalar field (in a Cartesian reference system):

$$\Delta f = \frac{\partial^2 f}{\partial x_1^2} + \frac{\partial^2 f}{\partial x_2^2} + \frac{\partial^2 f}{\partial x_3^2} = \sum_{i,k} \delta_{ik} f_{,ik} = \sum_k f_{,kk} \tag{11}$$

The Laplacian is also defined as the divergence of the gradient: $\Delta = \nabla \cdot \nabla$

0.5 Partial and total (substantive) derivative

Let the value of a property per unit mass be defined by ϕ. The total or substantive derivative of ϕ with respect to time following a fluid particle is:

$$\frac{D\phi}{Dt} = \frac{\partial \phi}{\partial t} + \frac{\partial \phi}{\partial x}\frac{dx}{dt} + \frac{\partial \phi}{\partial y}\frac{dy}{dt} + \frac{\partial \phi}{\partial z}\frac{dz}{dt} \tag{12}$$

since dx/dt, dy/dt and dz/dt are the component of the vector $\vec{u} = \sum u_i\,\vec{\imath}_i$, equation (12) can be written as:

$$\frac{d\phi}{dt} = \frac{\partial \phi}{\partial t} + \vec{u} \cdot \nabla(\phi) \tag{13}$$

where the right hand side is composed by a time-derivative term $\partial\phi/\partial t$ and a convective term $(\partial\phi/\partial x_i)\,u_i$

0.6 The Gauss theorem

For a vector $\vec{a}$ the Gauss theorem states:

$$\int_V \nabla \cdot \vec{a} \; dV = \int_A \vec{n} \cdot \vec{a} \; dA \tag{14}$$

where V is a control volume, A is the area of its boundaries and $\vec{n}$ the outward unit vector normal to the boundaries.

Chapter 1

Introduction

The sails of a yacht act like an engine, with the role to convert the energy of the wind into propulsive force for the yacht. Modern yachts generally adopt two configurations, the first for sailing upwind with a mainsail plus a fore-sail such as the Genoa or the jib; and the second for sailing downwind, in this case using Spinnakers or Gennakers (Figure 1.1).

High technology upwind sails are built as thin laminates including high resistance fibres oriented along the distributions of the internal stresses. Typical materials for this kind of sail are Mylar films with carbon or Kevlar fibres. Upwind sails mainly work as thin wing profiles at moderate angles of attack; they are therefore optimized for generating lift. Although the material and the construction technology for this kind of sail allow a fine shape control, it is not uncommon to see racing yachts where the mainsail is constituted by a rigid wing. This is the case for instance of the actual America's Cup class, where several rigid but independent panels allow an even finer control over the whole span of the sail. The effectiveness in terms of lift production of such a configuration was shown during the 33^{rd} America's Cup race.

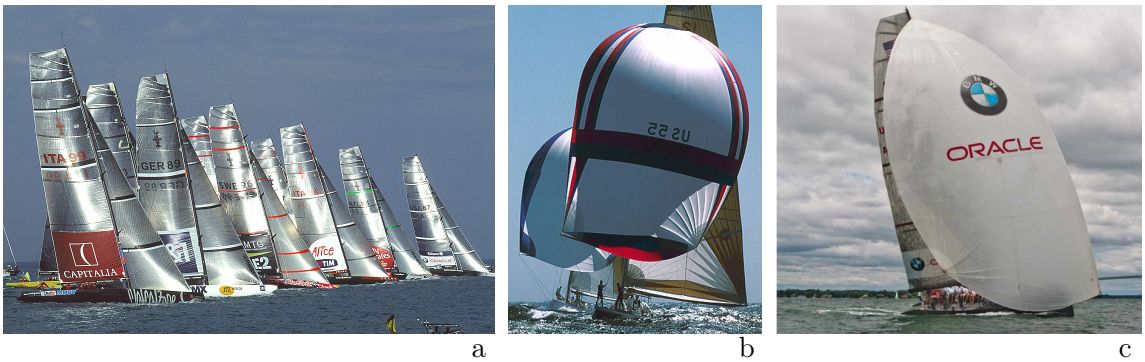

a b c

Figure 1.1: Types of sails: *a*: Upwind sails, *b*: Symmetric Spinnakers and *c*: Gennaker. Figures *a* and *b* are courtesy of *Christian Février*

Downwind sails are built as an assembly of initially flat nylon panels. They mainly operate as drag devices, where some lift generation is involved: the flow is then subjected to

separation bubbles and large zones of separation. In addition, due to characteristic sizes and velocities, transition to turbulence arises close to the leading edge, often in conjunction with the development of a separation bubble [21]. In addition to the external unsteadiness induced by the environment, such as the gusts or the motions of the boat, downwind sails can be subjected to vortex shedding induced unsteadiness.

Downwind sails are supported on three points, two of which are fixed and the third is held in place with a sheet. Due to the limited thickness and the type of the support, they are subjected to large displacements, which determine large differences between the initial design shape and the shape of the sail in operation, also called the *flying shape*.

The *wrinkling* is a buckling related phenomenon affecting the deformation of thin fabrics in general, and of downwind sails in particular. Wrinkling consists of the formation of oscillations on the fabric surface when particular combinations of stresses/boundary conditions arise. The development of wrinkling mainly begins on the stress concentration regions close to the supported points, but it is observed that it propagates for about one third of the sail from each side.

The problem of the analysis of the sail behaviour has interested engineers for at least the past 40 years. This problem has a direct impact on the performances of the yachts, where any small improvement can be crucial for the winning of the race. It is not uncommon in fact to see winning margins of less than 1% of the entire duration of the race [22]. In the same time, the problem is very challenging because it includes a variety of different phenomena, the complete understanding of which is far from being achieved.

The first attempts to simulate yacht sails in the literature generally neglected the structural deformation, and they concentrate in the use of inviscid codes based on the lifting line theory [23], panels codes or vortex lattice codes [24]. Only during the past 10 years the majority of authors started to use Reynolds Averaged Navier Stokes (RANS) solvers with turbulence models [25]. The number of works approaching the detailed analysis of downwind sails are however still limited, and only a few authors reported realistic estimates of the accuracy of the calculations [26].

Initial approaches to the structural deformation of the sails adopted simplified models [27], [28]. In a second phase the sail structure was approximated with general finite elements such as plates [29], [30] and in more recent years the Constant Strain Triangle (CST) membrane has become relatively popular [31], [32]. The use of shells was finally proposed [13].

The calculation of the structural deformation is generally used in a coupled framework, where the load calculated by the aero-dynamic code is the input for calculating a new deflected shape to be used in the fluid dynamic analysis. This type of coupling, used for finding a steady equilibrium shape, has generally been adopted for inviscid fluid codes. Mainly for a matter of computational cost and the intrinsic difficulty of the problem only a few authors in recent years attempted the steady coupling with RANS solvers [33].

The aim of this research is to improve the numerical analysis of downwind sails. In particular, in terms of the structural analysis the use of the shell finite elements allows to remove the ambiguity occurring when adopting membrane elements, e.g. the choice of a wrinkling model.

From a fluid point of view, the use of unsteady Reynolds Average Navier-Stokes Equations (RANSE) solvers with turbulence models provides a good compromise between accuracy and computational cost. Computations will be performed to demonstrate the prediction performances of these methods and validate the analysis to be used for the coupled fluid structure interactions. In addition, the impact of the wrinkles on the flow both in terms of the physics of the phenomenon and the numerical outcomes will be investigated.

From a structural perspective, the use of appropriate non-linear shell finite elements will be preferred to the generally adopted CST membrane, which is a rather simplified element and evidence shows this element produces inaccurate results. The membrane model in general completely neglects the bending stiffness, and it is therefore unable to take into account phenomena such as the wrinkling, which is controlled by the bending stiffness. Attempting to analyse situations where wrinkling occurs with such a technique generally ends up in singularity of the solution, which can only be avoided by means of *ad-hoc* wrinkling models. In the present approach the modelling of the structure is performed using MITC4 shell elements. Such a finite element considers all the relevant stiffness components, and it naturally allows for the simulations of wrinkled fabrics. Shell finite elements have been used in the past for simulations involving the wrinkling, and the accuracy of such a model for simplified test cases [5] was shown to be satisfactory. In this work the suitability of using shell elements for reproducing the wrinkling in sail-type configurations will be investigated.

The fluid and the structural calculations will then be coupled in a fully unsteady environment such as the Arbitrary Lagrangian Eulerian (ALE). The difficulties of this kind of coupled analysis will be shown and discussed, with particular emphasis on the sail type configurations.

Several test cases will be presented and validated with reference solutions.

The thesis is structured in four main Chapters. The first Chapter draws a bibliographic review. This is sub-divided in four Sections, each detailing the state of the art for fluid, structure, and fluid-structure interaction methods to sail analysis. An additional section is reported, which reviews the major works published in the field of wrinkling modelling and the direct simulation of wrinkled structures. The three following Chapters discuss the mathematical and the numerical modelling for the fluid dynamics, the structural mechanics and the fluid-structure interactions. Each one of these Chapters is sub-divided into three main Sections: a theoretical review, the numerical methods, and the presentation of some test cases and applications examples. The theoretical review has the specific intention of presenting the mathematical models, which constitute the base for the following part on the numerical methods. The Section on the numerical methods links the mathematical model and the numerical analysis. The focus is then particularly placed on the detailed explanation of the discretization techniques. The scope of the last Section is to illustrate the prediction performance of the adopted methods and to validate the results using test cases which are relevant for sail analysis.

Major achievements have been obtained in all the fields of interest, and in particular it should be mentioned the work done in the fields of the structural analysis and the fluid-structure interactions. Several previous works on sail analysis simulated the sail-structure using the membrane model. The use of the shell model allowed fine progresses in the representation and the understanding of the phenomena involved in the structural deformation of the sail. With this approach the analysis results in substantial improvements in terms of the accuracy and the possibility to reproduce fine details such as the wrinkling. A large amount of this work has been dedicated to opportunely calibrate the calculations, which are affected by several sources of instability and are therefore likely to diverge. A complete Arbitrary Lagrangian Eulerian (ALE) framework has then been adopted for performing unsteady fluid-structure interactions. Several test cases are presented, which validate the method against reference results, and its suitability is shown in typical sail-type applications with turbulent flow.

Chapter 2

Bibliographic review

The problem of the simulation of the behaviour of sails has interested engineers for at least the past 40 years. Extensive efforts have been placed in the numerical simulation of sails, applying computational methods primarily derived from the aeronautical research. A variety of methods has been adopted and developed over the years for the analysis of sails, and it is clear that sail science has always been at the cutting edge of the simulation technology. Today the numerical simulations are one of the most valuable supports to the design, and the requirement for accurate analysis is higher than ever.

The Chapter is organized with four main Sections: fluids, structure, fluid-structure interactions, and the wrinkling. The first Section regarding the fluid dynamics is further sub-divided into three main Sub-sections: Potential methods, RANS upwind and RANS downwind.

2.1 Fluid Dynamics Literature Review

2.1.1 Potential methods

One of the first works about a scientific approach to sail design was published by Milgram in 1969 [23]. After a general description of the physical phenomena involved in sails, for the first time a sail design method was proposed using a lifting line code. After this paper the potential theory has been extensively adopted for representing upwind sails, and numerous methods have been proposed, based upon panels [30], lifting surfaces or vortex lattice method [32]. These techniques are in fact able to describe well irrotational fields, an assumption which can be accepted for representing the general flow around a streamline-shaped object such as upwind sails. Unsteady calculations have been performed with such methods by Fukasawa [30].

Due to the high computational efficiency, these methods are particularly suitable for shape

optimisation purposes, such as the inverse method proposed by Greeley [34] or Boote [27]. These methods are based upon similar ideas: the *optimum* lift distribution is calculated using some sort of optimisation routine, where the independent variable of the cost function is represented by the shape of some sections of the sail. The method was further extended by Pilate [35] for a full 3D sail design. The author was then able to develop a theory which establishes a relationship between the camber of the sail and the resulting pressure map. The pressure field could then be optimized by iteratively modifying the camber distribution.

Speer [36] proposed a two-dimensional application of the software XFOIL for the analysis of the leading and trailing edge separation bubbles. Detailed investigations about the flow separation were also performed by Veiga [37], who coupled a panel code with an integral boundary layer method for viscous-inviscid interaction flow analysis. Finally the mast-flow interaction was investigated by Coiro [38] and then by Hobbs [29], who used the source-doublet method PALISUPAN [39] and validated its work using the experimental results of Wilkinson [21].

Despite the fact that these methods are relatively old and limited, numerous recent works still take advantage of the computational efficiency and the relative ease in coding [40]. The results of these methods have also been improved with corrections accounting for viscous effects [37].

Today however the use of Reynolds Averaged Navier Stokes equation solvers is generally preferred, because of the higher accuracy in the description of the turbulent flow. Although the computational expense is not comparable with a potential method, a RANS calculation is nowadays affordable for the majority of computers and university clusters.

Even for upwind sails however the validity of the assumption of the irrotational flow was shown to be quite poor [41]. Realistic upwind sails are in fact generally over-trimmed for maximising the driving force, especially in light-wind conditions. A potential code would then determine a substantial over-estimation of the performances of the sail, although results can be substantially improved by the viscous corrections.

2.1.2 RANSE method for upwind sail analysis

Compared to the inviscid codes analysed in the previous section, which generally solve a *Laplace* equation, RANS codes solve the *Navier-Stokes* equation (see Section 3.1). RANS techniques became available and cost effective for engineering analysis in the early 90's [42], and very soon they have been adopted for sail analysis.

Miyata in 1999 [43] used a finite volume RANS method and tested different turbulence models for sail-type applications; The Baldwin-Lomax turbulence model was finally chosen and used for performing a parametric study over several sail shapes. The author declared an over-estimation of the computed thrust force coefficient of 28% an under-estimation of the side force coefficient of 18% compared to wind tunnel data.

Two years later Collie [25] performed a systematic investigation on eight turbulence models with particular reference to sail type applications. They concluded that the Spalart-Allmaras turbulent model should be used for upwind sail configuration, and the Shear Stress Transport (SST) turbulence model is the most appropriate for downwind sail analysis. The application of such a review was shown in [44], where 2D unsteady computations were performed using FLUENT and CFX and a number of the most popular turbulence models ($\kappa - \epsilon$, realizable $\kappa - \epsilon$, $\kappa - \omega$, SST). The most accurate answer was obtained with the SST turbulence model.

Graf [45] analysed a full 3D rig using CFX and the $\kappa - \epsilon$ turbulence model. The design of the mast section used for the analysis of the complete rig was previously optimised with a parametric 2-dimensional investigation.

A comprehensive description of the flow details was presented by Parolini [46]. The laminar-turbulent transition region was estimated using XFOIL coupled with the 3D Boundary layer solver for non-separated flows called 3C3D. It was then possible to estimate the transition point to set in the RANS calculation, which was performed with FLUENT and the $\kappa - \epsilon$ turbulence model. The interaction with the hull and the free surface of the water was taken into account.

Krebber [47] considered the combined effect of the sails, the rig and the hull; the flying shape of the sail was determined by real-scale measurements. Around this configuration the authors conducted a parametric study on sails camber and twist, thus identifying some response surfaces for the aerodynamic coefficients and the centre of effort. The computations were performed with CFX and the $\kappa - \epsilon$ turbulence model on a fully structured grid. A rather similar procedure was followed by Schneider [48] with an in-house code adopting the Spalart-Allmaras turbulence model and by Querard [26] with CFX and the SST turbulence model. In the case of the latter authors, the flying shape of a sail model was acquired in the wind tunnel.

Chapin [49] presented a RANS comparison of the test case experimentally analysed by Wilkinson [21], with very good general agreement. The author used for his investigations FLUENT and the Spalart Allmaras turbulence model with a hybrid mesh computational

domain. The case is specifically analysed to serve as a validation for the consequent RANS-based mast-sail design optimization. Wilkinson's data then became a reference for the upwind sail aerodynamics validation in later works such as [50] and [51], both performed using CFX and the SST turbulence model. General good agreement is found for this test case between the experimental and the presented numerical results, which are however influenced by the lack of a transitional model.

Several numerical/experimental comparisons and validations have been presented for upwind sails in the last few years, and the scatter which is found between the various declared accuracy is indicative of how much work should still be done in the field. Yoo [52] obtained differences of about 83% in lift and 59% in drag with a structured mesh of 1.7 millions cells and y^+ values smaller than 50. Ciortan [53] obtained 86% in lift and 50% in drag using grids of 1 million of tetrahedra and prismatic layers thus realising $135 < y+ < 270$. Querard [26] showed differences lower than 12% in lift and 24% in the drag using CFX, SST turbulence model on a 2.4 millions hexahedra grid and $y^+ \approx 10$. Similar results were published by Masuyama [54] using a structured mesh of 0.5 millions hexahedra and $y^+ \approx 1$. Also Paton [50] presented similar data using CFX and the SST turbulence model for $y^+ \approx 3$. Viola [55] proposed results obtained with a grid consisting of 1.5 millions tetrahedra and prismatic layers, thus realising $y^+ \approx 1$. In this case the declared differences between the numerical and the experimental results are within the 3% in lift and 6% in drag.

2.1.3 RANSE method for downwind sail analysis

The literature in the field of the downwind sail aerodynamics is not extensive, primarily because it is not possible to analyse the main involved phenomena – separation and recirculation – with potential codes. The approach of this class of problems began therefore with the use of RANS solvers in the mid 90's. The analysis of downwind sails requires high computational efforts and the required computational resources have become available in recent years only.

The first work on downwind RANS aerodynamics has been published by Hedges [56] in the mid 90's using code called CFDS-FLOW3D and the κ-ϵ turbulence model. The numerical model was built as a relatively coarse structured mesh: the sail was described with less then 400 elements. The sail was set at 90° and the simulations did not consider the hull nor the rig. Despite the limited resources, the numerical/experimental comparison gave satisfying results, about the 15% in terms of lift and 3% in terms of drag.

A few years later Collie [57] used CFX and the SST turbulence model reviewed and

validated in previous works [25] for performing a parametric study over 2D spinnaker sections. The investigated parameters regard the shape in terms of camber, draft and the angle of attack, as well as the influence of a mainsail section over the general flow.

The sail-to-sail interaction effect has extensively been approached for upwind sails using potential codes [24]. This effect is often referred to as *blanketing*, when a boat sailing upwind covers the wind to a downwind sail boat, slightly decreasing the power available to the latter. Parolini [46] was the first to perform extensive calculations on the blanketing effect for downwind sails, and the outcome of the research was directly applied during the races for the 33^{th} America's cup. The author made calculations up to 10 millions cells – a resolution considered at the time as extreme – using Fluent and the κ-ϵ turbulence model.

Graf [33] presented some coupled calculations on spinnaker configurations. The fluid was analysed using CFX and the SST turbulence model. Comparison with experimental data from the wind tunnel are then reported in [58] with particular respect to mainsail/ symmetric spinnaker configurations for coupled fluid-structure calculations. The resulting accuracy lies around the 20% in terms of lift and 4% in terms of drag. Similar works were presented in the same period by Durand [59] and Paton [50]. Further comments on these coupled calculations will be given in the fluid structure interactions bibliographic review.

Lasher [60], [61] performed parametric variations on 12 spinnaker shapes, analysed with six different turbulence models and two grids (0.33 millions and 0.14 millions of tetrahedra for $30 < y^+ < 120$. The comparison of the numerical results with wind tunnel data was found to be between 11% and 7% in lift and between 12% and 5% in drag.

Viola [62] finally proposed some impressive calculations using – more than a billion elements – high resolution grids and various turbulence models. The author concluded that for the higher resolution grids (over 10^7 cells) the beneficial effect of the turbulence model decreases substantially, and purely laminar simulations produce accurate results. It is suggested that this happens because the smallest scales of the turbulence do not significantly affect the general flow, thus solving the Navier-Stokes equations with a high resolution grid might accurately represent the general flow development, as in a filtered DNS approach.

Comparisons of the results obtained with the RANSE and the DES methods were presented in [63]. The author declared differences exceeding 65 % in terms of drag, and exceeding 35 % in terms of side force.

2.2 Structural Literature review

Compared to the fluid dynamics calculations, the interest for the structural deformation of the sails started about 20 years later. This is mainly due to the fact that the deformation has been considered a higher order phenomenon, at least for the upwind sails. Also, for a number of years sails have been an application domain for the aerodynamics, which could directly apply the knowledge achieved from the aeronautical research.

A first example of the application of Finite Element techniques to the analysis of sail fabric is proposed by Atkinson [64], who proposed a calculation method for a mast-sail interaction. The sails are modelled with the curvilinear four node non-linear membrane elements suggested by Zienkiewicz [65], and an un-stayed mast is modelled. The wind loads are calculated using a lifting surface code and the static equilibrium is found by successive iterations between the fluid and the structural solver.

About three years later Boote [27] proposed an approach for the structural calculation of the mast. The wind loads were in this case calculated with a lifting surface code providing the pressures on the sail. The load to be applied to the mast was then derived using a rather simplified but clever scheme: a slack was imposed *a priori*, under the assumption that this parameter can be easily – empirically – evaluated. The sail was divided into horizontal stripes, the pressure distribution of which was known via the lifting surface code and the pressure was transformed into an applied load. The sail section was then divided into a number of segments, each supporting the calculated constant pressure load. Once geometrically expressed the equilibrium of the segment, it was then possible to assemble the whole set of segments together and calculate a deflected shape. The slack so calculated was compared with the initial one, and the procedure was repeated until convergence. Once this was done for all of the discretized sail sections, it was possible to derive the load to be applied to the mast.

Cable-nets structure have also been used for the analysis of sails. This is the case for Hauville, Mounoury et al. [66], Fantini [67].

Triangular elements were introduced by Fukasawa [30]. An extensive evaluation of the performances of a number of structural elements was performed by Hobbs [29], who implemented and validated linear and non-linear elements such as general 3D elements, plates and membranes the formulation of which is found in [68]. Membrane elements were implemented in the formulation of [69], the same chosen several years later by Coiro [38]. With particular reference to the design of the mast, the author identified significant differences if the loading is assumed as a constant load or if it derives from aero-elastic analysis.

Triangular elements became then quite popular in sail science, and in particular the Constant Strain Triangle (CST) non-linear formulation [70] [71] has extensively been adopted, also in recent years. Heppel [72] used a membrane theory which relates the Gaussian curvature with the strain and introduced the wrinkling in sail analysis using the wrinkling model proposed by Lu [73]. The code he developed is extensively used by sail designers. Graf [33] and Renzsch [58] implemented the Constant Strain Triangles proposed by Arcaro [74]. Two years later the code was further modified for taking into account the wrinkling [75] using the wrinkling model proposed by Kang[76]. CST elements were used also by Malpede [32], Trimarchi [1], Roux[31] and Durand[59].

Trimarchi [51], [2] suggested using some validation examples that the CST element might – in some configurations – produce inaccurate results, and proposed the use of MITC4 shell elements instead. A similar choice was independently done by Lombardi[19]. The simulation of the wrinkling development on sail-type structures was investigated by Trimarchi [3].

2.3 Fluid Structure Interactions Literature Review

As it was stated in the previous section, the structural deformation of the sails started to be taken into account from the late 70's. It was then possible to couple the fluid and the structural calculations. Initially – and for a long time – a steady coupling was performed. In such a coupling the fluid calculation is used to calculate the loads. These are opportunely converted and used within the structural framework for the calculation of a deformed shape. Generally the iteration loop converges in a few iterations (6 – 10) and the answer is a steady equilibrium shape for the coupled system.

Numerous examples can be found of this type of coupling [64] [27] [77], which is still adopted today [32] [1]. Examples can be also found, when this type of coupling is used in a quasi-static environment, where the unsteadiness is externally induced, for instance by the motion of the boat in the seaway [30] or by the manoeuvring of the crew [31].

In recent years the majority of authors proposed the coupling of a structural code with RANS fluid codes. Nothing changes in terms of steady coupling, and several works can be found reporting this approach using different fluid and structural solvers. For examples Paton, Heppel et al. [50] coupled the code Relax [72] and CFX for sails of the type used for the Volvo Ocean Race class; Renzsch, Muller et al. coupled FlexSail with CFX [58] and presented results with particular reference to spinnakers. Quasi-static approximations are often accepted and examples can be found of the simulation of the trimming process [58].

Several works reported comparisons between the coupled simulations and the experimental data, and often excellent agreement was found between the measured and the calculated forces [75], [59] . This type of steady coupling is nowadays an – almost – standard procedure used by designers for helping in the decision-making and the optimization process [78], [32].

Unsteady coupling is still a challenging procedure in sail science, because of the computational effort and the particular configurations, which determine a fluid-structure system which is likely to be unstable. A review on the types of coupling, as well as the sources of instability and the strategies adopted to overcome the problem is discussed in Chapter 5; here it is enough to recall the two main coupling algorithms: the *explicit* and the *implicit*. In an *explicit* coupling, the fluid and the structural calculations are performed only once per time-step. This kind of algorithms [79] generally has very high computational performances, but it might results in unstable calculations.

The instability being primarily introduced by artificial effects due to the incompressibility [80], one way to overcome the problem is to use compressible flow solvers. Example of the application of compressible Large Eddy Simulation (LES) solvers for fluid structure interaction analysis of a super-sonic parachute has been presented by Karagiozis [81] using *explicit* coupling. In the framework chosen for the analysis, the structure is represented in the fluid domain using a Ghost-cell approach and it is thus treated as a *free-slip* boundary condition (see the Chapter 5 and Section 5.2.7) .

In recent years the research on *explicit* algorithms has made progress, and algorithms have been formulated, which guarantee the stability of the system using incompressible flow even for conditions which are potentially unstable [82].

A second family of coupling algorithms, unconditionally stable but computationally more expensive is the *implicit* coupling. In this case sub-iterations are performed between the fluid and the structure, until a convergence criterion is met (see Section 5.1.5). Several works have been published on the stability of the coupled systems [80] [83], the main conclusions of which are reviewed in Section 5.1.3.

Examples of *implicit* coupling for sail type applications can be found [19] and in Chapter 5, where a review is also given on the coupling algorithms and the frameworks which are generally adopted for the coupled calculations.

2.4 Wrinkling Literature Review

The first attempt to the analysis of wrinkled membranes was the tension field theory proposed by Stein [84], who suggested to analyse the mean deformation induced by wrinkling rather than attempting to reproduce the details of a wrinkled region. The author suggested then that when wrinkling arises, one of the principal stresses should be imposed equal to zero, the deformation of the region can be calculated by means of a modified constitutive relationship, where the strains transversal to the direction of the wrinkles are mainly induced by the Poisson shrink. In the article, the relevant equations are formulated for the general case of a wrinkled membrane, and some simplified examples are reported, such as the case of a flat membrane with in plane loads and moments, or a cylinder loaded with internal pressure.

Wu [85] proposed a complete formulation for the analysis of wrinkling in the context of the finite plane-stress theory for isotropic membranes. Wrinkling is approached in 3 steps using the initial undeformed surface, a pseudo-surface (1 to 1 mapped) describing the deformed surface but without wrinkling, and the actual wrinkled surface. All the quantities are calculated on the pseudo-surface and then reported to the wrinkled surface. The main assumption – valid for isotropic materials – is that principal directions associated with the pseudo deformation field are equivalent to those associated with the wrinkled (true) stress field. The shape of the wrinkles is not detailed, but the answer is given in terms of the equivalent deformation of the pseudo surface.

Miller [86] introduced the idea that not all of the membrane is interested by wrinkling, and proposed to adopt a zonal approach. A wrinkling criterion is therefore proposed: if a wrinkled region is identified, this will be treated using one of the *ad-hoc* modified constitutive relationship. Three constitutive relationships are then used, for the slack, taut or wrinkled membrane. The wrinkling criterion is based on the evaluation of the principal strains.

Contri [87] suggested to use a wrinkling criterion based upon the principal stresses. The calculation is included in a finite element framework and an iterative procedure for the wrinkling. Once a first solution has been computed, the negative stresses are neglected and the resulting deflected shape is obtained with the new imposed stress field. Experimental validation examples are reported for the case of a wrinkled air-bag.

A similar criterion was chosen by Lu [88] for the analysis of the dynamics of a parachute. In this case, the wrinkling directions are also computed. Numerical examples are validated using analytical solutions, and qualitative comparisons show the impact of the wrinkling modelling in the shape computation process.

A new wrinkling criterion, based upon both the principal stresses and strains was introduced by Roddeman[89]. With this new criterion it was finally possible to remove the assumption that the principal directions associated with the pseudo deformation field are the same as those associated with the wrinkled (true) stress field. If in fact one or more negative Cauchy stresses are calculated within an element, it is not immediately possible to determine whether the membrane is wrinkled or slack. Using the Green-Lagrange strain tensor removes this uncertainty: if both the principal Green-Lagrange strains are negative, the membrane is slack; if only one principal strain is positive the membrane is wrinkled. The direction of wrinkling can therefore be identified, searching for the angle verifying the condition: $n_1 \cdot \sigma \cdot n_1 = 0$, $n_2 \cdot \sigma \cdot n_2 > 0$.

The opportunity of using such a formulation was detailed later by Kang [76], who showed that criteria based on the principal stresses or on the principal strains alone can cause wrong predictions of wrinkled regions. An algorithm is proposed, which allows for the calculation of the wrinkled stress field and for the direction of wrinkling. The same wrinkling criterion was chosen later by Stanuszek [90], and Lee [91].

Direct representation of the wrinkling pattern using shell finite elements was first proposed by Tessler [92]. The authors used the reduced integration Mindlin shell elements implemented in the commercial software Abaqus. Wrinkles are generated on a flat Mylar film with imposed boundary displacements and the numerical solution appear to adequately capture the experimentally measured out-of-plane wrinkled shape. The numerical out-of-plane solution was initialised using an adequate guess displacement map, from which the final solution is shown to be independent.

A similar approach was undertaken by Wong [5], who published a series of articles on the wrinkling from a numerical, experimental and analytical perspective. Validation examples are given with particular reference to flat membranes where wrinkling is induced by imposed displacements. Simulations on inflatable wrinkling structures such as parachutes have been proposed by [81] and [93] using the shell elements formulated in [94].

In terms of sail structural analysis, however, only a few works considered wrinkling, and to the author's knowledge no attempt was made for directly simulating the wrinkling development in sail-type structures using shell elements. Muttin [95] proposed a quadrilateral finite element for wrinkled isotropic membranes, with particular reference to sail design analysis. A modified constitutive matrix is proposed for taking into account the wrinkling, and the wrinkling criterion is based upon the principal stresses. Validation examples are shown,

derived from [89]. Some applications examples are then given with respect to a gennaker geometry, discretized with 16 finite elements. Heppel [72] derived a formulation for wrinkled membranes from [88] and implemented this approach in the code RELAX, currently used by sail designers. Renzsch [75] adopted the wrinkling model [76] for modifying the code FlexSail, which primarily adopts the membrane definition proposed by [74].

2.5 Summary

Based on the review presented here, the fluid will be analysed using a Finite Volume method and turbulence modelling. Although some authors proposed in recent years the use of more advanced methods such LES or DES, the drawback represented by the computational cost seems prohibitive for the scopes of the present work.

The membrane model, traditionally used for the simulation of the structural fabric will be substituted with the shell model. This allows a direct representation of the wrinkling, and thus improves the prediction performances, because with the shell model no wrinkling model is required. Comparisons between the accuracy of the two models will be also presented in terms of the global deformed shape.

Unsteady fluid structure interactions will be considered, and the Arbitrary Lagrangian Eulerian (ALE) framework will be chosen. Although some authors use a ghost-cell type approach, here high accuracy is required when calculating the boundary layer development and the separation point. An implicit coupling will be chosen, which guarantees the stability of the calculations.

Chapter 3

Fluid dynamics

This chapter discusses the fluid dynamics, both theoretically (see Section 3.1) and in terms of the techniques available for the numerical modelling (see Section 3.2). The last part of the chapter (Sections 3.3 and 3.4) is dedicated to the application of the reviewed techniques to a number of test cases. The role of these computations is to give an insight on the accuracy and the type of analysis which can be afforded with the *state-of-the-art* solvers with particular reference to fluid phenomena relevant for sail analysis.

Several techniques are suitable for the Computational Fluid Dynamics (CFD), but two main families can be identified: the potential flow solvers [96] and the Navier-Stokes solvers [20]. In the first case the calculation solves for a Laplace Equation, but important phenomena from a sail perspective such as the separation can not be taken into account. Navier-Stokes equations provide a more complete description of the flow and can be used for the simulation of all the fluid phenomena. Navier Stokes equations detail the conservation of momentum and are typically presented for a Newtonian fluid which represents a linear relationship between stress and strain. These equations must be enforced with the continuity equation, which states the mass conservation. The Laplace equations are a sub-set of the Navier Stokes formulation which assumes inviscid, incompressible and irrotational flow [6].

These partial differential equations can be solved using different techniques, but three main families can be identified: finite differences [20], finite elements [97] and finite volumes [6]. In the first case the quantities are directly discretized on a computational grid; in the finite element framework the quantities of interest are transformed in terms of energy using a variational formulation. With the finite volumes the equations are modified using the Gauss theorem (Section 0.6) to be solved for the fluxes, thus verifying the conservation of the momentum (see Section 3.2). Although the three different techniques are generally suitable for the solution of the flow, the larger part of the CFD community prefers today the use

of finite volumes solvers. For each of the above mentioned discretization schemes, different solution strategies can be adopted, as well as different time/space discretizations. The solution can be afforded at once, by solving a system of equations considering the whole set of the unknowns of the problem – namely the pressure and the velocity – at some grid nodes. Another strategy is the Semi-Implicit Method for Pressure-Linked Equations (SIMPLE) type approach (see Appendix A.11). In this case the pressure and the velocity are separated and iteratively solved, thus avoiding the overload represented by the solution of the whole system of equations. Different strategies can then be adopted for avoiding non-physical – but computationally admissible – fields, such as the use of staggered or collocated grids (see Appendix A.10). Also different time marching scheme can be chosen in the case of unsteady or quasi-steady computations.

Different approaches have been proposed for treating turbulence, are all part of two big families: the turbulence modelling [42] or the direct numerical simulation (DNS) [98]. The DNS directly solves all the scales of the turbulence using an appropriate grid; in the case of engineering analysis however the DNS is not affordable in terms of computational effort. The use of turbulence models with for adequately modified Reynolds Average Navier-Stokes Equations (RANSE, see Section 3.1.4) is a valid alternative for the numerical approximation of engineering flows. Several hybrid methods are today more and more suitable for increasing the accuracy but maintaining an affordable computational cost, such as Large Eddy Simulations (LES) or Detached Eddy Simulations (DES).

Here it was chosen to use a finite volume scheme with collocated grids and a semi-projection solver. Euler, Backward and Crank Nicholson time-marching schemes have been used for the different analysis. A turbulence model (SST) is used to represent the turbulent flow development, as turbulence modelling represent a good compromise in terms of the accuracy/computational cost ratio. The calculations are performed using the finite volume implementation available in the library OpenFOAM, to date one of the most promising and powerful codes available for fluid dynamics.

Validation examples have been performed for investigating the accuracy of the fluid calculations. The flow over a bump with separation and reattachment is investigated in Section 3.3.1 using the experimental data presented in [7]. Data are reported in terms of mesh sensitivity, the wall shear stress and the velocity profile at the reattachment. The effect of a wrinkled surface on the flow is investigated in Section 3.3.2, and the numerical results are compared with the case of an equivalent smooth domain. This test is a link between the

fluid analysis and the analysis of the wrinkling development performed in Chapter 4. Finally, the experimental setting proposed by [9] is used for validating the prediction performances in terms of the flow development around a parachute canopy. The parachute is represented in Section 3.3.3 as a fixed wall, the shape of which approximates the mean deformed shape of the parachute, which is reported to evolve in time.

Evaluation on the unsteady flow generation is primarily performed following the reference solution [97], where the vortex shedding generation behind a 2D cylinder section is triggered as a function of the Reynolds number. The case is then extended to a 2D circular section, representative for a purely drag device such as a Spinnaker. In particular the force generation process is investigated with respect to the unsteadiness, which is found to generally improve the performances of the device in terms of the drag generation. Similar evaluations are then performed for 2D section, the shape of which is typical for sails such as Gennakers [57]. A 3D Spinnaker-type fixed device is analysed and the results are compared with the previous 2D cases. Some additional analyses involving unsteady flows are then reported in Chapter 5, with particular respect to fluid structure interaction analysis.

3.1 Fluid dynamics theory

In this section some of the basic concepts used for the definition of the fluid dynamics equations are reviewed. Scope of the section is to give a – as complete as possible – insight of the choices which have been done for the modelling of the fluid dynamics. Section 3.1.1 presents the derivation of the Navier-Stokes equations; a brief discussion about the turbulence and the associated phenomena is done in section 3.1.2 and 3.1.3. The methods currently available for the numerical simulation of turbulent flows such as the Reynolds averaging and the turbulence models are discussed in Section 3.1.4 Section 3.1.5. The discretization of the fluid equations via the Finite Volume (FV) method is then discussed in Section 3.2.

Finally, a practical example of the implementation of some simple calculations in the fluid domain with the Finite Volume library OpenFOAM is shown in section 3.2.

3.1.1 Derivation of the Navier-Stokes equations

The Cauchy axiom

The Cauchy axiom is the basis of all continuum mechanics. It states the concept of the traction $\vec{t}$ in differential form. Defining a force $\vec{F}$ and a moment $\vec{M}$ acting on a surface S, the

Cauchy axiom states:

$$\lim_{S\to 0} \frac{d\vec{F}}{dS} = \vec{t} \quad ; \quad \lim_{S\to 0} \frac{d\vec{M}}{dS} = 0 \tag{3.1}$$

The Momentum conservation theorem

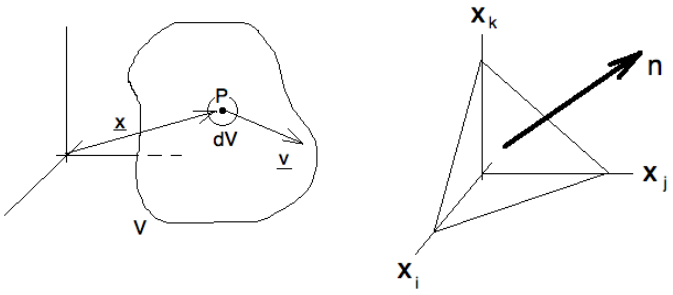

Figure 3.1: Definition of the quantities used for the momentum conservation and the Cauchy tetrahedron.

Defined the momentum of an infinitesimal volume:

$$\vec{q} = m\ \vec{v} = \rho\ \vec{v}\ dV \tag{3.2}$$

the momentum in the control volume V is calculated as:

$$\vec{Q} = \int_V \rho\ \vec{v}\ dV \tag{3.3}$$

It is possible to consider variation of quantities as the sum of two different contributions (Cauchy hypothesis), namely the surface and the mass forces:

$$\frac{d\vec{Q}}{dt} = \frac{d}{dt}\int_V \rho\ \vec{v}\ dV = \int_V \rho\ \vec{f}\ dV + \int_S \vec{t}\ dS \tag{3.4}$$

applying the equilibrium of the infinitesimal tetrahedron then:

$$\int_V \rho\ \vec{f}\ dV + \int_S \vec{t}\ dS = 0 \tag{3.5}$$

where the first term (the volume force) is negligible because its order of magnitude is ℓ^3 compared with the order of magnitude (ℓ^2) of the surface forces. Developing equation (3.5) for the surface of the tetrahedron in figure 3.1:

$$\int_{A_i} \vec{t}\ dS + \int_{A_j} \vec{t}\ dS + \int_{A_k} \vec{t}\ dS + \int_{A_n} \vec{t}\ dS = 0 \tag{3.6}$$

$$t^{-i} \cdot A_i + t^{-j} \cdot A_j + t^{-k} \cdot A_k + t^{n} \cdot A_n = 0 \tag{3.7}$$

where t^{-i} indicates the traction applied on the *i-th* face[1]. By geometrical projection it is possible to express the area of the tetrahedron as: $A_i = n_i \cdot A_n$, and dividing by A_n the equilibrium of the Cauchy tetrahedron reads:

$$t^n = t^i n_i + t^j n_j + t^k n_k \tag{3.8}$$

It is now convenient to define the stress tensor $\mathbf{T}$, the component of which T_{ij} are the stresses in direction j acting on the face of normal i. The stress on the face of normal n face results then, from equation (3.8): $\vec{t^n} = \vec{n} \cdot \mathbf{T}$

Cauchy equation

The equilibrium equation (3.5) can now be rewritten using the divergence theorem (A.5) as:

$$\int_S \vec{t}\, dS = \int_S \vec{n} \cdot \mathbf{T}\, dS = \int_V \nabla \cdot \mathbf{T}\, dV \tag{3.9}$$

thus Cauchy's hypothesis (equation (3.4)) can be rewritten as:

$$\frac{d}{dt}\int_V \rho\, \vec{v}\, dV = \int_V \rho\, \vec{f}\, dV + \int_S \vec{t}\, dS = \int_V \rho\, \vec{f}\, dV + \int_V \nabla \cdot \mathbf{T}\, dV \tag{3.10}$$

The Cauchy equation is derived by applying the second form of the transport theorem to the first term of equation (3.10) (see appendix A.3):

$$\frac{d}{dt}\int_V \rho\, \vec{v}\, dV = \int_V \rho\, \frac{d\vec{v}}{dV}\, dV \tag{3.11}$$

Equation (3.10) can be then rewritten as:

$$\int_V \left[\rho \frac{d\vec{v}}{dt} - \nabla \cdot \mathbf{T} - \rho\vec{f}\right] dV = 0 \quad \Rightarrow \quad \rho\frac{d\vec{v}}{dt} = \nabla \cdot \mathbf{T} + \rho\vec{f} \tag{3.12}$$

where the last equality is inferred, since the equation must hold for every infinitesimal volume dV.

Euler theorem

The Euler theorem states that for a still fluid the stress tensor is a function of the pressure only. This contribution is spherical, thus no shear terms are present. Under this hypothesis, the stress tensor may be rewritten as:

$$\mathbf{T} = -p \cdot \mathbf{I} \tag{3.13}$$

allowing the Cauchy's equation (3.12) to be simplified. Considering a still fluid ($\vec{v} = 0$):

$$0 = \nabla \cdot \mathbf{T} + \rho\vec{f} \quad \Rightarrow \quad \rho\vec{f} = \nabla p \tag{3.14}$$

where the last expression is demonstrated in appendix A.4.

[1]The negative sign (-1) takes into account for the direction of the traction

Stokes axioms

Stokes axioms are used for the formulation of the constitutive relationships. They express the stress components as a function of the velocity and pressure terms. Stokes axioms consist of four propositions:

- Euler's theorem: $\mathbf{T} = -p\mathbf{I}$;
- $\mathbf{T} = f(p, \mathbf{D})$, where $\mathbf{D}$ the strain velocity tensor, the components of which are expressed as: $D_{ij} = \frac{1}{2}\Big(\frac{\partial v_i}{\partial x_j} + \frac{\partial v_j}{\partial x_i}\Big)$.
- $\mathbf{T}$ is not dependent from the adopted reference system;
- The constitutive relationship is linear.

the constitutive relationship is then formulated as:

$$\mathbf{T} = \Big(-p + \lambda \nabla \cdot v \Big) \cdot \mathbf{I} + 2\mu\mathbf{D} \tag{3.15}$$

where λ, μ are viscosity coefficients ($\lambda = \frac{2}{3}\mu$). Fluids for which this description is valid are called *Newtonian* fluids.

Navier-Stokes equations

The *i-th* components of the Cauchy equation is:

$$\rho \frac{dv_i}{dt} = \rho f_i + \Big(\nabla \mathbf{T} \Big)_i \tag{3.16}$$

leading to (see appendix A.5 for the treatment of the last term):

$$\rho \frac{dv_i}{dt} = \rho f_i - \nabla p + \lambda \nabla \Big(\nabla \cdot \vec{v} \Big) + \mu \Big[\Delta v_i + \frac{\partial}{\partial x_i} \Big(\nabla \cdot \vec{v} \Big) \Big] \tag{3.17}$$

since $\nabla \cdot \vec{v} = 0$ (see appendix A.1), the final form can be rewritten as:

$$\rho \frac{d\vec{v}}{dt} = \rho \vec{f} - \nabla p + \mu \Delta \vec{v} \tag{3.18}$$

3.1.2 Turbulence

Turbulence is a fluid flow phenomenon characterised by random or chaotic behaviour. The state of a fluid flow can be characterised by the Reynolds number, defined as in Equation (3.19).

$$Re = \frac{uL}{\nu} \tag{3.19}$$

where u is the value of the reference velocity, L a length scale and ν the fluid viscosity. In general, when the Reynolds number is below some critical value (typically $Re < 2.\ 10^3$), the flow is "laminar", the motion of the fluid is characterized by a high degree of order and coherency. When the Reynolds number increases ($Re > 10^4$), turbulent behaviour is exhibited. A transition region is identified when $2.\ 10^3 < Re < 10^4$. The turbulent behaviour can be described in terms of energy transport. In a turbulent flow it is in fact possible to identify some "eddies", or zones of randomly rotating fluid. The main role of the eddies is to allow energy exchanges: the larger eddies are dominated by inertia effects and the conservation of the angular momentum is respected, because the viscous effects are negligible. In the rotation the larger eddies create smaller eddies, to which some energy is released. This progressively arises for all the scales of the turbulence, thus determining the "cascade of energy" [42]. This phenomenon continues until the motion of the smallest eddies is dissipated by the molecular viscosity. At this scale the kinetic energy is converted into heat. Due to the high rate of change of the flow arising with the eddies, the stresses in turbulent flows are much higher than in laminar flows.

Laminar flows are completely described by the Navier-Stokes equations reviewed in Section 3.1.1. Turbulent flows are also completely described by the Navier-Stokes equations. However, in order to numerically solve all the scales of the turbulence the requirements for grid resolution are prohibitive. This is the approach adopted by *Direct Numerical Simulations* (DNS) techniques, but such a type of simulation is so expensive, that it is non suitable for flows of engineering interest.

The most economic and practical way to solve turbulent flows is the *Reynolds Averaged Navier-Stokes* (RANS) approach [42], which is described in section 3.1.4. Using this statistical approach the turbulence is considered as a fluctuation of the velocity over a mean flow. Some modified Navier-Stokes Equations (the RANS Equations, reviewed in Section 3.1.4) are then solved with a minimum increase in terms of computational cost. Although the assumptions on which RANS Equations are based are strong, this approach represents a practical way to solve flows of engineering interest.

The Large Eddy Simulation (LES) approach operate a filter on the Navier-Stokes equations to reduce the range of the length scales, thus reducing the computational cost. Scales from the domain size to a filter size are resolved, where smaller scale eddies are modelled. The assumption here is then that the smaller eddies are similar for all flows, and they can thus be treated by a "sub-grid" model. The method is in between the RANS and the DNS approach

in terms of resolution, thus it requires more computational effort than the RANS approach, but the flow representation is more accurate.

Several other methods are then available, such as for example the Detached Eddy Simulations (DES). These methods are generally based upon hybrid approaches mixing RANS and LES. The purpose is of course to reduce the computational cost of LES while accurately resolving the flow details.

Table 3.1: Cost of CFD analysis in terms of required number of grid points for a three dimensional analysis

RANS	LES	DNS
Re^0	$Re^1.8$	$Re^{\frac{9}{4}}$

As a rule of thumb, the cost of a CFD solution can be estimated as in Table 3.1 (see [98], [99]), where the values are given for a three dimensional CFD analysis in terms of grid point requirements. This estimate regards the resolution of the turbulence, thus the cost of a RANS analysis is Re^0 because the turbulence is fully modelled. Of course, the grid size is still determined by the mean flow features and the geometrical resolution required.

For sail type flows, typical *Reynolds* numbers are in the range 10^5- 10^6; the values estimated in Table 3.1 can then be severely increased when performing Fluid Structure Interactions, as described in Chapter 5. For this reason it was chosen in this work to use the RANS turbulence modelling for the whole set of the computations.

3.1.3 Boundary layers

The presence of solid boundaries such as walls strongly influences the flow and in particular the structure of the turbulence. Unlike the free flow, in the close-to-the-wall region the viscous effects become predominant over the inertia forces.

The boundary layer is a region influenced by the presence of a wall. The velocity profile in this region primarily depends upon the distance to the wall, but the profiles are slightly different if the flow is laminar or turbulent. If the flow is laminar the velocity in the boundary layer follows the Blasius profile for a flat plate. In this case the outer velocity value is multiplied by a function $f(y)$, the values of which are zero at the wall and one in the far field.

In the turbulent case, the flow close to the wall is not dependent on free stream parameters, and the mean flow velocity in the boundary layer only depends upon the distance from the

wall. This is described by the so-called *law-of-the-wall*:

$$u^+ = f\left(\frac{\rho\, u_\tau\, y}{\mu}\right) = f(y^+) \tag{3.20}$$

where y^+ and u^+ are non dimensional velocity and distance from the wall, and:

$$y^+ = \frac{u_*\, y}{\nu} \quad ; \quad u_* = \sqrt{\frac{\tau_w}{\rho}}; \quad ; \quad \tau_w = \mu \left.\frac{\partial u}{\partial y}\right|_{y=0} \tag{3.21}$$

where u_* is the friction velocity at the nearest wall, y is the distance of the nearest wall, ν is the kinematic viscosity of the fluid and τ_w the wall shear stress. Reference experimental

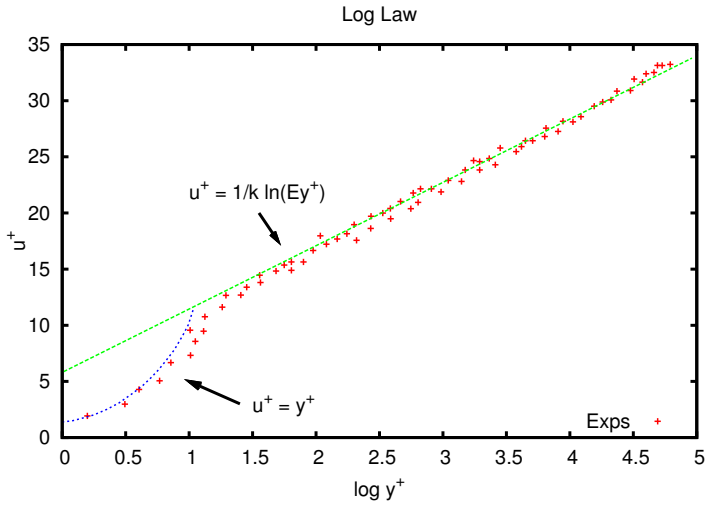

Figure 3.2: Velocity distribution near a solid wall in turbulent flow. k and E are calibration constants valid for all turbulent flows: k=0.4; E=9.8. See [6]

measurements in Figure 3.2 shows how the *law-of-the-wall* has different behaviour at different distances y^+ from the wall.

Three main regions can be then identified:

- *Linear sub-layer*: in this region, developed for $y^+ < 5$ the fluid is stationary. The motion is dominated by viscous shear stress, which is approximately constant and equal to the wall shear stress defined in Equation (3.21).

- *buffer layer*: viscous and turbulent stresses are of similar magnitude for $5 < y^+ < 30$. In this region arises the transition from the linear sub-layer and log-law layer

- *Log-law layer*: for $y^+ > 30$ viscous and turbulent effects are also of the same order of magnitude. The shear stress is assumed to be constant and equal to the wall shear stress.

In a numerical environment, the boundary value for the velocity can be directly solved using grids, the resolution of which produces $y^+ \approx 1$ on the wall. A second option is to use *wall functions* [42], the role of which is to assign a correct value to the first wall boundary cell, in order to respect the flow as it this was completely resolved. In this case the value of y^+ should overcome 30, thus assuring to avoid the buffer region, where the log law has the connection of the two curves. The use of *wall functions* allows then to reduce the number of cells required for modelling the boundary layer. The drawback of such approach is assuming that generic flows behave as the log law, which was tuned for a flat plate with imposed pressure. This is of course not always the case, and in particular the wall functions show weakness when analysing adverse pressure gradients and separation [42]. In Section 3.3 some results are presented where the accuracy of the calculations using the wall functions is validated against experimental results.

Good resolution of the boundary layer is of primary concern for two main reasons: the flow in this region determines the viscous forces acting on the body and it constitutes the boundary condition for the whole outer field.

3.1.4 Reynolds Averaging and the closure problem

As it was stated in Section 3.1.2 a practical way to solve the turbulence for engineering problems is the RANS approach. This is based upon the assumption that the turbulence can be represented as an oscillation occurring around a mean velocity. The mean flow velocity is then expressed as:

$$\overline{u} = \lim_{T\to\infty} \frac{1}{T} \int_0^T u \; dt \tag{3.22}$$

and it is assumed that:

$$u = \overline{u} + u' \qquad \overline{u'} = 0 \qquad \overline{\overline{u}u'} = \overline{u'\overline{u}} = 0 \tag{3.23}$$

Substituting these results into the Navier-Stokes Equations (3.18), the RANS assumption leads to the expression (component, see demonstration in appendix A.7):

$$\rho \left(\frac{\partial(\overline{u_j u_i} + \overline{u'_j u'_i})}{\partial x_j} \right) = \rho f_i + \frac{\partial}{\partial x_j} \Big[-p\delta_{ij} + \mu \Big(\frac{\partial \, \overline{u_i}}{\partial x_j} + \frac{\partial \, \overline{u_j}}{\partial x_i} \Big) \Big] \tag{3.24}$$

Six new unknown terms are then produced: $\overline{u'_i u'_j}$. This determines the *closure* problem: six new unknowns have been added to the principal four (u, v, w, p), but the number of equations is four (three component of the RANS equations + continuity equation). Turbulence models

provide six more equations in order to close the problem. Equation (3.24) is then reformulated as:

$$\rho \frac{\partial(\overline{u_j u_i})}{\partial x_j} = \rho f_i + \frac{\partial}{\partial x_j}\Big[- p\delta_{ij} + \mu\Big(\frac{\partial \overline{u_i}}{\partial x_j} + \frac{\partial \overline{u_j}}{\partial x_i}\Big) - \rho\overline{\partial u_j' u_i'}\Big] \tag{3.25}$$

The velocity fluctuations multiplied by ρ appear to the right hand side. Since this term has the dimension of a stress, it is known as the *Reynolds* stresses, and it constitutes the component of the *Reynolds* stress tensor $\mathbf{T}|^{turb}$, which is symmetric and therefore composed of six (unknown) components.

3.1.5 Turbulence models

The Boussinesq approximation

The Boussinesq approximation is historically the first approach to turbulence modelling [42]. Under this hypothesis, the unknown terms of the stress tensor in Equation **??** are assumed to be a linear combination of the velocity deformation gradient:

$$- \overline{u_i' u_j'} + \frac{1}{3}\overline{u_i' u_j'}\delta_{ij} = \nu_T \Big(\frac{\partial \overline{u_i}}{\partial x_j} + \frac{\partial \overline{u_j}}{\partial x_i}\Big) \tag{3.26}$$

where ν_T is the scalar *eddy viscosity*. This parameter is determined from the characteristic scales of the turbulence, such as the velocity scale q and the length scale ℓ, scaled by a coefficient C:

$$\nu_T = C\ q\ \ell \tag{3.27}$$

Several commonly adopted turbulence models are based upon the Boussinesq approximation, and they differ in the way the velocity, length time scales and the coefficient C are determined. Common models are algebraic models (zero equations), one equation models, two equation models.

Algebraic Turbulence models

It was shown in the previous section how the Boussinesq approximation reduces the closure problem to the determination of the eddy viscosity ν_T. Algebraic turbulence models define this value directly. Since no additional transport (differential) equations are introduced, these models are computationally very efficient. However they are incomplete, since velocity and length scales must be set. The calibration is then a key aspect, and results will be especially

accurate in predicting flows for which the model has been tuned. For example in the Baldwin-Lomax turbulence model ν_T is defined as:

$$\nu_T = \begin{cases} \nu_{T_i} = & f(\ell_{mix}, \Omega) & \text{if } y \leq y_m \\ \nu_{T_0} = & f(y) & \text{if } x > y_m \end{cases} \tag{3.28}$$

where y_m is the value of y for which the inner layer eddy viscosity and the outer layer eddy viscosity have the same value. $\ell_{mix} = \ell_{mix}(y)$ is a characteristic length scale and Ω is the magnitude of the vorticity.

Several results are presented in [42] for boundary layer flows, where it is shown how algebraic turbulence models perform well for attached flows, but they are not reliable for complex flows where adverse pressure gradients and separation must be adequately evaluated.

One equation turbulence models

Generally one-equation turbulence models solve a transport equation for the turbulent kinetic energy of the large-scale eddies k. k has dimensions ℓ^2/t^2, so the turbulent velocity scale can be then represented as $2\sqrt{k}$.

$$k = \frac{1}{2}(\overline{u_i' u_i'}) = \frac{1}{2}(u'^{\,2} + v'^{\,2} + w'^{\,2}) \tag{3.29}$$

Recalling the Reynolds stress tensor (see equation (3.25)) , its trace represents then the turbulent kinetic energy: $\tau_{ii} = -\,\overline{u_i' u_i'} = -2k$.

The transport equation for k is (see appendix A.8):

$$\frac{\partial k}{\partial t} + \overline{u}_j \frac{\partial k}{\partial x_i} = \tau_{ij}\, \frac{\partial \overline{u}_i}{\partial x_j} - \epsilon + \frac{\partial}{\partial x_j}\left[\left(\nu + \frac{\nu_T}{\sigma_k}\right)\frac{\partial k}{\partial x_j}\right] \tag{3.30}$$

In order to close the problem, an expression is needed for ϵ, which represents the dissipation of the kinetic energy and ν_T . The way of calculating these quantity differs from model to model. In Prandtl's model ϵ is determined as:

$$\epsilon = \frac{C_\mu k^{3/2}}{\ell_{mix}} \tag{3.31}$$

where C_μ is a calibration constant, and ℓ_{mix} is a characteristic length scale. The Reynolds stress tensor can then be computed as:

$$\tau_{ij} = 2\nu_T D_{ij} - \frac{2}{3}\, k\, \delta_{ij} \tag{3.32}$$

where **D** is the strain velocity tensor (see Section 3.1), and he eddy viscosity ν_T then still remain to calculate, and this is done using the mixing length and the mixing velocity, which is a characteristic velocity of the flow:

$$\nu_T = \frac{1}{2} u_{mix} \ell_{mix} \tag{3.33}$$

Such an approach is not complete then, since some empirical quantities still need to be introduced. A rather improved approach for one equation turbulence models is the Spalart Allmaras model. This is based on one transport equation for the eddy viscosity, and it is thus complete, since it solves for eddy viscosity directly. In this model, the kinematic eddy viscosity is described as:

$$\nu_T = \tilde{\nu}\ f_{v1} \tag{3.34}$$

where $\tilde{\nu}$ is an opportunely tuned viscosity value and f_{v1} a viscous damping function. The transport equation is written for the eddy viscosity ν is then formulated as:

$$\frac{\partial \nu}{\partial t} + \overline{u}_i \frac{\partial \nu}{\partial x_i} = c_{b1} \tilde{S} \tilde{\nu} - c_{\omega 1} f_\omega \Big(\frac{\tilde{\nu}}{d}\Big)^2 + \frac{1}{\sigma} \frac{\partial}{\partial x_k} \left[(\nu + \tilde{\nu}) \frac{\partial \tilde{\nu}}{\partial x_j} \right] + \frac{c_{b2}}{\sigma} \frac{\partial \tilde{\nu}}{\partial x_k} \frac{\partial \tilde{\nu}}{\partial x_k} \tag{3.35}$$

The transport equation is then expressed in terms of ν, u and a series of coefficients experimentally calibrated. Although the Spalart-Allmaras model work well for attached flows, it gives unacceptable results if used to compute free-shear layers. In general, it can be concluded that one equation models lack the extensiveness and reliability that can be provided when more transport equations are solved.

Two equation turbulence models: k-ϵ

In general, two equation models solve an equation for the turbulent kinetic energy k and one other transport equation. In the k-ϵ turbulence model, this is an equation for the dissipation of turbulent kinetic energy per unit mass ϵ. The transport equation for ϵ can be derived; however such a formulation is too complex to solve [42]. The standard k-ϵ model is then derived using dimensional considerations. The equation for k is the same as for one-equation turbulence model (see Equation (3.30)). The transport equation for ϵ is modelled on this equation, but corrections are inserted in order to respect the dimensional coherence. The production term, as for the k equation must contain the term $\tau_{ij} \frac{\partial u_i}{\partial x_j}$. The term is then multiplied for dimensional reasons by $C_{\epsilon 1} \frac{\epsilon}{k}$, where $C_{\epsilon 1}$ is a non-dimensional constant. The

dissipation term is obtained with dimensional considerations: it depends upon ϵ and k, it is then written as $-C_{\epsilon 2}\frac{\epsilon^2}{k}$. The turbulent transport is written in the form of a diffusion term taking into account molecular and turbulent viscosity. The two equations then read:

$$\frac{\partial k}{\partial t} + \overline{u}_j \frac{\partial k}{\partial x_i} = \tau_{ij} \frac{\partial \overline{u}_i}{\partial x_j} - \epsilon + \frac{\partial}{\partial x_j}\left[\left(\nu + \frac{\nu_T}{\sigma_k}\right)\frac{\partial k}{\partial x_j}\right] \qquad ((3.30))$$

$$\frac{\partial \epsilon}{\partial t} + \overline{u}_j \frac{\partial \epsilon}{\partial x_i} = C_{\epsilon 1}\frac{\epsilon}{k}\tau_{ij} \frac{\partial \overline{u}_i}{\partial x_j} - C_{\epsilon 2}\frac{\epsilon^2}{k} + \frac{\partial}{\partial x_j}\left[\left(\nu + \frac{\nu_T}{\sigma_k}\right)\frac{\partial k}{\partial x_j}\right] \qquad (3.36)$$

where the coefficients have been inserted in the latter equation for dimensional reasons, and:

$\nu_T = C_\mu \frac{k^2}{\epsilon}, \quad C_{\epsilon 1} = 1.44, \quad C_{\epsilon 2} = 1.92, \quad C_\mu = 0.09, \quad \sigma_K = 1 \quad \sigma_\epsilon = 1.3$

The standard k-ϵ model has produced good results for simple flows. However, it generally over-predicts the turbulent length scale (and thus the eddy viscosity) when analysing regions with adverse pressure gradients. In the case of an airfoil analysis for example this family of turbulence models produce an over-prediction of lift and an under-prediction of drag [42].

Two equation turbulence models: k-ω

In the k-ω turbulence model the k-equation is solved together with an equation for the specific rate of dissipation of turbulent kinetic energy: $\omega = \frac{\epsilon}{k}$. Commonly ω is thought of as the characteristic frequency of the turbulence decay process. The reciprocal of ω is then the time scale on which dissipation of the turbulent energy occurs. In the standard k-ω model, derived by Wilcox ([42]), the eddy viscosity is defined as:

$$\nu_T = \frac{k}{\omega} \qquad (3.37)$$

Performing dimensional analysis, the turbulent kinetic energy and the specific dissipation rate writes then:

$$\frac{\partial k}{\partial t} + \overline{u}_j \frac{\partial k}{\partial x_i} = \tau_{ij} \frac{\partial \overline{u}_i}{\partial x_j} - \beta^* k\omega + \frac{\partial}{\partial x_j}\left[\left(\nu + \frac{\nu_T}{\sigma_k}\right)\frac{\partial k}{\partial x_j}\right] \qquad (3.38)$$

$$\frac{\partial \omega}{\partial t} + \overline{u}_i \frac{\partial \omega}{\partial x_i} = \alpha\frac{\omega}{k}\tau_{ij} \frac{\partial \overline{u}_i}{\partial x_j} - \beta\omega^2 + \frac{\partial}{\partial x_j}\left[\left(\nu + \frac{\nu_T}{\sigma_k}\right)\frac{\partial \omega}{\partial x_j}\right] \qquad (3.39)$$

This model performs well for shear flows and flat plate boundary layer flows, as well as for more complex flows with adverse pressure gradients and separation. The k-ω model has a large dependency on the free stream boundary condition for ω. As it has been shown by Wilcox [42], this free stream boundary condition can effect the eddy-viscosity by up the 100%.

Two equation turbulence models: SST

A way to overcome the limitations of the k-ω model was proposed by Menter [100]. It was shown in fact that the sensitivity of the model to the boundary value for ω is less pronounced for boundary layer flows than for free shear layer flows. Introducing appropriate cross diffusion terms can then reduce this dependency.

The major effect of the cross diffusion in free-shear flows is to increase the production of ω, thus the dissipation of the turbulent kinetic energy k. The cross diffusion terms introduced by [100] make use of non-linear *blending functions*, the value of which is zero at the inner edge of a turbulent boundary layer and one at the outer edge of the layer. Consequently the model behaves like the k-ϵ away from walls and like the k-ω in the near-wall region, thus retaining the best performances of both models.

The calibration of the blending functions was derived with free-shear and boundary layer flows. The Shear Stress Transport (SST) model has been shown to considerably decrease the dependency on free stream boundary condition, while it produces good results for adverse pressure gradients and separation.

3.2 Numerical methods

The finite volume method is one of the most commonly adopted methods for the discretization and numerical solution of complex systems involving partial derivatives. Even the method is well known, the basics will be recalled here for a matter of clarity. For a more complete overview, one should refer to e.g. [6].

Equation (3.18) reports the Navier-Stokes equation in conservative form. In general a transport equation in conservative form[2] for a generic variable ϕ writes:

$$\frac{\partial \rho\phi}{\partial t} + \nabla \cdot (\rho\phi\vec{u}) = \nabla \cdot (\Gamma \nabla\phi) + S_\phi \tag{3.40}$$

rate of change of ϕ of fluid element	Net rate of flow of ϕ out of fluid element	rate of increase of ϕ due to diffusion	rate of increase of ϕ due to sources

where ρ, Γ are physical properties of the flow, such as density and viscosity. Integrating equation (3.40) over the control volume CV:

$$\int_{CV} \frac{\partial(\rho\phi)}{\partial t}\, dV + \int_{CV} \nabla \cdot (\rho\phi\vec{u})\, dV = \int_{CV} \nabla \cdot (\Gamma\ \nabla\phi)\, dV + \int_{CV} S_\phi\, dV \tag{3.41}$$

and applying Gauss' divergence theorem (see section 0.6):

$$\frac{\partial}{\partial t}\Big(\int_{CV} (\rho\phi)\, dV \Big) + \int_A \vec{n} \cdot (\rho\phi\vec{u})\, dA = \int_A \vec{n} \cdot (\Gamma\ \nabla\phi)\, dA + \int_{CV} S_\phi\, dV \tag{3.42}$$

where the first term represents the net rate of increase of ϕ in the fluid element due to diffusion. The product $\vec{n} \cdot (\rho\phi\vec{u})$ expresses the flux component of the property ϕ due to the fluid flow along the outward normal vector $\vec{n}$. The second term of the left hand side (convective term) takes the meaning of net rate of decrease of ϕ of the fluid element due to convection. The product $\Gamma\nabla\phi$ assumes the meaning of positive diffusion flux into the fluid element. The last term gives the rate of increase of ϕ as a result of sources inside the fluid element.

For time-dependent problems, this equation must be integrated in time. Defining the time interval Δt then:

$$\int_{\Delta t} \frac{\partial}{\partial t}\Big(\int_{CV} (\rho\phi)\, dV \Big)\, dt + \int_{\Delta t}\int_A \vec{n}\cdot(\rho\phi\vec{u})\, dA\, dt = \int_{\Delta t}\int_A \vec{n}\cdot(\Gamma\nabla\phi)\, dA\, dt + \int_{\Delta t}\int_{CV} S_\phi\, dV\, dt \tag{3.43}$$

[2] conservative and nonconservative are equivalent forms of the conservation equations, which differ by the use of Equation 13. The conservative form states the conservation laws through a control volume fixed in space; the nonconservative form enforces the conservation laws in a control volume as it moves with the fluid, see e.g. [20], [6].

In a numerical scheme these terms can be discretizated as follows:

Time derivative:

$$\frac{\partial}{\partial t}\int_{CV}\rho\phi\ dV = \frac{(\rho_P\phi_P V)^n - (\rho_P\phi_P V)^0}{\Delta t} \tag{3.44}$$

where P is the cell centre and an Euler first order scheme was adopted.

Convection term:

$$\int_A \vec{n}\cdot(\rho\phi\vec{u})\ dA = \sum_f \vec{S}_f\cdot(\rho\vec{u})_f\ \phi_f \tag{3.45}$$

Laplacian term:

$$\int_A \vec{n}\cdot(\Gamma\ \nabla\phi)\ dA = \sum_f \Gamma_f\vec{S}_f\cdot(\nabla\phi)_f \tag{3.46}$$

with:

$$\vec{S}_f\cdot(\nabla\phi)_f = |S_f|\ \frac{\phi_N - \phi_P}{|d|} \tag{3.47}$$

Source term:

$$\int_{CV}\rho\phi\ dV = \rho_P V_P\ \phi_P \tag{3.48}$$

where $\vec{S}_f = A\,\vec{n}$ is the face area vector of the face of interest, ϕ_f and Γ_f the values of the variable ϕ and the constant Γ across the face. Being P the cell center, and N the center of the neighbouring cell. d is the distance $\vec{PN}$ in the case of orthogonal cells. For non-orthogonal cells a correction must be applied. The superscripts $.^n$ and $.^0$, used for the evaluation of the derivative refer to the current and previous time-steps. For the source term, V_p is the volume of the cell and ϕ_P the value of ϕ calculated at the cell centre.

An example of the application of the finite volume method for a mono-dimensional case is reported in Appendix A.9.

When discretizing a fluid field, situations may arise where the computed velocity/pressure field is legal in terms of the continuity equation and the boundary conditions, but it assumes non-physical oscillatory behaviours. Two main strategies are generally adopted for avoiding the insurgence of such a phenomenon: the staggered (see Appendix A.10) and the collocated grids (see [101], Appendix A). These method are based upon very similar ideas, but the solver which has been used here, OpenFOAM, makes use of collocated grids.

Finally, a note should be done on the solution strategy. OpenFOAM uses a Semi-projection scheme of the Semi Implicit Method for Pressure Linked Equations (SIMPLE) family. The basic idea of this approach, reviewed in Appendix A.11, is to split the unknowns describing the pressure and the velocity, and to find opportune corrections for iteratively reaching the final solution.

Using schemes of this family is advantageous in terms of computational effort for two main reasons. Primarily, solving twice a smaller system of equation is generally more advantageous than solving a big system once. Secondarily, the pressure and the velocity having in general different orders of magnitude, the splitting allows for an improvement of the conditioning of the sub-systems. More complete references on the finite volume method can be found, e.g. in [6], or in [20].

OpenFOAM (Open Field Manipulation and Operation) is a CFD toolbox implemented in C++. It contains numerous applications and libraries, and it is nowadays extensively used in the scientific community. For a detailed description, one should refer to the OpenFOAM website (www.openfoam.com) or the OpenFOAM-extend project website (http://www.extend-project.de/)[3]. Due to its high level syntax, solving Equations in a fluid domain is made particularly easy with OpenFOAM. Primarily three different solvers have been used in this work: icoFOAM, pisoFOAM and pimpleDyMFOAM. The first one, being an implementation of the PISO algorithm treated in the previous section for laminar flows. The second solver is based upon icoFOAM, but it includes several turbulence models. The third solver has dynamic mesh (Arbitrary Lagrangian Eulerian) capabilities, and it has been used for test cases involving moving meshes and fluid structure interactions. Although to go further in the details of the OpenFOAM implementation is beyond the scope of this manuscript, an example is reported here, and additional details will be given in chapter 5 about the major modifications performed to the PimpleDyMFOAM solver to be used for Fluid Structure Interactions.

The example reported in this Section regards the calculation of the Normalised Invariant of the Deformation Tensor ($\mathbf{D}$). This scalar field is defined as:

$$\mathbf{D} = \frac{(S_{ij}^D S_{ij}^D - W_{ij}^D W_{ij}^D)}{(S_{ij}^D S_{ij}^D + W_{ij}^D W_{ij}^D)} \tag{3.49}$$

where:

$$S_{ij}^D = \frac{1}{2}\left(\frac{dU_i}{dx_j} + \frac{dU_j}{dx_i}\right) \qquad Symmetric\ part\ of\ the\ deformation\ gradient \tag{3.50}$$

$$W_{ij}^D = \frac{1}{2}\left(\frac{dU_i}{dx_j} - \frac{dU_j}{dx_i}\right) \quad Anti-symmetric\ part\ of\ the\ deformation\ gradient \tag{3.51}$$

where the symmetric part of the deformation gradient expresses the strain, and the anti-symmetric part expresses the rotation. The tensor $\mathbf{D}$ can be computed on a domain where

[3]The two main distributions of OpenFOAM share the basics of the program and the general structure; the extend project contains however some additional features, especially for dynamic mesh handling.

velocity and pressure are defined using the code reported in appendix A.12. The terms are calculated as:

- velocity gradient ∇U: `volTensorField gradU = fvc::grad(U);`
- symmetric part of gradU: `volSymmTensorField Sd = 0.5 * symm(gradU);`
- Anti-symmetric part of gradU: `volTensorField Wd = 0.5 * skew(gradU);`
- Scalar product between tensors: `volScalarField SSd = Sd & & Sd;`
- Scalar product between tensors: `volScalarField WWd = Wd & & Wd;`
- Calculate NIDT: `D = ( SSd - WWd) / (WWd + SSd)`

Provided a calculation domain where a velocity field **U** is defined the calculation is then performed by a few line of high level syntax code. An example of the use of this calculation is provided in section 3.3.3

3.3 Steady numerical tests and validation

In this section test cases are presented for validating the analysis on steady flows relevant to sail analysis. The aim is here to establish how the methods described in the previous sections predict the flow development and its details.

The investigation regards the boundary layer development on a bump geometry in Section 3.3.1, where results are validated using the experiments reported in [7]. It is found that, although the numerical results are accurate and coherent, some inconsistency can be identified in the experimental results. Despite this, the case shows well the prediction performance of the RANS method adopted here.

Some results are then presented regarding the effect of the surface wrinkling on the flow (Section 3.3.2). Wrinkling is a buckling related phenomenon affecting the structural deformation of fabrics such as sails, and it will be detailed in Sections 4.1.10, 4.3.3 and 4.3.4. The analyses presented here attempt the evaluation of the influence of the geometrical change represented by the wrinkles, and the results obtained for the wrinkled configuration are compared with those obtained for an equivalent smooth surface.

In the end of the Section the experiments conducted by Desabrais [8] on a parachute canopy are numerically repeated. General good agreement is found in terms of mean flow, however the reported unsteadiness is not predicted at all. Some hypothesis are then formulated in order to explain the difference.

3.3.1 Bump: comparison with experimental results for the prediction of boundary layers

The flow over a bump geometry has been analysed and compared with experimental results published by Song [7]. In the article experiments have been conducted for momentum thickness Reynolds number $Re_{\delta 2}$, defined in Equation (3.52), varying from $1.1 \cdot 10^3$ to $2.01 \cdot 10^4$. Measurements were performed with a high-resolution laser Doppler anemometer, able to resolve turbulence measurements over the full Reynolds number range. The experiments showed that the mean flow is at most a very weak function of Reynolds number while turbulence quantities strongly depend on Reynolds number. This case is taken as representative for the detailed flow generation analysis for a wrinkled sail surface with a flow across or perpendicular to the wrinkles. The CFD analysis evaluated one value of Reynolds number, the case is described in Table 3.2 and the geometry is shown in Figure 3.3.

$$Re_{\delta 2} = \frac{\rho u_\infty \delta_2}{\mu} \quad ; \quad \delta_2 = \int_0^\infty \frac{\rho\, u}{\rho_\infty u_\infty}\left(1 - \frac{u}{u_\infty}\right) dy \tag{3.52}$$

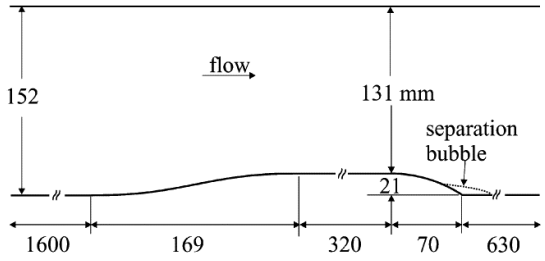

Figure 3.3: Geometry used for the bump experiments. From [7], Figure 1

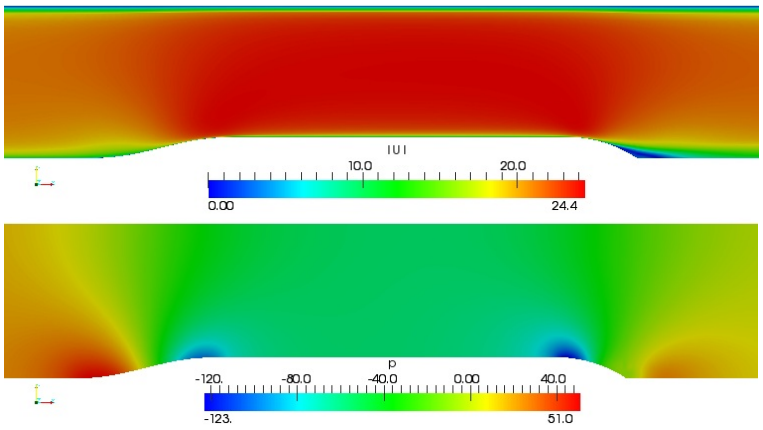

Figure 3.4: Velocity and the pressure fields

Table 3.2: Bump case description

Re_θ	U_{in} [m/s]	δ_{99} [mm]	T [°C]	P [Pa]	$\nu \cdot 10^{-6}$
3400	20.2	27.6	297	101300	15.5

A two dimensional computational grid was analysed. Boundary conditions imposed to the domain are reported in Table 3.3. Standard wall functions have been adopted, provided in the distribution of the fluid solver. The initial values for κ and ω have been calculated as: $\kappa = \frac{3}{2}(\frac{5}{100}\, U_{in})^2$ and $\omega = \frac{\sqrt{k}}{h}$, being h the bump height, as defined in Figure 3.3.

Results have been compared in terms of law of the wall, pressure profile, detachment and reattachment position for 6 different grids and two solvers, as they are detailed in the following table. Simulations were performed with the SST turbulence model, since this was shown to

Table 3.3: Boundary conditions adopted for the bump case

	$U\ [m/s]$	$p\ [N/m^2]$	$k\ [m^2/s^2]$	$\omega\ [1/sec]$
Inlet	20.2	Zero Gradient	1.5	58.61
outlet	Zero Gradient	0	Zero Gradient	Zero Gradient
top	0	Zero Gradient	Wall Function	Wall Function
bottom	0	Zero Gradient	Wall Function	Wall Function
sides	empty	empty	empty	empty

Table 3.4: Specifications of the meshes used for the bump case. N_v is the number of vertical subdivisions, N_H^{Ramp} is the number of horizontal subdivisions on the bump and Ne is the total number of volume elements

	Bump0	Bump1	Bump1a	Bump1b	Bump2	Bump3	Bump4
N_v	40	65	72	72	80	80	80
N_H^{Ramp}	25	25	25	25	24	40	80
Ne	15600	25600	28400		31600	37525	44635
dt	$1 \cdot 10^{-4}$	$8 \cdot 10^{-5}$	$5 \cdot 10^{-5}$	$4 \cdot 10^{-5}$	$3 \cdot 10^{-5}$	$1 \cdot 10^{-5}$	$1 \cdot 10^{-5}$
y^+_{AVG}	48.1073	8.037	3.29	1.3	0.268	0.321	0.308
C_d	0.638	0.669	0.727	0.727	0.763	0.859	0.865
C_l	-4.247	-4.691	-5.243	-5.243	-5.246	-6.444	-6.517

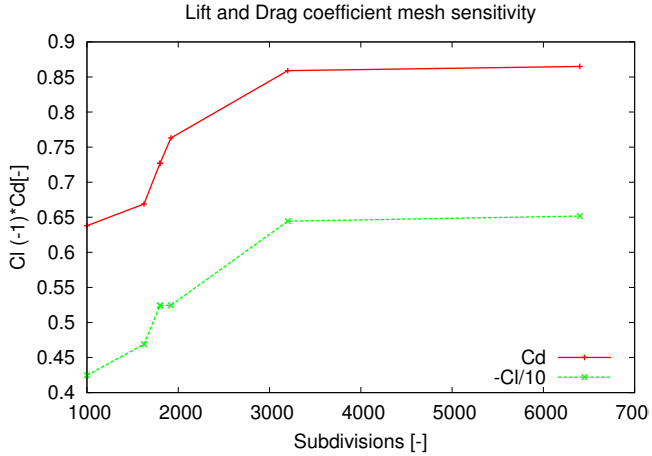

Figure 3.5: Mesh sensitivity in terms of force coefficients

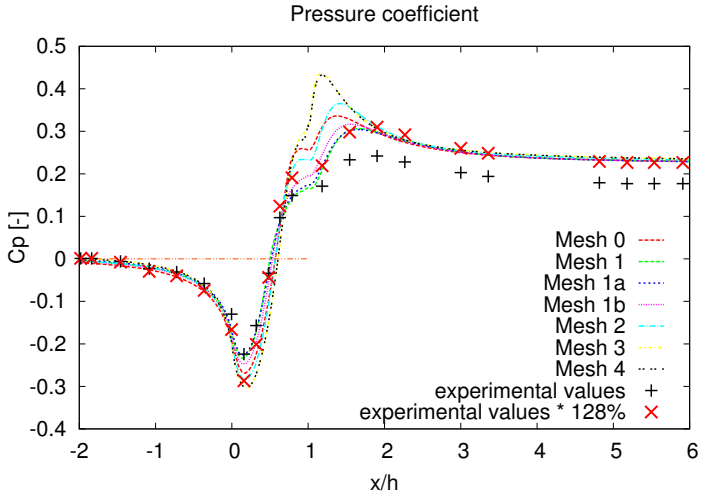

Figure 3.6: Mesh sensitivity in terms of pressure coefficient, and comparison with the experimental data in [7]

be the most suitable for this kind of flow, and for sail analysis applications [25]. Result are well converged in terms of forces for the two finer meshes (Figure 3.5). However, such results are not the closest when comparing the pressure coefficient against the experimental data (Figure 3.6). The pressure coefficient recovery is in fact not complete, since results are translated to start from zero, and a higher pressure is encountered at the outlet. This means that the velocity in the constrained section is higher for the numerical case than in the experimental measurements. The best fit of the extreme pressure values is obtained multiplying the experimental curve for a factor of 1.28. With such a factor the numerical evaluation shows a very good prediction of the pressure drop and the recovery region, for y^+ values close to one. Further decreasing the y^+ value produces a degradation of the solution.

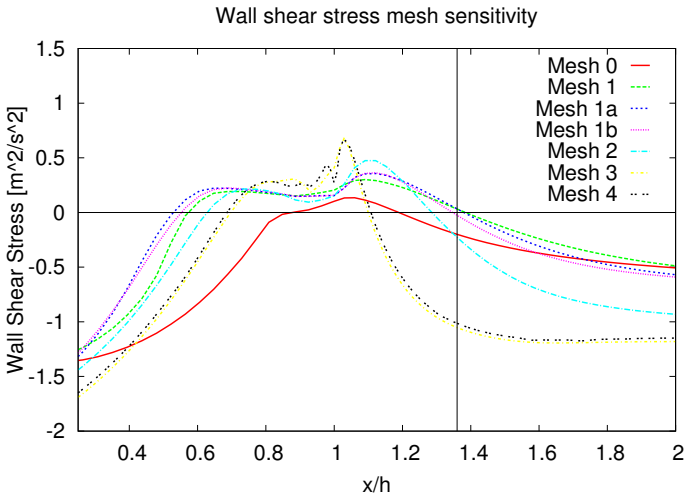

Figure 3.7: Wall shear stress on the bottom surface for the analysed meshes. The reattachment point declared in the experiments is underlined by the black straight lines.

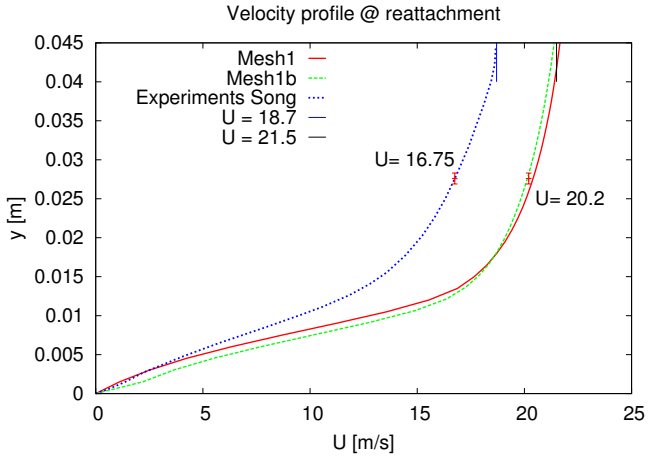

Figure 3.8: Velocity profile at reattachment for mesh 1, 1b and comparison with the experimental values. The crosses underlined in the figure show the value of the velocity at the height declared as δ_{99}. The experimental curve shows a discrepancy with the declared value U=20.2, correctly reproduced by the numerical calculations.

$$\tau_w = \mu \frac{\partial u}{\partial y}\Big|_{y=0} \tag{3.53}$$

Results in terms of the wall shear stress defined in Equation (3.53) are reported in Figure 3.7. A very good correspondence is found for the reattachment point – identified by the zero crossing point – compared to the experimental values for the meshes 1, 1a and 1b. These are the computational grids which produced the results closer to the experimental value in terms of pressure coefficient comparison.

The reason for the difference in the pressure coefficient value is not clear, but a remark

should be made about the experimental data. In the paper [7] in fact an inconsistency become apparent, regarding the boundary layer thickness δ_{99}, the value of which is declared 27.6 mm. The velocity value at this height is about 17.5 m/s, value which is inconsistent with the free stream velocity (20.2 m/s). The reported graph might then relate to a lower velocity than 20.2 m/s. This would be in accordance with the velocity profile at the reattachment, reported in Figure 3.8.

3.3.2 Influence of the surface wrinkling on two-dimensional flow

In order to understand the impact of the wrinkling development on the flow and the required grid resolution, a set of numerical test is presented here.

The effect of hill and waves on the flow was investigated in the past by several works [102], [103]. Generally however the analysed geometry is constituted by relatively low sloped oscillations, leading to linear description. In the case here analysed however, the slopes are very steep and different phenomena, strongly nonlinear, appear [104].

The geometry which is analysed is an initially flat plate affected by the formation of wrinkles. The geometrical characteristics of the calculation domain are reported in Table 3.5. The wrinkles are designed using a B-Spline curve, the control points of which are placed on a sinusoidal curve. This explains why the parameter H is measured on a higher position in Figure 3.9. The actual amplitude of the wrinkles can be estimated as $\approx$ H/2. The mesh was designed using the open-source software GMSH. For selected meshes, the solution was compared with an analogous case, with a smooth bump offsetting the wrinkled pattern.

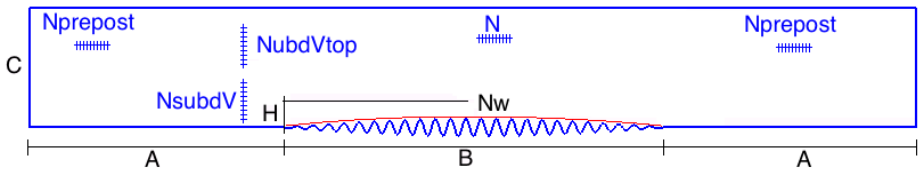

Figure 3.9: base geometry used for the calculations. The red curve represents the trace of the smooth section offsetting the wrinkled pattern

The mesh was designed using the parameters in Figure 3.9 and imposing the value for the horizontal and the vertical number of subdivisions (N and SsubdV). Then NprePost was set as $N/10$, with the progression for the vertical subdivision (bottom) calculated as: $pV = 1 + 2.5/SubdV$; The top part of the mesh was equally spaced.

The physical quantities used for the analysis are summarised in Table 3.6. SST turbulence

Table 3.5: base geometry parameters.

A	B	C	H	Nw
[mm]	[mm]	[mm]	[mm]	[-]
2*B/3	214	=H	15	25

model was used, where the initial values for k and ω were calculated as in Section 3.3.1.

Table 3.6: Physical quantities for the wrinkled flow analysis

U	$Re_{L_{wrinkle}}$	$Re_{L_{bump}}$	k	ω	ρ_{air}	ν_{air}
[m/s]	[-]	[-]	$[m^2/s^2]$	[Hz]	$[Kg/m^3]$	$[m^2/s]$
6	8.510^4	ii	0.135	0.01926	1.225	$1.51e^{-5}$

Velocity was imposed at the inlet as a Dirichlet boundary condition. Free slip walls were chosen for the flat surfaces connecting the wrinkled surface with the inlet and the outlet. This choice was done in order to avoid any boundary layer development before the wrinkled surface, thus decreasing the number of variables. On the whole set of surfaces except the outlet, Newman pressure boundary condition were imposed (zeroGradient). On the outlet, the pressure value was set equal to zero and a Newman boundary condition was applied for the velocity.

Tests were performed in order to investigate the mesh sensitivity for this case, as detailed in Table 3.7; all other parameters were defined as described in the previous section. The three finer meshes were derived from mesh 10, by increasing the vertical progression. This produced finer grids in the region close to the wall. For these three mesh the value of pV was set to 1+α/SubdV, with $\alpha = 3.5, 4.5, 5.5$. Although the meshes obtained with these parameters did not verify $y^+_{min} < 1$ on the whole wrinkled patch (see Table 3.8), further increasing the vertical progression value of the mesh was not possible for this mesh topology. The reason for this is the angle of the wrinkles sides, which causes high non-orthogonality and eventually the collapse of some volume elements. However, the y^+ realised for the finer mesh was judged satisfactory, being < 1 in the larger part of the surface of interest (see Figure 3.10).

Figure 3.11 displays the drag/lift coefficient time history. As the mesh is refined, oscillations are encountered in terms of the generated forces. After an initial transient the solution converges however to a steady final state. In the finer cases, the solution is affected by high

Table 3.7: mesh parameters and dt values

	NsubdV				dt values			
N	15	30	45	60	15	30	45	60
500	1	2	3	-	0.01	0.005	0.002	-
1000	4	5	6	-	0.03	0.005	0.001	-
1500	7	8	9	10 →13	0.002	0.00125	0.0005	0.0002 → 0.00005

Table 3.8: y^+ values for the wrinkled surface for the set of analysed meshes

	1	2	3	4	5	6	7	8	9	10
y^+_{max}	3472	1304	782	3732	1578	175	3642	1831.3	1186	864.2
y^+_{avg}	886	310	175	899	314	14	954	395.6	219	180.8
y^+_{min}	147	31.5	4.23	139	32	951	151	65.5	17	21.85
	11	12	13							
y^+_{max}	467.9	217	96							
y^+_{avg}	72.9	32	12.8							
y^+_{min}	2.36	0.18	0.155							

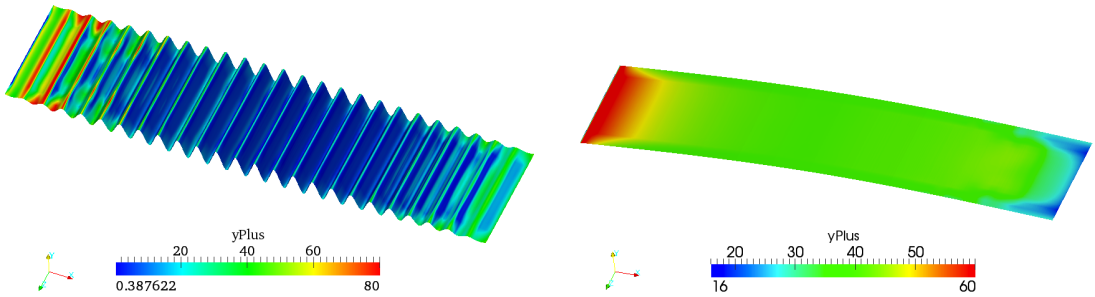

Figure 3.10: y^+ plot for the finer analysed case. Wrinkled and smooth surface

instability and no complete steady solution can be identified. The values declared for this mesh in the following are therefore time-averaged. The average is performed on a suitable period of time, where the oscillation of the solution is relatively small (typically the last two second of the simulation). The curves in Figure 3.12 report the value of the time-converged Lift and Drag coefficients. The points are connected with iso-horizontal subdivision curves ($N = cost$), as in Table 3.7. A relatively high mesh sensitivity is experienced for the Lift,

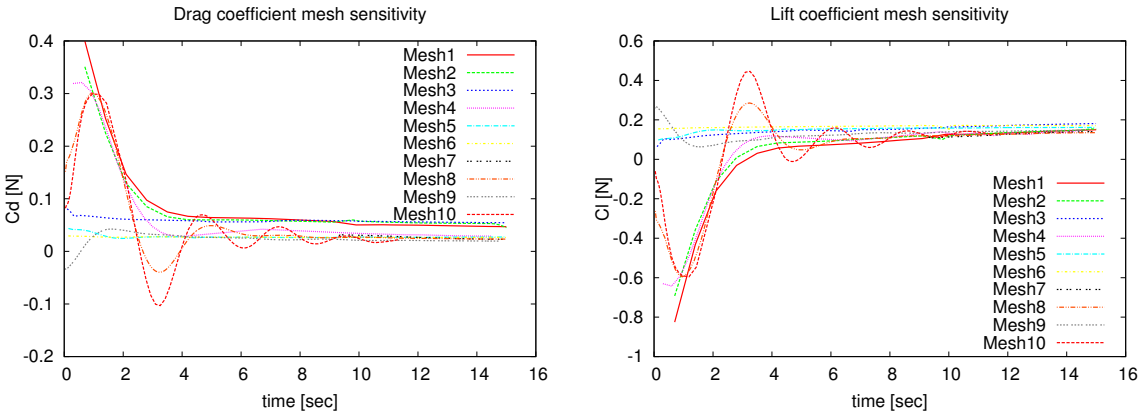

Figure 3.11: Cd and Cl time history for the analysed meshes

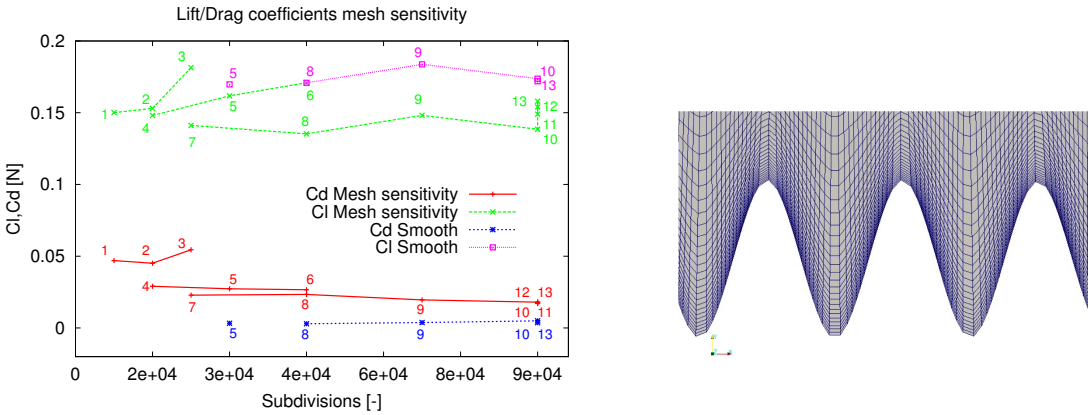

Figure 3.12: Cd and Cl mesh sensitivity; zoom over the wrinkled mesh zone.

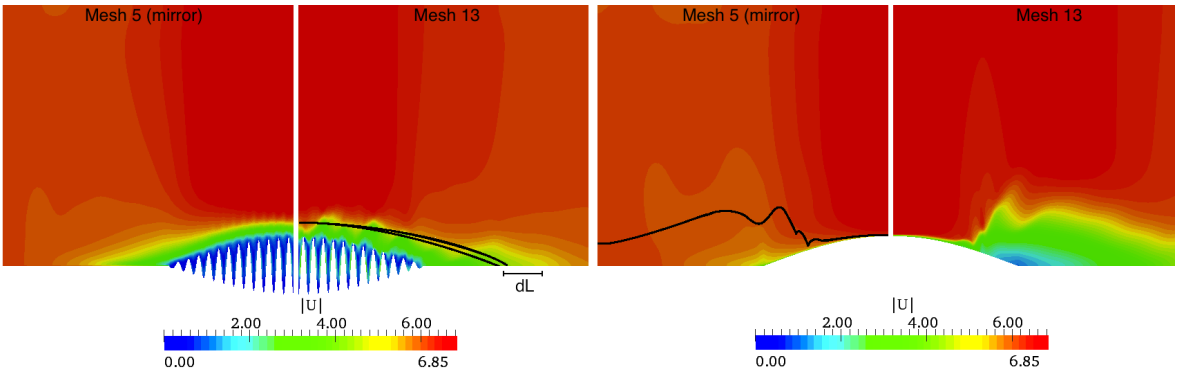

Figure 3.13: Comparing the response in terms of velocity field for $Mesh_5$ and $Mesh_{13}$. The geometry has bees collapsed (scale factor = 0.2) in x direction for visualisation purposes. The superposed black curves shows the offset of the velocity ($5.5\,m/s$). In the wrinkled case (*left* Figures) the mesh influence is remarkably less pronounced, than in the smooth case (*right* Figures) for the effect of the high mixing produced by the wrinkles

while the Drag is more stable. Comparing the wrinkled and the smooth case, it appears that the effect of the wrinkles is to increase the Drag and to reduce the Lift. However, full con-

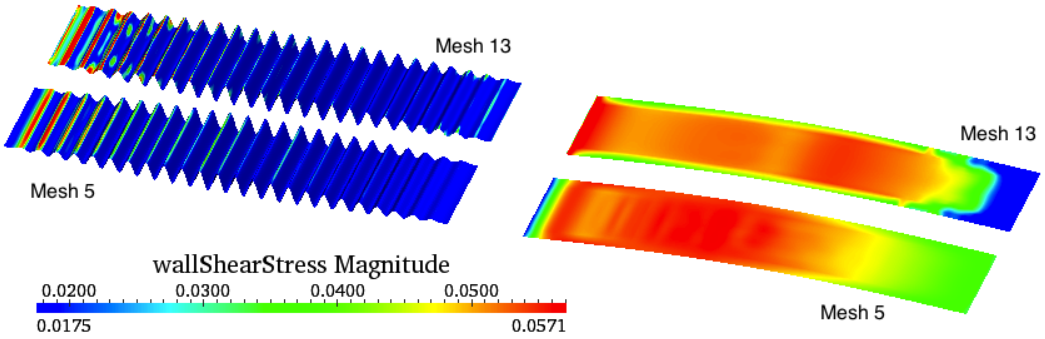

Figure 3.14: Comparing the response in terms of wall shear stress for $Mesh_5$ and $Mesh_{13}$

vergence in terms of mesh sensitivity was not achieved for the analysed cases. Despite this, it was not possible to obtain results with much more refined meshes for the adopted mesh topology, as previously explained.

The mesh sensitivity is displayed in terms of velocity field in Figure 3.13, for both the wrinkled and the smooth cases for $Mesh_5$ and $Mesh_{13}$. The black lines which have been superposed to the Figure highlight the difference in the computed fields. In the wrinkled case some mesh sensitivity is experienced; due the high mixing however the thickness and the extension of the predicted boundary layer remains relatively stable. The mesh sensitivity is increased when analysing the smooth surface. In this case the flow predicted by $Mesh_5$ remains almost attached, whereas $Mesh_{13}$ predicts separation and a high increase of the boundary layer thickness.

It can be then concluded that, although wrinkling introduces some instability in the analysis, it decreases the dependency upon the close-to-the-wall region treatment and it is thus beneficial in terms of mesh sensitivity. Figures 3.14 and 3.16 display a comparison between the response in terms of wall shear stress (see Equation (3.53)) and pressure for the wrinkled and the smooth case, again for $Mesh_5$ and $Mesh_{13}$. The main effect of the wrinkles is to severely decrease the wall shear stress, while the pressure oscillates around values similar to those obtained with the smooth mesh. This confirms that the influence of the wall treatment results reduced. The schematic behaviour for the wall shear stress is reported in Figure 3.16 *left*, while a similar sketch reports the behaviour of the pressure in Figure 3.16 *right*. The positive spike in correspondence of the first part of the bumps is due to the recirculation internal to the wrinkles (see Figure 3.15): in this region, the flow is counter-rotating. Going towards the outer region, the wall shear stress becomes negative, i.e. the bump is affected by the external flow. The second (minor) positive spike is due to the effect of the internal flow, which rotates with lower speed close to this part of the wall (see figure 3.18). The pressure

also follows the bumps. A peak is identified in correspondence of the primary stagnation point (see Figure 3.18); proceeding on the right the pressure then progressively decreases until the detachment arises. After this point, a pressure recovery arises, with a spike on the secondary stagnation point and it keeps a constant value over the hollows. It increases in the first half of the bump and it shows a complex behaviour in the second part, for the effect of the adverse pressure gradient.

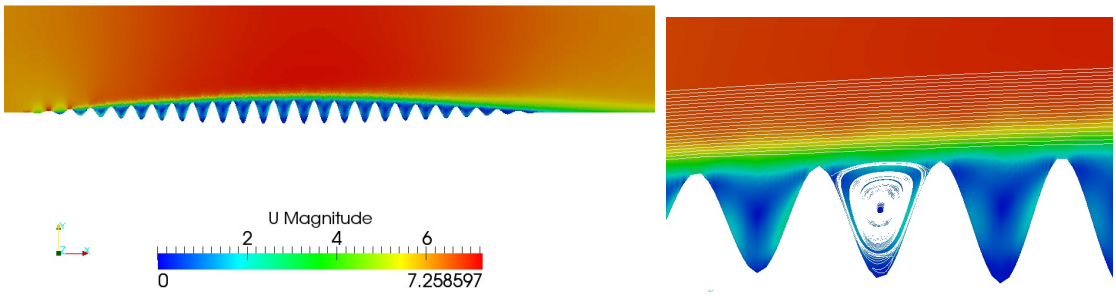

Figure 3.15: Velocity field and zoom on the pressure field with stream lines in the central part of the wrinkled surface ($Mesh_5$)

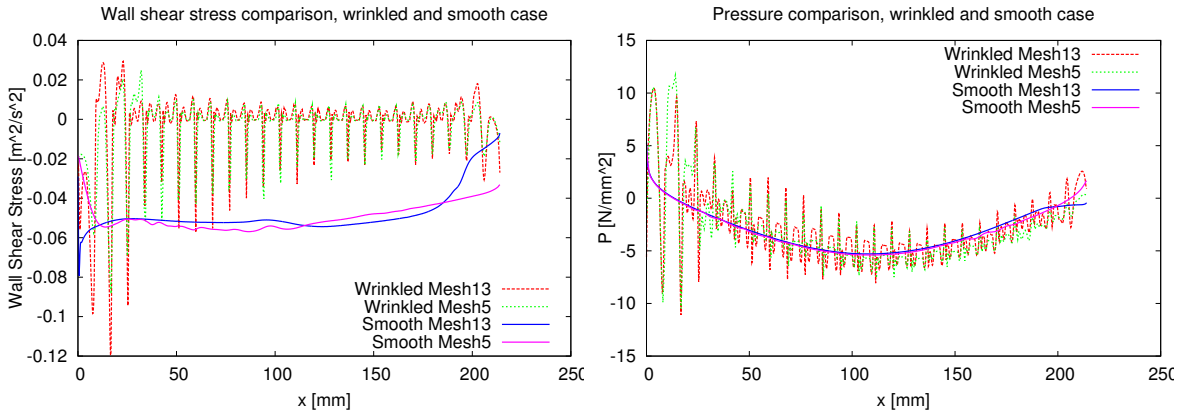

Figure 3.16: Wall shear stress and pressure behaviour over the wrinkled zone. $Mesh_5$ and $Mesh_{13}$

3.3.3 Fixed geometry canopy, comparison with experimental results of a drag device

Table 3.9: Canopy geometry and test specifications

$D_0\,[m]$	$U\,[m/s]$	Re_D	$\rho_{water}[Kg/m^3]$	$\nu_{water}[m^2/s]$
0.305	0.2	6.0×10^4	998	10^{-6}

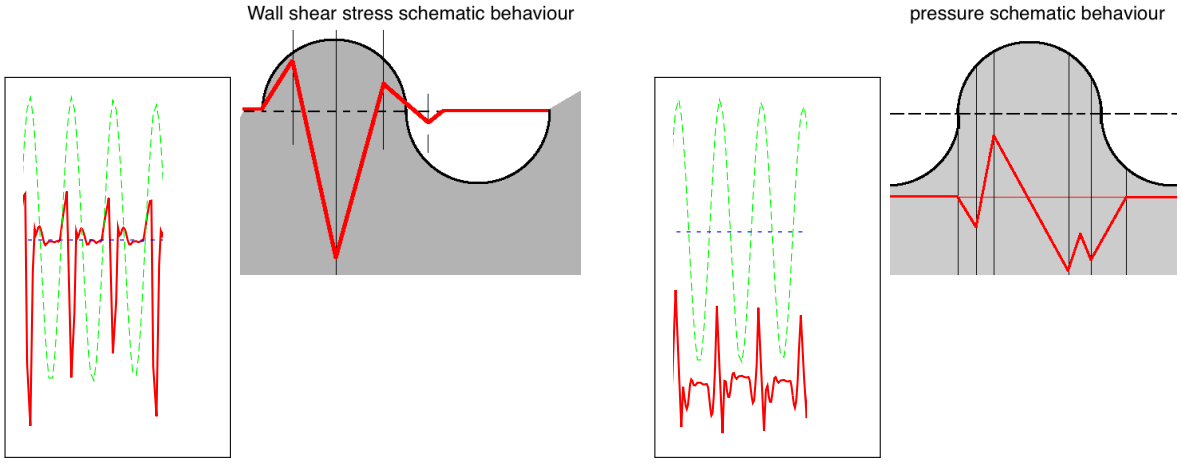

Figure 3.17: Zoom on the wall shear stress (left) and the pressure (right) curves. Central part of $Mesh_5$. The green curve represents the trace of the wrinkled surface

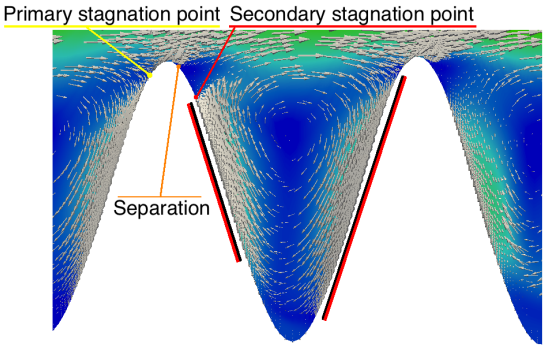

Figure 3.18: Zoom on one wrinkle ($mesh_{13}$) with vectors representing the local flow velocity. It can be observed how the recirculation region in the wrinkle is not symmetric: higher velocities arise on the right side

The experimental setup proposed in [8] is intended to be used as a validation for Fluid Structure Interactions calculations. In this section the experimental setup is shown and fluid dynamic results are presented. The structural analysis of this case is presented in chapter 4, section 4.3.2, and fluid structure interactions results are presented in chapter 5, section 5.2.7.

In the experiments, a parachute canopy was analysed in the water tunnel; the generated flow was analysed with PIV measurements. The setup was of the type shown in figure 3.19. The canopy is made out of a flat fabric (standard 1.1 oz/yd^2 rip-stop nylon) and is held in place by 24 cables on its external diameter. The device is held in place by an external structure, the effect of which is said to be negligible. The diameter D_0 reported in table 3.9 is intended as the initial undeformed diameter of the flat circular fabric. It is stated that for Reynolds numbers (based on the diameter) exceeding 10^4 the flow becomes fully turbulent [8]

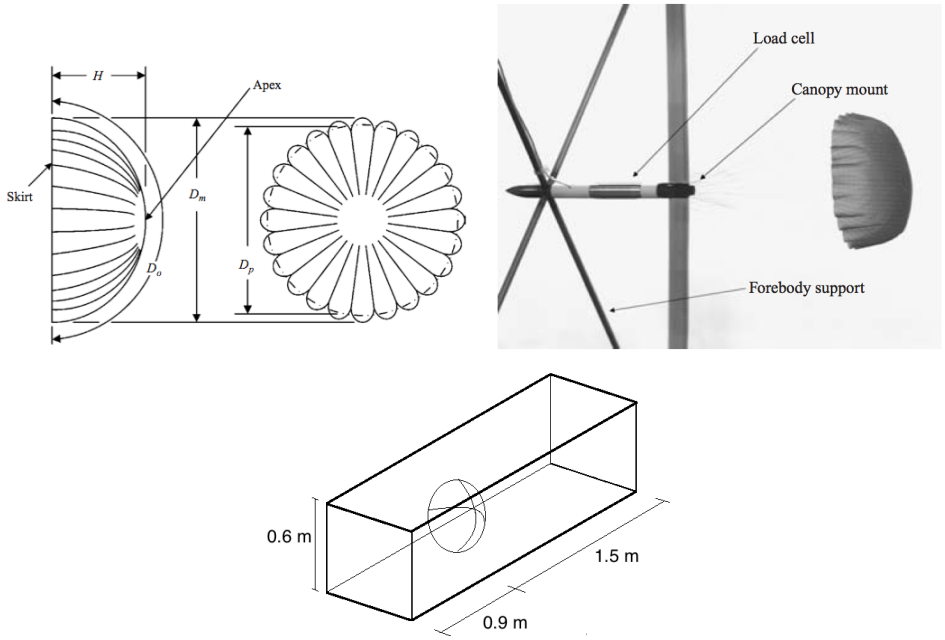

Figure 3.19: Experimental setup for the canopy. From [8], Figures 1 and 2

Table 3.10: Geometrical data used for the construction of the canopy mesh

D_P [m]	H [m]	*IN to Canopy* [m]	*Canopy to OUT* [m]	Tunnel sect. [m]
0.2135	0.0854	0.9	1.5	0.6

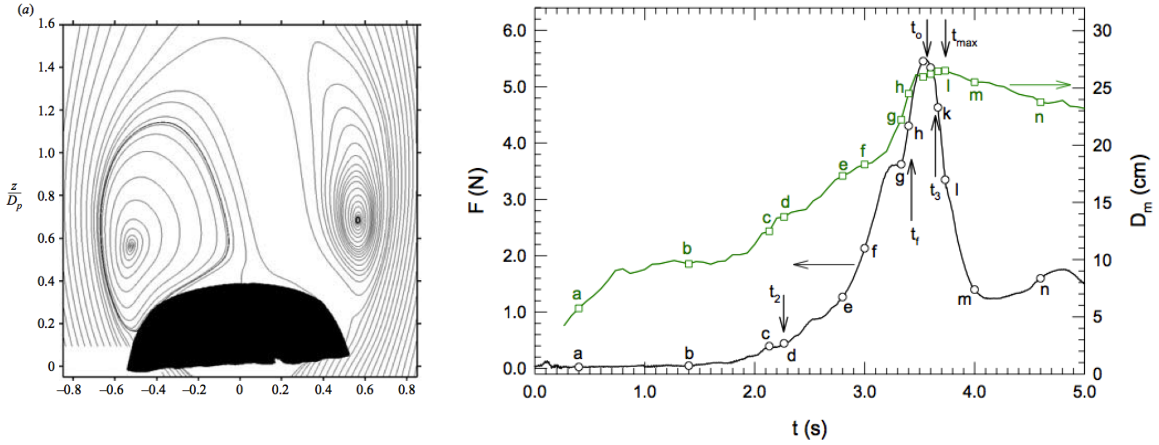

Figure 3.20: Average flow field (from [8] Fig.6a) and measured forces in the opening process (from [9], Fig.4.14)

with quasi-periodic spaced vortex loops or rings [105].

Table 3.11: Mesh specifications

	Coarse Mesh	Medium Mesh	Fine Mesh
Nels	104.736	784.032	1.535.040
y^+ range	1.3 - 20.4 - 73.2	1.3 - 20.5 - 75.6	0.037 - 0.4 - 1.87
dt	$6 \cdot 10^{-3}$	$5.5 \cdot 10^{-3}$	$1.8 \cdot 10^{-3}$

The mean flow field produced in the rear wake of the canopy is shown in figure 3.20. From the left figure it is possible to appreciate the a-symmetry of the experimental setting, where the canopy was held in place at an angle of 5°. The figure on the right reports the force generation process during the canopy inflation. During the experiments a *breathing* behaviour was observed, where the canopy's diameter oscillates in phase with the vortex shedding development. The amplitude of the oscillation reduced the projected diameter of the device by about 25% under this regime.

Results reported in the following refer to the larger canopy tested in the article. The experimental setting is reproduced using a mesh where all the geometrical features are respected as much as possible. The canopy flying shape is estimated from the data in the article, and approximated with elliptical sections. The geometry is specified in Table 3.10, where D_P is the projected diameter of the canopy flying shape with H the camber (depth) of the section, from the device side to its centre. No wrinkles are represented in this phase. The mesh consists of a fully structured grid, as is shown in Figure 3.21, where only the central portion of the calculation domain is shown. Three meshes were analysed, the details of which are reported in Table 3.11. It should be noted that the medium mesh was derived from the coarse mesh by only increasing the number of elements on the surface of the structural interface, but no change was performed in the element's height close to the wall. This explains the value of y^+ being almost constant. The fine mesh was derived from the medium mesh by only increasing the number of elements in the canopy region and close to the wall. The y^+ value is then significantly decreased. This mesh was judged sufficient for capturing the flow features by inspecting the force generation. Even if the experimental value is subjected to oscillations, its mean value can be estimated about 1.6 N (see Figure 3.20), which is the value obtained with the finer mesh. Such values are also consistent with empirical evaluations: for such geometries the $C_d \approx 2$ [106]. then $F = \frac{1}{2} c_d \rho s v^2 \approx 1.5\ N$ and $\Delta p \approx 40\ N/m^2$, where the

pressure value can be estimated to be $(0.03 + 0.01)\,\rho \approx 39.9$ from Figure 3.23. The results in terms of forces are then accurate enough, and within the band of experimental uncertainty. The mesh resolution was then judged sufficient for the analysed case.

Table 3.12: Boundary conditions in the domain

	Inlet	Outlet	Tunnel Walls	Canopy
U $[m/s]$	0.2	Zero Gradient	0	0
P $[m^2/s^2]$	Zero Gradient	0	Zero Gradient	Zero Gradient
k $[m^2/s^2]$	Wall Function	Zero Gradient	Wall Function	Wall Function
ω $[1/s]$	Wall Function	Zero Gradient	Wall Function	Wall Function

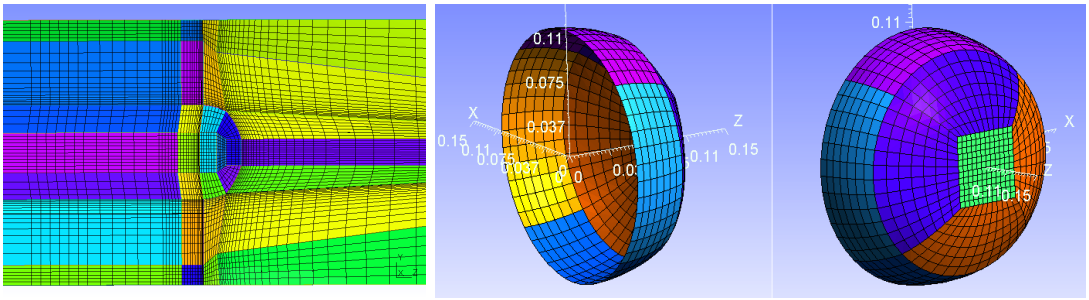

Figure 3.21: Coarse mesh adopted for the fluid calculations

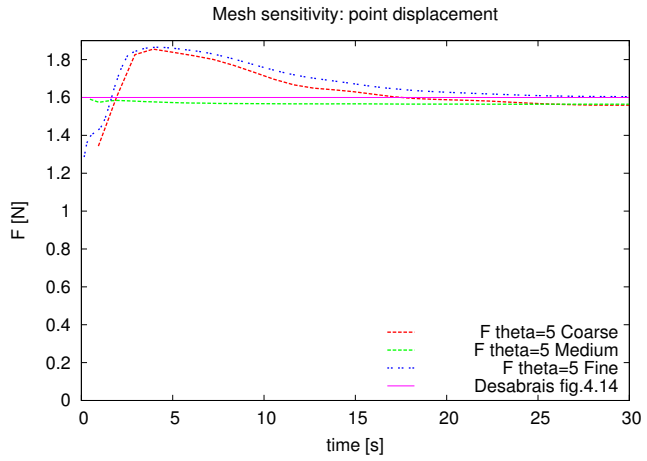

Figure 3.22: Force generation for the fixed geometry analysed case: mesh sensitivity

The assigned boundary conditions on the fluid domain are summarised in Table 3.12. The SST turbulence model was employed, and initial values for k and ω are assigned to the wall function as defined in Section 3.3.1. The internal field is initialised with constant velocity.

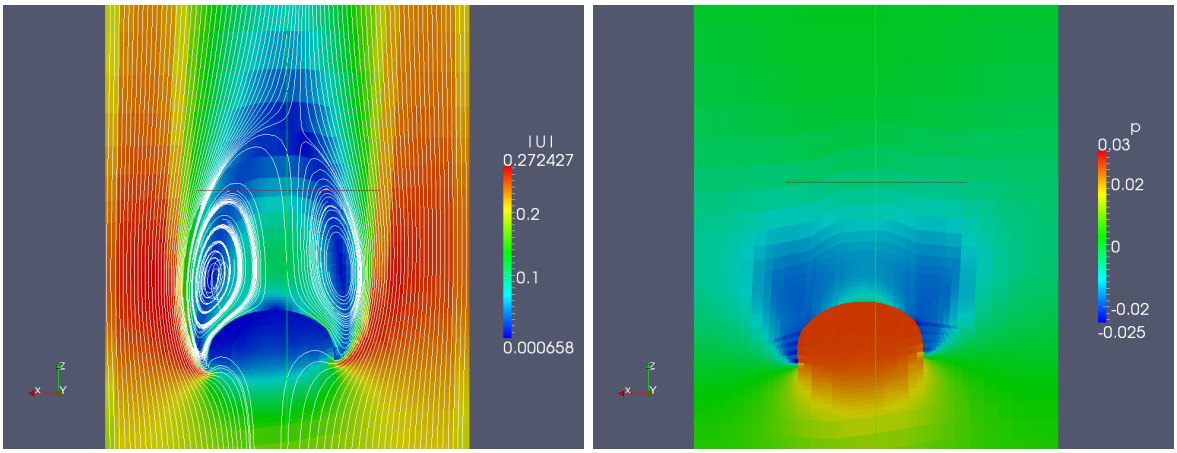

Figure 3.23: Velocity and pressure field [kinematic pressure: p/ρ $[m^2/s^2]$] for the 5° degrees canopy

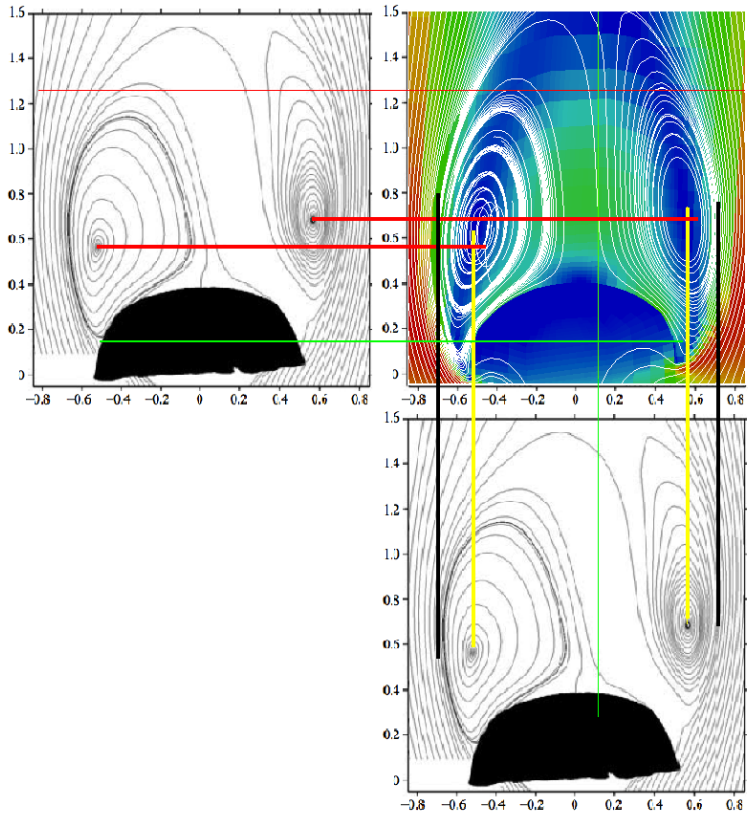

Figure 3.24: Visual comparison of the experimental (black and white Figures on the *left* and *bottom*) and the numerical mean flow field (colour Figure on the *top-right*). The lateral extension and the center of the vortices are highlighted using the black, red and yellow straight lines

Numerical results have been compared with the experimental data in Figure 3.24 in terms of streamlines and figure 3.25 in terms of vorticity.

The general velocity field has been well resolved (see Figure 3.24). In particular the right vortex seems well captured both in terms of the vortex centre, and the position of the transition

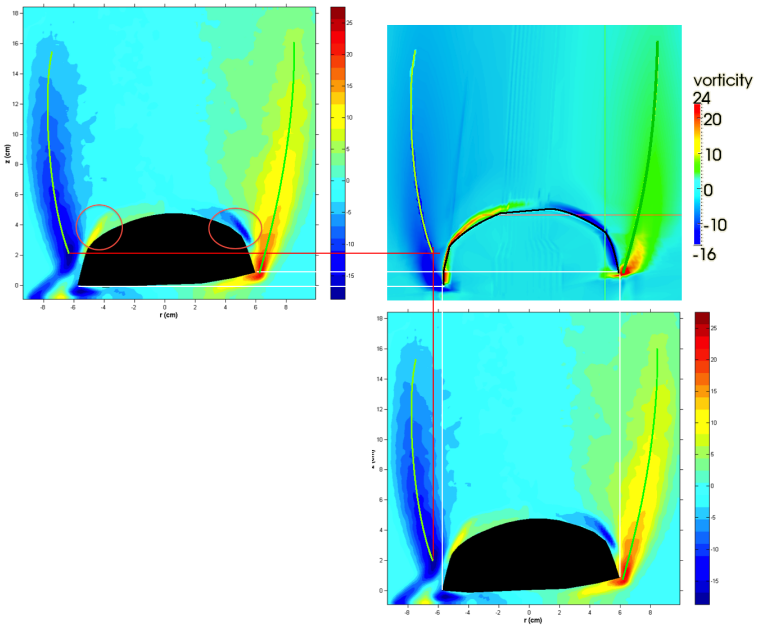

Figure 3.25: Visual comparison of the experimental (Figures on the *left* and *bottom*) and the numerical (Figure on the *top-right*) mean vorticity field. The general behaviour of the vorticity for the experimental result is highlighted using the green lines. These lines have been superposed to the numerical computed field for comparison

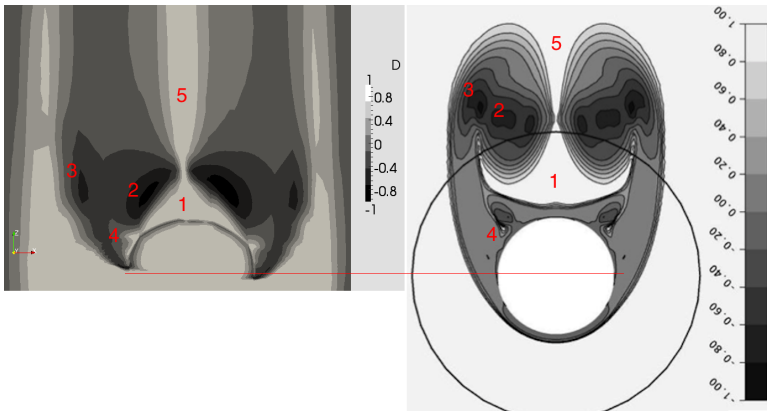

Figure 3.26: Normalised Invariant of the Deformation Tensor and comparison with a cylindrical shape from [10]

between the recirculating and the potential regions. The computation is less accurate in terms of the left vortex positioning; this might be due to a wrong evaluation of the separation point: a remarkable difference is in fact identified in terms of the separation point behind the device. The beginning of the recirculation region arises in fact close to the sharp edges for the numerical case, whereas in the experiments this region starts developing from about one third of the canopy's camber (see Figure 3.24). This difference might be primarily due

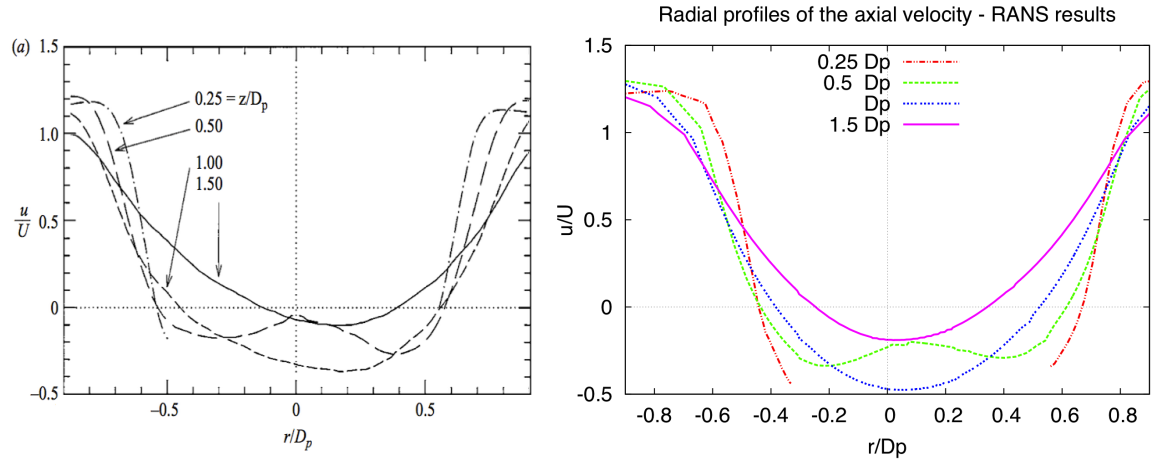

Figure 3.27: Radial profile of the axial velocity (from [8], fig.7(a)) and numerical results.

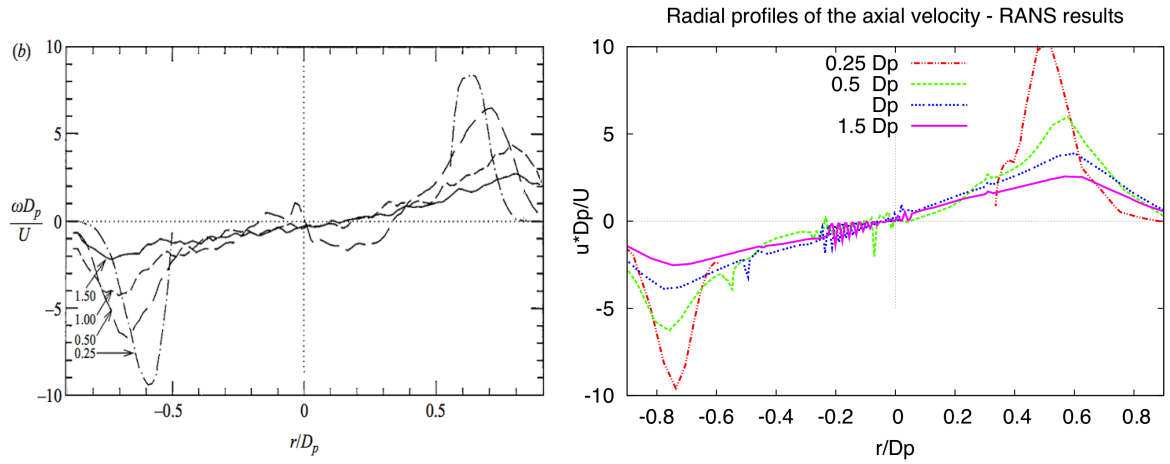

Figure 3.28: Radial profile of the vorticity (from [8], fig.7(b)) and numerical results.

to the geometry adopted for the numerical model: as it was previously stated the numerical model was reproduced as a regular surface (see figure 3.21), while in the experimental setup the large wrinkles may have affected the extent of the flow separation.

The vorticity field in figure 3.25 is also close enough to the experimental value. Some smoothing however appears, which is a typical feature of the RANS approach. The vorticity tends in fact to be concentrated in the region close to the body, and it propagates less downstream.

The normalised invariant of the deformation tensor (NIDT), defined as in section 3.2 gives information about the fluid field, and it varies from $-1 \rightarrow 1$; where -1 indicates pure rotation, 0 indicates shear and 1 indicates strain. This field is reported in figure 3.26 and it is compared to the field generated by a cylindrical shape (from [10]). Even if the geometry is different, there is some blockage and the present mesh is quite coarse, some of the general

flow features can be identified (numbered on the figure). D is equal to 1 in the potential flow outer region and in the diametral plane (5), with a larger region (1) close to the device and on the corners (4). D is equal to 0 on the walls and in the downwind shear region. Multiple systems in pure rotation ($D = 1$) are identified (2, 3).

Radial profiles of the velocity and the vorticity are reported in figure 3.27 and 3.28. It should be highlighted that the experimental data refers to the 15 cm canopy, whereas the numerical setting was performed with the 30 cm device. However, several factors show a good scalability of the system [9]. The main difference in term of velocity (figure 3.27) is found at 1.5 D_P, where the computed velocity is higher, probably due to the blockage effect. For the same reason the negative velocity in the recirculation region is higher.

The results in terms of the computed vorticity are also close to the experimental value, and in particular the slope of the curve looks well predicted. Only the peak on the right is over-estimated.

Despite the good accuracy in reproducing the time-averaged fields, the results obtained with the numerical evaluation here presented are steady, while the experimental setting shows a high degree of unsteadiness. It is reported in fact that in the experiments the parachute canopy is subjected to a periodic motion, called *breathing*, the period of which can be estimated as 1.75 [sec] (see [8], Figure 4a). The stability of the numerical solution can then be explained with two major hypothesis:

- the turbulence model smooths unsteadiness away.
- The unsteadiness is induced by the canopy motion, and it is therefore a fluid structure interaction effect.

The first hypothesis could eventually be tested using some LES or DES simulations (see Section 3.1.2). Investigation using these techniques are however beyond the scope of this work. An evaluation of the second hypothesis will be attempted in Section 5.2.7.

3.4 Fluid analysis in the time domain

The aim of this section is to investigate the capability of the fluid dynamics method in predicting the unsteady features of the flow.

A classic test case is reported in Section 3.4.1, where unsteady vortex shedding for a 2D cylinder section in laminar flow is triggered when overcoming the critical Reynolds number $Re_c = 100$. Results are compared with reference solutions [97].

Similar evaluations are presented in Section 3.4.2 for a 2D semi-circular section, representative of downwind sail sections. It is shown for this case that unsteadiness induces some additional force, beneficial for the performances of the devices of this type. The analysis is then extended to a full 3D Spinnaker-type geometry.

Some additional analyses regarding unsteady flows are reported in Chapter 5, Sections 5.2.1 and 5.2.2. These tests have been moved to the Fluid Structure Interaction chapter because the unsteady flow is either induced by the motion of a solid boundary, either the base validation case for fluid structure interactions analysis.

3.4.1 Vortex shedding prediction for 2D cylinder at varying Reynolds number

The flow around a two-dimensional cylinder section is analysed with the unsteady OpenFOAM routine icoFOAM. Several works discussed the flow past bluff bodies such as cylinders, both in 2d and 3d configurations see e.g. [107], [108], [109]. The test proposed here has been widely adopted in the literature as a validation test case, see e.g.[97] who proposed the settings which are reported in Table 3.13.

Table 3.13: Vortex shedding case settings

	$U[m/s]$	$\nu[m^2/s^2]$	$D[m]$	Re_D
Case1	0.5	0.02	2	50
Case2	1	0.02	2	100

The calculation domain is a two dimensional slice with a unit radius cylinder. A uniform structured O-grid type mesh was adopted, discretized with 10388 hexahedra and refinements in the region close to the cylinder section. Two inlet velocities are tested: the first is intended to produce a stationary flow (for $Re < 100$) where the second speed generates vortex shedding,

as in the following figures. The velocity probe is placed at one radius length behind the cylinder. In the first case, as expected, the flow remains perfectly stationary and stable. The transversal velocity component is very small (10^{-4}), and although it is initially transient it stabilizes. In the second case, a vortex shedding regime is generated, and vortices are shed behind the cylinder. The value of vortex shedding frequency f_s can be estimated at around $1/12[Hz]$. The Strouhal number, describing the non dimensional shedding period, can be calculated as:

$$St = \frac{f_s \ D}{\nu} = 1.\overline{6} \tag{3.54}$$

which is in accordance with the value given in the literature [97].

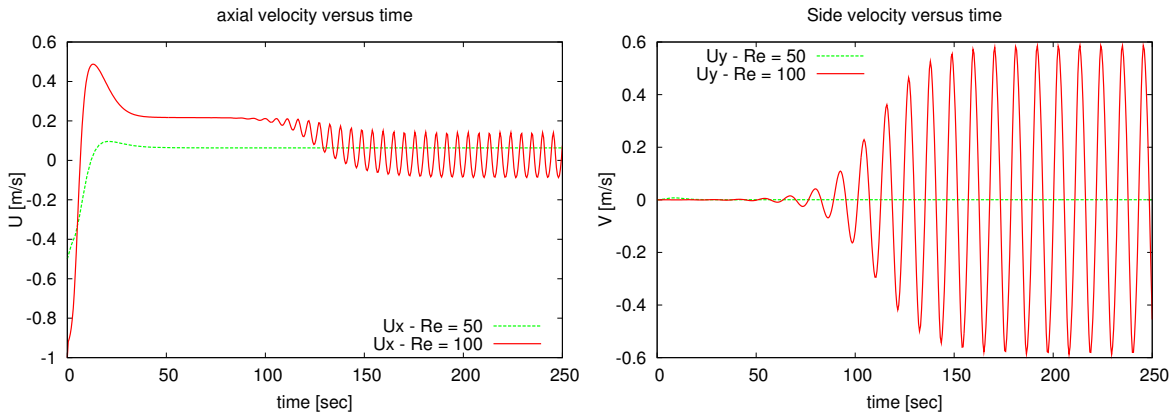

Figure 3.29: Velocity probe placed one radius behind the cylinder for Re_D=50 and Re_D=100.

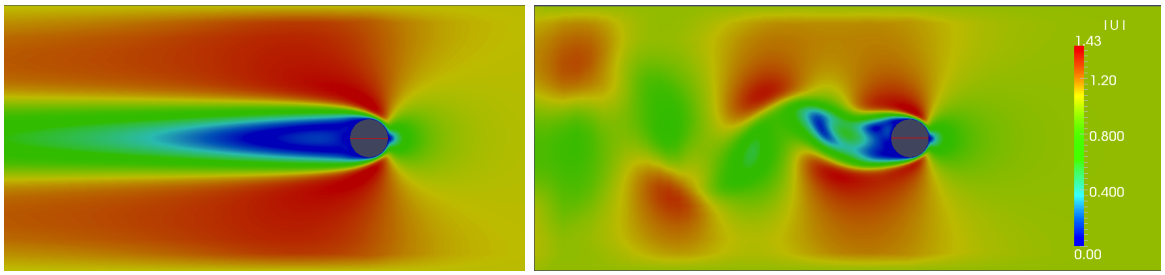

Figure 3.30: Variation of the flow behind a cylinder (zoom on a portion of the computational domain). On the left the stationary flow field for Re_D=50; on the right the vortex shedding arising for Re_D=100

3.4.2 Influence of the induced unsteadiness in the drag prediction for 2D circular sections

In the following some analyses are presented regarding the flow generation around two-dimensional sail sections. The scope of the section is to numerically investigate the development of the unsteady flow around such devices and to understand whether the unsteadiness

can affect the Lift/Drag generation process. A separated and unsteady flow is in fact expected for such devices, similar to bluff bodies. The external motions caused by the yacht in a seaway can then generate further unsteadiness.

A universal flow representation for the case of a symmetric spinnaker in symmetric, or almost symmetric flow, can be approximated as in Figure 3.31, where velocity contours are sketched. On the leeward side of the sail, a bluff flow type is generated. On the windward side, since the particular shape of such a device, the sail's stagnation point is not placed on the sail surface, but about 0.75 R upstream. This is particularly evident by looking at the iso-velocity contour in Figure 3.31 *left*. The same phenomenon can be observed later in terms of pressure (Figure 3.33), the distribution of which remains constant in the inner part of the sail. The device can then be assumed to a thick type body, as it is illustrated by the dashed line in Figure 3.31 *right*.

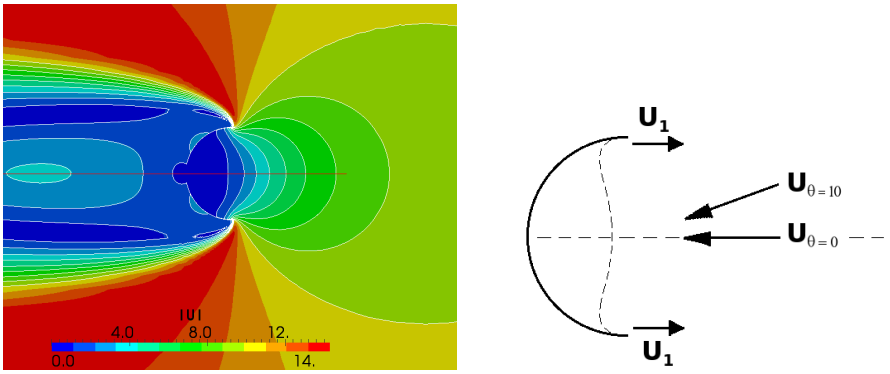

Figure 3.31: Expected flow type for symmetric bluff bodies (flow right to left)

The flow developing on such a device was analysed with two sets of simulations. In the first set, zero degrees angle of attack was imposed, whereas in the second set of simulations the angle of attack was 10 degrees. The direction of the flow in this case was defined as shown in Figure 3.31 *right*. The expected value for the symmetric case is calculated using the Euler's formula, where the force generated by the device derives from the mass flow rate; typical values for the physical quantities are given in Table 3.14

$$F_x = \rho_a \, Q \, (cos\theta \, U_1 + U_0) \tag{3.55}$$

The value of the backward velocity U_1 was estimated from the CFD analysis as 3.75 m/s. This value was established averaging the velocities in the device's boarder region, about the 10% of the section width. Using such values the calculated force is equal to 250 N for the 2D case, or $C_d = 1.92$, where the coefficient for any generic force is expressed as: $C_f = F \,/\, 0.5 \, \rho \, A_p \, u^2$. In the following, all forces are expressed in terms of non-dimensional

Table 3.14: Adopted physical quantities

ρ_a $[Kg/m^3]$	b $[m]$	U_0 $[m/s]$	Q $[m^3/s]$	ν $[m^2/s]$	Re_d [-]
1.225	4	10	40	1.1510^{-5}	3.47

coefficients. In the present case the forces F_x and F_y are measured on a local reference system, the x-axis of which is directed along the direction of the flow.

Table 3.15: Mesh specifications for the adopted meshes

Mesh	Number of elements	y^+	C_d	C_l	$T[s]$	$dt[s]$
coarse	3774	1500	3.14	-0.016	4.6	$5 \cdot 10^{-3}$
base	19245	300	3.3	0,135	5	10^{-3}
fine	45594	200	3.266	-0.231	5.5	$7 \cdot 10^{-4}$
finer	121519	100	3.277	-0.213	5.2	$5 \cdot 10^{-4}$

A structured mesh was used, in order to preserve central symmetry at all mesh points, thus second order accuracy. A C-grid was adopted for meshing the region close to the sail section. D being the diameter of the circular sail section, the computational domain was extended 5D upwind, 15D downwind in the flow stream direction and 5D in the transverse direction.

Four meshes were used for the mesh sensitivity study, the characteristics of which are summarised in terms of time averaged quantities in Table 3.15, where the values have been obtained by time averaging the force history reported in Figure 3.35. A considerable mesh sensitivity is experienced, and this affects both the magnitude of the force and its oscillation period. However, the average Drag tends to stabilize, once the y^+ value (see Equation 3.21) assumes smaller values.

Uniform velocity and pressure were imposed at the inlet; uniform pressure and zero gradient velocity were imposed at the outlet. A constant slip velocity was imposed on upper

and lower walls. Wall functions were used for the kinetic energy of the turbulence k and the vorticity ω. Freestream turbulence intensity was assumed 5%. The initial value for k and ω were calculated with the standard formulations reported in section 3.3.1. SST-kOmega turbulence model was used, with the Crank-Nicholson time marching scheme (relaxation factor: $\alpha = 0.66$). Three steps were imposed for the pressure corrector algorithm, plus one for the non-orthogonal corrector. This takes into account the distortion of the mesh, the cells of which are not always constituted by regular blocks. The time step was chosen in order to satisfy the Courant-Friedrichs-Lewy (CFL) condition, i.e maximum Courant number < 1. The Courant number (Co, equation (3.56)) is an indicator of the propagation of the numerical error within the computational domain, and it is a function of the calculation time step and the mesh size. The CFL condition $Co < 1$ assures that numerical errors are smoothed away, rather than propagated in the domain.

$$Co = \frac{u \cdot \Delta t}{\Delta x} \tag{3.56}$$

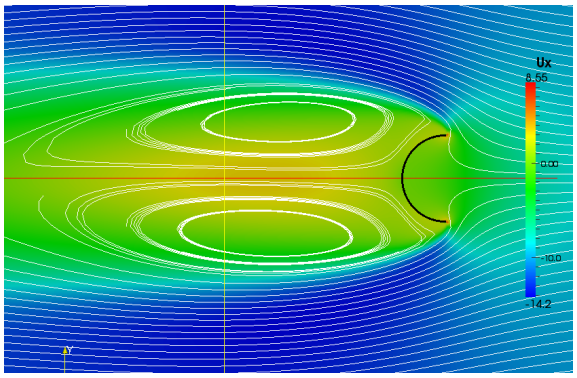

Figure 3.32: Symmetric attached flow, velocity and streamlines

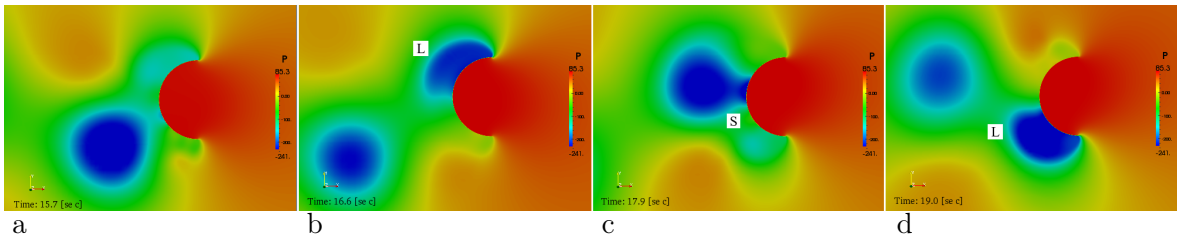

Figure 3.33: Vortex shedding generation cycle. $St = 0.5$

In Figure 3.32 the field is visualized in terms of velocities and streamlines for a flow with zero angle of attack. In this case, the flow remains steady and two symmetric vortices are formed behind the sail. When the flow rotates the symmetry is removed for the effect of

the angle of attack. This produces a highly unsteady flow with periodic vortex shedding, as visualized in Figure 3.33, where the four images represent one cycle of vortex generation in terms of pressure.

In Figure 3.33$-a$ the vortex is located on the left side of the sail section. A new vortex is then generated on the right side (Figure 3.33$-b$). This is underlined on the Figure with the letter L, which stands for lower pressure vortex. Proceeding in time this vortex splits into a primary vortex, which continues downstream, and a secondary vortex (here marked with S) which collapses back onto the sail's surface (Figure 3.33$-c$). A periodic system cycle is then closed with the formation of the last vortex on the left side of the sail section (Figure 3.33$-d$).

For *zero* angle of attack the measured transverse force is negligible, and the driving force is -237 N (drag). This value is comparable with that obtained with the Euler's formula, and the error can be roughly estimated as 5%. When introducing an angle of attack, the related flow unsteadiness produces an additional force generation. The average drag coefficient value increases by about 90%, from 1.82 to 3.48. In the Figure, the vortex markers L and S are reported, as in Figure 3.34. In the following the geometry has been updated in order to

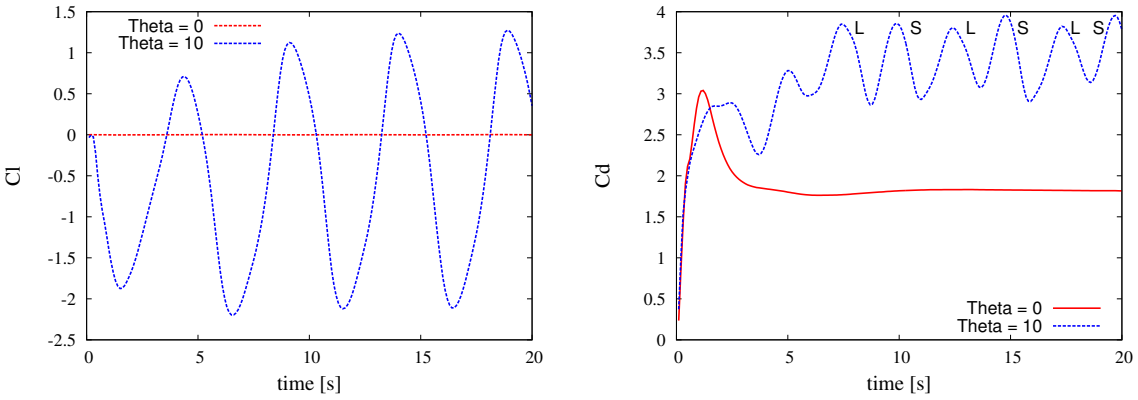

Figure 3.34: Steady/unsteady force coefficients comparison

analyse a much more realistic sail section. A typical Gennaker section was then derived by Collie [25]. The angle of attack was imposed at 22.50°, which was shown to be the angle of maximum Lift for this type of sections [57]. The new mesh was designed in order for the average y^+ (see Equation 3.21 to be around 100). A set of analysis was performed, with the objective of investigating the influence of the velocity in the force generation process. Five different inlet velocities were imposed, as summarized in the Table 3.16:

The flow field is represented in Figure 3.36 in terms of velocity magnitude and streamlines. The flow in this case does not produce vortex shedding, and remains steady. A separation bubble is generated at the leading edge, leeward side, for the effect of the sharp edge. Some

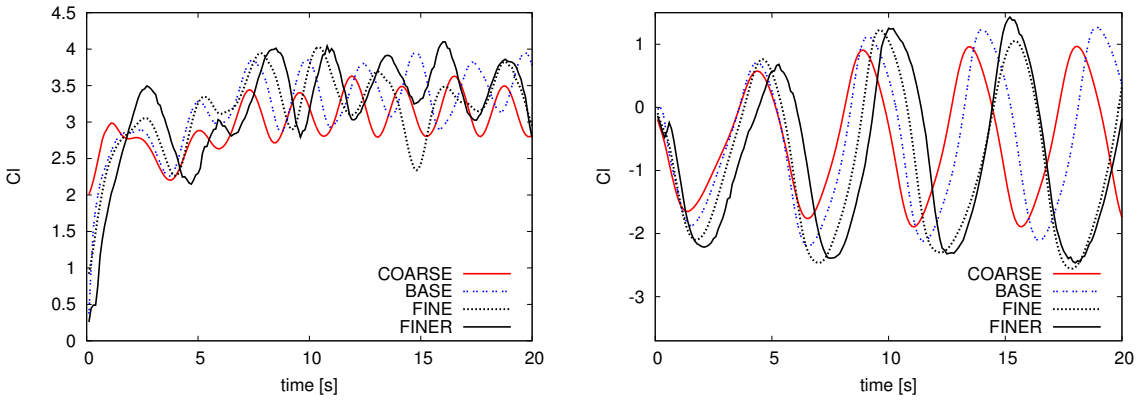

Figure 3.35: Mesh sensitivity in terms of force generation

Table 3.16: Velocities imposed for the Gennaker section analysis, and corresponding Reynolds number

$U[m/s]$	2	3.5	5	7	10
Re_d	6.910^6	1.210^7	1.710^7	2.410^7	3.510^7

recirculation can also be identified in the large separated region, the development of which is driven by the adverse pressure gradient on the second half of the leeward side of the sail.

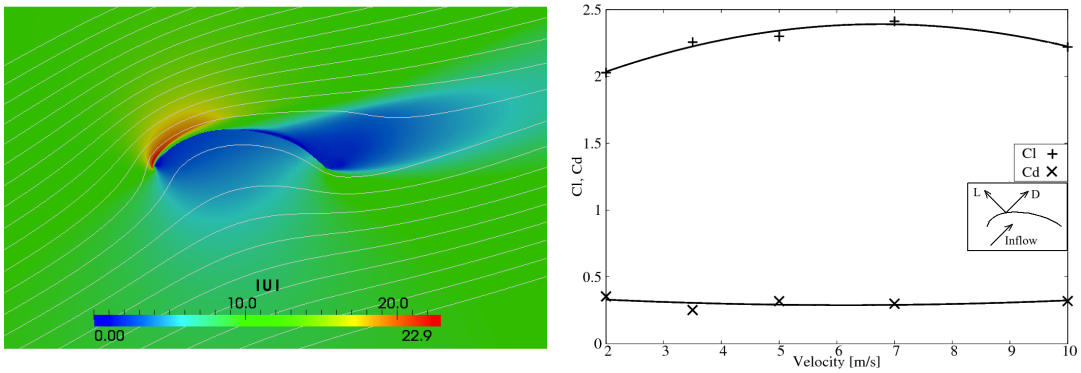

Figure 3.36: The flow on a typical Gennaker section

Results in terms of lift and drag coefficients versus inlet velocity are reported in Figure 3.36. Some stability issues must be highlighted for the slower (2 m/s) and for the faster (10 m/s) cases. This was overcome with the use of a lower time-step value. This must be related, for the slowest case, to the value of y^+, the average of which is 27.7. Such a value is close to the limit of the validity range for using wall functions (see section 3.1.3). For the higher speed, the instability could be due to prediction of the separation point, when a recirculation zone starts to develop in the separated region.

3.4.3 Influence of the induced unsteadiness in the drag prediction for a 3D downwind sail

Analysis similar to those obtained in two dimensions have been performed for the three dimensional case. The mesh was in this case derived from the two-dimensional mesh, by extruding the lower sections and adding a spherical dome at the top of the device. In figure 3.37 the sail surface and the surrounding C-grid mesh structure are shown. 1.6 million elements were used for the entire domain discretization, and a time-step $dt = 0.002\,[s]$. was chosen, in order to respect the CFL condition. The field was initialised as in the previous section, with an angle of attack of 10°. All relevant calculation parameters were left unchanged, as in the two-dimensional case. The case was run in parallel on the University of Southampton cluster IRIDIS3 using 24 processors. The solution was obtained in about 10 sec for every time-step, and a global solution, resolving the flow for 35 [sec] was obtained in about 48 hours. An

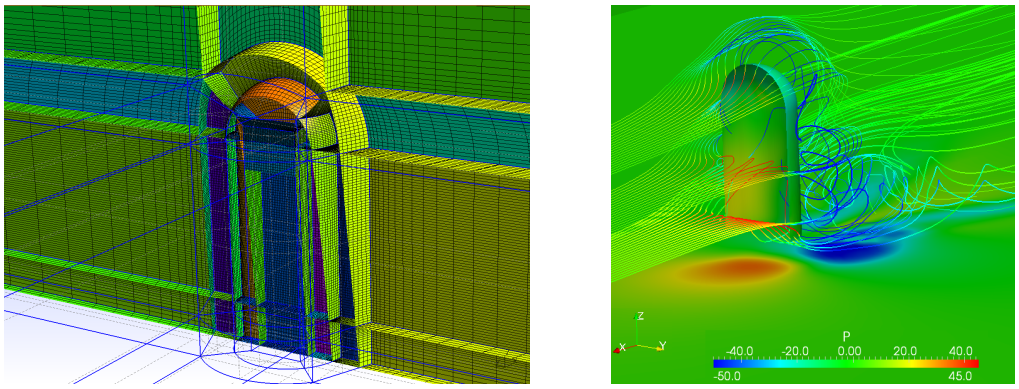

Figure 3.37: Three dimensional structured mesh and stream line representation of the flow

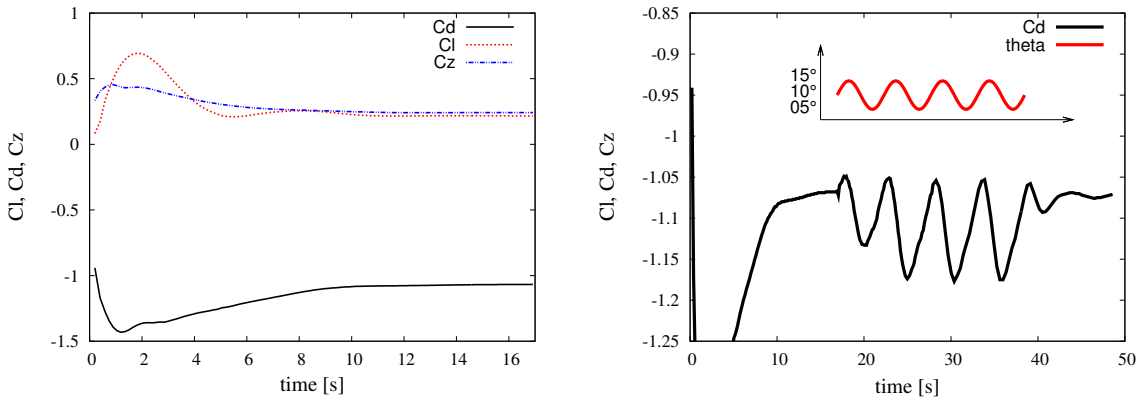

Figure 3.38: Force coefficient generation in time for the three-dimensional sail

overview of the flow regime is shown in figure 3.37 *right*, where three orders of streamlines are reported, and the colormap represents the pressure. A very large separation zone can be

identified behind the sail, where the flow behaviour seems quite chaotic and it is not possible to identify any defined flow structures. Unlike for the 2-dimensional case, the higher degree of flow mixing causes the flow to remain steady (figure 3.38, where forces coefficients are reported versus time).

The question arises then whether an induced unsteadiness, caused by the boat's motions, can induce some additional drag. The three dimensional analysis was then carried on by imposing unsteady boundary conditions at the domain inlet. It was chosen to investigate a variation in the angle of attack, by leaving all other relevant parameters unchanged. It can be shown that a boat's rolling period can be estimated as:

$$T_n = \frac{\alpha \cdot B}{\sqrt{g \cdot GM_T}} \approx 5.4[sec] \tag{3.57}$$

where $\alpha \approx 5.5$ for a sailing boat, $B = 3.7[m]$ is the boat's beam and $GM_T = 1.452[m]$ is the metacentric height.

A rotating velocity was then imposed, varying angle of attack with a symmetrical oscillation of 5 degrees around the initial value. The inlet condition was then imposed in order for the angle of attack to vary between 5 to 15 degrees with a 5.4 s period. Results from this analysis are reported in Figure 3.38., where the drag behaviour and the angle of attack variation are plotted against time. 4 cycles were imposed, in order to get a fully developed periodic behaviour. The average value of the unsteady induced drag coefficient can be estimated as 1.143, whereas the steady drag coefficient is about 1.09. Compared to the steady case, the induced unsteadiness produces an increase of about 5% in the average generated drag.

3.5 Summary

This chapter reviewed the fluid dynamic for analysis for sail-type flows. The performances of the finite volume method with SST turbulence model were demonstrated with the application to a series of test cases.

The details of the wrinkle/flow interactions were analysed in the beginning of the chapter, where the method was validated for the boundary layer development and the effect of cross-flow wrinkles was analysed. Such an effect was shown to be non negligible, and to substantially alter the force generation process. Also, it was shown that the mesh sensitivity are reduced by the presence of the wrinkles.

The prediction performances of the method were analysed for drag devices made of thin fabric with very good agreement in terms of the mean flow generation.

The unsteady characteristics of sail-type flows were analysed, and unsteadiness resulted beneficial in terms of the final performances of the device.

The fluid calculation presented here give an insight on the flow characteristics and the prediction performances of the method. This will be used with no major modifications in Chapter 5 for the analysis of the fluid structure interactions.

Chapter 4

Structural dynamics

This chapter focuses on the structural analysis with particular reference to the structural models adopted for resolving the fabric deformation and the wrinkling. The same structure as in the previous chapter has been adopted: the first part refers to the general theory (Section 4.1), then the numerical modelling is reviewed (Section 4.2) and finally a number of test cases are presented and used for demonstrating the prediction performances of the adopted methods (Section 4.3).

The structural analysis is generally approached by means of finite elements techniques, therefore a variational – energetic – approach is preferred to the other possible approaches, such as for example Finite Volumes, see e.g. [110]. A number of finite elements can be formulated, each of them discretizing a different structural model, the characteristics of which are more or less adapted to a particular type of analysis [68].

Structural simulation of sails, and of fabrics in general, is usually approached with the *Membrane* [111] [70] or the *Shell* [4] model. Both of these models are valid for thin structures, e.g. structures the thickness of which is small compared to their extension. The main difference between the shell and the membrane model lies in the bending stiffness, which is considered by the shell model (see Section 4.1.5) and neglected by the membrane model. The use of the membrane model can be considered as an acceptable assumption if wrinkling does not arise. Wrinkling is a buckling related phenomenon affecting the deformation of fabrics and thin laminates. It consists in the formation of out-of-plane oscillations on the surface of the structure in correspondence with particular combinations of stresses and boundary conditions, typical for instance of sail type configurations (see Section 4.1.10). Wrinkling is mainly controlled by the bending stiffness, therefore attempting the analysis of wrinkled fabrics with the membrane model generally produces singularities of the solution. The problem has been often overcome with the use of *ad-hoc* wrinkling models [76] [73], the role of which is to lo-

cally modify the constitutive relationship and artificially eliminate the singularity. Another possibility is to use a shell model, which considers all the relevant stiffness components; it is then possible to numerically reproduce the wrinkles if the computational mesh is fine enough [92]. If the mesh is too coarse the wrinkles are filtered and therefore they are not entirely reproduced, but still no singularity arises [81].

When using shell finite elements the problem converges to a stable and equilibrated solution; however intermediate – transient – states are observed, for which the solution is intrinsically unstable. This is due to the fact that wrinkling is a post-buckled configuration triggered by local instability (see Section 4.1.10). In addition, when the wrinkle forms a sudden change in the shape of the structure arises – called *mode jumping* – [5] which might affect the numerical resolution of the structural deformation.

Furthermore, the numerical system of equations which represents the shell is ill posed when the thickness becomes very small. The *well posedness* of a problem can be measured by the conditioning number of the system matrix. When the conditioning number is small the problem is said to be *well posed*; as the conditioning increases the problem becomes *ill posed* . The conditioning number is defined as the ratio between the highest and the smallest eigen-values, and it measures how much a function changes in proportion to small changes in the argument. In other words, the conditioning number is a measure of the difficulty in solving numerical problems. The limit case is represented by a singular matrix, for which the determinant is equal to zero. In this case the system can not be solved, and the conditioning number is ∞. The numerical system which approximates the shell problem contains terms representing the membrane stiffness, which is proportional to the thickness t, and other terms representing the bending stiffness, proportional to the cube of the thickness t^3 (see Section 4.1.6). When the thickness is very small then the system of equations associated with the stiffness operator results in a ill conditioned matrix with diagonal terms differing by several order of magnitude, thus the system is ill conditioned.

One possible strategy to overcome these problems is to adopt a pseudo-dynamic scheme with damping (see Sections 4.1.9 and 4.2.2), and potentially a *well-chosen* first guess for the solution [92]. The local instability is then counter-balanced by the additional mass and damping terms, thus allowing the numerical method to converge to a final configuration. Also the global conditioning results improved for the effect of the mass matrix terms. Several definitions of the damping are suitable, but one of the most commonly adopted is the Rayleigh damping, detailed in Section 4.1.9. In this section numerical examples are presented showing

the influence of the damping on the behaviour of the structural system, both for the linear and the non linear cases.

Not all shell formulations are suitable for the analysis of wrinkled fabrics, because very thin finite elements are subjected to a phenomenon called *Locking* [4] (see Section 4.1.8). This is due to the presence of spurious stresses within the finite element, which determines an artificial stiffening as the thickness decreases. Two main techniques are suitable for overcoming such a problem: the mixed interpolation of tensorial components (MITC) [68] and the reduced integration [65].

It was chosen here to adopt for the structural analysis the four node shell finite elements of the Mixed Interpolation type [4] (See Section 4.2.1), with a Newmark implicit dynamic scheme (mid-point rule, see section 4.2.2) and Rayleigh damping.

Numerical examples are then presented, which demonstrate the ability of the method in reproducing the deformation of thin laminates or fabrics. A comparison of the prediction performances of the shells compared to the CST membranes, which have often been employed in sail analysis, is presented in Section 4.3.1 while performing validation of the results against the experimental results [1] for a flat membrane loaded with constant pressure. A qualitative comparison is also given for a Spinnaker like structure. The inflation of a parachute canopy build as an initially flat fabric hold with cables is then analysed in Section 4.3.2 and validation for the final deformed shape is performed using experimental results [9] already used in Section 3.3.3 for the validation of the fluid dynamic method. The capability of reproducing wrinkling is validated using experimental results in Section 4.3.3. Finally the analysis is extended to sail type structures in terms of mesh sensitivity and parametric material and shape variations in Section 4.3.4.

4.1 Structural theory

This section is subdivided into four main parts. The first details the shell model, and the necessary notation is introduced (Section 4.1.2) as well as the curvilinear reference systems (Section 4.1.1). The discussion focuses then on the geometric and kinematic description of the shell (Sections 4.1.3 and 4.1.4). The basic shell model is reviewed in Section 4.1.5 and it is particularized in Section 4.1.6. Finally, the formulation of the non-linear shell problem is detailed in Section 4.1.7. The second main subject is the Locking, which is introduced in Section 4.1.8. An example of this phenomenon and the way of circumventing it is given for the simplified case of the beam model. Thirdly, the Rayleigh damping used for assuring the

convergence of the analysis is detailed in Section 4.1.9. Finally, the occurrence of wrinkling is investigated in Section 4.1.10, with particular reference to its implications in terms of equilibrium. A method is proposed for the evaluation of wrinkled sections based on geometrical considerations.

4.1.1 Curvilinear coordinate systems

An extension of the framework presented in Chapter 0.1 is represented by curvilinear coordinate systems, commonly used in the formulation of shell elements as the most *natural* reference for describing curved geometries. Such a coordinate system is defined on a *reference domain* $\Omega \subset \mathbb{R}^3$ using the smooth injective mapping $\vec{\Phi} : \overline{\Omega} = \Omega \cup \partial\Omega \to \mathcal{E}$, where $\mathcal{E}$ is the Euclidean space already defined in Chapter 0.1. The mapping $\vec{\Phi}$ is called a *chart*.

Any point M in the space is then uniquely defined by its coordinates in the curvilinear coordinate system: $O\vec{M} = \vec{\Phi}(\xi^1, \xi^2, \xi^3)$ and a local base is defined using the vectors

$$\vec{g}_m = \frac{\partial \vec{\Phi}(\xi^1, \xi^2, \xi^3)}{\partial \xi^m} \qquad m = 1,\, 2,\, 3 \tag{4.1}$$

where it is assumed that the vectors $(\vec{g}_1,\, \vec{g}_2,\, \vec{g}_3)$ are linearly independent at all points M in $\vec{\Phi}(\overline{\Omega})$. Using this local basis it is possible to define the components of vectors and tensors as before, but these components are now locally defined.

4.1.2 Covariant and contravariant basis, metric tensor

The basis introduced in Section 4.1.1 is called *covariant* basis. For curvilinear geometries it is convenient to introduce a new basis, called *contravariant*. This is inferred from the original *covariant* basis $(\vec{g}_1,\, \vec{g}_2,\, \vec{g}_3)$ by the relation:

$$\vec{g}_m \cdot \vec{g}^{\,n} = \delta^n_m \tag{4.2}$$

where δ denotes the Kroneker simbol ($\delta^n_m = 1$ if m=n; 0 otherwise). Then the components of any vector $\vec{u}$ defined in the covariant basis $(\vec{g}_1, \vec{g}_2, \vec{g}_3)$ can be expressed as the contravariant components (u^1, u^2, u^3). These components can be easily calculated with the formula:

$$u^m = \vec{u} \cdot \vec{g}^{\,m} \tag{4.3}$$

Using the Einstein's implicit summation convention then, a vector $\vec{u}$ can be expressed in covariant or contravariant basis as:

$$\vec{u} = u^m \vec{g_m} = u_m \vec{g^m} \tag{4.4}$$

The components of the vectors can be calculated using the covariant basis noting that:

$$\vec{u} \cdot \vec{g}^n = u^m \vec{g}_m \cdot \vec{g}^n = u^m \delta_n^m = u^n \tag{4.5}$$

and similarly:

$$\vec{u} \cdot \vec{g}_n = u_n \tag{4.6}$$

The metric tensor is a matrix with covariant or contravariant components defined by:

$$g_{mn} = \vec{g}_m \cdot \vec{g}_n \quad ; \quad g^{mn} = \vec{g}^m \cdot \vec{g}^n \quad ; \quad g^m_{\cdot n} = g^{\cdot m}_n = \delta^m_n \qquad m,\ n\ =\ 1,2,3 \tag{4.7}$$

For any vector $\vec{u}$ and $\vec{v}$:

$$\vec{u} \cdot \vec{\vec{g}} \cdot \vec{v} = u^m g_{mn} v^n = (u^m \vec{g}_m) \cdot (v^n \vec{g}_n) = \vec{u} \cdot \vec{v} \tag{4.8}$$

This justifies the name "metric tensor", since the dot product allows to compute lengths of vectors, hence distances. An practical example of the calculation of the metric tensor is given in Appendix B.10.

The components of the metric tensor can be used to obtain contravariant components from covariant components and vice-versa. For a vector $\vec{u}$:

$$u^m = \vec{u} \cdot \vec{g}^m = (u_n\, \vec{g}^n) \cdot \vec{g}^m = g^{mn} u_n \tag{4.9}$$

and similarly:

$$u_m = g_{mn} u^n \tag{4.10}$$

Similar conversions can be computed for second order tensors (see Appendix B.1), for instance:

$$T_{mn} = g_{mk}\ T^k_{\cdot n} = g_{nk}\ T^{\cdot k}_m = g_{mk}\ g_{nl}\ T^{kl} \tag{4.11}$$

4.1.3 Geometric definition of a shell

Consider a shell with mid-surface S defined by a 2D chart $\vec{\phi}$ which is an injective mapping $\omega : \mathbb{R}^2 \to \mathcal{E}$, hence $S = \vec{\phi}(\vec{\omega})$. Assume that at each point of the mid-surface it is possible to define the linearly independent vectors

$$\vec{a}_\alpha = \frac{\partial \vec{\phi}(\xi^1, \xi^2)}{\partial \xi^\alpha} \qquad \alpha = 1,\ 2 \tag{4.12}$$

and the unit normal vector is defined as

$$\vec{a}_3 = \frac{\vec{a_1} \times \vec{a_2}}{\|\vec{a_1} \times \vec{a_2}\|} \tag{4.13}$$

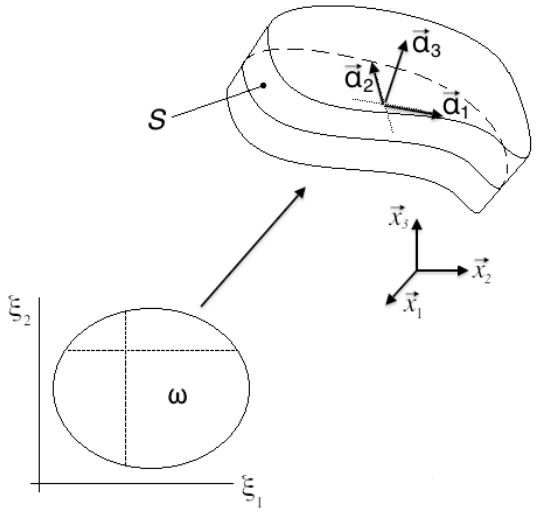

Figure 4.1: Geometric definition of a shell

The 3D medium corresponding to the shell is then defined by the 3D chart given by:

$$\vec{\Phi}(\xi^1, \xi^2, \xi^3) = \vec{\phi}(\xi^1, \xi^2) + \xi^3 \, \vec{a}_3(\xi^1, \xi^2) \tag{4.14}$$

for (ξ^1, ξ^2, ξ^3) in Ω, defined as:

$$\Omega = \left\{ (\xi^1, \xi^2, \xi^3) \in \mathbb{R}^3 \,\middle|\, (\xi^1, \xi^2) \in \omega, \, \xi^3 \in \left] -\frac{t(\xi^1, \xi^2)}{2}, \frac{t(\xi^1, \xi^2)}{2} \right[\right\} \tag{4.15}$$

where $t(\xi^1, \xi^2)$ is the thickness of the shell at the point of coordinates (ξ^1, ξ^2).

It is now possible to define a covariant basis $\vec{a}_1, \vec{a}_2$ and a contravariant basis $\vec{a}^1, \vec{a}^2$ of the tangent plane at the point considered. The restriction of the metric tensor to the tangent plane, also called *first fundamental form* of the surface is given by:

$$a_{\alpha\beta} = \vec{a}_\alpha \cdot \vec{a_\beta} \qquad ; \qquad a^{\alpha\beta} = \vec{a}^{\,\alpha} \cdot \vec{a}^{\,\beta} \tag{4.16}$$

The *second fundamental form*, or curvature tensor is defined as:

$$b_{\alpha\beta} = \vec{a}_3 \cdot \vec{a}_{\alpha,\beta} \tag{4.17}$$

and (see appendix B.2):

$$b_{\alpha\beta} = -\vec{a}_{3,\beta} \cdot \vec{a}_\alpha \tag{4.18}$$

The *third fundamental form* is defined as:

$$c_{\alpha\beta} = b^\lambda_\alpha \, b_{\lambda\beta} \tag{4.19}$$

where the term b^λ_α is defined as (see Appendix B.3):

$$b^\lambda_\alpha = a^{\lambda\mu} \, b_{\mu\alpha} = -a^{\lambda\mu} \vec{a}_{3,\alpha} \cdot \vec{a}_\mu = -\vec{a}_{3,\alpha} \cdot \vec{a}^\lambda = \vec{a}^\lambda_{,\alpha} \cdot \vec{a}_3 \tag{4.20}$$

Further it is valid that (see Appendices B.4 and B.6):

$$\vec{a}_{3,\alpha} = (\vec{a}_{3,\alpha} \cdot \vec{a}_\lambda)\, \vec{a}^\lambda \tag{4.21}$$

$$\vec{a}_{3,\alpha} = -b_{\alpha\lambda}\vec{a}^\lambda = -b^\lambda_\alpha \vec{a}_\lambda \tag{4.22}$$

In what follows, it is introduced the covariant differentiation of the surface tensors. This is done using a vector $\vec{u}$, where it is assumed that the vector is tangent to the surface at the every point:

$$\frac{d}{dx}[\vec{u}(\xi^1(x), \xi^2(x))] = \frac{\partial \vec{u}}{\partial \xi^\alpha}\frac{\partial \xi^\alpha}{\partial x} = \frac{\partial \vec{u}}{\partial \xi^\alpha} \cdot (\xi^\alpha)'(x) \tag{4.23}$$

recalling the decomposition of a vector stated in equation (4.4) $\vec{u} = u_\beta\, \vec{a}^\beta$, so the second term rewrites:

$$\frac{\partial \vec{u}}{\partial \xi^\alpha} = u_{\beta,\alpha}\, \vec{a}^\beta + u_\lambda\, \vec{a}^\lambda_{,\alpha} = (u_{\beta,\alpha} + u_\lambda\, \vec{a}^\lambda_{,\alpha} \cdot \vec{a}_\beta)\, \vec{a}^\beta + (u_\lambda\, \vec{a}^\lambda_{,\alpha} \cdot \vec{a}_3)\, \vec{a}_3 \tag{4.24}$$

where for the last equality it has been used the identity:

$$\vec{w} = (\vec{w} \cdot \vec{a}_\beta)\, \vec{a}^\beta + (\vec{w} \cdot \vec{a}_3)\, \vec{a}_3 \tag{4.25}$$

this holds because of the choice of the local basis, with $\vec{a}_3$ unit vector normal to the tangent plane defined by the two vectors $\vec{a}_\beta$. The *surface Christoffel symbols* are defined as:

$$\Gamma^\lambda_{\beta\alpha} = \vec{a}_{\beta,\alpha} \cdot \vec{a}^\lambda = -\vec{a}_\beta \cdot \vec{a}^\lambda_{,\alpha} \tag{4.26}$$

where the last equality is obtained by differentiating the definition in (4.2): $\vec{a}_\beta \cdot \vec{a}^\lambda = \delta^\lambda_\beta \Rightarrow d(\vec{a}_\beta \cdot \vec{a}^\lambda) = 0$. Equation (4.24) rewrites then, using (4.26) and (4.20):

$$\frac{\partial \vec{u}}{\partial \xi^\alpha} = (u_{\beta,\alpha} - \Gamma^\lambda_{\beta\alpha} u_\lambda)\, \vec{a}^\beta + b^\lambda_\alpha\, u_\lambda \vec{a}_3 \tag{4.27}$$

The first part of the expression being tangent to the surface, it represents the components of the surface gradient denoted by $\underline{\underline{\nabla}}\vec{u}$, where the symbol $\underline{\underline{\cdot}}$ is used to indicate that the operator lies in the plane tangent to the surface at every point. The covariant-covariant components of the gradient tensor will be indicated as:

$$u_{\beta|\alpha} = u_{\beta,\alpha} - \Gamma^\lambda_{\beta\alpha} u_\lambda \tag{4.28}$$

where $u_{\beta|\alpha}$ is called the *surface covariant derivative* of u_β

It is then possible to express the differential geometry of the shell in terms of 3D covariant base vectors:

$$\begin{aligned} \vec{g}_\alpha &= \frac{\partial \vec{\Phi}}{\partial \xi^\alpha} = \vec{a}_\alpha + \xi^3 \vec{a}_{3,\alpha} = \vec{a}_\alpha - \xi^3 b_\alpha^\lambda \vec{a}_\lambda = (\delta_\alpha^\lambda)\, \vec{a}_\lambda - \xi^3\, b_\alpha^\lambda\, \vec{a}_\lambda \\ \vec{g}_3 &= \frac{\partial \vec{\Phi}}{\partial \xi^3} = \vec{a}_3 \end{aligned} \tag{4.29}$$

the components of the 3D metric tensor are then directly derived as (see Appendix B.7):

$$\begin{cases} g_{\alpha\beta} = \vec{g}_\alpha \cdot \vec{g}_\beta = a_{\alpha\beta} - 2\,\xi^3\, b_{\alpha\beta} + (\xi^3)^2\, c_{\alpha\beta} \\ g_{\alpha 3} = \vec{g}_\alpha \cdot \vec{g}_3 = 0 \\ g_{33} = \vec{g}_3 \cdot \vec{g}_3 = 1 \end{cases} \tag{4.30}$$

4.1.4 Shell kinematics

Most classical shell models are based upon kinematic assumptions, such as the *Reissner-Mindlin* kinematic assumption. This assumption regards the displacements of points located on a straight material line that is orthogonal to the mid-surface in the undeformed configuration, and it states that this material line remains straight and unstreched during the deformation. This is expressed as:

$$\vec{U}(\xi^1, \xi^2, \xi^3) = \vec{u}(\xi^1, \xi^2) + \xi^3 \theta_\lambda(\xi^1, \xi^2)\, \vec{a}^\lambda(\xi^1, \xi^2) \tag{4.31}$$

where it has been considered a material line in the direction of $\vec{a}_3$ at the coordinates (ξ^1, ξ^2). The displacement $\vec{u}(\xi^1, \xi^2)$ represents a global infinitesimal displacement, and the contribution to the displacement given by the rotations θ_1 and θ_2 is represented by the term: $\xi^3\, \theta_\lambda(\xi^1, \xi^2)\, \vec{a}^\lambda(\xi^1, \xi^2)$. Note that it is assumed that the rotation of an infinitely-thin straight material line is uniquely defined by a rotation vector normal to that line, hence with no components on $\vec{a}_3$.

The linearised Green-Lagrange strain tensor is then defined (see Appendix B.5) for a general displacement $\vec{U}(\xi^1, \xi^2, \xi^3)$:

$$e_{ij}(\vec{U}) = \frac{1}{2}(\vec{g}_i \cdot \vec{U}_{,j} + \vec{g}_j \cdot \vec{U}_{,i}) \quad i,\, j{=}\ 1,\, 2,\, 3 \tag{4.32}$$

the components of such tensor can be calculated using the identity (4.25):

$$\frac{\partial \vec{u}}{\partial \xi^\alpha} = \frac{\partial}{\partial \xi^\alpha}[u_\lambda \vec{a}^\lambda + u_3 \vec{a}_3] \tag{4.33}$$

The first part being the tangent component, it can be equalled to the components of the gradient expressed in (4.27), rewritten using (4.28):

$$\frac{\partial}{\partial \xi^\alpha}(u_\lambda \vec{a}^\lambda) = u_{\lambda|\alpha} \vec{a}^\lambda + b_\alpha^\lambda\, u_\lambda \vec{a}_3 \tag{4.34}$$

thus:

$$\frac{\partial \vec{u}}{\partial \xi^\alpha} = u_{\lambda|\alpha}\vec{a}^\lambda + b_\alpha^\lambda\, u_\lambda \vec{a}_3 + u_{3,\alpha}\,\vec{a}_3 + u_3\,\vec{a}_{3,\alpha} = (u_{\lambda|\alpha} - b_{\lambda\alpha}u_3)\vec{a}^\lambda + (u_{3,\alpha} + b_\alpha^\lambda u_\lambda)\vec{a}_3 \quad (4.35)$$

Similarly to (4.34) then:

$$\frac{\partial}{\partial \xi^\alpha}(\theta_\lambda \vec{a}^\lambda) = \theta_{\lambda|\alpha}\vec{a}^\lambda + b_\alpha^\lambda\,\theta_\lambda \vec{a}_3 \quad (4.36)$$

the complete derivative of the displacement expressed in (4.31) then writes:

$$\begin{aligned} \frac{\partial \vec{U}}{\partial \xi^\alpha} &= (u_{\lambda|\alpha} - b_{\lambda\alpha}u_3 + \xi^3\theta_{\lambda|\alpha})\vec{a}^\lambda + (u_{3,\alpha} + b_\alpha^\lambda u_\lambda + \xi^3 b_\alpha^\lambda \theta_\lambda)\,\vec{a}_3 \\ \frac{\partial \vec{U}}{\partial \xi^3} &= \theta_\lambda \vec{a}^\lambda \end{aligned} \quad (4.37)$$

Substituting the equations below, (4.29) into (4.32):

$$\begin{cases} e_{\alpha\beta} = \gamma_{\alpha\beta}(\vec{u}) + \xi^3\chi_{\alpha\beta}(\vec{u},\underline{\theta}) - (\xi^3)^2 k_{\alpha\beta}(\underline{\theta}), \alpha,\ \beta = 1,\ 2 \\ e_{\alpha 3} = \zeta_\alpha(\vec{u},\theta), \alpha = 1,\ 2 \\ e_{33} = 0 \end{cases} \quad (4.38)$$

where:

$$\begin{cases} \gamma_{\alpha\beta}(\vec{u}) = \frac{1}{2}(u_{\alpha|\beta} + u_{\beta|\alpha}) - b_{\alpha\beta}\,u_3 \\ \chi_{\alpha\beta}(\vec{u},\underline{\theta}) = \frac{1}{2}(\theta_{\alpha|\beta} + \theta_{\beta|\alpha} - b_\beta^\lambda u_{\lambda|\alpha} - b_\alpha^\lambda u_{\lambda|\beta}) + c_{\alpha\beta}\,u_3 \\ k_{\alpha\beta}(\underline{\theta}) = \frac{1}{2}(b_\beta^\lambda \theta_{\lambda|\alpha} + b_\alpha^\lambda \theta_{\lambda|\beta}) \\ \zeta_\alpha(\vec{u},\underline{\theta}) = \frac{1}{2}(\theta_\alpha + u_{3,\alpha} + b_\alpha^\lambda u_\lambda) \end{cases} \quad (4.39)$$

4.1.5 The basic shell model

In order to establish a constitutive relationship the Hooke law will be here used. This, in a general curvilinear coordinate system reads:

$$\sigma_{ij} = H^{ijkl}\,e_{kl} \quad (4.40)$$

with

$$H^{ijkl} = L_1\,g^{ij}g^{kl} + L_2\,(\,g^{ik}g^{jl} + g^{il}g^{jk}\,) \quad (4.41)$$

where:

$$L_1 = E\frac{\nu}{(1+\nu)(1-2\nu)} \quad ; \quad L_2 = \frac{E}{2(1+\nu)} \quad (4.42)$$

L_1 and L_2 are the shell specific Lamé constants, E is the Young modulus and ν the Poisson ratio.

Because of the considerations on the geometry of the shell reviewed in the previous sections, namely $g^{33} = 1$, $g^{\alpha 3} = 0$ and using the assumption $\sigma^{33} = 0$, the constitutive relationship (4.40) simplifies as:

$$\begin{cases} \sigma^{\alpha\beta} = C^{\alpha\beta\lambda\mu} e_{\lambda\mu} \\ \sigma^{\alpha 3} = \frac{1}{2} D^{\alpha\lambda} e_{\lambda 3} \end{cases} \tag{4.43}$$

with:

$$C^{\alpha\beta\lambda\mu} = \frac{E}{2(1+\nu)} \left(g^{\alpha\lambda} g^{\beta\mu} + g^{\alpha\mu} g^{\beta\lambda} + \frac{2\nu}{1-\nu} g^{\alpha\beta} g^{\lambda\mu} \right) \tag{4.44}$$

$$D^{\alpha\lambda} = \frac{2E}{1+\nu} g^{\alpha\lambda} \tag{4.45}$$

and the *basic shell model* is then represented by the variational formulation:

$$\int_\Omega \left[C^{\alpha\beta\lambda\mu} \, e_{\alpha\beta}(\vec{U}) \, e_{\lambda\mu}(\vec{V}) + D^{\alpha\lambda} \, e_{\alpha 3}(\vec{U}) \, e_{\lambda 3}(\vec{V}) \right] \mathrm{d}V = \int_\Omega \vec{F} \cdot \vec{V} \, dV \tag{4.46}$$

where $\vec{U}$ is the unknown that satisfies the Reissner-Mindlin kinematic assumption (see section 4.1.4) and the boundary conditions; $\vec{V}$ is an arbitrary test function satisfying the same kinematic assumption as is Equation (4.31) and the boundary conditions. $\vec{F}$ is the external loading. The first term in the left hand side represents the membrane and bending deformation energy, while the second term represents the shear deformation energy. The terms in left and the right hand side are normally referred to as, respectively, internal and external virtual work.

4.1.6 The "shear-membrane-bending" model

The s-m-b model is derived from the basic shell model reviewed in the previous section and it is the conceptual model used for the numerical analysis presented in this thesis. The term $e_{\alpha\beta}$ (see Equation (4.38)) will then be substituted by $\gamma_{\alpha\beta} + \xi^3 \chi_{\alpha\beta}$, by truncation to the lowest order terms with respect to the transverse coordinate ξ^3. The volume dV will be calculated as $dV = \sqrt{a} \; d\xi^1 d\xi^2 d\xi^3$ (see Appendix B.9) and the terms ${}^0C^{\alpha\beta\lambda\mu}$ and ${}^0D^{\alpha\lambda}$ will be substituted in Equation (4.46), where:

$${}^0C^{\alpha\beta\lambda\mu} = \frac{E}{2(1+\nu)} \left(a^{\alpha\lambda} a^{\beta\mu} + a^{\alpha\mu} a^{\beta\lambda} + \frac{2\nu}{1-\nu} a^{\alpha\beta} a^{\lambda\mu} \right) \tag{4.47}$$

$${}^0D^{\alpha\lambda} = \frac{2E}{1+\nu} a^{\alpha\lambda} \tag{4.48}$$

The assumption is then made, that the load is constant through the thickness. Integrating then with respect to ξ^3 it is obtained the variational problem for the s-m-b model:

$$\begin{aligned} \int_\omega {}^0C^{\alpha\beta\lambda\mu} \left[t \, \gamma_{\alpha\beta}(\vec{u}) \, \gamma_{\lambda\mu}(\vec{v}) + \frac{t^3}{12} \, \chi_{\alpha\beta}(\vec{u}, \theta) \, \chi_{\lambda\mu}(\vec{v}, \eta) \right] dS \\ + k \int_\omega t \; {}^0D^{\alpha\lambda} \, \zeta_\alpha(\vec{u}, \underline{\theta}) \, \zeta_\lambda(\vec{v}, \underline{\eta}) \, dS = \int_\omega t \, \vec{F} \cdot \vec{v} \, dS \end{aligned} \tag{4.49}$$

for arbitrary test functions $(\vec{v}, \eta)$, and the thickness t being a parameter that may depend upon (ξ^1, ξ^2). The tensors $\underline{\underline{\chi}}$, $\underline{\underline{\gamma}}$, $\underline{\underline{\zeta}}$ are respectively the bending, membrane and shear strain tensors, and they are defined as follows:

$$\chi_{\alpha\beta}(\vec{u}, \underline{\theta}) = \frac{1}{2}(\theta_{\alpha|\beta} + \theta_{\beta|\alpha} - b^{\lambda}_{\beta}\, u_{\lambda|\alpha} - b^{\lambda}_{\alpha}\, u_{\lambda|\beta}) + c_{\alpha\beta}\, u_3 \tag{4.50}$$

$$\gamma_{\alpha\beta}(\vec{u}) = \frac{1}{2}(u_{\alpha|\beta} + u_{\beta|\alpha}) - b_{\alpha\beta}\, u_3 \tag{4.51}$$

$$\zeta_{\alpha}(\vec{u}, \underline{\theta}) = \frac{1}{2}(\theta_{\alpha} + u_{3,\alpha} + b^{\lambda}_{\alpha}\, u_{\lambda}) \tag{4.52}$$

where the terms used here are defined in Equations (4.17), (4.19), (4.20), (4.28). The shear correction factor k is then introduced on heuristic basis.

4.1.7 The non-linear shell problem

In the previous sections the shell model was reviewed and this led to a variational formulation. In this section it will be shown how this variational formulation is used for solving the non-linear elastic problem in a numerical environment. All the concepts expressed here will be used for showing the discretization of the shell model in Section 4.2.1.

The principle of virtual work states the balance of internal deformation and external work, and it is formulated (see also Equations (4.46) and (4.49)) as:

$$\int_V \sigma^{ij}(\vec{U})\, \delta e_{ij}\, dV = \int_V \vec{f}\, \delta\vec{v}\, dV \tag{4.53}$$

or, in terms of internal-external work:

$$W^{int}(\vec{U})(\delta\vec{\phi}, \delta\underline{\alpha}) = W^{ext}(\vec{U})(\delta\vec{\phi}, \delta\underline{\alpha}) \tag{4.54}$$

where the work is here expressed as a function of the position $\vec{\phi}$ and the rotations $\underline{\alpha}$, the unknown variables on which the shell model is based. This balance is solved using a Newton algorithm, the role of which is searching for the solution $\vec{U} \in \mathcal{V}_h$ which satisfies Equation (4.53), where $\mathcal{V}_h$ is the space of the finite element solutions. A Newton step then consists in solving:

$$d\left(\int_V \sigma^{ij}(\vec{U})\, \delta e_{ij}\, dV\right) \cdot \Delta\vec{U} = \int_V \vec{f}\, d\vec{v}\, d\vec{V} - \int_V \sigma^{ij}(\vec{U})\, \delta e_{ij}\, dV \tag{4.55}$$

The term on the left-hand side is the derivative of the internal deformation energy and the right-hand side is called the residual, comprising the last term named non-linear right-hand side. The internal deformation energy in the left hand side writes:

$$\int_V \frac{\partial\sigma^{ij}}{\partial(\vec{\phi}, \underline{\alpha})} d(\vec{\phi}, \underline{\alpha})\, \delta e_{ij}\, dV + \int_V \sigma^{ij} \frac{\partial\delta e_{ij}}{\partial(\vec{\phi}, \underline{\alpha})} d(\vec{\phi}, \underline{\alpha})\, dV \tag{4.56}$$

where in the right hand side the first term represents the linear elasticity and the second term represents the non-linear elasticity. The linear part is further developed using a constitutive relationship of the type $\sigma = \mathbf{C} \cdot \vec{\epsilon}$. The linear elasticity becomes then:

$$\frac{\partial \sigma^{ij}}{\partial(\vec{\phi}, \underline{\alpha})} \, d(\vec{\phi}, \underline{\alpha}) \, \delta e_{ij} \; = \; \sigma \cdot \vec{\epsilon} = \; \vec{\epsilon}^{\,T} \cdot \mathbf{C} \cdot \vec{\epsilon} \tag{4.57}$$

associated with a matrix called the linearised stiffness matrix.

The non-linear part requires some more manipulations. The variation of the strains δe_{ij} is calculated using the definition (4.32). Differentiating then:

$$\delta e_{ij} = \frac{1}{2}[\vec{g}_i \cdot \delta \vec{V}_{,j} + \vec{g}_j \cdot \delta \vec{V}_{,i} + \vec{U}_{,i} \cdot \delta \vec{V}_{,j} + \vec{U}_{,j} \cdot \delta \vec{V}_{,i}] \tag{4.58}$$

where is was used the relation: $\delta \vec{g}_i$, $\delta \vec{g}_j = 0$, valid because the $\vec{g}_i$ are constant vectors referring to the reference configuration.

Because of the decoupled definition of the shell as in (4.14) the derivatives will be expressed as $\partial / \partial(\vec{\phi}, \underline{\alpha})$, indicating the partial derivative with respect to the position $\vec{\phi}$ or the rotations $\underline{\alpha}$. Thus the non-linear strain rate term in (4.56):

$$\begin{aligned}
\frac{\partial \, \delta e_{ij}}{\partial(\vec{\phi}, \underline{\alpha})} \;\; &= \;\; \frac{1}{2}\Bigg[\frac{\partial \vec{g}_i}{\partial(\vec{\phi}, \underline{\alpha})} \cdot \delta \vec{V}_{,j} + \frac{\partial \vec{g}_j}{\partial(\vec{\phi}, \underline{\alpha})} \cdot \delta \vec{V}_{,i} + \vec{g}_i \cdot \frac{\partial \delta \vec{V}_{,j}}{\partial(\vec{\phi}, \underline{\alpha})} + \vec{g}_j \cdot \frac{\partial \delta \vec{V}_{,i}}{\partial(\vec{\phi}, \underline{\alpha})} + \frac{\partial \vec{U}_{,i}}{\partial(\vec{\phi}, \underline{\alpha})} \cdot \delta \vec{V}_{,j} + \\
&+ \;\; \vec{U}_{,i} \cdot \frac{\partial \delta \vec{V}_{,j}}{\partial(\vec{\phi}, \underline{\alpha})} + \frac{\partial \vec{U}_{,j}}{\partial(\vec{\phi}, \underline{\alpha})} \cdot \delta \vec{V}_{,i} + \vec{U}_{,j} \cdot \frac{\partial \delta \vec{V}_{,i}}{\partial(\vec{\phi}, \underline{\alpha})} \Bigg] = \\
&= \;\; \frac{1}{2}\Bigg[\frac{\partial \vec{U}_{,i}}{\partial(\vec{\phi}, \underline{\alpha})} \cdot \delta \vec{V}_{,j} + \frac{\partial \vec{U}_{,j}}{\partial(\vec{\phi}, \underline{\alpha})} \cdot \delta \vec{V}_{,i} + \left(\vec{g}_i + \vec{U}_{,i} \right) \cdot \frac{\partial \delta \vec{V}_{,j}}{\partial(\vec{\phi}, \underline{\alpha})} + \left(\vec{g}_j + \vec{U}_{,j} \right) \cdot \frac{\partial \delta \vec{V}_{,i}}{\partial(\vec{\phi}, \underline{\alpha})} \Bigg]
\end{aligned} \tag{4.59}$$

where the terms in parenthesis are defined $\vec{G}_i = \left(\vec{g}_i + \vec{U}_{,i} \right)$ and $\vec{G}_j = \left(\vec{g}_j + \vec{U}_{,j} \right)$, as in (B.26) and, once again, the derivatives of the constant vectors $\vec{g}_i$ are equal to zero. The third and the fourth terms can be then reformulated observing that:

$$\begin{aligned}
d\vec{U} \;\; &= \;\; \frac{\partial \vec{U}}{\partial(\vec{\phi}, \underline{\alpha})} \cdot d(\vec{\phi}, \underline{\alpha}) = \\
&= \;\; \frac{\partial}{\partial(\vec{\phi}, \underline{\alpha})} \left[\vec{\phi} - \vec{\varphi} + \xi^3 (\vec{A}_3 - \vec{a}_3) \right] \cdot d(\vec{\phi}, \underline{\alpha}) = \\
&= \;\; \frac{\partial \vec{\phi}}{\partial(\vec{\phi}, \underline{\alpha})} \cdot d(\vec{\phi}, \underline{\alpha}) + \xi^3 \frac{\partial \vec{A}_3}{\partial(\vec{\phi}, \underline{\alpha})} \cdot d(\vec{\phi}, \underline{\alpha}) = \\
&= \;\; d\vec{\phi} + \xi^3 \left(d\alpha_1 \vec{V}_1 + d\alpha_2 \vec{V}_2 \right)
\end{aligned} \tag{4.60}$$

where $\vec{V}_1$ and $\vec{V}_2$ are defined so that they constitute an ortho-normal reference system with the normal vector $\vec{A}_3$ (see equations (4.137) and (4.138)). Then it can be shown that:

$$\frac{\partial \delta \vec{V}}{\partial(\vec{\phi}, \underline{\alpha})} \cdot d(\vec{\phi}, \underline{\alpha}) = \xi^3 \vec{A}_3 \, d\underline{\alpha} \cdot \delta \underline{\alpha} = \xi^3 \vec{A}_3 \left(d\alpha_1 \delta \alpha_1 + d\alpha_2 \delta \alpha_2 \right) \tag{4.61}$$

with α_1 and α_2 the rotations along the unit vectors $\vec{V}_1$ and $\vec{V}_2$ lying in the tangential plane of the shell midsurface. It is now possible to further differentiate:

$$\frac{\partial \delta \vec{V}_{,j}}{\partial(\vec{\phi}, \underline{\alpha})} = \left[\xi^3 \vec{A}_3 \, d\underline{\alpha} \, \delta\underline{\alpha}\right]_{,j} \tag{4.62}$$

Equation (4.59) then rewrites using (4.61):

$$\begin{aligned}
\frac{\partial \, \delta e_{ij}}{\partial(\vec{\phi}, \underline{\alpha})} \cdot d(\vec{\phi}, \underline{\alpha}) &= \frac{1}{2}\Bigg[\left(\frac{\partial \vec{U}_{,i}}{\partial(\vec{\phi}, \underline{\alpha})} \cdot d(\vec{\phi}, \underline{\alpha})\right) \cdot \delta\vec{V}_{,j} + \left(\frac{\partial \vec{U}_{,j}}{\partial(\vec{\phi}, \underline{\alpha})} \cdot d(\vec{\phi}, \underline{\alpha})\right) \cdot \delta\vec{V}_{,i} + \\
&\quad \vec{G}_i \cdot \left(\xi^3 \vec{A}_3 \, d\underline{\alpha} \cdot \delta\underline{\alpha}\right)_{,j} + \vec{G}_j \cdot \left(\xi^3 \vec{A}_3 \, d\underline{\alpha} \cdot \delta\underline{\alpha}\right)_{,i}\Bigg] = \\
&= \frac{1}{2}\Bigg[\left(\frac{\partial \vec{U}_{,i}}{\partial(\vec{\phi}, \underline{\alpha})} \cdot d(\vec{\phi}, \underline{\alpha})\right) \cdot \delta\vec{V}_{,j} + \left(\frac{\partial \vec{U}_{,j}}{\partial(\vec{\phi}, \underline{\alpha})} \cdot d(\vec{\phi}, \underline{\alpha})\right) \cdot \delta\vec{V}_{,i} + \\
&\quad \vec{G}_i \cdot \left(\xi^3 \vec{A}_3 \cdot (d\alpha_1 \delta\alpha_1 + d\alpha_2 \delta\alpha_2)\right)_{,j} + \\
&\quad \vec{G}_j \cdot \left(\xi^3 \vec{A}_3 \cdot (d\alpha_1 \delta\alpha_1 + d\alpha_2 \delta\alpha_2)\right)_{,i}\Bigg]
\end{aligned} \tag{4.63}$$

4.1.8 Numerical Locking

Locking is a phenomenon affecting the analysis of thin structures associated with the presence of spurious stresses, and it consists a strong artificial stiffening of the elements as the thickness/length ratio decreases.

A complete description of locking is well beyond the scope of this manuscript. An illustration of the occurrence of locking is however here reported using a beam model as a simplified example. Such an example is not exhaustive nor valid for all the situations in which locking occurs. Three sub-sections will be treated: in the first one the basic axial, Bernoulli and Timoshenko beam models will be reviewed in order to introduce the formulations to be used afterwards. In the second part an asymptotic analysis will be performed, where the length-/thickness ratio $\epsilon \to 0$. The occurrence of locking will then be shown and explained. Finally, the third section will treat the mixed interpolation of tensorial components (MITC) as a way to avoid the occurrence of locking.

Axially loaded bar

The axial equilibrium of the beam is here treated. The internal/external potential energy can then be written as:

$$\Pi = \frac{1}{2}\int_V \sigma \cdot \epsilon \, \mathrm{d}V - \int_V f^B \cdot u \, \mathrm{d}V - u_L \cdot R \tag{4.64}$$

where u_L represents the boundary conditions in terms of displacements, and it is used because it is imposed that $u|_\Gamma = u_L$. R is the reaction force. Chosen a constitutive relationship (in this case: $\sigma = E \cdot \epsilon$), remembering the definition of the axial strains ($\epsilon_{xx} = \frac{du}{dx}$) and assuming that the beam has a constant section, the potential energy writes:

$$\Pi = \frac{1}{2} EA \int_0^L \left(\frac{du}{dx}\right)^2 \mathrm{d}x - \int_0^L f^B \cdot u \, \mathrm{d}x - u_L \cdot R \tag{4.65}$$

the principle of stationary potential energy reads then, by means of differentiating:

$$\delta\Pi = \frac{1}{2} EA \int_0^L 2 \frac{du}{dx} \delta\Big(\frac{du}{dx}\Big) \, \mathrm{d}x - \int_0^L f^B \, \delta u \, \mathrm{d}x - R \, \delta u_L = 0 \tag{4.66}$$

Remembering then that $\delta\Big(\frac{du}{dx}\Big) = \frac{d(\delta u)}{dx}$ and integrating by parts:

$$- \int_0^L \Big(EA \frac{\partial^2 u}{\partial x^2} + f^B\Big) \, \delta u \, dx + \left[EA \frac{du}{dx}\Big|_{x=L} - R\right] \delta u_L - EA \, \frac{\partial u}{\partial x}\Big|_{x=0} \cdot \delta u_0 = 0 \tag{4.67}$$

The first term vanishes because it is imposed that the value of the (arbitrary) test function δu is zero in 0 and L.[1] Equation (4.67) becomes then:

$$EA \, \frac{\partial u}{\partial x}\Big|_{x=L} - R = 0 \tag{4.68}$$

Euler-Bernoulli beam theory

Unlike the previous section, the transverse equilibrium of the beam is here treated. The Bernoulli beam model is the representation of the "elastic line", i.e. no shear deformations are allowed.

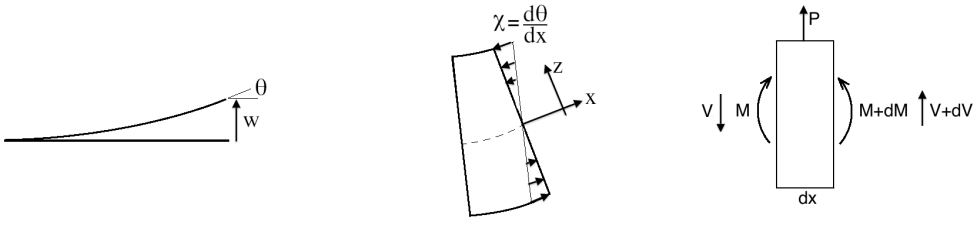

Figure 4.2: Definitions used for the Euler-Bernoulli beam model

From geometrical considerations then:

$$tg\theta = \frac{sin\theta}{cos\theta} = \frac{dw}{dx} \approx \theta \Rightarrow \theta = \frac{dw}{dx} \quad ; \quad \chi = \frac{d\theta}{dx} = \frac{d^2 w}{dx^2} \quad ; \quad \epsilon_{xx} = -\chi z \tag{4.69}$$

[1] It is also possible to show that the term in the parenthesis vanishes; this can be demonstrated by expressing the horizontal equilibrium of an infinitesimal beam element.

The constitutive relationship and resultants should be evaluated as:

$$\sigma_{xx} = E \cdot \epsilon_{xx} \quad ; \quad M_x = \iint z \cdot \sigma_{xx}\, dydz \quad ; \quad V = \iint \sigma_{xz}\, dydz \tag{4.70}$$

The equilibrium is then derived from simple geometric considerations:

$$-M+(M+dM)+V\cdot dx = 0 \Rightarrow V = -\frac{dM}{dx} \quad ; \quad -V+(V+dV)+pdx = 0 \Rightarrow -p = \frac{dV}{dx} \tag{4.71}$$

differentiating:

$$\frac{d^2M}{dx^2} = \frac{dV}{dx} = p \quad ; \tag{4.72}$$

and using the definition of M:

$$\begin{aligned} \frac{d^2}{dx^2}\left[\iint z \cdot \sigma \,\mathrm{d}y\,\mathrm{d}z\right] &= p \\ \frac{d^2}{dx^2}\left[\iint z \cdot E \cdot \left(-\chi\, z\right)\,\mathrm{d}y\,\mathrm{d}z\right] &= p \\ \frac{d^2}{dx^2}\left[\iint z \cdot E \cdot \left(-\frac{d^2w}{dx^2}\, z\right)\,\mathrm{d}y\,\mathrm{d}z\right] &= -p \\ E \cdot \left[\iint z^2 dydz\right]\frac{d^4w}{dx^4} &= -p \end{aligned} \tag{4.73}$$

Finally it is possible to obtain the governing differential equation for the Euler-Bernoulli Beam:

$$E\,I\,\frac{d^4w}{dx^4} = -p \tag{4.74}$$

Timoshenko beam theory

Unlike the Euler-Bernoulli mode, the Timoshenko beam model allows for shear deformations. Such deformations are considered constant within a section. The model considers then both bending and shear deformation. Figure 4.3 shows a case where only shear deformations arise. In this case equation (4.69) must be then modified considering the superposition of bending and shear effects.

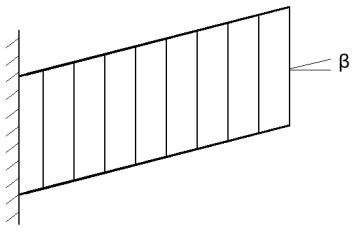

Figure 4.3: only shear deformations are allowed for this beam

$$\frac{dw}{dx} = \theta_{bending} + \beta_{shear} \tag{4.75}$$

since shear and bending effects are decoupled then, the axial displacement of a point of the beam due to bending effects is defined:

$$u = -z\ sin(\theta(x)) \approx -z\ \theta(x) \quad \Rightarrow \quad \begin{cases} u(x,y,z) = & -z \cdot \left[\frac{dw}{dx} - \beta(x)\right] \\ v(x,y,z) = & 0 \\ w(x,y,z) = & w(x) \end{cases} \tag{4.76}$$

The strains are described by:

$$\begin{cases} \epsilon_{xx} = & \frac{du}{dx} = -z\frac{d\theta}{dx} \\ \epsilon_{xz} = & \frac{1}{2}(\frac{du}{dz} + \frac{dw}{dx}) = \frac{1}{2}(-\frac{dw}{dx} + \beta(x) + \frac{dw}{dx}) = \frac{1}{2}\beta(x) \end{cases} \tag{4.77}$$

Using a linear constitutive relationship, the equilibrium to rotation held:

$$M = \iint_{-\frac{h}{2}}^{\frac{h}{2}} \sigma_{xx}\, z\, \mathrm{d}y\, \mathrm{d}z = E\, I\, \frac{d\theta}{dx} \tag{4.78}$$

Shear is similarly evaluated. An coefficient k is introduced in order to scale the sectional area, thus taking into account the assumption that the shear is constant within a section.

$$V = \iint_{-\frac{h}{2}}^{\frac{h}{2}} \sigma_{xz}\, \mathrm{d}y\, \mathrm{d}z = \sigma_{xz} A_{section} = 2\, k\, G\, \epsilon_{xz}\, A_{section} = G\, k\, \beta(x)\, A_{section} = k\, G\, A_{section}\, \beta(x) \tag{4.79}$$

It is now possible to write the functional Π:

$$\Pi = \frac{1}{2}\int_V \sigma_{xx}\, \epsilon_{xx}\, \mathrm{d}V + \int_V \sigma_{xz}\, \epsilon_{xz}\, \mathrm{d}V - \int_0^L q\, w\, \mathrm{d}x \tag{4.80}$$

where the contribution of bending is:

$$\tau_{xx} = E\, \epsilon_{xx} = -E\, z\, \frac{d\theta}{dx}$$

and the contribution of shear:

$$\sigma_{xz} = 2\, G\, k\, \epsilon_{xz} = G\, k\, \beta(x)$$

The first two terms in equation (4.80) can be rearranged:

$$\begin{aligned} \frac{1}{2}\int_V \sigma_{xx}\, \epsilon_{xx}\, \mathrm{d}V &= \frac{1}{2}\int_0^L \int_0^y \int_{-t/2}^{t/2} E\, \epsilon_{xx}\, \epsilon_{xx}\, \mathrm{d}x\, \mathrm{d}y\, \mathrm{d}z = \\ &= \frac{1}{2}\, E\, b \int_0^L \int_{-t/2}^{t/2} \left(-z\, \frac{d\theta}{dx}\right)^2 \mathrm{d}x\, \mathrm{d}z = \\ &= \frac{1}{2}\, E\, b \frac{t^3}{12} \int_0^L \left(\frac{d\theta}{dx}\right)^2 \mathrm{d}x = \frac{EJ}{2} \int_0^L \left(\frac{d\theta}{dx}\right)^2 \mathrm{d}x \end{aligned} \tag{4.81}$$

$$\begin{aligned}\int_V \sigma_{xz}\,\epsilon_{xz}\,\mathrm{d}V &= \int_0^L \int_0^y \int_{-t/2}^{t/2} k\,G\,\beta(x)\,\frac{\beta(x)}{2}\,\mathrm{d}x\,\mathrm{d}y\,\mathrm{d}z = \\ &= \frac{kG}{2}\,A\int_0^L \beta(x)^2\,\mathrm{d}x = \\ &= \frac{kGA}{2}\int_0^L \left(\frac{dw}{dx}-\theta(x)\right)^2\mathrm{d}x \end{aligned} \tag{4.82}$$

rewriting, differentiating and imposing the stationariness of the potential ($\delta\Pi = 0$) then:

$$\delta\Pi = \int_0^L \left[EI\,\frac{d\theta}{dx}\delta\Big(\frac{d\theta}{dx}\Big) + kGA\Big(\frac{dw}{dx}-\theta(x)\Big)\,\delta\Big(\frac{dw}{dx}-\theta(x)\Big) - q\,\delta w\right]dx = 0 \tag{4.83}$$

The principle of virtual work directly derives from this formulations, by removing the differential quantities $\delta(...)$.

Bi-linear forms

In the following, the notation will be used:

$$\frac{d(..)}{dx} = (...)' \quad ; \quad \delta w = v \quad ; \quad \delta\theta = \eta$$

Equation (4.83) writes then:

$$\int_0^L \Big[EI\,\theta\,\eta' + kGA\,\Big(w'-\theta\Big)\cdot\Big(v'-\eta\Big) - p\,v - m\,\eta\Big]dx = 0 \tag{4.84}$$

this can be rewritten in the shape:

$$EI\int_0^L \theta'\,\eta'\,\mathrm{d}x = \frac{t^3E}{12}\int_0^L \theta'\,\eta'\,\mathrm{d}x = t^3\cdot A(\theta,\eta) \tag{4.85}$$

$$kG\,bt\int_0^L \Big(w'-\theta\Big)\Big(v'-\eta\Big)\,\mathrm{d}x = t\cdot B(w,\theta;v,\eta) \tag{4.86}$$

$$\int_0^L \Big(p\,v + m\,\eta\Big)\,\mathrm{d}x = F(v,\eta) \tag{4.87}$$

where the expressions A, B and F are called *bi-linear forms*, because they are bi-linear functions of the state variables present in the integral, and in the second expression the area has been expressed as $A = b\,t$ in order to isolate the thickness t. These expressions are here derived for the case of the beam model. However they can be representative for other mathematical models, see for example the formulation of the s-m-b shell model in Equation 4.49.

Using bi-linear forms the principle of stationary potential can be rewritten as:

$$t^3\,A(\theta,\eta) + t\,B(w,\theta\,;\,v,\eta) = F(v,\eta) \tag{4.88}$$

Similarly it is possible to re-write the axial (membrane) potential, expressed in equation (4.66), as:

$$t\,D^m(u,\theta_{\|}) = F(\theta_{\|}) \tag{4.89}$$

where u represents the axial displacement and $\theta_{\|}$ the variational longitudinal displacement.

The Timoshenko (complete) beam model is written in terms of bi-linear forms as:

$$\begin{cases} t^3\, A(\theta,\eta) + t\, B(w,\theta\,;\, v,\eta) = F(v,\eta) \\ t\, D^m(u,\theta_{\|}) = F(\theta_{\|}) \end{cases} \tag{4.90}$$

In the simplified case of the Euler-Bernoulli beam, it is assumed that the shear strain is zero. This means, in terms of bi-linear forms, $B(w,\theta\,;\, v,\eta) = 0$. In other words:

$$\Big(w' - \theta\Big) = 0 \tag{4.91}$$

Asymptotic analysis

Locking arises when the thickness asymptotically tends to zero. The Timoshenko beam model will then be used for explaining the phenomenon. In the following, the bi-linear forms previously defined will be scaled using the parameter:

$$\epsilon = \frac{t}{L} << 1 \tag{4.92}$$

where L is a characteristic length. Using this parameter then:

$$\overline{A} = A\, L^3 \quad ; \quad \overline{B} = B\, L^3 \quad ; \quad F = \epsilon^3\, \overline{F} \tag{4.93}$$

equation (4.88) becomes then:

$$\overline{A}(\theta,\eta) + \epsilon^{-2}\, \overline{B}(w,\theta\,;\, v,\eta) = \overline{F}(v,\eta) \tag{4.94}$$

in order for this equation to remain finite when $\epsilon \to 0$, it must hold the condition that the term $\overline{B}$ tends to zero at least as fast as ϵ^{-2}:

$$\begin{aligned} &\overline{B}(w,\theta\,;\, v,\eta) = 0 \quad O(\geq 2) \\ &t \to 0 \end{aligned} \tag{4.95}$$

which implies that, in the limit, $w' - \theta = 0$, corresponding to the Euler-Bernoulli kinematic assumption.

The occurrence of locking becomes visible when observing the asymptotic analysis in terms of potential. The solution of the Timoshenko beam model corresponds to the solution of the minimization problem:

$$\min_{v,\eta} \Big\{ \frac{1}{2}\, \overline{A}(\eta,\eta) + \frac{\epsilon^{-2}}{2}\, \overline{B}(v,\eta\,;\, v,\eta) - \overline{F}(v) \Big\} \tag{4.96}$$

if we restrict this minimisation problem over the elements satisfying $w' - \theta = 0$, we obtain that the shear energy term $\overline{B}(w, \theta\,;\, v, \eta)$ vanishes, and equation (4.96) gives:

$$\min_{v,\eta=v'} \left\{ \frac{1}{2}\,\overline{A}(v', v') - \overline{F}(v) \right\} \tag{4.97}$$

which corresponds to the minimisation problem associated with the Euler-Bernoulli model. Since this last equation comes from the minimization of a sub-space, and since the min on a sub space is always $\geq$ of the min on the whole space:

$$\left[\min_{v,\eta} \left\{ \frac{1}{2}\,\overline{A}(\eta, \eta) + \frac{\epsilon^{-2}}{2}\,\overline{B}(v, \eta\,;\, v, \eta) - \overline{F}(v) \right] \leq \left[\min_{v,\eta=v'} \left\{ \frac{1}{2}\,\overline{A}(v', v') - \overline{F}(v) \right\} \right] \tag{4.98}$$

Locking arises when discretizing in finite elements. The complete formulation in equation (4.96) is then re-written in the finite elements subspace V_h. This is the space of all the functions able to interpolate nodal values onto the element. In other words, this is the space of the so-called *shape-functions*. For P1 kind elements for example linear *shape-functions* are defined. In the case of a beam then the deformation of the element is evaluated by linearly interpolating the nodal displacement values. The finite element solution is then given by the

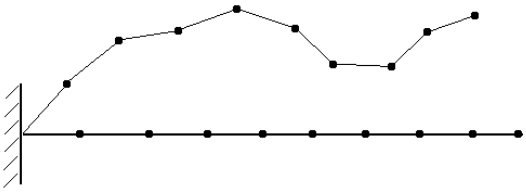

Figure 4.4: P1 kind finite element discretization

discrete minimisation principle:

$$\min_{(v,\eta)\in V_h} \left\{ \frac{1}{2}\,\overline{A}(\eta, \eta) + \frac{\epsilon^{-2}}{2}\,\overline{B}(v, \eta\,;\, v, \eta) - \overline{F}(v) \right\} \tag{4.99}$$

the solution w_h depends upon ϵ in V_h. It can be proved that:

$$\begin{aligned} &\overline{B}(w_h, \theta_h\,;\, v_h, \eta_h) = 0 \quad O(\geq 2) \\ &\epsilon \to 0 \end{aligned} \tag{4.100}$$

Therefore the solution of the asymptotic problem for $t \to 0$ will be in the subspace defined by the intersection of the finite element space V_h and the space where equation (4.100) is verified:

$$V_h \cap \{\, \overline{B}(w_h, \theta_h\ ;\ v_h, \eta_h) = 0 \,\} \tag{4.101}$$

which simply reduces to the element $w_h, \theta_h \in V_h$ satisfying

$$w_h' - \theta_h = 0 \tag{4.102}$$

Since the element is linear, the derivative w'_h is piecewise constant. Hence, since θ_h is a continuous function:

$$\theta_h = \text{const in } [0, L] \tag{4.103}$$

One boundary of the beam being clamped, the value θ_h is zero at the boundary, hence $\theta_h = 0$ in $[0, L]$. By returning to equation (4.102), using all the above considerations we infer that:

$$w_h = 0 \text{ in } [0, L] \tag{4.104}$$

For the P1 elements discretization the asymptotic behaviour of the Timoshenko beam leads then to a sub-space of admissible displacement which contains the element 0 only. In other words, in the finite element space the only possible limit solution is Zero, when $t \to 0$. This is the cause of the phenomenon normally referred as *Locking*. This terminology comes from the fact that the mechanical interpretation of:

$$\Big(w_h \, , \, \theta_h\Big) \xrightarrow{\epsilon \to 0} \Big(0, 0\Big) \tag{4.105}$$

can be seen as an increasing stiffening of the structure. This problem arises from the unbalance in the constraint $(w' - \theta) = 0$, where the value of a finite element function is imposed to be equal to the value of the derivative of another finite element function.

A solution strategy for locking consists in relaxing this formulation by imposing it in the centre of the element only:

$$(w' - \theta)\Big|_{centre} = 0 \tag{4.106}$$

This leads to a sub-space of admissible solutions which is bigger, because imposing the condition in the center only is equivalent to imposing the condition *in average*. One degree of freedom is therefore gained: i.e. the space of admissible solution is now non trivial. Recalling a geometrical example, the situation is now as represented in Figure 4.5, where a linear function is imposed to be passing through a point. Such a procedure has been discussed

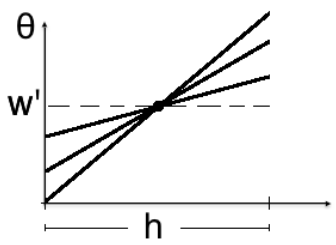

Figure 4.5: Imposing the condition on one point, rather than on the whole element adds one degree of freedom to the system and it is the basic idea of the mixed interpolation.

Table 4.1: Asymptotic behaviour for standard elements, no treatment for Locking. The values reported in the table represent the ratio between the finite element and the analytical solutions: $u_h^\epsilon(L)/u^\epsilon(L)$ From [4], table 7.1

N	$\epsilon = 1$	$\epsilon = 0.1$	$\epsilon = 0.01$
1	0.7742	0.0331	0.0003
10	0.9971	0.7742	0.0331
100	1.0000	0.9971	0.7742

Table 4.2: Asymptotic behaviour for mixed interpolation elements. The values reported in the table represent the ratio between the finite element and the analytical solutions: $u_h^\epsilon(L)/u^\epsilon(L)$ From [4], table 7.2

N	$\epsilon = 1$	$\epsilon = 0.1$	$\epsilon = 0.01$
1	0.8654	0.7521	0.7500
10	0.9986	0.9975	0.9975
100	1.0000	1.0000	1.0000

and assessed in [4], ch.7. A detailed description of the tying points locations for a number of elements is given in [68], ch.5. In the following some results are reported, showing the occurrence of the locking and the effectiveness of the mixed interpolation. In the following, N indicates the number of elements of the considered mesh. A relative error is defined as the ratio of the numerical maximum displacement value u_h^ϵ over the analytical value u^ϵ. Table 4.1 reports results obtained with no treatment for locking. For (the non-physical) value $\epsilon = 1$, 10 elements are enough in order to calculate an acceptable solution. As the thickness decreases, the error value increases, and more elements are needed in order to get an acceptable error value. When using the mixed interpolation (table 4.2), the dependency upon the relative thickness ϵ is substantially reduced.

4.1.9 Structural dynamics and the Rayleigh damping

The use of a dynamic system – even when analysing static cases such as a fabric loaded with constant pressure – is one of the possible strategies adopted for overcoming the low

stability of the system. As stated in the introduction in fact, the present analysis involves very thin shells which are likely to wrinkle. The low thickness and the wrinkling determine several stability issues, both from a physical and a numerical perspective. From a physical perspective, the wrinkling is a post-buckled configuration triggered by local instability. From a numerical perspective the analysis of very thin shells produces ill conditioned systems. For the shell elements in fact, the stiffness operator holds both membrane and bending terms. The membrane terms are proportional to the thickness t, and the bending terms are proportional to the cube of the thickness t^3. When the thickness is very small the diagonal terms of the stiffness operator may differ then by several orders of magnitude. This affects the conditioning of the matrix, which is the ratio of the extremes eigen-values, and thus compromises the stability of the numerical scheme.

When using a damped dynamical system the time assumes the meaning of a *pseudo*-time because the definition of the damping is arbitrary. In this case the *Rayleigh* damping definition was adopted. Although all the evaluations presented in the beginning of this section refer to linear systems, it will be shown that the general conclusions are also valid in the non-linear framework. The description of a non-damped dynamic system, with opportune boundary conditions, reads:

$$\begin{cases} \mathbf{M} \cdot \ddot{\vec{U}} + \mathbf{K} \cdot \vec{U} = \vec{F} \\ \vec{U}(0) = 0 \\ \dot{\vec{U}}(0) = 0 \end{cases} \tag{4.107}$$

the solution can be searched in the form:

$$u(t) = u_0 \, e^{i\omega t} = u_0 \left(cos(\omega t) + i \, sin(\omega t) \right) \tag{4.108}$$

which leads to:

$$\begin{aligned} \dot{u}(t) &= i \, \omega \, u_0 \, e^{i\omega t} = i \, \omega \, u(t) \\ \ddot{u}(t) &= (\, i \, \omega \,)^2 \, u_0 \, e^{i\omega t} = -\omega^2 \, u_0 \, e^{i\omega t} = -\, \omega^2 \, u(t) \end{aligned} \tag{4.109}$$

rewriting:

$$-\, \omega^2 \, \mathbf{M} \cdot \vec{u}_0 + \mathbf{K} \cdot \vec{u}_0 = 0 \quad \Rightarrow \quad \mathbf{K} \cdot \vec{u}_0 = \omega^2 \, \mathbf{M} \cdot \vec{u}_0 \tag{4.110}$$

$$\left(\mathbf{M}^{-1} \mathbf{K} \right) \cdot \vec{u}_0 = \omega^2 \, \vec{u}_0 \tag{4.111}$$

such a formulation is in the shape of a standard eigen-problem of the type: $\mathbf{A} \cdot \vec{v} = \lambda \vec{v}$. This is solved for a series of solutions λ_i, $\vec{\phi}_i$ called eigen-values and eigen-vectors. In a

physical representation, eigen-vectors represent vibration modes, where the eigen-values are proportional to the corresponding frequency. The response of the dynamic system is the linear superposition of such modes. The first eigen-value represent the square of the structure's natural frequency ($\lambda = \omega^2$; $\omega\,[rad/sec]$) and for a continuous structure: $0 \leq \lambda_1 \leq \lambda_2 \leq ... \rightarrow \infty$. As the eigen value increases, the correspondent eigen-vector increases its oscillation. Using a beam as example, every eigen-vector verifies $n-1$ zero-crosses: For a discrete system,

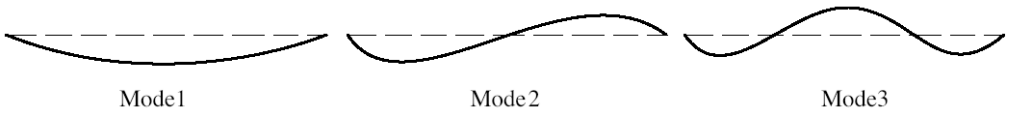

Figure 4.6: Schematic representation of the first three modes for a beam

the number of eigen-modes is finite: the stiffness is described by a matrix $[Ndof \times Ndof]$, where $Ndof$ is the number of degrees of freedom. By definition, such a matrix will have $Ndof$ eigen-values. The first eigen-modes, corresponding to the lower frequencies, are similar for every discretization, whereas finer the mesh higher the modal frequency which is represented.

It can be shown that the eigen-vectors $\vec{\phi}_i$ form an orthogonal base for the matrices $\mathbf{M}$ and $\mathbf{K}$:

$$\begin{cases} \vec{\phi}_i^T \cdot \mathbf{M} \cdot \vec{\phi}_j = \delta_{ij} \\ \vec{\phi}_i^T \cdot \mathbf{K} \cdot \vec{\phi}_j = \delta_{ij}\,\omega_{ij}^2 \end{cases} \tag{4.112}$$

and it is common rule to norm this base on the mass matrix: $\vec{\phi}_i^T \cdot \mathbf{M} \cdot \vec{\phi}_i = 1$. Chosen this norm, it follows that:

$$\begin{array}{ccccccc} \mathbf{K}\,\vec{\phi} = \lambda\,\mathbf{M}\,\vec{\phi} & & & & \vec{\phi}_i^T\,\mathbf{M}\,\vec{\phi}_i = 1 & & \\ \downarrow & & & & \downarrow & & \\ \vec{\phi}_i^T \cdot \mathbf{K} \cdot \vec{\phi}_i & = & \vec{\phi}_i^T\,\lambda_i \cdot \mathbf{M}\,\vec{\phi}_i & = & \lambda_i & = & \omega_i^2 \end{array}$$

the eigen-vectors forming an orthogonal base, the displacements $\vec{U}(t)$ can be expressed as a linear combination of the eigen-vectors $\vec{\phi}_i$ as:

$$\vec{U}(t) = \sum_i \alpha_i(t)\vec{\phi}_i \tag{4.113}$$

where the effect of the coefficients $\alpha_i(t)$ is to weight the influence of every mode on the final shape, and in general $\alpha_i(t) \xrightarrow{i\rightarrow\infty} 0$.

When introducing a time dependent force into the system, using equations (4.107), (4.111)

and (4.113):

$$\mathbf{M} \cdot \sum_i \alpha_i''(t)\, \vec{\phi}_i + \omega^2\, \mathbf{M} \cdot \sum \alpha_i(t)\, \vec{\phi}_i = \vec{f}(t)$$

$$\sum_i \Big(\alpha_i'(t) + \omega^2\, \alpha_i(t)\Big)\mathbf{M}\, \vec{\phi}_i = f(t) \tag{4.114}$$

projecting this vectorial equation on the sub-space generated by the eigen-vector $\vec{\phi}_j$ (i.e. multiplying the equation times $\vec{\phi}_j$), and using the norm defined onto the mass matrix:

$$\vec{\phi}_j^T \cdot \sum_i \Big(\alpha_i''(t) + \omega^2 \alpha_i(t)\Big)\mathbf{M}\, \vec{\phi}_i = \vec{\phi}_j^T \cdot \vec{f}(t) \tag{4.115}$$

$$\sum_i \Big(\alpha_i''(t) + \omega^2\, \alpha_i(t)\Big) = \vec{\phi}_j^T\, \vec{f}(t) \tag{4.116}$$

In components, every mode reacts independently as an harmonic oscillator, which contributes to global structural dynamic motion according to the value of the weighting factor α.

$$\alpha_j''(t) + \omega^2\, \alpha_j(t) = f_j(t) \quad \forall j = 1, Ndof \tag{4.117}$$

the solution of such an equation can be searched, after Fourier decomposition of the force term $f_j(t) = F_0 e^{i\omega t}$, in the form:

$$\alpha_j = \alpha_{0j}\, e^{i\omega t} \quad \Rightarrow \quad \alpha_i' = i\,\omega\,\alpha_{0j}\, e^{i\omega t} \quad \Rightarrow \quad \alpha_i'' = -\omega^2 \alpha_{0j}\, e^{i\omega t} \tag{4.118}$$

$$-\omega^2\, \alpha_{0j} + \omega^2\, \alpha_{0j} = F_{0j} \quad \Rightarrow \quad \Big(\omega_i^2 - \omega^2\Big)\alpha_{0j} = F_{0j} \tag{4.119}$$

which describes the un-damped harmonic oscillator, where the oscillation's amplitude $\to \infty$ on the natural frequency and $\to 0$ for the higher frequencies, as shown in figure 4.7:

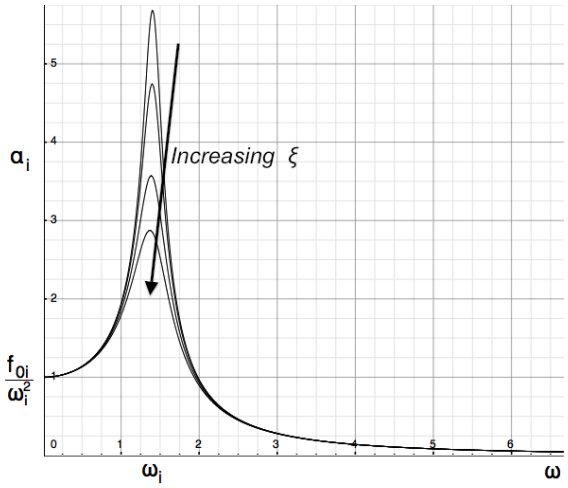

Figure 4.7: Harmonic oscillator behaviour in the frequency domain

A damping term can be introduced with the aim of smoothing the oscillatory behaviour of the system in time. The damping can be defined as a term proportional to the velocity:

$\partial_t\left[\omega_j^2\,\alpha_j(t)\right]$ scaled by a coefficient ξ_j, which should be tuned for every frequency ω_j. The governing equation (4.117) can then be reformulated as:

$$\alpha_j''(t) + 2\xi_j\omega_j\,\alpha_j'(t) + \omega^2\,\alpha_j(t) = F_{0j}\,e^{i\omega t} \tag{4.120}$$

where in a linear matrix system of the type: $\mathbf{M}\ddot{\vec{U}} + \mathbf{C}\dot{\vec{U}} + \mathbf{K}\vec{U} = \vec{F}$, this is equivalent to choosing the damping matrix as: $\mathbf{C} = 2\xi\omega_j\,\mathbf{M}\,\vec{\phi}_j$. Substituting these expressions as was done previously (see equation (4.119)):

$$\Big(-\omega^2 + 2\,\xi_j\,\omega_j i\omega + \omega_j^2\Big)\alpha_{0j} = F_{0j} \tag{4.121}$$

the solution can be found in the equivalent form of the time domain: $\alpha_j = \alpha_{0j}e^{i\lambda t}$. This leads, after expressing the derivatives and substituting, to the second order equation in the unknown λ:

$$-\lambda^2 + 2\,\xi_j\,\omega_j i\lambda + \omega_j^2 = 0 \tag{4.122}$$

which is solved by: $\lambda_{1,2} = \xi_j\,\omega_j\,i \pm \omega_j\sqrt{1-\xi_j^2}$.

The damping behaviour of a mechanical system can now be analysed in terms of the damping coefficient ξ. For $\xi = 0$ the system continues to oscillate:

$$\lambda_{1,2} = \pm\,\omega_j \Rightarrow \alpha_j = \alpha_{j0}\,e^{i\lambda t} = \alpha_{j0}\,e^{\pm i\omega_i t} \tag{4.123}$$

When $0 < \xi < 1$

$$\lambda_{1,2} = \xi_j\,\omega_j\,i \pm \omega_j\sqrt{1-\xi_j^2} = \omega_j\Big(\pm\sqrt{1-\xi_j^2} + \xi_j\,i\Big) \tag{4.124}$$

the system reads:

$$\alpha_j = \alpha_{j0}\,e^{i\,\lambda t} = \alpha_{j0}\,e^{i\,\omega_j\left(i\,\xi_j \pm \sqrt{1-\xi_j^2}\right)t} = \alpha_{j0}\,e^{-\xi_j\omega_j t}\,e^{\pm i\left(\omega_j\sqrt{1-\xi_j^2}\right)} \tag{4.125}$$

where the real part represents the amplitude of the oscillation and the imaginary part is its phase. Since the amplitude $e^{-\xi_j\omega_j t} \xrightarrow{t\to\infty} 0$ the system is said to be damped.

Critical damping arises when $\xi = 1$, then:

$$\lambda_{1,2} = \omega_j\,i \Rightarrow \alpha_j = \alpha_{j0}\,e^{-\omega_j t} \tag{4.126}$$

In this case the system converges without any oscillation, since there is no imaginary part.

An over-damped system is defined for $\xi > 1$. in this case:

$$\lambda_{1,2} = \xi_j\,\omega_j i \pm \omega_j\sqrt{1-\xi_j} = i\,\omega_j\Big(\xi_j \pm \sqrt{\xi_j^2 - 1}\Big) \tag{4.127}$$

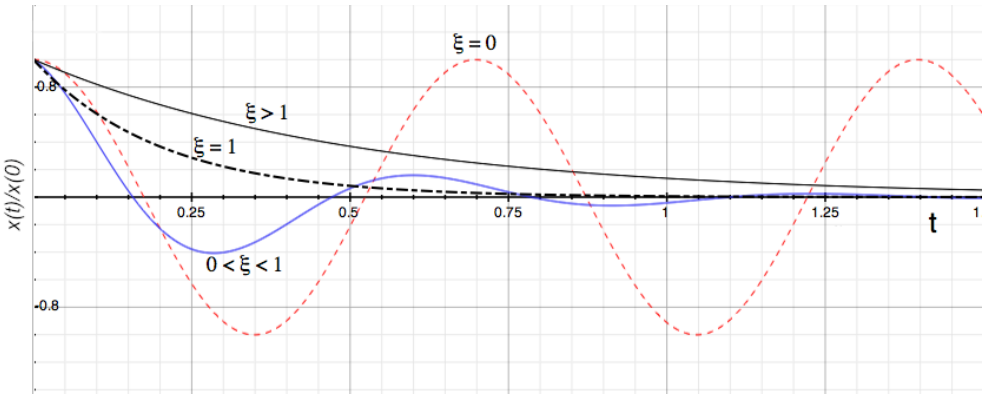

Figure 4.8: Harmonic oscillator behaviour in the time domain

where the term in the parenthesis is always > 0. The solution reads then:

$$\alpha_j = \alpha_{j0}\, e^{i\lambda t} = \alpha_{j0}\, e^{-\omega_j\left(\xi_j \pm \sqrt{\xi_j^2 - 1}\right)t} \tag{4.128}$$

The same concepts, which have been detailed for an harmonic oscillators, can be used in a Finite Element environment. The main purpose of imposing a correct damping value will be to assure stability and optimise the convergence rate of the solution, which might be affected by slow-down due to the eventual oscillations. Assuming a linear framework then the governing equation for the damped system reads:

$$\mathbf{M} \cdot \ddot{\vec{U}} + \mathbf{C} \cdot \dot{\vec{U}} + \mathbf{K} \cdot \vec{U} = \vec{F}(t) \tag{4.129}$$

Rayleigh damping can be used for the definition of the damping matrix $\mathbf{C} = c_1\mathbf{M} + c_2\mathbf{K}$. The damping matrix is then defined as a linear combination of mass and stiffness matrices, and thus it decomposes on the same eigen-modes of the structure. Decomposing then in eigen-modes:

$$\begin{aligned} \mathbf{M}\sum_i \alpha_i''\vec{\phi}_i + \mathbf{C}\sum_i \alpha_i'\vec{\phi}_i + \mathbf{K}\sum_i \alpha_i\vec{\phi}_i &= \vec{F}(t) \\ \mathbf{M}\Big(\sum_i \alpha_i''\vec{\phi}_i + c_1\sum_i \alpha_i'\vec{\phi}_i\Big) + \mathbf{K}\Big(c_2\sum_i \alpha_i'\vec{\phi}_i + \sum_i \alpha_i\vec{\phi}_i\Big) &= \vec{F}(t) \end{aligned} \tag{4.130}$$

which leads, after projecting and applying equations (4.112) and the following expression to the equation, the j-*th* component of which is:

$$\alpha_j'' + \Big(c_1 + \omega^2 c_2\Big)\alpha_j' + \omega^2\alpha_j = f_j \tag{4.131}$$

the system has been transformed into a system of parallel harmonic oscillators similar to those analysed in the beginning of the section. The damping coefficient $2\xi\omega_i$ (see equation (4.120))

is now expressed as $c_1+\omega^2 c_2$. Equalling the two expressions, the Rayleigh damping coefficient for the j-*th* mode results:

$$\xi_j = \frac{c_1 + c_2\,\omega_i j2}{2\omega_j} \tag{4.132}$$

The choice of the damping coefficients c_1 and c_2 is not unique, but effective values can be calculated in order to reduce the time needed for the system to reach a steady state. Recalling the (double) solution for the over-damped system in equation (4.128) and considering the less damped solution:

$$\alpha_j = \alpha_{j0}\, e^{-\omega_j\left(\xi_j - \sqrt{\xi_j^2-1}\right)t} \tag{4.133}$$

where the exponent can be rewritten using an algebraic manipulation such:

$$\left(\xi_j - \sqrt{\xi_j^2-1}\right)\left(\frac{\xi_j + \sqrt{\xi_j^2-1}}{\xi_j + \sqrt{\xi_j^2-1}}\right) \approx \left.\frac{1}{2\xi_j}\right|_{\xi>>1} \tag{4.134}$$

the solution can then be rewritten in the shape: $\alpha_j = \alpha_{j0}\, e^{\frac{-\omega_j t}{2\xi_j}}$. The convergence time, obtained comparing this solution with the original one, is scaled now by the factor: $2\xi_j/\omega_j$. Such factor will be called from now convergence time-scale t_c^s. Smaller ξ_j fastest the convergence, provides that $\xi_j \geq 1$.

Higher frequency modes are then damped in a time-scale proportional to t_c^s. In fact:

$$t_c^s = \frac{2\xi_j}{\omega_j} = \frac{c_1 + c_2\omega_j^2}{\omega_j^2} \xrightarrow{\omega_j\to\infty} c_2 \tag{4.135}$$

a good choice is then to impose the higher frequencies to be damped in the time of a semi natural period, thus $c_2 = T_n/2 = \pi/\omega_n$. The value of c_1 can be calculated imposing the condition: $\left.\frac{d\xi}{d\omega}\right|_{\omega_n} = 0$. This condition ensures the minimum damping value to be in correspondence of the natural frequency, and a higher value (linearly increasing with slope 2ω) for the higher frequencies:

$$\frac{d\xi(\omega_n)}{d\omega_n} = \frac{2\,c_2\,\omega_n^2 - 2\,c_1}{4\,\omega_n^2} = 0 \xrightarrow{c_2=\pi/\omega_n} c_1 = \pi\,\omega_n \tag{4.136}$$

The value for the damping coefficient in correspondence of the natural frequency is then $\xi_j(\omega_n) = \pi$. It is then convenient to scale both the damping coefficients by a factor π, which assures a critical damping for the natural frequency and a higher damping for higher frequencies:

$c_1 = \omega_1$	$c_2 = \frac{1}{\omega_1}$

Although the present result was derived for linear systems, its validity can in general be extended to non linear systems. Damping coefficients are then tuned as specified above in order to assure an optimal convergence rate, thus reducing as much as possible the computational cost of the simulation.

Table 4.3: Characteristics of the test case used for the evaluation of the damping effects

L	b	t	E	ν	Nels	Load	c_1	c_2
$[m]$	$[m]$	$[m]$	$[N/m^2]$	$[-]$	$[-]$	$[N/m^2]$	$[rad/s]$	$[sec]$
1	0.1	0.002	250	0	9	0.0001	0.0041	243.7

An example is here reported of the behaviour of a two dimensional fabric strip, the characteristics of which are reported in Table 4.3. The first four eigen-vectors are represented in Figure 4.9, where it is possible to recognise the behaviour already shown in the scheme in Figure 4.6

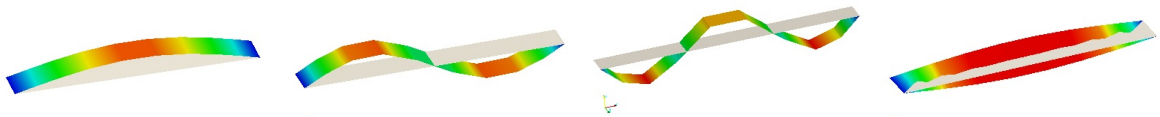

Figure 4.9: First four modes for the structure analysed. The fourth is a torsional mode

In a linear framework, the natural period of oscillation of the structure is calculated as $T_n = 2\pi/\omega_n = 1526\,[sec]$. In Figure 4.10 the curve represents the evolution of the structure, after being released from an imposed deformation map constituted by the first eigen-vector. In this case only the (first) natural frequency is excited, thus the un-damped response is a perfect sinusoidal curve. When including the damping, the oscillation is progressively smoothed away. No oscillation is encountered for the critical damping value. The natural period respects the calculated value ($1526\,[sec]$) and a satisfying convergence for the critical damped case is achieved in about $T_n/2$, as it has been imposed after Equation (4.136).

Figure 4.11 reports the evolution of the structure, when it has been released from the deformed shape obtained applying one single point load. Compared to Figure 4.10, in this case the displacement path is not smooth, since the point load excited higher order modes. These higher frequency modes are however smoothed away when setting the damping coefficient $\xi(\omega_n) = 1$.

A rather different situation arises in a non-linear framework. In this case setting zero

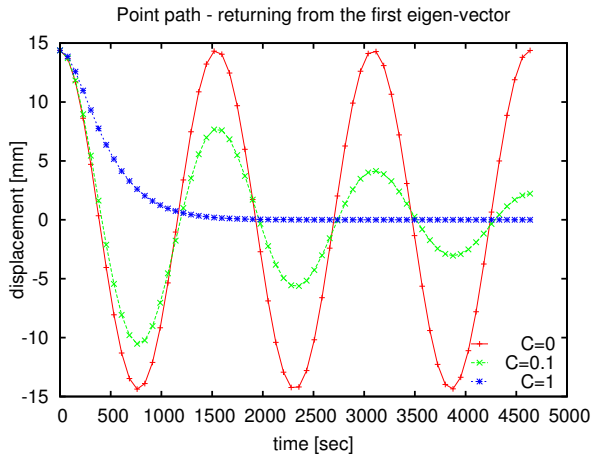

Figure 4.10: Time path of one node of the structure when returning from the first eigen-vector

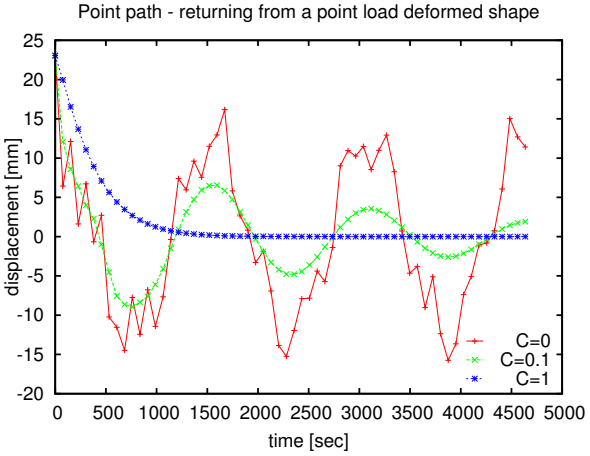

Figure 4.11: Time path of one node of the structure when releasing after loading with a point load

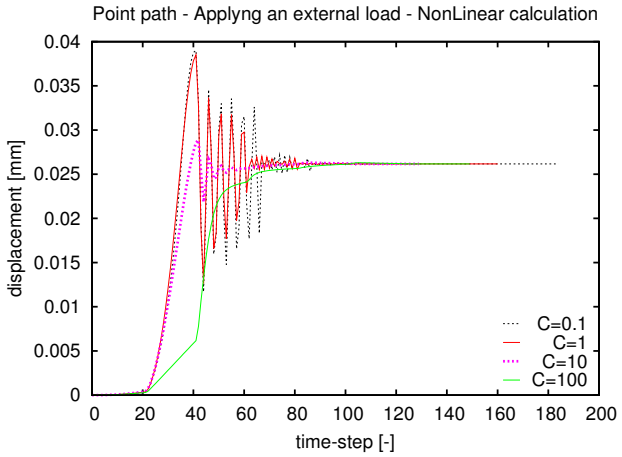

Figure 4.12: Time-step path of one node of the structure when applying a uniform load. The time-step value is variable, in terms of pseudo-time the oscillations arise in the initial part of the calculation only. Non-Linear calculation, influence of the damping coefficient values

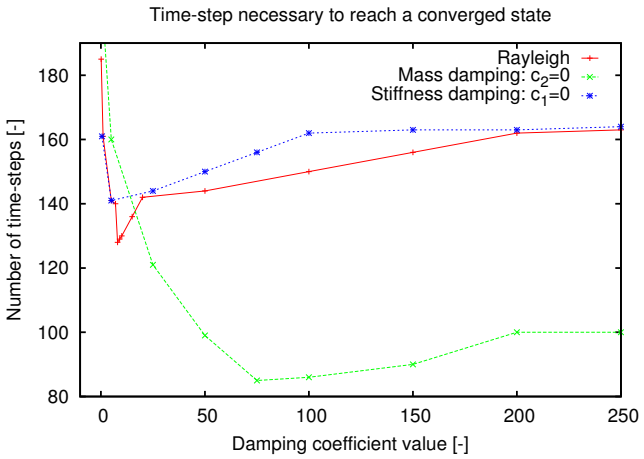

Figure 4.13: Number of (variable) time-steps needed for reaching a converged state as a function of the damping coefficient value. If $c_1 = 0$ the damping is defined with the stiffness matrix only, thus it is a visco-elastic damping. If $c_2 = 0$ the damping is defined with the mass matrix only, thus it is a viscous damping

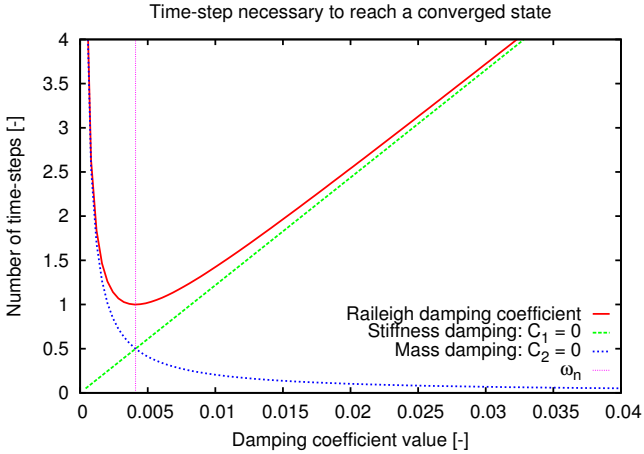

Figure 4.14: Damping coefficient value for the proposed setup in the region close to the natural pulsation ω_n. If $c_1 = 0$ the damping is defined with the stiffness matrix only, thus it is a visco-elastic damping. If $c_2 = 0$ the damping is defined with the mass matrix only, thus it is a viscous damping

damping ($c_1 = c_2 = 0$) produces the divergence of the solution. Damping is needed for overcoming the transient and reaching a steady final state. Also when applying a critical damping with c_1 and c_2 as in Table 4.3 large oscillations are encountered.

This is shown in Figure 4.12, where in abscissa is reported the timestep number. This number is not linearly proportional to the pseudo-time, since a variable timestep was used, the value of which is calculated as in Section 4.2.2. Very small timestep values are then used in the beginning of the calculation while the time step value is potentially ∞ at convergence. In the plot several over-damped solutions are reported and it appears how the damping

coefficient value should overcome at least 10 for completely avoiding oscillations in a non-linear framework.

The cost of the solution in terms of timesteps is shown in Figure 4.13 versus the damping coefficient value. This was calculated using Equation (4.132) for the value of the natural frequency $\omega_n = 0.0041$, estimated from the eigen analysis of the structure. Three situations are here analysed, the first of which makes use of the Rayleigh damping, where c_1 and c_2 are defined as in table 4.3 and multiplied by a constant factor. In the second case the coefficient c_2 is set to zero, thus the damping is entirely defined using the mass matrix and it assumes the meaning of a viscous damping. The third case is the opposite situation, where $c_1 = 0$, thus defining a visco-elastic damping.

It appears how the Rayleigh damping performs better than the visco-elastic damping; however the viscous damping generally produces better performances in the analysed frequency range. These results can be explained observing the Figure 4.14. In the viscous case the higher damping value arises for the natural frequency, while the higher frequencies are under-damped. This might produce situations where the higher frequencies take long time to smooth. However in the test case here analysed the mesh is so coarse, that the higher frequencies are neglected by the discretization. The visco-elastic damping shows a linear behaviour, and the slope of the curve follows the damping coefficient value. In this case the higher frequencies are over damped, and they may take a long time to reach the final solution. This is probably the cause of the bad performances of this type of damping.

In general it can be concluded that a Rayleigh over-damped setup produces the best performances in the non-linear framework; in the following the structural static analysis will then be performed using an over-damped dynamic scheme, with damping coefficient $\xi(\omega_n) = 5 - 10$. In the case where the analysed mesh is particularly coarse, the use of a purely viscous damping may decrease the computational cost. These conclusions will be recalled in Chapter 5, Secion 5.2.3.

4.1.10 Wrinkling

Wrinkling is a buckling related phenomenon which affects the deformation of fabric structures. When one principal stress is particularly high, the contraction of the material tends to induce a negative secondary stress. Since the very low bending stiffness of the fabric, the effect of this stress field results in the production of wrinkles which propagate following the streamlines of the stress field. When approaching the analysis of fabrics it is important to consider

this phenomenon, which locally modifies the stress-strain field thus changing its structural behaviour. Furthermore, a wrinkled surface determines an additional roughness, which can influence the flow (see Section 3.3.2). A typical example of wrinkling arises when applying

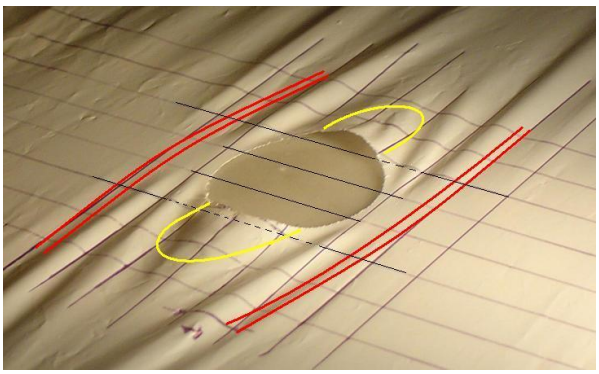

Figure 4.15: *Left*: Wrinkling generation arising on the sides of a flat membrane with a hole. *Right*: wrinkles propagates from the corner of a Gennaker

a b c

Figure 4.16: Different types of wrinkling arising on downwind sails. a: large amplitude wrinkles, b: singular wrinkle, producing a cusp; c: small amplitude wrinkles induced by the seams of the sail

a tensile load to a flat membrane with a hole. Although no out-of-plane loads are applied, several wrinkles generate in the direction of the local stress field as in Figure 4.15.

A similar behaviour can be identified when observing a downwind sail. In this case the wrinkles are generated in correspondence of the constrained points, where stress concentrations are higher. From the corners, wrinkles tends to propagate following an "almost" radial path towards the centre of the sail. This is particularly evident in Figure 4.16-a, where oscillations are propagated from the gennaker's tack line.

Three different type of wrinkling can be identified comparing Figure 4.16-a, b and c: in the first case, macroscopic oscillations propagates from the corner regardless the sail reinforcements and the seams. In the second case the stress concentrates on one single wrinkle,

which propagates through almost mid sail. The wave length is very small, and the impact on the global sail shape is dramatic: two different regions divided by a cusp can be identified on the sail surface for about a half of the extension of the sail. In the third case, very small wave length wrinkles are generated along the sails reinforcements and seams. In all the three cases, wrinkles propagate in a region extended between one third and a half of the sail height.

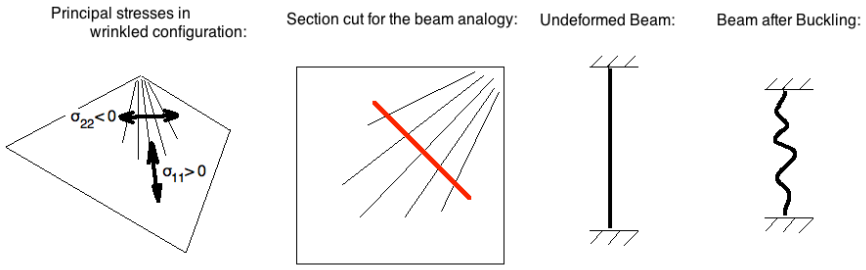

Figure 4.17: Different types of wrinkling arising on downwind sails

Wrinkling can locally be compared to a post-buckled beam (see Figure 4.17.): the deformation energy is counter-balanced by the bending component of the structural stiffness, and the membrane stiffness can be considered negligible. When wrinkling occurs, the membrane model result is ill posed, since it completely neglects the bending stiffness. This is equivalent to consider the connections between the discretized structure as hinges. If hinges were placed in the post-buckled beam, it would not be possible to find any equilibrium, because the structure would result under constrained and any external load would produce unlimited displacements and no deformation energy. Two possibilities are then available in order to solve the wrinkling problem: to use membrane elements with an additional *ad-hoc* wrinkling model, or to use a more complete formulation such as the shell model, as has been done in this thesis.

Wrinkles and equilibrium

As wrinkling is a form of buckling, its development can be analysed in terms of stability. An equilibrium configuration is called stable when after a small disturbance the system returns to its initial configuration. An indifferent equilibrium configuration is encountered when any perturbed configuration is an equilibrium configuration. In the unstable equilibrium configuration, there exist arbitrarily small disturbances under which the system moves to a new (not necessary stable) equilibrium configuration.

The Lagrange-Dirichlet theorem states that a minimum of the potential energy in a conservative mechanical system is a stable equilibrium configuration. As the potential energy for

linear analysis is given by $W = \frac{1}{2}\ (\mathbf{Y}^T \cdot \mathbf{K}_0 \cdot \mathbf{Y})$, a correspondence can be found between the positiveness of the tangent stiffness matrix, which is defined as:

$$\mathbf{K}_T(\mathbf{Y}) = \frac{\partial \mathbf{K}}{\partial \mathbf{Y}},$$

and the system stability. This is represented by the sign of the eigenvalues, as summarized in Table 4.4.

Table 4.4: Equilibrium and eigenvalues of the tangent stiffness matrix

Matrix property	Eigenvalues	Equilibrium
Positive definite	$\lambda_i > 0\ \forall i = 1, ndof$	Stable
Non-positive definite	$\lambda_j < 0$ for some j	Unstable
Semi-Positive	$\lambda_i \geqslant 0\ \forall i$ and $\lambda_j = 0$ for some j	Critical

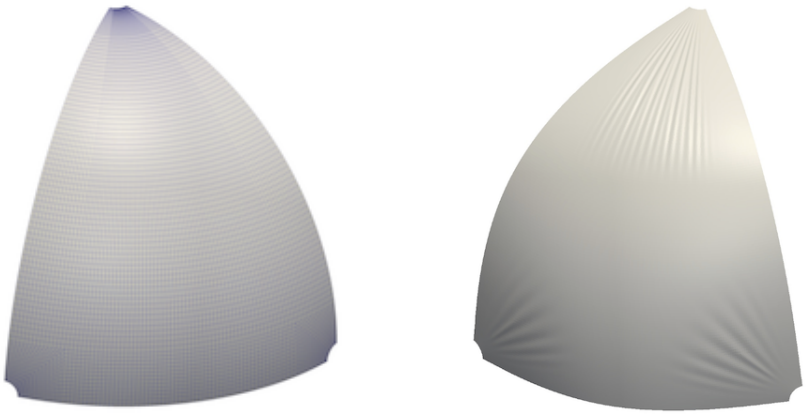

Figure 4.18: The analysed shell geometry; The sample point location, the path of which is described in Figure 4.19, is on the structure's symmetry line. On the *right*, the final deformed shape, where wrinkling occurs

To illustrate this discussion, a sail-type geometry has been loaded with a typical constant pressure (10^{-4} N/mm^2) and analysed in order to detect the equilibrium behaviour in relation to the generation of wrinkles. A mesh with about 1800 elements was chosen, with 28 elements per horizontal section and 18 elements in the circular section close to the side corner. By observing the deformed wrinkled shape with six wrinkles on the corners and 13 wrinkles on the top, this mesh resolution was judged sufficient, at least for a limited number of eigenvalues. Of course, after discretization the number of eigenmodes is finite unlike the continuous case, and is equal to the number of degrees of freedom of the structure. The analysis specifications are summarised in Table 4.5. The tangent stiffness matrix has been extracted every 20 time

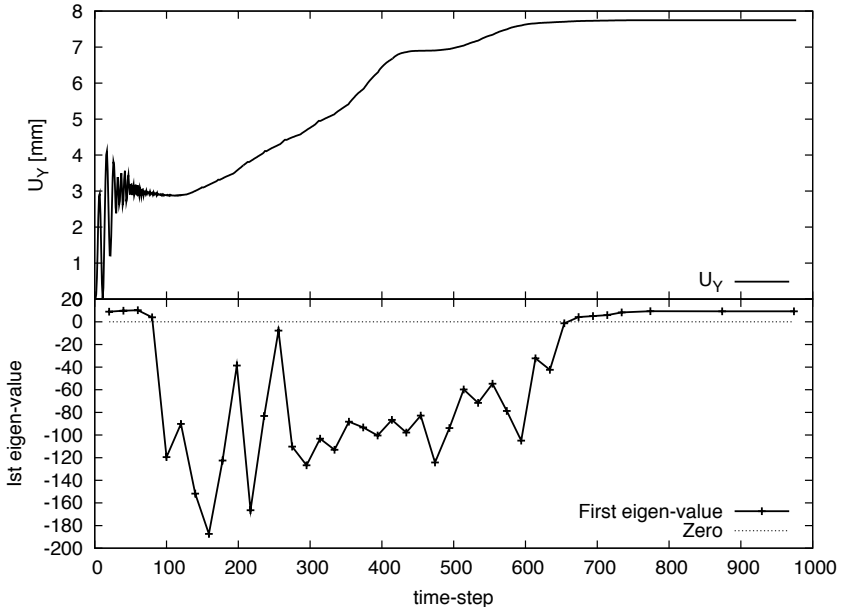

Figure 4.19: *Top*: one node path and *bottom*: the first eigenvalue during the deformation time path

steps, and an eigen-analysis was performed for the first 10 eigenmodes of lowest associated frequencies. Figure 4.19-*top* visualizes the displacement of a node of the discretized structure over time, while Figure 4.19-bottom shows the evolution of the first eigenvalue.

Table 4.5: Analysis settings for the eigenvalue analysis

$Height$	$Circ.\,sect.$	$Elements$	t	E	ν
[mm]	[Rad]	[-]	[mm]	[N/mm^2]	[-]
1000	$\pi/5$	1761	0.05	376	0.4

Instability is soon encountered after starting the calculation process, and it only disappears near the end of the time path, when the structure is established in a stable configuration. This instability is the cause of the wrinkling generation, as it appears by inspecting the eigenvectors during the time path. Figure 4.20 reports on the first eigenvector for time steps 120, 236 and 394, all representing unstable modes. In the first case, the unstable mode spreads to the whole sail. As the calculation proceeds, the instability tends to concentrate on the wrinkled zones. At the end of the calculation no unstable mode remains, but the first eigenmodes still represent wrinkling patterns. This indicates the dynamics of the wrinkling generation, as it appears to play the role of absorbing the instabilities in well-circumscribed zones.

The strong link between instability and wrinkling is confirmed when inspecting a number of eigenmodes for a single time step. Taking for instance the 394^{th} time step, in the middle

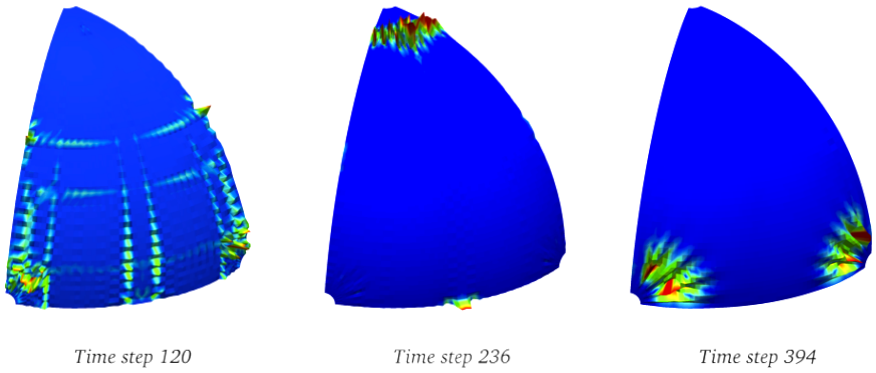

Figure 4.20: First eigenvector plot for three time-steps

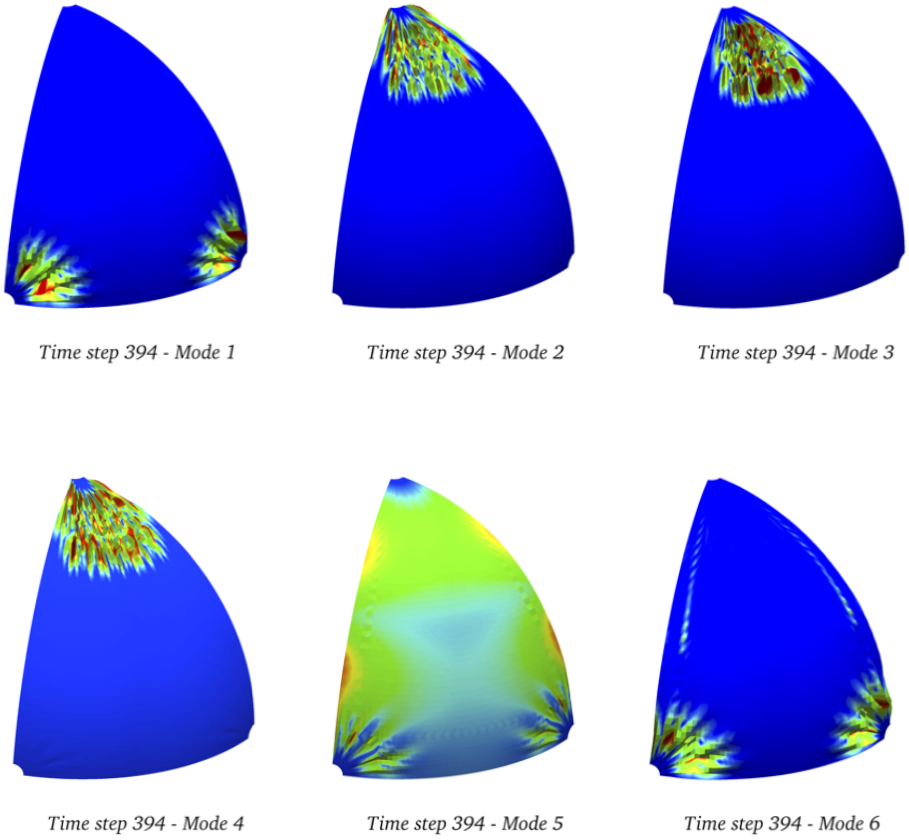

Figure 4.21: First six eigenvectors for time-step 394

of the unstable time period, the majority of the first eigenvectors represent the wrinkling deformation components, as shown in Figure 4.21 where the first six eigenvectors are reported.

Measures of Wrinkling

Two main measures are generally used in order to characterize surface wrinkling: the number n_w – or wavelength L_w – of the wrinkles appearing on the deformed surface and their amplitude A_w [5, 112]. A third measure is here introduced, which describes the global state of a wrinkled section. This is defined as $I_w = n_w \cdot \sigma$, where n_w is the number of wrinkles and σ is the standard deviation of the section from a smooth regression curve fitting the wrinkled cross-section. This index takes similar values for a large number of small wrinkles or a small number of large wrinkles and of course for a smooth surface the index vanishes.

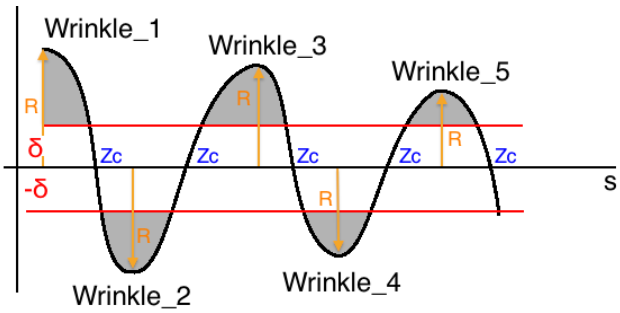

Figure 4.22: Wrinkling recognition criterion

Wrinkling measures were computed with an automatic wrinkling recognition algorithm for planar cross-sections. This algorithm uses a regression of the cross-section with a polynomial of order five, and a re-parametrization with the arc length of the polynomial curve. Consequently, the transformed cross-section is compared to the straight arc-length axis as visualized in Figure 4.22. Calculating the standard deviation σ, the number of wrinkles is determined by following the arc-length and counting a new wrinkle every time the curve intersects the thresholds $-\delta$ or $+\delta$, where

$$\delta = \max(\alpha\sigma, \sigma_{MIN}),$$

directly after a zero crossing Z_c, for a well-chosen factor α. The minimum height of the threshold σ_{MIN} is calculated as a percentage of the section length, and avoids taking into account excessively small oscillations, which may be induced by the finite element discretization. In practice, suitable values are $\alpha = 0.2$, $\sigma_{MIN} = s_{MAX}/1000$, where s_{MAX} is the maximum coordinate of the arc-length. The complete calculation for the regression of order n is detailed in Appendix B.8.

4.2 Numerical methods

The focus of this section is placed on the discretization of the various aspects of the mathematical model previously discussed in Section 4.1. The discretization of the shell model is presented in Section 4.2.1, where a purely matrix form has been employed, which is intended to be particularly clear for implementation purposes. The Newmark type dynamic scheme adopted for discretizing the structural behaviour in time is then detailed in Section 4.2.2. Finally, the non-linear cable boundary condition which has been implemented for the description of the sail sheet is discussed in Section 4.2.3

4.2.1 Discretization of the structural model: MITC4 shell finite element formulations

The non-linear isoparametric four-node shell elements of the MITC family (Mixed Interpolation Tensorial Components) are based on the underlying mathematical shell model described in Section 4.1.5. The non-linear finite element solution of such a model relies on the formulations presented in Section 4.1.7. In this Section, the theoretical considerations previously presented will be further expanded with particular respect to the discretisation of the model.[2] The Section is so organised:

- Discretisation of the shell kinematics
- Calculation of the linear stiffness matrix
- Calculation of the non-linear elasticity matrix
- Calculation of the non-linear right hand side

Discretisation of the shell kinematics

The discretisation of the shell is based upon the standard isoparametric construction. Here standard bilinear interpolation functions for four-node elements are used, as described in Table 4.6: One local orthonormal frame is calculated for every node. Once the normal vector at the node $\vec{a}_3^{(k)}$ is defined (given or calculated) then:

$$\vec{V}_1^{(k)} = \frac{\vec{e}_2^{(k)} \times \vec{a}_3^{(k)}}{\|\vec{e}_2^{(k)} \times \vec{a}_3^{(k)}\|} \tag{4.137}$$

[2]The formulations presented in this Section refer in particular to [4] and the implementation of the MITC4 elements in the fortran Code *Modulef*, which has been used in the thesis for the Finite Element analysis

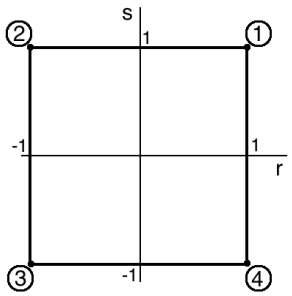

Figure 4.23: Definition of the element in the local coordinate system and node numbering

Table 4.6: Standard four nodes shape functions definition

λ_1	λ_2	λ_3	λ_4
$\frac{1}{4}(1+r)(1+s)$	$\frac{1}{4}(1-r)(1+s)$	$\frac{1}{4}(1-r)(1-s)$	$\frac{1}{4}(1+r)(1-s)$

$$\vec{V}_2^{(k)} = \frac{\vec{a}_1^{(k)} \times \vec{a_3}^{(k)}}{\|\vec{a}_1^{(k)} \times \vec{a_3}^{(k)}\|} \tag{4.138}$$

Denoting the local coordinates by (r, s, z) varying between -1 and +1 inside an element, the Euclidean position vector of a point within this element for a configuration indexed by ℓ is given by (compare with (4.14)):

$${}^{\ell}\vec{X} = \sum_{k=1}^{4} \lambda_k(r,s)\left({}^{\ell}\vec{X}^{(k)} + z\frac{t^{(k)}}{2}\,{}^{\ell}\vec{V}_n^{(k)}\right), \tag{4.139}$$

where ${}^{\ell}\vec{X}^{(k)}$, ${}^{\ell}\vec{V}_n^{(k)}$ and $t^{(k)}$ respectively denote the position vector, unit transverse direction vector[3], and thickness parameter at node k in configuration ℓ, while λ_k is the associated finite element shape function as in Table 4.6. With the position $\vec{X}$ thus defined, it is then possible to calculate the 3D covariant basis vectors $\vec{g}_i$ (see Equation (4.1)) as:

$$\vec{g}_1 = \frac{\partial\,{}^{\ell}\vec{X}}{d\xi^1} = \frac{\partial\,{}^{\ell}\vec{X}}{dr} = \sum_{k=1}^{4} \frac{\partial\lambda_k(r,s)}{\partial r}\left({}^{\ell}\vec{X}^{(k)} + z\frac{t^{(k)}}{2}\,{}^{\ell}\vec{V}_n^{(k)}\right) \tag{4.140}$$

$$\vec{g}_2 = \frac{\partial\,{}^{\ell}\vec{X}}{d\xi^2} = \frac{\partial\,{}^{\ell}\vec{X}}{ds} = \sum_{k=1}^{4} \frac{\partial\lambda_k(r,s)}{\partial s}\left({}^{\ell}\vec{X}^{(k)} + z\frac{t^{(k)}}{2}\,{}^{\ell}\vec{V}_n^{(k)}\right) \tag{4.141}$$

$$\vec{g}_3 = \frac{\partial\,{}^{\ell}\vec{X}}{d\xi^3} = \frac{\partial\,{}^{\ell}\vec{X}}{dz} = \sum_{k=1}^{4} \lambda_k(r,s)\left(\frac{t^{(k)}}{2}\,{}^{\ell}\vec{V}_n^{(k)}\right) \tag{4.142}$$

where the generic coordinate system (ξ^1, ξ^2, ξ^3) was instantiated using the local coordinate system (r, s, z).

[3]The transverse director vector is not normal to the mid-surface in general deformed configurations

Then, based on the isoparametric construction, discrete displacements of the shell within a total Lagrangian formulation are obtained as (see Equation (4.31)):

$$ {}^{\ell}\vec{U} = \sum_{k=1}^{4} \lambda_k(r,s)\left({}^{\ell}\vec{U}^{(k)} + z\frac{t^{(k)}}{2}\left({}^{\ell}\vec{V}_n^{(k)} - {}^{0}\vec{V}_n^{(k)}\right)\right), \tag{4.143} $$

where ${}^{\ell}\vec{U}^{(k)}$ denotes nodal displacements with respect to the initial configuration. Under a small displacement assumption – used for instance when calculating the linearised increments of the normal vector in the Newton's algorithm– the difference between transverse directors can be parametrized in the standard form

$$ {}^{\ell}\vec{V}_n^{(k)} - {}^{0}\vec{V}_n^{(k)} = \alpha_1^{(k)}\, {}^{0}\vec{V}_1^{(k)} + \alpha_2^{(k)}\, {}^{0}\vec{V}_2^{(k)} \tag{4.144} $$

where $\left({}^{0}\vec{V}_1^{(k)}, {}^{0}\vec{V}_2^{(k)}, {}^{0}\vec{V}_n^{(k)}\right)$ defines an orthonormal basis in the reference configuration – hence, $\left({}^{0}\vec{V}_1^{(k)}, {}^{0}\vec{V}_2^{(k)}\right)$ are unit vectors lying in the tangential plane to the midsurface – and $\alpha_1^{(k)}, \alpha_2^{(k)}$ denote associated rotation angles. Concerning the parametrization of the finite rotation of the director vector, at every time step and every Newton iteration this rotation is reparametrized using an updated orthonormal triedron including the current position of the director vector. This gives a first-order differential consistent with the linear formula (4.144). In the computation of the tangent stiffness matrix also the use the non-zero second-order differential is needed, associated with the parametrization curvature.

Similarly it is possible to calculate the derivatives of the displacements as:

$$ \frac{\partial\, {}^{\ell}\vec{U}}{dr} = \sum_{k=1}^{4} \frac{\partial\lambda_k(r,s)}{\partial r}\left({}^{\ell}\vec{U}^{(k)} + z\frac{t^{(k)}}{2}\left({}^{\ell}\vec{V}_n^{(k)} - {}^{0}\vec{V}_n^{(k)}\right)\right) \tag{4.145} $$

$$ \frac{\partial\, {}^{\ell}\vec{U}}{ds} = \sum_{k=1}^{4} \frac{\partial\lambda_k(r,s)}{\partial s}\left({}^{\ell}\vec{U}^{(k)} + z\frac{t^{(k)}}{2}\left({}^{\ell}\vec{V}_n^{(k)} - {}^{0}\vec{V}_n^{(k)}\right)\right) \tag{4.146} $$

$$ \frac{\partial\, {}^{\ell}\vec{U}}{dz} = \sum_{k=1}^{4}\left(\frac{t^{(k)}}{2}\lambda_k(r,s)\left({}^{\ell}\vec{V}_n^{(k)} - {}^{0}\vec{V}_n^{(k)}\right)\right) \tag{4.147} $$

Calculation of the linear stiffness matrix

The linear stiffness matrix associated with the linear stiffness operator described in Section (4.1.7) is defined as:

$$ \mathbf{K} = \int_V \mathbf{B}^T \cdot \mathbf{C} \cdot \mathbf{B}\, dV \tag{4.148} $$

where the matrix $\mathbf{B}$ is the matrix of the derivatives – e.g. the transformation which verifies: $\epsilon = \mathbf{B} \cdot \mathbf{U}$. The elasticity matrix $\mathbf{C}$ is defined in Equation (4.44) and (4.45).

Recalling the expression of the Green-Lagrange strain tensor in Equation 4.32, and passing from the indexes i, j to the local reference coordinates r, s then:

$$\begin{aligned} \epsilon_{rr} &= \vec{g}_r \cdot \vec{U}_{,r} \qquad \epsilon_{ss} = \vec{g}_s \cdot \vec{U}_{,s} \qquad 2\,\epsilon_{rs} = \vec{g}_r \cdot \vec{U}_{,s} + \vec{g}_r \cdot \vec{U}_{,s} \\ 2\,\epsilon_{rz} &= \vec{g}_r \cdot \vec{U}_{,z} + \vec{g}_z \cdot \vec{U}_{,r} \qquad 2\,\epsilon_{sz} = \vec{g}_s \cdot \vec{U}_{,z} + \vec{g}_z \cdot \vec{U}_{,s} \end{aligned} \tag{4.149}$$

and the term ϵ_{zz} is assumed to be *zero* for shells (see [4], Equation (4.9)). The components of the displacement derivatives and of the base vectors in the global reference system (x_1, x_2, x_3) will be indicated as: ${}^{\ell}\vec{U}_{,r} = (({}^{\ell}\vec{U}_{,r})_1, ({}^{\ell}\vec{U}_{,r})_2, ({}^{\ell}\vec{U}_{,r})_3)$, $\vec{g}_r = ((\vec{g}_r)_1, (\vec{g}_r)_2, (\vec{g}_r)_3)$ (and similarly for ${}^{\ell}\vec{U}_{,s}$, ${}^{\ell}\vec{U}_{,z}$, $\vec{g}_s$, $\vec{g}_z$). Equations (4.149) can be then rearranged in matrix form as:

$$\epsilon = \left[\begin{array}{ccc|ccc|ccc} (\vec{g}_r)_1 & 0 & 0 & (\vec{g}_r)_2 & 0 & 0 & (\vec{g}_r)_3 & 0 & 0 \\ 0 & (\vec{g}_s)_1 & 0 & 0 & (\vec{g}_s)_2 & 0 & 0 & (\vec{g}_s)_3 & 0 \\ (\vec{g}_s)_1 & (\vec{g}_r)_1 & 0 & (\vec{g}_r)_2 & (\vec{g}_s)_2 & 0 & (\vec{g}_s)_3 & (\vec{g}_r)_3 & 0 \\ (\vec{g}_z)_1 & 0 & (\vec{g}_r)_1 & (\vec{g}_z)_2 & 0 & (\vec{g}_r)_2 & (\vec{g}_z)_3 & 0 & (\vec{g}_r)_3 \\ 0 & (\vec{g}_z)_1 & (\vec{g}_s)_1 & 0 & (\vec{g}_z)_2 & (\vec{g}_s)_2 & 0 & (\vec{g}_z)_3 & (\vec{g}_s)_3 \end{array}\right] \cdot \begin{bmatrix} ({}^{\ell}\vec{U}_{,r})_1 \\ ({}^{\ell}\vec{U}_{,s})_1 \\ ({}^{\ell}\vec{U}_{,z})_1 \\ ({}^{\ell}\vec{U}_{,r})_2 \\ ({}^{\ell}\vec{U}_{,s})_2 \\ ({}^{\ell}\vec{U}_{,z})_2 \\ ({}^{\ell}\vec{U}_{,r})_3 \\ ({}^{\ell}\vec{U}_{,s})_3 \\ ({}^{\ell}\vec{U}_{,z})_3 \end{bmatrix} \tag{4.150}$$

Under the assumption stated in (4.144), the displacement derivatives in (4.145) rewrite:

$${}^{\ell}\vec{U}_{,r} = \sum_{k=1}^{4} \frac{\partial \lambda_k(r,s)}{\partial r} \left({}^{\ell}\vec{U}^{(k)} + z\frac{t^{(k)}}{2} \left(\alpha_1^{(k)\,0}\vec{V}_1^{(k)} + \alpha_2^{(k)\,0}\vec{V}_2^{(k)} \right) \right), \tag{4.151}$$

in matrix form then, denoting by $u_i^{(k)}$ the translation along the direction i of the k-th node

of the element (and similarly for the rotations $\alpha_i^{(k)}$):

$$\begin{bmatrix} ({}^{\ell}\vec{U}_{,r})_1 \\ ({}^{\ell}\vec{U}_{,r})_2 \\ ({}^{\ell}\vec{U}_{,r})_3 \end{bmatrix} = \left[\begin{array}{ccc|cc|cc} \frac{\partial\lambda_1}{\partial r} & 0 & 0 & \frac{zt}{2}\frac{\partial\lambda_1}{\partial r}(\vec{V}_1^{(1)})_1 & \frac{zt}{2}\frac{\partial\lambda_1}{\partial r}(\vec{V}_2^{(1)})_1 & \frac{\partial\lambda_2}{\partial r} & \dots \\ 0 & \frac{\partial\lambda_1}{\partial r} & 0 & \frac{zt}{2}\frac{\partial\lambda_1}{\partial r}(\vec{V}_1^{(1)})_2 & \frac{zt}{2}\frac{\partial\lambda_1}{\partial r}(\vec{V}_2^{(1)})_2 & \dots & \dots \\ 0 & 0 & \frac{\partial\lambda_1}{\partial r} & \frac{zt}{2}\frac{\partial\lambda_1}{\partial r}(\vec{V}_1^{(1)})_3 & \frac{zt}{2}\frac{\partial\lambda_1}{\partial r}(\vec{V}_2^{(1)})_3 & \dots & \dots \end{array}\right] \cdot \begin{bmatrix} u_x^{(1)} \\ u_y^{(1)} \\ u_z^{(1)} \\ \alpha_1^{(1)} \\ \alpha_2^{(1)} \\ u_x^{(2)} \\ u_y^{(2)} \\ u_z^{(2)} \\ \alpha_1^{(2)} \\ \dots \\ \dots \end{bmatrix} \tag{4.152}$$

similar evaluations are performed with respect to the second direction s. The evaluation along the third direction z is rather different, since $\partial\lambda(r,s)/\partial z = 0$:

$$\begin{bmatrix} ({}^{\ell}\vec{U}_{,z})_1 \\ ({}^{\ell}\vec{U}_{,z})_2 \\ ({}^{\ell}\vec{U}_{,z})_3 \end{bmatrix} = \left[\begin{array}{ccc|cc|cc} 0 & 0 & 0 & \frac{t}{2}\lambda_1(\vec{V}_1^{(1)})_1 & \frac{t}{2}\lambda_1(\vec{V}_2^{(1)})_1 & 0 & \dots \\ 0 & 0 & 0 & \frac{t}{2}\lambda_1(\vec{V}_1^{(1)})_2 & \frac{t}{2}\lambda_1(\vec{V}_2^{(1)})_2 & \dots & \dots \\ 0 & 0 & 0 & \frac{t}{2}\lambda_1(\vec{V}_1^{(1)})_3 & \frac{t}{2}\lambda_1(\vec{V}_2^{(1)})_3 & \dots & \dots \end{array}\right] \cdot \begin{bmatrix} u_x^{(1)} \\ u_y^{(1)} \\ u_z^{(1)} \\ \alpha_1^{(1)} \\ \alpha_2^{(1)} \\ u_x^{(2)} \\ u_y^{(2)} \\ u_z^{(2)} \\ \alpha_1^{(2)} \\ \dots \\ \dots \end{bmatrix} \tag{4.153}$$

It is now possible to express the components of the matrix of the derivatives $\mathbf{B}$. Expressing (4.150) as $\epsilon = \mathbf{G} \cdot \nabla\mathbf{U}$, and rearranging in a single matrix the components of Equation 4.152, the analogous components along the direction s and of Equation 4.153, such that $\nabla\mathbf{U} = \mathbf{D}\cdot\mathbf{U}$, with $\mathbf{U}$ the vector of nodal displacements:

$[5\times 1]$		$[5\times 9]$	$[9\times 1]$		$[5\times 9]$	$[9\times(5\times NoE)]$	$[(5\times NoE)\times 1]$
ϵ	$=$	$\mathbf{G}$	$\cdot$	$\nabla\mathbf{U}$	$=$	$\mathbf{G}$ $\cdot$ $\mathbf{D}$	$\cdot$ $\mathbf{U}$

where Noe is the number of nodes defining the element (4, in the case of the shell considered in this work). The matrix of the derivatives is then calculated as: $\mathbf{B} = \mathbf{G} \cdot \mathbf{D}$, and it has size $[5 \times NoE]$.

Once the matrices in (4.148) have been calculated, the terms must be integrated over the element. Gauss Numerical integration is performed, which (in 1-D) consists in assuming that:

$$\int_{-1}^{1} f(x)\, dx \approx \sum_{i=1}^{n} w_i\, f(x_i) \tag{4.154}$$

where the terms w_i are well-chosen weighting factors, and the x_i are the coordinates of the integration points. Of course, the points and the weighting factors are chosen in order to minimize the error between the numerical estimate and the analytical value, and the error tends to zero as the number of Gauss points increases. In the case of numerical integration using two Gauss points (in 1D), the values are $r = \pm 1/\sqrt{3}$ and $w_i = 1$.

Numerical integration in 2D is similar to the drawing in Figure 4.24. In this case two integration points are used for each direction, where the values of the weighting functions are calculated as in Table 4.7. Integrating in 3D does not create any further difficulty, and it is just a matter of multiplying again the values for the 2D numerical integration for the weights.

Table 4.7: Values for 2D numerical integration

x_i	$-1/\sqrt{3}$	$-1/\sqrt{3}$	$1/\sqrt{3}$	$1/\sqrt{3}$
y_i	$-1/\sqrt{3}$	$+1/\sqrt{3}$	$-1/\sqrt{3}$	$1/\sqrt{3}$
w_i^{Plane}	$w_1^2 = 1$	$w_1\, w_2 = 1$	$w_2\, w_1 = 1$	$w_2^2 = 1$

In order to perform numerical integration over the volume of the element as in (4.154), we need to calculate the determinant of the Jacobian matrix, defined as:

$$J = det(\nabla X) = det\left(\begin{bmatrix} \frac{\partial X_1}{\partial r} & \dots & \dots \\ \dots & \dots & \dots \\ \dots & \dots & \frac{\partial X_3}{\partial z} \end{bmatrix}\right) = \left[det\left(\begin{bmatrix} g_{rr} & \dots & \dots \\ \dots & \dots & \dots \\ \dots & \dots & g_{zz} \end{bmatrix}\right)\right]^{\frac{1}{2}} \tag{4.155}$$

The mixed terms rz and sz can be neglected, since $\vec{g}_z$ points in the normal direction. The

determinant of the Jacobian matrix is then equivalent to:

$$J = \sqrt{g_{zz} \cdot det\left(\begin{bmatrix} g_{rr} & g_{sr} \\ g_{rs} & g_{ss} \end{bmatrix}\right)} \tag{4.156}$$

The numerical integration can then be performed as in (4.154), as:

$$\int_V \mathbf{B}^T \cdot \mathbf{C} \cdot \mathbf{B}\, dV = \sum_{i=1}^{N} w_i^{Plane}\, w_i^z\, J \cdot \mathbf{B}^T \cdot \mathbf{C} \cdot \mathbf{B} \tag{4.157}$$

where N is the total number of integration points (in this case 8 in 3D); for every integration point w_i^{Plane} is the value of the in-plane weighting factor (see table 4.7) and w_i^z is the value of the transverse weighting factor. In the case of the considered four in-plane integration points the value of all the weightings is *one*.

In the case of the MITC interpolation, an additional treatment needs to be done. This interpolation is performed only for the *out-of-plane* mixed components of the strains rz and sz (see [4], Chapter 7.2.4), e.g. in the case of the matrix $\mathbf{B}$, the last two rows. The re-interpolation is then performed using the *tying points* as described in Figure 4.24. The interpolation is based on the following principle:

$$f(r,s,z) = \sum_{lt=1}^{nt} \lambda_t(r,s,z) \cdot f(r^{lt}, s^{lt}, z^{lt}) \tag{4.158}$$

where x^{lt}, y^{lt}, z^{lt} are the coordinates of the *lt-th* tying point, and λ_t is an re-interpolation function. It can be remarked how the formulation presented here recalls the general principle upon which is based the whole finite element discretization. The idea is the usual: a continuous function can be represented as the sum of the contributions calculated in a finite number of locations.

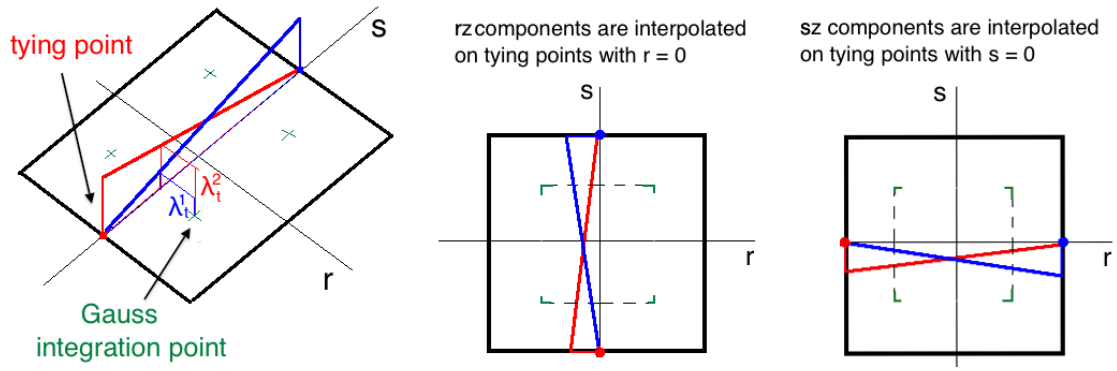

Figure 4.24: Mixed interpolation and base functions used for the interpolation

The calculation of the re-interpolated components of **B** acts on the value of the base functions calculated at the Gauss integration point coordinates: (r_g, s_g). So the value $\partial\lambda(r_g, s_g)/\partial r$ is in essence substituted by:

$$\sum_{lt=1}^{nt} \lambda_t(r_g, s_g) \cdot \frac{\partial\lambda(r^{lt}, s^{lt})}{\partial r} \tag{4.159}$$

where the re-interpolation functions λ_t are defined, for the rz component, using the two tying points placed at $r = 0$:

$$\lambda_t(0, s) = .5\,(1 + s/s^{lt}(i)) \tag{4.160}$$

and similarly for the sr component, using the two tying points placed at $s = 0$:

$$\lambda_t(r, 0) = .5\,(1 + r/rlt(i)) \tag{4.161}$$

The elasticity matrix **C** is defined in Equation (4.44) and (4.45). This matrix is constituted by two diagonal blocks, the first of which stores the membrane and the bending terms, and the second stores the shear terms:

$$\begin{bmatrix} c_{11} & c_{12} & c_{13} & & \\ c_{12} & c_{22} & c_{23} & & \\ c_{13} & c_{23} & c_{33} & & \\ & & & c_{44} & c_{45} \\ & & & c_{45} & c_{55} \end{bmatrix}$$

The terms represented here are the terms defining the constitutive relationship. The first diagonal block is the membrane and bending elasticity $C^{\alpha\beta\lambda\mu}$ and the second block represents the shear term $D^{\alpha\lambda}$. Since elasticity matrices are symmetric, only nine terms need to be calculated.

The metric tensor in contravariant components g^{rr}, g^{ss}, g^{rs} is calculated inverting the metric tensor previously calculated as defined in Equations (4.140) – (4.142).

Calculation of the non-linear elasticity matrix

The non-linear elasticity matrix is defined in the second term of the right hand side of Equation (4.56) as:

$$\int_V \sigma^{ij} \frac{\partial\delta e_{ij}}{\partial(\vec{\phi}, \underline{\alpha})}\, d(\vec{\phi}, \underline{\alpha})$$

First, the strain tensor e_{ij} is defined in Equation (4.32) using the components of the covariant base vectors and of the displacement derivatives calculated as in Equations (4.140) – (4.142) and (4.145) – (4.147). The components of the stress tensor σ^{ij} are then calculated using the

definition $\sigma = \mathbf{C} \cdot \mathbf{e}$.

The strain rate is defined in Equation (4.59) as:

$$\frac{\partial\, \delta e_{ij}}{\partial(\vec{\phi}, \underline{\alpha})} = \frac{1}{2}\left[\frac{\partial \vec{U}_{,i}}{\partial(\vec{\phi}, \underline{\alpha})} \cdot \delta\vec{V}_{,j} + \frac{\partial \vec{U}_{,j}}{\partial(\vec{\phi}, \underline{\alpha})} \cdot \delta\vec{V}_{,i} + \vec{G}_i \cdot \frac{\partial \delta\vec{V}_{,j}}{\partial(\vec{\phi}, \underline{\alpha})} + \vec{G}_j \cdot \frac{\partial \delta\vec{V}_{,i}}{\partial(\vec{\phi}, \underline{\alpha})}\right] \tag{4.162}$$

The variation of the test function around the current deformed configuration is then expressed as (see Equations (4.143) and (4.144)):

$$\delta\vec{V} = \sum_k \lambda_k(r,s)\Big[\delta\vec{\phi}^{(k)} + z\frac{t^{(k)}}{2}\Big(\delta\alpha_1^{(k)}\vec{V_1^{(k)}} + \delta\alpha_2^{(k)}\vec{V_2^{(k)}}\Big)\Big] \tag{4.163}$$

where the vectors $\vec{V}_1^{(k)}, \vec{V}_2^{(k)}, \vec{A}_3^{(k)}$ are ortho-normal. Using the matrix form then:

$$d\vec{U}_{,i} \cdot \delta\vec{V}_{,j} = d\mathbf{U}^T \cdot (\mathbf{D}^i)^T \cdot \mathbf{D}^j \cdot \delta\mathbf{V} \tag{4.164}$$

where the matrix $\mathbf{D}^i$ is the sub-matrix corresponding to the i-th derivative of $\mathbf{D}$. was previously defined as the matrix operator performing the gradient, $\mathbf{U}$ is the (unknown) vector of nodal displacements and $\mathbf{V}$ represents the test functions. It is then possible to express the product $(\mathbf{D^i})^T \cdot \mathbf{D^j}$ using the definition in (4.152). The resulting matrix is square and it has size $[Ndof \times Nnoe]$, $Ndof$ being the number of degrees of freedom per node and $Nnoe$ being the number of node per element. The first part of the matrix, referring to the first node and the directions $i = j = r$) can be shown for illustration purposes. Developing, simplifying the terms and observing that $\vec{V}_\alpha \cdot \vec{V}_\beta = 0$:

$$\left[\begin{array}{ccccc|c}
\left(\frac{\partial\lambda_1}{\partial r}\right)^2 & 0 & 0 & \left(\frac{\partial\lambda_1}{\partial r}\right)^2\frac{zt}{2}(\vec{V}_1^{(1)})_1 & \left(\frac{\partial\lambda_1}{\partial r}\right)^2\frac{zt}{2}(\vec{V}_2^{(1)})_1 & \cdots \\
 & \left(\frac{\partial\lambda_1}{\partial r}\right)^2 & 0 & \left(\frac{\partial\lambda_1}{\partial r}\right)^2\frac{zt}{2}(\vec{V}_1^{(1)})_2 & \left(\frac{\partial\lambda_1}{\partial r}\right)^2\frac{zt}{2}(\vec{V}_2^{(1)})_2 & \cdots \\
 & & \left(\frac{\partial\lambda_1}{\partial r}\right)^2 & \left(\frac{\partial\lambda_1}{\partial r}\right)^2\frac{zt}{2}(\vec{V}_1^{(1)})_3 & \left(\frac{\partial\lambda_1}{\partial r}\right)^2\frac{zt}{2}(\vec{V}_2^{(1)})_3 & \cdots \\
 & SYMM & & \left(\frac{zt}{2}\frac{\partial\lambda_1}{\partial r}\right)^2 \cdot \|\vec{V}_1^{(1)}\|^2 & 0 & \cdots \\
 & & & & \left(\frac{zt}{2}\frac{\partial\lambda_1}{\partial r}\right)^2 \cdot \|\vec{V}_2^{(1)}\|^2 & \cdots \\
\hline
\vdots & \vdots & \vdots & \vdots & \vdots & \ddots
\end{array}\right] \tag{4.165}$$

The calculation of the last two terms of equation (4.162) is done by differentiating Equation (4.163) with respect to $\underline{\alpha}$:

$$\frac{\partial\delta\vec{V}}{\partial(\vec{\phi}, \underline{\alpha})} \cdot d(\vec{\phi}, \underline{\alpha}) = \sum_k \lambda_k(r,s) z\frac{t^{(k)}}{2}\vec{A}_3^{(k)}(d\alpha_1^{(k)}\delta\alpha_1^{(k)} + d\alpha_2^{(k)}\delta\alpha_2^{(k)}) \tag{4.166}$$

the derivative with respect to the first direction results then:

$$\frac{\partial\delta\vec{V}_{,r}}{\partial(\vec{\phi}, \underline{\alpha})} \cdot d(\vec{\phi}, \underline{\alpha}) = \sum_k \frac{\partial\lambda_k(r,s)}{\partial r} z\frac{t^{(k)}}{2}\vec{A}_3^{(k)}(d\alpha_1^{(k)}\delta\alpha_1^{(k)} + d\alpha_2^{(k)}\delta\alpha_2^{(k)}) \tag{4.167}$$

The first part of the resulting matrix for the first direction r, shown in the same form as in (4.165), gives:

$$\left[\begin{array}{ccccc|c} 0 & 0 & 0 & 0 & 0 & \cdots \\ 0 & 0 & 0 & 0 & 0 & \cdots \\ 0 & 0 & 0 & 0 & 0 & \cdots \\ 0 & 0 & 0 & \mathcal{A} & 0 & \cdots \\ 0 & 0 & 0 & 0 & \mathcal{A} & \cdots \\ \hline \vdots & \vdots & \vdots & \vdots & \vdots & \ddots \end{array}\right] \tag{4.168}$$

where the term $\mathcal{A}$ for the node 1 is equal to:

$$\mathcal{A} = \frac{\partial \lambda_1(r,s)}{\partial r} z \frac{t}{2} \vec{G}_r \cdot \vec{A}_3^{(1)} \tag{4.169}$$

Calculation of the non-linear right hand side

The non-linear right hand side is calculated as in Equation (4.55):

$$\int_V \sigma^{ij}(\vec{U})\, \delta e_{ij} \tag{4.170}$$

where $\delta e_{ij} = \mathbf{B} \cdot d\mathbf{V}$, and $\mathbf{V}$ represents the value of the test (shape) functions at the considered integration point, while $\mathbf{B}$ is the matrix of the derivatives, see Equation (4.150). $\vec{\sigma}$ is computed when calculating the non-linear elasticity. The calculation of the non-linear right hand side is thus performed as:

$$RHS = \sum_i J\, w_i^{Plane}\ w_i^z\ \sigma \cdot \mathbf{B} \tag{4.171}$$

where J is the determinant of the Jacobian matrix (see Equation (4.156)) and w_i^{Plane} and w_i^z are the weighting factors used for Gauss integration in 3d, see Table 4.7 and Equation (4.157).

The contribution of the external force is finally calculated as in Equation (4.53) as:

$$\int_V \vec{f}\, d\vec{v}\, dV \tag{4.172}$$

where as in the previous case the integral is calculated numerically.

4.2.2 Discretization of the dynamic scheme

A dynamic scheme can be represented in the form of Equation (4.129), where the behaviour of the structural system is described by the displacements, the velocity and the acceleration, or the displacements and its time derivatives.

In order to time-integrate this kind of differential equations a time discretization is required, where the velocity and the acceleration are written as a function of the discrete

displacements. More generally, a method is required for the discrete integration of ordinary differential equations. The Euler method is the most elementary adopted procedure. This is a first order accurate method based on a Taylor expansion. In this framework the derivative term in the differential equation

$$\dot{y}(t) = f\big(t, y(t)\big) \quad , \quad y(t_0) = y_0 \tag{4.173}$$

is replaced by its discrete approximation:

$$\dot{y}(t) \approx \frac{y(t+dt) - y(t)}{dt} \quad \Rrightarrow \quad y(t+dt) \approx y(t) + dt \cdot y'(t) \tag{4.174}$$

this formulation is easily transformed in its recursive formulation:

$$y_{n+1} = y_n + dt\, y_n \tag{4.175}$$

The Euler method is explicit, since the value of the function y_{n+1} is uniquely defined by

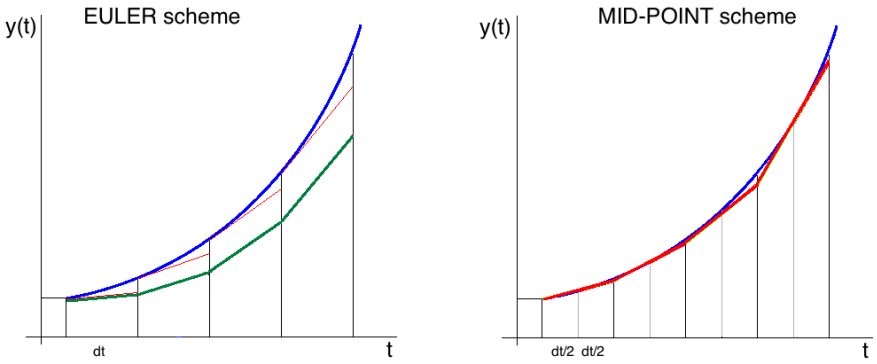

Figure 4.25: *Left*: Euler and *right*: mid-point time marching schemes

the value of the function calculated at the previous step y_n. The accuracy of such method is generally poor, the error being proportional to dt^2. A rather more accurate scheme is the mid-point method, which is based on the use of an implicit Euler scheme between the time instants $t^{n+\frac{1}{2}}$ and t^{n+1}. Such results are used for extrapolating the velocity and the acceleration at the time t^{n+1}. The formulation of the discrete velocity and the acceleration in this case are:

$$\ddot{y}_{n+1} \simeq \frac{\dot{y}_{n+1} - \dot{y}_n}{\delta t} \;\; ; \;\; \dot{y}_{n+\frac{1}{2}} \simeq \frac{\dot{y}_{n+1} + \dot{y}_n}{2} \simeq \frac{y_{n+1} - y_n}{\delta t} \simeq \frac{2(y_{n+\frac{1}{2}} - y_n)}{\delta t} \tag{4.176}$$

the name of such a method derives from the fact that the function y is evaluated for $t = t_n + dt/2$, therefore in the middle between the location (instant) where the function is known and where it needs to be calculated. This scheme is second order accurate, and the error is proportional to dt^3. The gain is evident when comparing the performances of the numerical

schemes in Figure 4.25. The mid-point rule is then commonly used for the time-marching scheme in the structural domain. This is often preferred to other schemes – as example the Euler first order scheme – which is not accurate enough and might then be too dissipative. In a linear structural framework it can be then proved that the mid-point rule scheme guarantees the conservation of the mechanic energy [113].

In the present work a mid-point rule was adopted for the structural calculations. The reason for using a dynamic scheme – even when performing static analysis – is due to the need of providing an additional source of stability to the problem. When analysing very thin shells in fact the finite element analysis is likely to encounter convergence issues (see Section 4.1.10).

Various techniques can be adopted in order to overcome such instabilities, one of which is to use a pseudo-dynamic procedure with artificial damping. Namely, the solution is calculated following a dynamical path in which the inertia and stiffness effects are naturally modelled (see Section 4.2.1), and some *Rayleigh damping*, defined in Section 4.1.9, is employed. Of course, when performing static analysis the time variable takes the meaning of a 'pseudo-time', rather than the physical time. The effect of such a damping definition when preforming fluid structure interactions will be investigated in Section 5.2.3.

Defined then $\mathbf{Y}$ the vector of displacement degrees of freedom, $\mathbf{F}$ the load vector, $\mathbf{M}$ the mass matrix, $\mathbf{K}(\mathbf{Y})$ the non-linear stiffness matrix-operator (see section 4.2.1, the structural dynamic equation to be solved is then of the type (see e.g. [68])

$$\mathbf{M}\,\ddot{\mathbf{Y}} + \mathbf{C}\,\dot{\mathbf{Y}} + \mathbf{K}(\mathbf{Y}) = \mathbf{F}(t), \tag{4.177}$$

where

$$\mathbf{C} = c_1\mathbf{M} + c_2\mathbf{K}_0 \tag{4.178}$$

with c_1, c_2 constant values defined as in Section 4.1.9 and $\mathbf{K}_0$ a reference stiffness matrix to be specified – e.g., the tangent stiffness matrix in the undeformed configuration.

Velocities and accelerations are defined using the mid-point rule as in (4.179):

$$\begin{cases} \ddot{\mathbf{Y}}_{n+\frac{1}{2}} = \dfrac{\dot{\mathbf{Y}}_{n+1} - \dot{\mathbf{Y}}_n}{\Delta t} \\ \dot{\mathbf{Y}}_{n+\frac{1}{2}} = \dfrac{\dot{\mathbf{Y}}_{n+1} + \dot{\mathbf{Y}}_n}{2} = \dfrac{\mathbf{Y}_{n+1} - \mathbf{Y}_n}{\Delta t} = \dfrac{2(\mathbf{Y}_{n+\frac{1}{2}} - \mathbf{Y}_n)}{\Delta t} \end{cases} \tag{4.179}$$

to be substituted in the dynamical equation (4.177) written at time '$n + \frac{1}{2}$'. This non-linear implicit equation is solved based on a Newton-Raphson algorithm. The resulting global solution algorithm is then summarized in Figure 4.26.

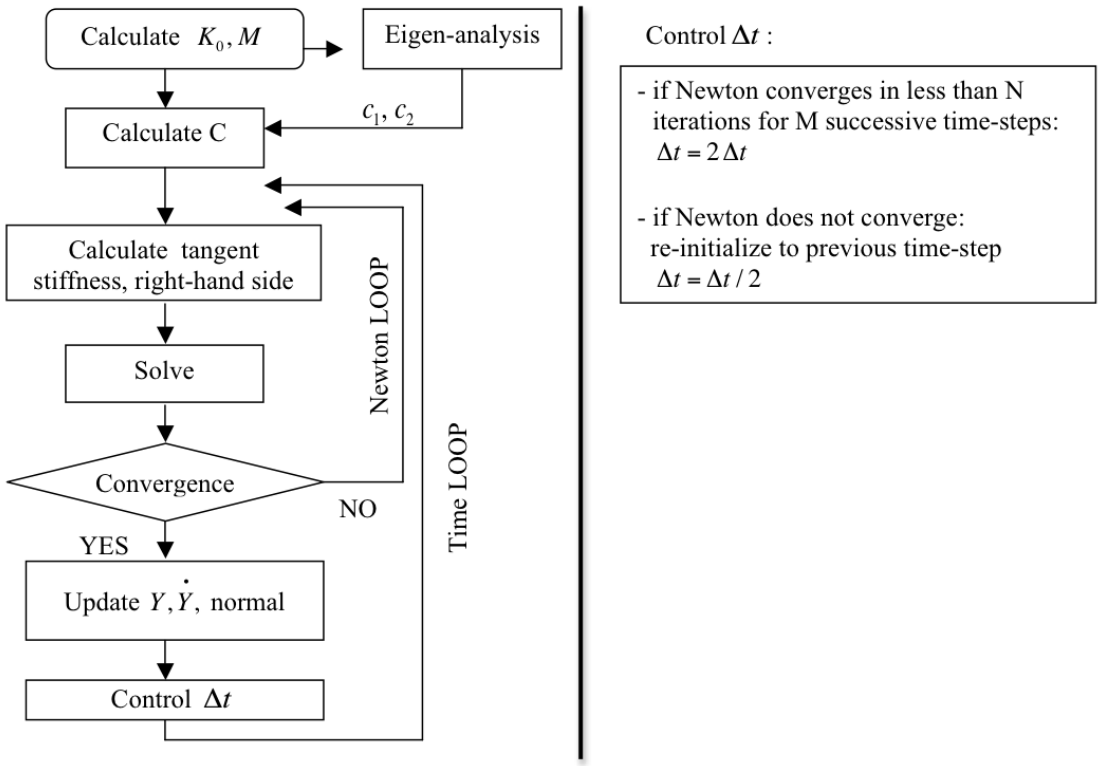

Figure 4.26: Calculation flow chart

When performing static analysis, an adaptive time-step is employed. At the beginning of the solution process in fact the physical instability and the rapidly-changing stiffness operator tend to produce oscillations, which can only be handled with small time-steps (see Figures 4.12, 4.19-*bottom*). As the calculation proceeds the time step can be progressively increased, until it ideally takes infinite values for a steady equilibrium state. The use of a variable time-step is thus necessary both for handling stability issues and for reducing the computation time. The strategy chosen for the adaptation of the time step is simply based on the convergence history of the solution: in the case where a chosen number of time steps converge in a few Newton iterations, the time step value is doubled. Accordingly, if convergence of the solution is not achieved within a number of Newton iterations, the calculation is re-initialised to the beginning of the time step, and the time step value is divided by a factor two. Additionally, when performing Fluid Structure Interactions (see Chapter 5), sub-cycling is allowed within the time-step. When convergence of the structural analysis is not reached, the structural solver is reset to the initial configuration of the time-step, the time step value is divided by two and two time-steps are calculated prior to send the results (in terms of displacements) to the fluid solver. Of course the sub cycling is not limited to a factor two, but it allows multiple subdivisions, until a lower bound for the time-step value is reached.

4.2.3 Imposing a cable boundary condition

The cable boundary condition has been imposed by locally modifying the matrices describing the existing problem, rather then adding new finite elements. This approach has the advantage of leaving unaltered the largest part of the problem's definition, such as the mesh and the assembly of the global stiffness, mass and damping operators. The concepts expressed here are similar, but more generic, to what expressed in Section 4.1.7. For a matter of completeness then these concepts are repeated here with particular reference to the case of the cable.

An hyper-elastic material is described using the Saint-Venant material model, where the strain-energy density is expressed (in general) as a function of the Green-Lagrange strain tensor ϵ :

$$W(\epsilon) = \frac{\lambda}{2}[tr\epsilon]^2 + \mu\, tr(\epsilon^{\,2}) \Rightarrow W(\epsilon) = \frac{\lambda}{2}[tr\epsilon]^2 \tag{4.180}$$

where the last expression holds since μ=0 if no-shear is allowed such as in the example of the cable.

The total energy of the system can then be expressed as:

$$W_{tot} = \int_\Omega W \,\mathrm{d}\Omega - \int_\Omega \vec{f} v \,\mathrm{d}\Omega \tag{4.181}$$

the equilibrium is imposed as $\delta W = 0$. Thus (see also Equation (4.53)):

$$\frac{\partial W(\epsilon)}{\partial \epsilon}\,\delta\epsilon = 0 \tag{4.182}$$

$$\int_\Omega \frac{\partial W(\epsilon)}{\partial \epsilon} : \delta\epsilon \,\mathrm{d}\Omega = \int_\Omega \vec{f}\delta v \,\delta\Omega \tag{4.183}$$

where the first term in the left hand side integral is called the second Piola-Kirchoff stress tensor and it is denoted as σ. Introducing the assumption of small strains then:

$$\delta\epsilon = \epsilon\,\delta v \tag{4.184}$$

$$\int_\Omega \sigma : \epsilon\,\delta v \,\mathrm{d}\Omega = \int_\Omega \vec{f}\delta v \,\mathrm{d}\Omega \tag{4.185}$$

The second Piola-Kirchhoff stress tensor can now be expressed, using a Taylor development, as:

$$\sigma = \frac{\partial W(\epsilon)}{\partial \epsilon} = \frac{\partial W(\epsilon)}{\partial \epsilon}\Big|_0 + \frac{\partial^2 W(0)}{\partial \epsilon^2}\delta\epsilon \tag{4.186}$$

Therefore:

$$\int_\Omega \left(\frac{\partial W(\epsilon)}{\partial \epsilon}\Big|_0 + \frac{\partial^2 W(0)}{\partial \epsilon^2}\delta\epsilon \right) : \epsilon\,\delta v \,\mathrm{d}\Omega = \int_\Omega \vec{f}\delta v \,\mathrm{d}\Omega \tag{4.187}$$

where the terms :

$$\int_\Omega \frac{\partial W(\epsilon)}{\partial \epsilon}\Big|_0 : \vec{\vec{\epsilon}}\,\delta v \,\mathrm{d}\Omega \qquad \int_\Omega \frac{\partial^2 W(0)}{\partial \epsilon^2} : \epsilon\,\delta v \,\mathrm{d}\Omega \tag{4.188}$$

are the so-called pre-stress (or non-linear right hand side) and the non-linear stiffness. In order to model the cable then, once the Energy density function has been expressed it is possible to calculate directly the terms to be added into the stiffness operator and the right hand side (pre-stress) of the finite-element discretized problem. A natural measure of strain is

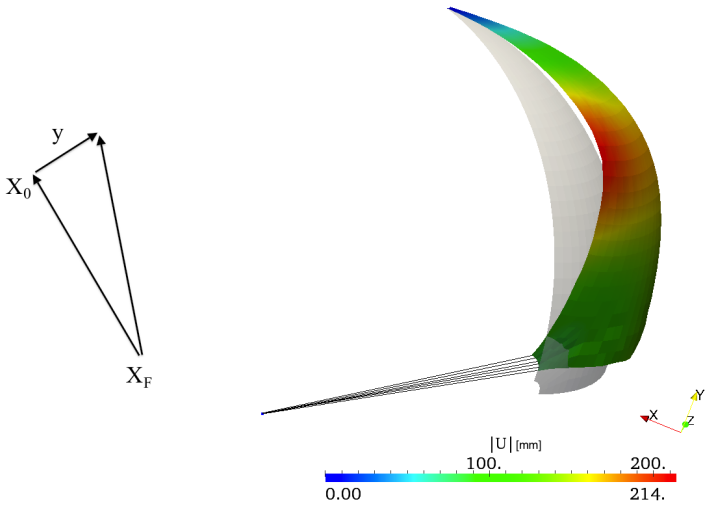

Figure 4.27: Definition of the quantities used in the following and impression of the deformation of a sail hold with a cable

the Green-Lagrange strain tensor, which in the mono-dimensional case of the cable reduces to the difference of the squared lengths. Defined then: $d\vec{x} = (\vec{x}_0 - \vec{x}_f + \vec{y})$ and $d\vec{X} = (\vec{x}_0 - \vec{x}_f)$:

$$\epsilon = (d\vec{x}^{\,2} - d\vec{X}^2)/d\vec{X}^2 \tag{4.189}$$

defined then the cable stiffness $k = EA$ then, the internal work can be expressed as:

$$W^{int} = \frac{1}{2}\, k \left[(\vec{x}_0 - \vec{x}_f + \vec{y})^2 - (\vec{x}_0 - \vec{x}_f)^2\right] \tag{4.190}$$

the term to be added into the non-linear right hand side is then the integrand term of Equation (4.188) *left*. Considering that the strain is represented in this mono-dimensional case by $\vec{y}$, as it can be seen in equation (4.190):

$$\begin{aligned} \frac{\partial W(\epsilon)}{\partial \epsilon} &= \frac{\partial W(\epsilon)}{\partial \vec{y}} = \frac{k}{2}\Big[2\Big((\vec{x}_0 - \vec{x}_f + \vec{y})^2 - (\vec{x}_0 - \vec{x}_f)^2\Big) \cdot 2\,(\vec{x}_0 - \vec{x}_f + \vec{y})\,\delta\vec{y}\Big] = \\ &= 2k\Big[(\vec{x}_0 - \vec{x}_f + \vec{y})^2 - (\vec{x}_0 - \vec{x}_f)^2\Big](\vec{x}_0 - \vec{x}_f + \vec{y})\,\delta\vec{y} \end{aligned} \tag{4.191}$$

In a three-dimensional framework this generates three entries per node to be added to the entries of the right hand side describing the translations in the space. Similarly, the term to add to the stiffness matrix is obtained by further differentiating with respect to $\vec{y}$:

$$\frac{\partial^2 W(\epsilon)}{\partial \epsilon^2} = 4k\Big[(\vec{x}_0 - \vec{x}_f + \vec{y})\,\delta\vec{y}\Big](\vec{x}_0 - \vec{x}_f + \vec{y})\,\delta\vec{y} + 2k\Big[(\vec{x}_0 - \vec{x}_f + \vec{y})^2 - (\vec{x}_0 - \vec{x}_f)^2\Big]\delta\vec{y}\,\delta\vec{y} \tag{4.192}$$

In this case the term $\delta\vec{y}\,\delta\vec{y}$ generates a 3x3 matrix. The entries of this matrix will be added to the relevant terms of the stiffness operator, as it is graphically shown in Figure 4.28. In the example the entries corresponding to the degrees of freedom of three nodes only are represented; the cable boundary condition affects the node 2, the values calculated with Equations (4.191) and (4.192) will be added in the zones highlighted in orange. The formulation ex-

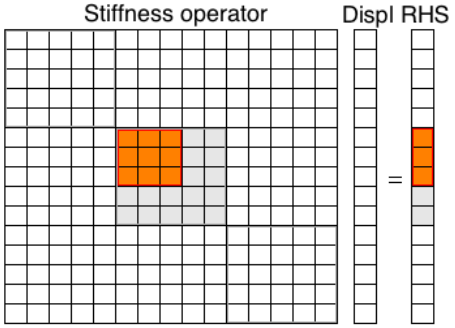

Figure 4.28: Adding the cable entries to the terms of the non linear stiffness operator and the right hand side

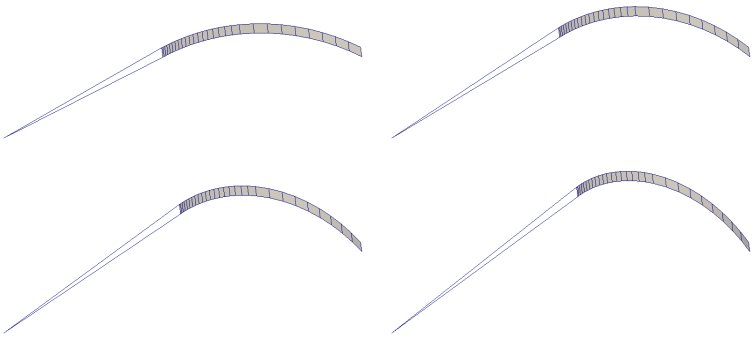

Figure 4.29: Incrementally increasing the length of the cable for a two dimensional sail strip

pressed in Equation (4.190) can be easily modified in order to impose variable lengths of the cable. In this case a new parameter δ can be added ($|y| = |y| + \delta$), which must be calibrated to incrementally increase or reduce the cable's length. Although no major difficulties are encountered, increasing the length of the cable produces in fact an additional instability in the analysis, and this might cause divergence. The incremental value δ must therefore be small enough to assure convergence in the whole deformation path.

Some results are reported in Figure 4.29, where the initial cable's length was increased by a factor 180%. The value of δ was here imposed to be 0.1% per time-step.

4.3 Numerical tests and validation

The scope of this section is to present some numerical cases as applicative examples of the numerical methods which have been described in Section 4.2. Different test cases will be shown, relevant for the fabric or the sail deformation analysis. The inflation of a flat membrane is simulated in Section 4.3.1 and numerical results – obtained with both MITC shells and membrane CST – are compared against experimental values. The case of the deformation for an initially flat parachute canopy is then analysed in Section 4.3.2. The results are compared to experimental values. These experiments have already been discussed from a fluid perspective in Section 3.3.3 and will be further investigated in terms of Fluid Structure Interactions in Section 5.2.7. The rest of the section is entirely dedicated to the simulation of the wrinkling. Some reference test cases are analysed as a validation of the adopted technique in Section 4.3.3, including some mesh sensitivity analysis and a discussion on the reference results. The method is then applied for the simulation of the wrinkling development is sail type-structures in Section 4.3.4.

4.3.1 Comparing results of CST membrane and MITC4 elements: flat membrane in pressure and spinnaker

The constant strain triangle (CST) membrane model has often been adopted for inflatable structures [69, 71, 74] or sail-type analysis [33, 31, 32]. The longevity of this model is partially a result of its simplicity: this element is in fact based on the assumption that the strain within the finite-element can be uniquely defined from the length of the three sides. The non-linearity is taken into account geometrically projecting the stiffness of the element on the plane tangent to the element in the actual configuration. For a more complete description of the CST elements one should refer to [65], [70] However the CST membrane is not without problems, and examples can be found where this class of models produce wrong answers [114]. A comparison is performed in this chapter between the performances of the CST elements implemented in [1] and those obtained with the shell MITC4.

The first comparison regards the experimental results published by the author in [1]. A wooden box was built and a Dacron membrane was fixed on the top. The fabric physical quantities reported here in Table 4.8 have been experimentally measured by means of traction tests, the results of which are also published in [1]. The box was been made air-proof by a gasket and a special paper on the edges. The Dacron fabric was fitted onto the box with fibres oriented along the box directions. Compressed air was pumped into the box and the

Figure 4.30: Experimental apparatus used for the membrane in pressure shape measurements

pressure was measured by water columns, providing very accurate measurements in the range of interest (11 to 88 mmH_2O i.e. $10 \rightarrow 80$ mbar). A laser device was used to measure the fabric displacements. Measurements were carried out for six transverse sections and six pressures in the range of interest. A non-negligible noise was experienced during the measurement: the oscillation of the data determined an incertitude estimated in $\leq 10\%$. The experimental data reported for the deformed central sections in Figure 4.32 are then the result of a second order polynomial regression. The experimental apparatus is shown in Figure 4.30.

Table 4.8: Case settings from [1]

Box length $[mm]$	Box beam $[mm]$	E_S $[N/mm^2]$	ν_S $[-]$	t_S $[mm]$	P $[N/mm^2]$
440	980	1667	0.4	0.3	0.011

The calculation meshes, as well as the deformed shapes obtained with CST and MITC4 finite elements reported in Figure 4.32. Results are reported here in terms of the mid-section deformed shape (Figure 4.32), and curvature (Figure 4.33).

Both the numerical results looks rather different to the experimental measured shape. In the case on the CST membranes, the calculated shape does not look smooth: the cross-section remains flat near the edges and a sudden change arises in curvature close to the centre of the device. The vertical displacement in the centre of the membrane exceeds about 30% the experimental value.

When performing the analysis with MITC4 shells, the displacement in the centre of the membrane is about 20% lower compared to the experimental value. However, the solution is more smooth in terms of curvature. Multiplying the numerical answer by a constant factor

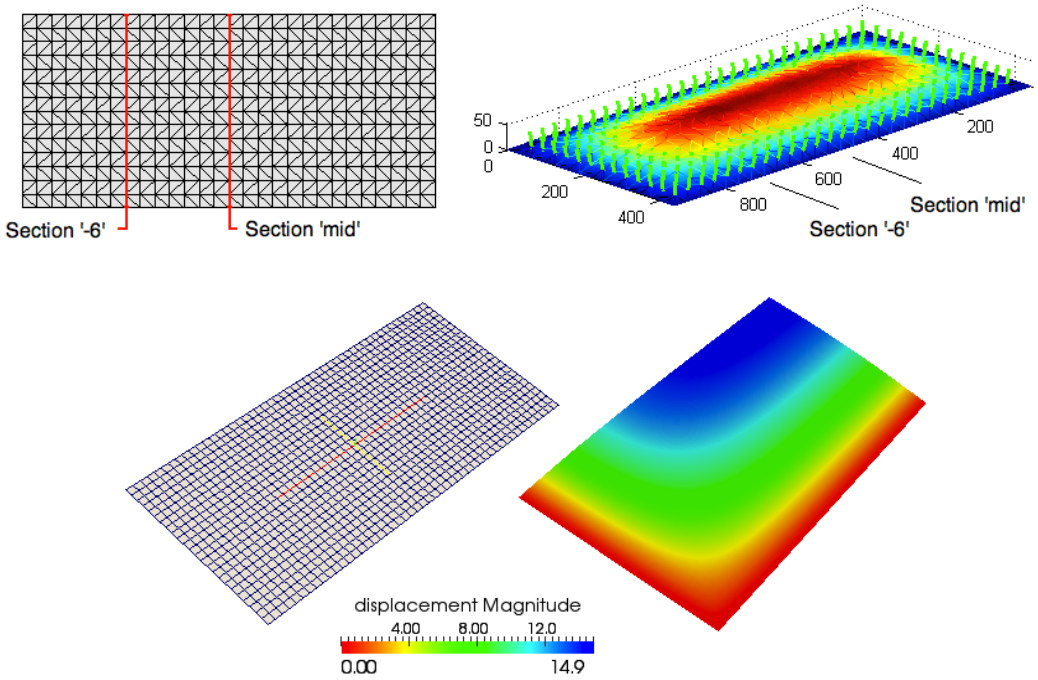

Figure 4.31: Numerical results obtained *top:* with CST membrane elements; *bottom* with MITC4 shell elements

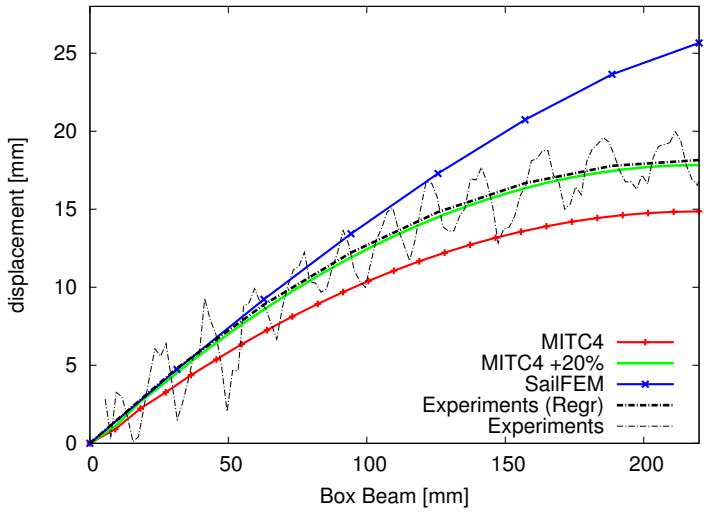

Figure 4.32: Central cross section deformed shape comparison for the results obtained with the CST membranes, the MITC4 shells and the experimental results

in fact the numerical results is perfectly reproduced.

Such behaviours are confirmed when analysing the same data in terms of curvature (Figure 4.33, calculated with a finite-difference scheme as in Equation (4.193). Here the sudden curvature change of the CST solution becomes more evident, as the improvement of the

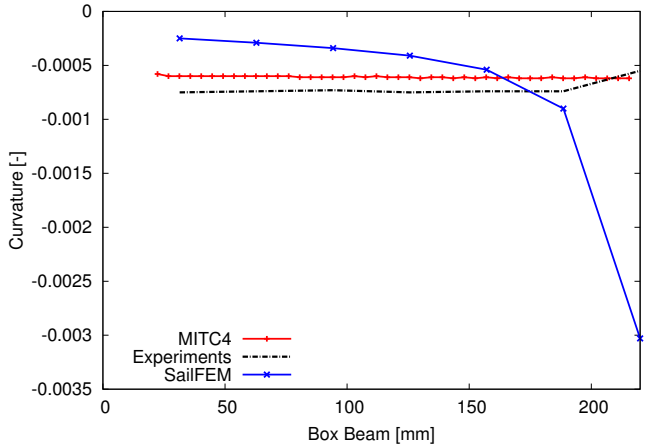

Figure 4.33: Central cross section curvature comparison for the results obtained with the CST membranes, the MITC4 shells and the experimental results

quality of the solution obtained with the MITC4 shells.

$$\frac{\partial^2 u}{\partial x^2}\Big|_n = 4\,\frac{u_{n+1} - 2u_n + u_{n-1}}{(x_{n+1} - x_{n-1})^2} \tag{4.193}$$

The solution obtained with CST triangles is poor both in terms of displacements and the curvature. It is not easy to explain the origin of such error, which may be caused by an excessively simplified formulation of the element: the kinematic assumptions on which the CST elements are based might be too strong. The reliability of such elements has never been really assessed, but in the literature examples can be found about the poor performances of these elements [114].

The MITC4 solution results affected by some static error. The main sources of such an error is to be ascribed to the experimental uncertainty, in terms of displacements and the material characterisation. The general trend is however globally well captured, both in terms of displacements and curvature.

In the following, the comparison of the CST membranes and the MITC4 shells has been extended to the calculation of a typical spinnaker geometry. The comparison is performed on similar mesh size, but it is worth remarking that elements implemented in SailFEM are triangular (CST), whereas nonlinear shells MITC4 are quadrilateral. The same characteristic material properties, loadings and boundary conditions were applied to the two calculations.

In Figure 4.34 the results of this comparison are shown, where the colour map represents the norm of nodal displacements. The calculated shape is quite different, and the membrane CST looks very “stiff” compared to nonlinear shell MITC4 elements. However, the order

of magnitude of global displacements is the same in the two analyses. The four sections

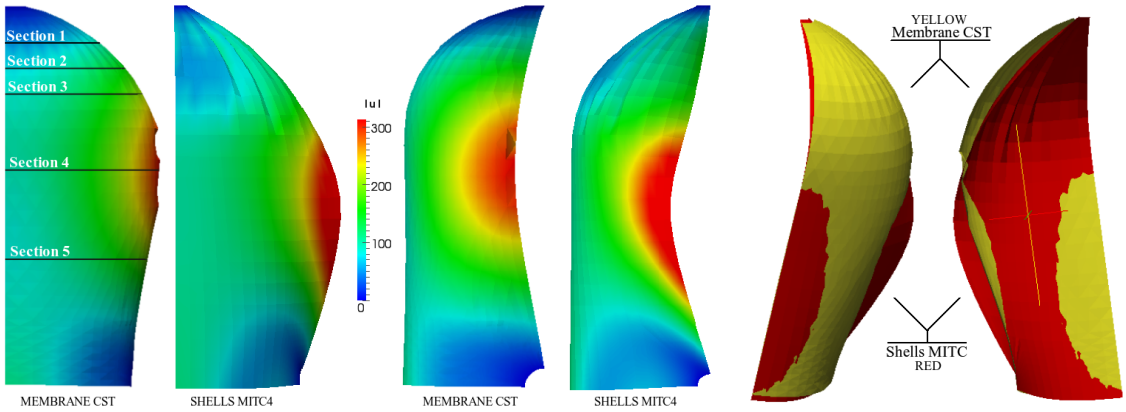

Figure 4.34: Deformed shape obtained with the CST membranes and the MITC4 shell elements

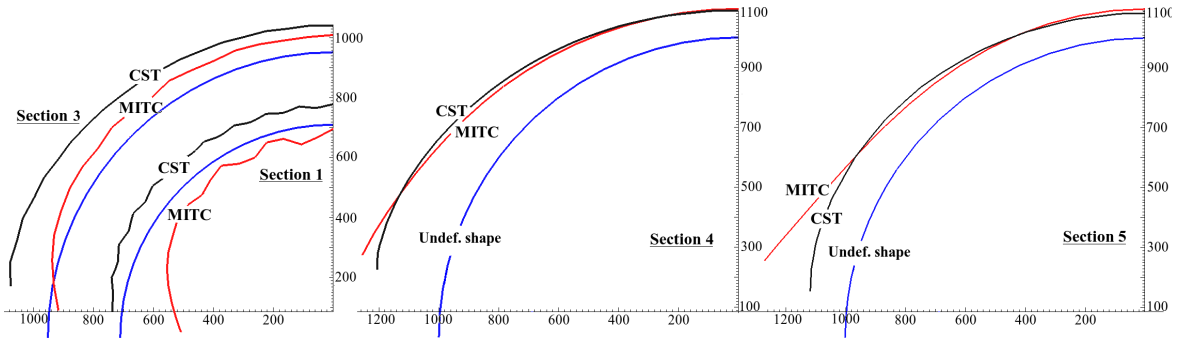

Figure 4.35: Deformed sections obtained with the CST membranes and the MITC4 shell elements. The location of such sections is specified in Figure 4.34

identified in the three dimensional plot in Figure 4.34 are drawn in Figure 4.35, where four sail sections are compared against the initial un-deformed section shape. In the higher part of the sail displacements are much higher for CST elements where the shell answer predicts a higher stretch. In the lower third of the sail the behaviour predicted by the shell model is less stiff. This arises especially on the sail's trailing edge, where the angle of the fabric looks much more "opened" compared to the membrane model.

Instabilities arising on the free sides of the spinnaker for the membrane calculations can be identified in Figure 4.36. These correspond to a locally ill posed problem for the membrane model (see [4], Par 5.3). In this region, the membrane deformation itself is unable to control the displacement field induced by the loading, and the bending energy must be taken into account in order to adequately solve the problem. The shell model is capable of controlling such deformation energy, since it includes the bending stiffness. However, due to the very limited thickness, the shell response still reflects the instabilities, albeit in a smoother form.

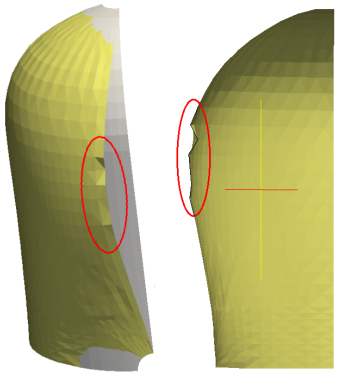

Figure 4.36: Instability arising for the membrane problem on the sail's free side

4.3.2 Deformation of a flat canopy: Experimental comparison (constant and fluid pressure load)

The experiments reported in [8] and used in chapter 3, section 3.3.3 for the validation of fluid dynamics calculations will be used here from a structural perspective. The initially flat fabric used in the experiments will be loaded with constant load, and the results will be discussed and compared with respect to the experimental-measured deformed shape. Cable boundary condition is applied to 16 points on the border of the canopy, all the cables are fixed on a point placed in the middle of the canopy, and have length equal to the initial diameter of the canopy.

An initially flat physical membrane presents a very low initial bending stiffness. The surface is in fact developable; this means that there are configurations for which the membrane deformation energy is zero. For all such configurations, called "pure bending displacements", the deformation is controlled by the bending stiffness. Because of the very limited thickness of the physical membrane the bending stiffness is very low, thus the structure is likely to produce large displacements. Because of the particular boundary conditions and the out-of-plane loading, the flat developable undeformed surface will tend to form a curved non-developable surface. This will be achieved through the formation of large folds, as it is experimentally shown in Figure 3.19.

Table 4.9: Geometrical specification for the flat mesh analysis.

$D_0\ [m]$	$t\ [mm]$	$E\ [N/mm^2]$	ν	$\rho\ [Kg/mm^3]$	c_1	c_2
0.305	0.05	188	0.4	1.1510^{-6}	0.05	22.06

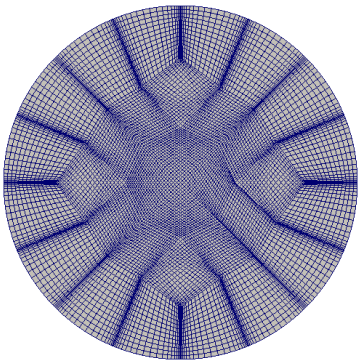

Figure 4.37: Flat geometry mesh

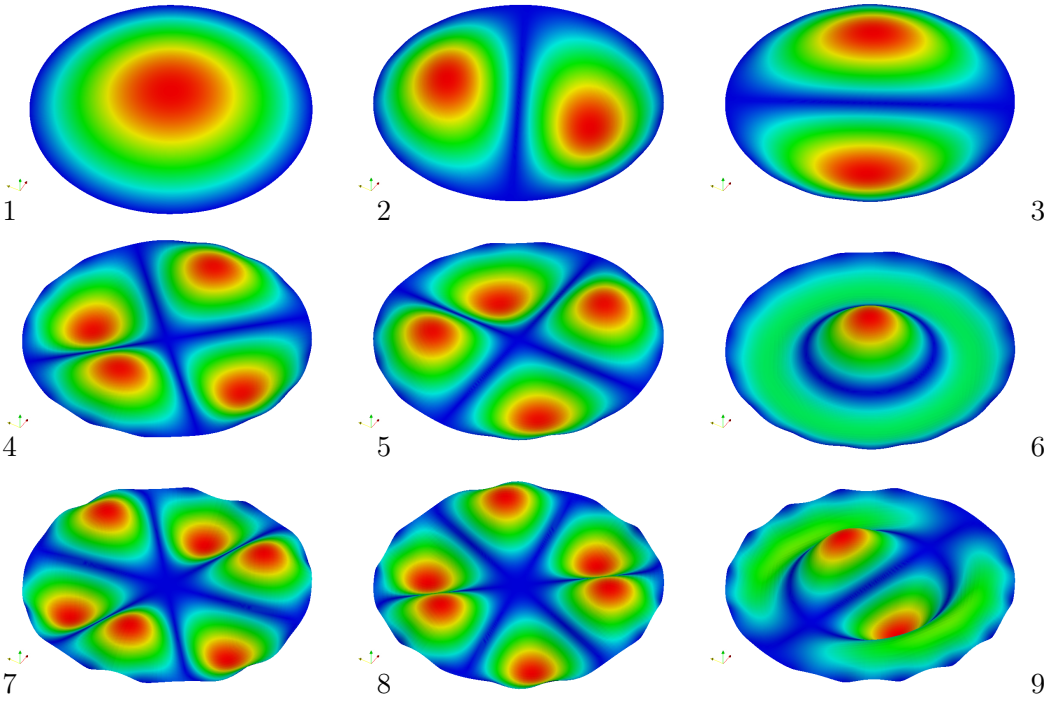

Figure 4.38: First nine eigen-values for the initially flat geometry

The mesh in Figure 4.37 respects the initial geometry used in the experiments, as in able 4.9. The mesh has finer regions in correspondence of the cable attachments, where the formation of large folds is expected.

When inspecting the eigen-vectors reported in Figure 4.38, these configurations are those typical for a circular membrane. Oscillations on the cable constrained side appear only for higher modes, and their relative magnitude is small compared to the other deformation components. This is true in a linear framework: during its deformation the structure acquires geometrical stiffness, thus slightly changes its characteristics in terms of eigen-modes. When this happens, the structure deforms and the folds are generated. As for a buckling related

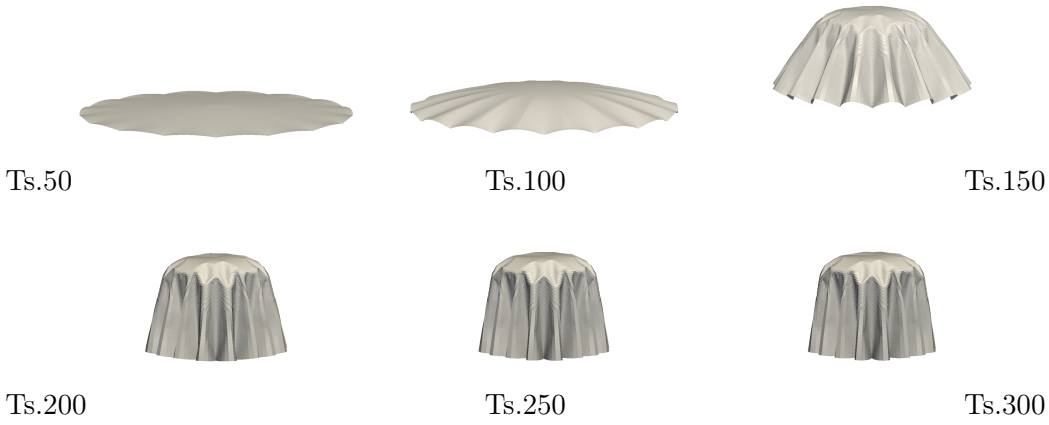

Figure 4.39: Deformation path for the fabric with constant (not following) applied load

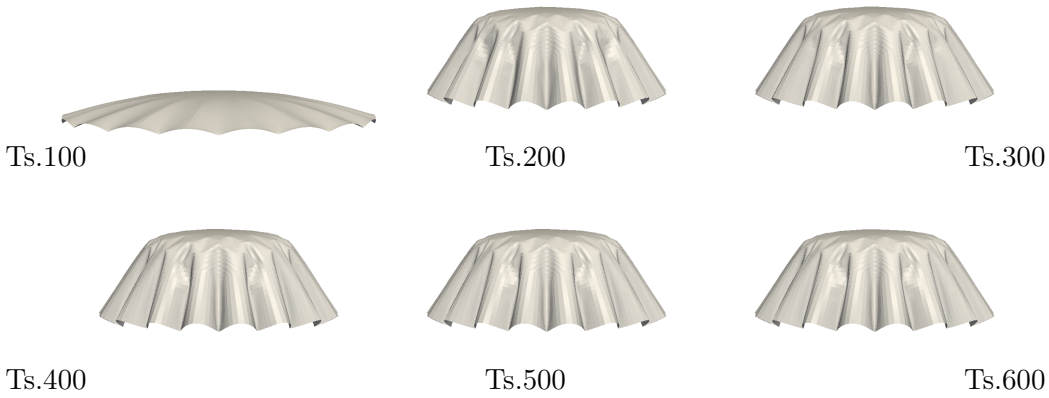

Figure 4.40: deformation path for the fabric with following load

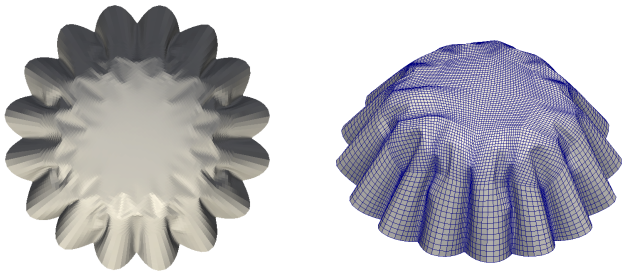

Figure 4.41: top view and side view with mesh

phenomenon, the formation of such wrinkles accelerates the evolution of the structure to a new and configuration, where the folds are even more pronounced.

In a first analysis the load direction is left unaltered during the time path as if it was a weight. As expected large displacements arises and large folds are generated, see Figure 4.39. Some problems are encountered, due to the lack of a self-contact calculation routine.

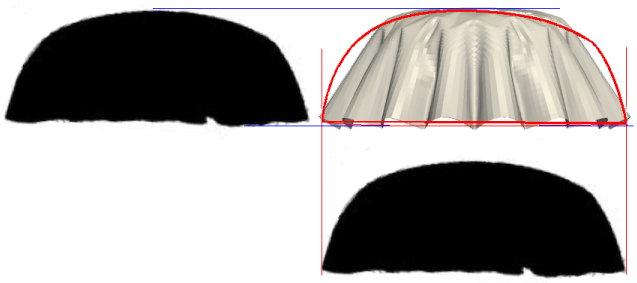

Figure 4.42: Comparison of the deformed shape obtained with constant following load superposed with the experimental measured shape [9]

In the last part of the deformation path in fact the folds start to interfere, thus non-physical configurations are encountered. This problem and its major effects on the solution will be detailed in chapter 5, section 5.2.7. Here this problem disappears when applying a following load. The deformed geometry being brought on a much more wider configuration, folds generate but do not interfere (see Figure 4.41). Such shape is compared with the experimental shape in Figure 4.42. From this comparison it appears that global proportions are respected, even if the constant pressure loaded structure shows very straight sides compared with the experimental shape, the sides of which have higher curvature. This difference is probably due to the pressure loading which is in this case constant. Observing Figure 3.23 however, the fluid pressure map has its maxima on the structure's sides. This is likely to modify the deformed shape of the device, getting the result closer to the experimental measured shape.

4.3.3 Wrinkling prediction for a flat membrane in shear

Wrinkle evaluations were proposed by [92, 112, 5]. Here it has been followed the work of [5], which analysed an initially planar rectangular membrane with prescribed shearing displacements on one side, as shown in Figure 4.43. The membrane was made of a thin film of Kapton®, the physical quantities of which are reported on in Table 4.10. The aspect ratio of this particular Kapton® membrane ($t/L = 1.9510^{-4}$) lies in the same range as the material used for downwind sail construction.

In this configuration the membrane is in a shear-dominated mode, hence it is likely to produce several wrinkles oriented at 45 °. It was reported that, although the imposed displacement was increased gradually and monotonically, changes in the number of wrinkles occur suddenly, as the effect of an instability originating near the edge. The number, the amplitude and the wave-length of such oscillations is dependent upon the material and the magnitude of the prescribed displacement. The deformed central cross-section of the mem-

brane is reported in Figure 4.44. A discrepancy should however be underlined: the declared length of the membrane is 380 mm, whereas the graph maximum x-value in Figure 4.44 is only ≈ 360 mm. The symmetry properties expected from the loading considered are not entirely obtained in the response. In particular, a rather surprising irregularity in the amplitude of the oscillations is observed near the center for $x > 180$ mm. This might be due to a slip in the displacement prescription, as is clearly noticeable in Figure 4.43 (right-hand side of top edge).

An initial *out-of-plane* displacement map – defined as a linear combination of eigenmodes – was applied on the undeformed structure for the numerical results published in [5]. However, the influence of this map was negligible in the final result, and the need for this initialization procedure is probably due to the use of the static solver implemented in the Abaqus commercial code.

The experiment was reproduced with MITC4 shell elements. Lateral sides were left free, whereas all degrees of freedom of the bottom edge were fixed, and displacements were prescribed on the top edge. No initial *out-of-plane* mapping or pre-stress was needed. The *pseudo*-dynamic algorithm was able to capture the final deformed shape. However, of course since no initial imperfections were applied, *out-of-plane* oscillations only appear when the top edge displacements reach a given finite value.

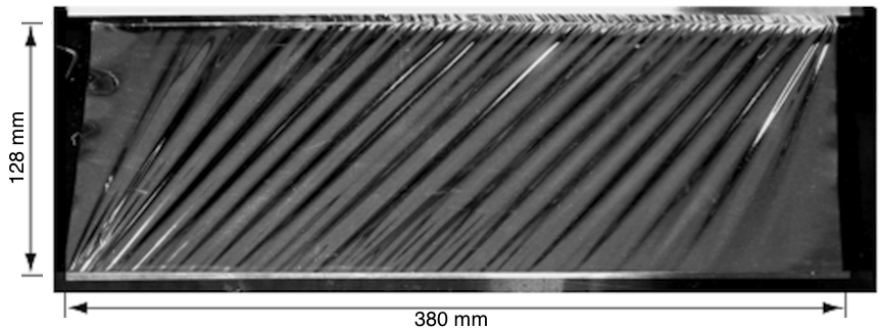

Figure 4.43: Experimental setting for the membrane in shear

Table 4.10: Kapton® physical quantities reported by [5]

t	E	ν	L	H
[mm]	[N/mm^2]	[-]	[mm]	[mm]
0.025	3500	0.31	380	128

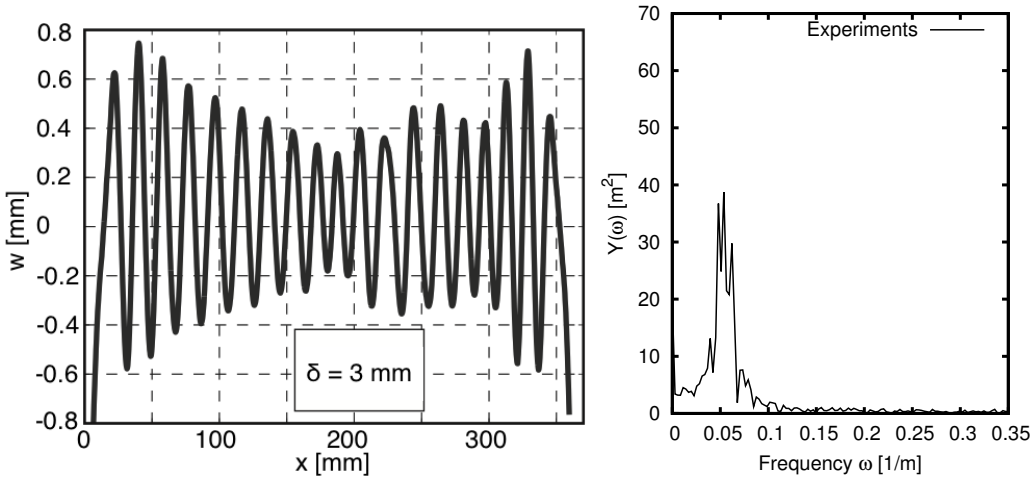

Figure 4.44: *left*: experimentally measured deformed section with 3mm imposed displacement. Reproduced from Figure 4 in [5]. *Right*: FFT analysis of the experimental results

Mesh sensitivity for the validation test case

Mesh sensitivity was explored for seven meshes, the characteristics of which are reported in Table 4.11. Figure 4.45 *left* shows the mesh sensitivity in terms of number n_w and the proposed wrinkling index I_w defined in Section 4.1.10. Figure 4.45 *right* reports the mesh sensitivity in terms of the amplitude of wrinkles H and the standard deviation σ, defined with respect to the undeformed straight configuration of the center cross-section.

Table 4.11: MITC4 results for series of meshes considered

Subdivisions	Elements	N. wrinkles	$W_{centre-line}$ [mm]	σ	I_w
65x50	3038	13	0.47	0.250	3.25
105x50	4998	15	0.47	0.362	5.43
160x50	7693	19	0.40	0.232	4.41
210x50	10143	20	0.38	0.178	3.56
420x75	28638	19	0.40	0.136	2.58
420x100	42183	21	0.35	0.155	3.23
630x150	55803	20	0.37	0.140	2.8
880x150	130673	20	0.37	0.140	2.8

A significant mesh sensitivity is experienced. This is not surprising since several elements are needed in order to reproduce every wrinkle, the wave-length of which may be very small,

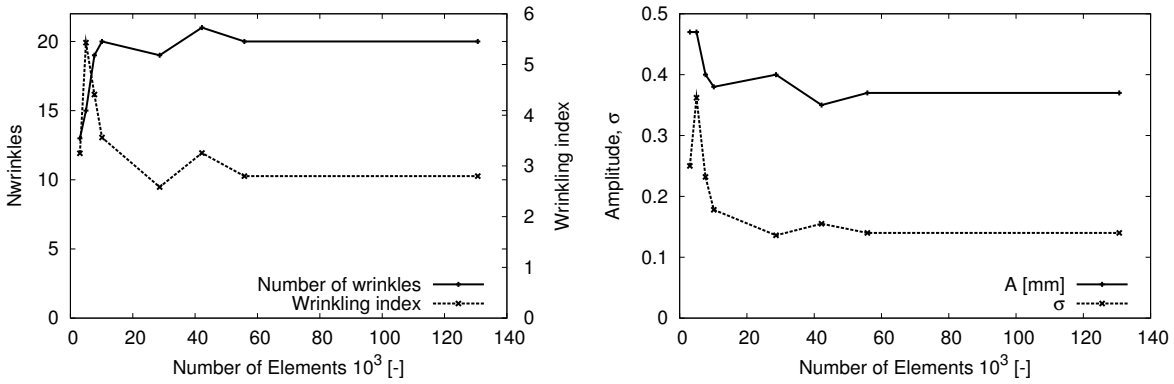

Figure 4.45: *left*: Mesh sensitivity for the number of wrinkles and the wrinkling index I_w; *right* the amplitude and the standard deviation σ

especially along the constrained sides. As a general rule of thumb, the mesh should exceed 20 elements per wrinkle in order to capture the correct structural behaviour. When the mesh is fine enough the results converge to the solution; this is confirmed by the good degree of accuracy achieved in the comparison with the experiments.

Comparison with experimental results

The results discussed here are those obtained with a converged mesh (630x150 elements). The general behaviour is well-captured in terms of wrinkle shape, size and orientation. Fine details are also well-represented, such as the smaller oscillations observed in between two large wrinkles near the top and bottom edges, see Figure 4.43. Compared to the experimental results, however, the present numerical solutions feature a more regular response and the predicted number of wrinkles (20) exceeds the experimental value (19).

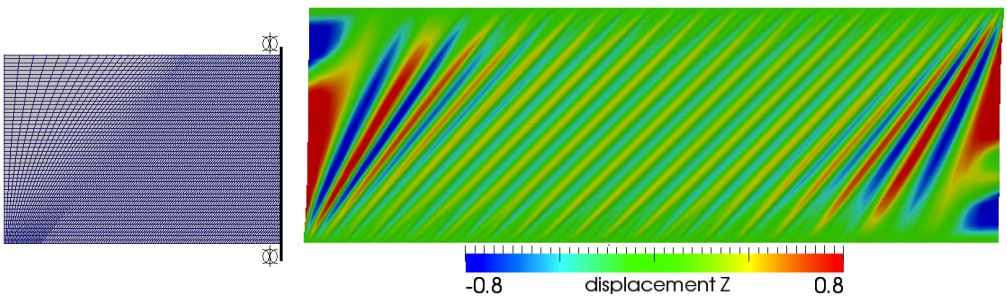

Figure 4.46: *left:* 210x50 els adapted mesh (symmetry). *Right:* deformed shape for 3[mm] displacement

Figure 4.47 compares the experimental and the numerical cross-sections. Since the experimental curve is of non-zero mean, an appropriate shift – of specific value (-7, 0.8) [mm]

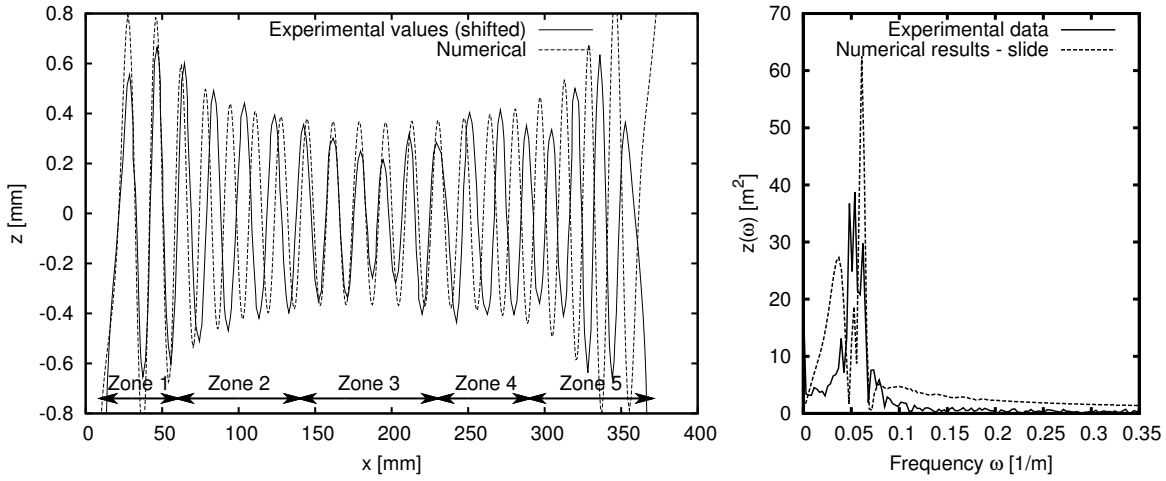

Figure 4.47: Superposing the experimental and the numerical section cut (finer mesh, 630x150) and FFT of the results

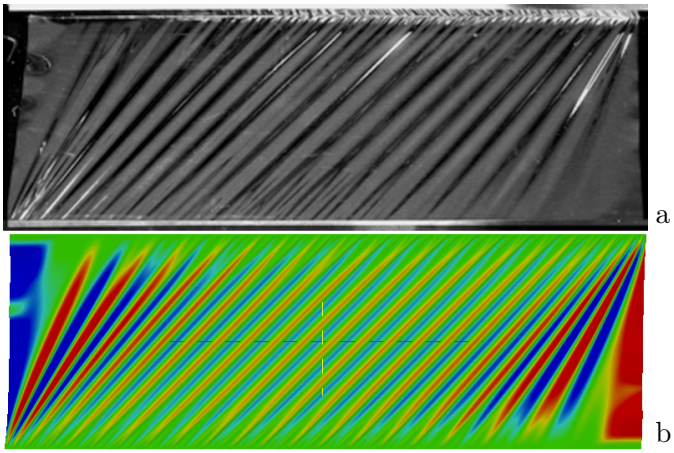

Figure 4.48: Comparison of (a) experimental (b) numerical deformed shapes

– was applied to make the curves comparable.

This comparison shows a good accuracy in reproducing the experimental behaviour. The response is particularly accurate both in terms of amplitude and wave-length. Five zones can be identified, as illustrated in Figure 4.47. In Zone 1 the three "boundary" wrinkles are well-captured. A transition region (Zone 2) is then seen where the amplitude is well-captured, but five wrinkles are found instead of four. In the centre of the membrane (Zone 3), the solution is accurate in terms of wave-length. The amplitude is less accurate, but this could be due to possible imperfections in the experimental setup, as already mentioned, or in the material – constitutive and geometric – properties.

Zones 4 and 5 display anti-symmetry – with respect to Zones 2 and 1, respectively – in the numerical solution, compared to which a phase inversion is seen in the experimental curve

for $x > 250\,\text{mm}$. This further justifies investigating material and boundary conditions effects, as follows.

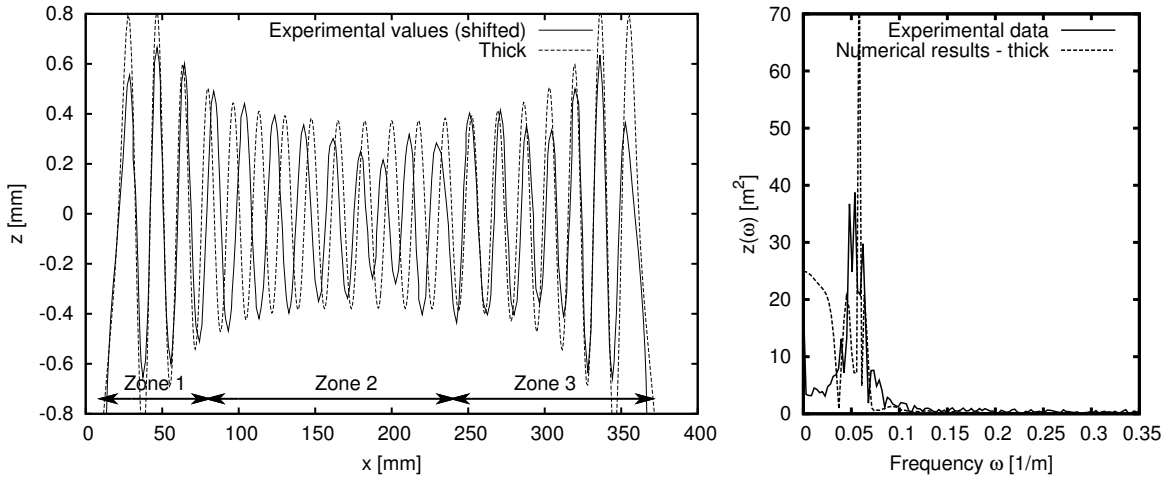

Figure 4.49: Effect of the thickness ($t = 110\%$) on the deformed shape of the physical membrane

The effect of the material was then investigated with a new analysis, where the fabric thickness was increased by 10%. The results are displayed in Figure 4.49. A good representation of the experimental behaviour can be identified in the two lateral parts – see new Zones 1 and 3 in this Figure – whereas the numerical wave-length of the wrinkles is still higher – although lower than for the thinner membrane – in the central Zone 2. This is also confirmed by the comparison of the Fourier transforms of the experimental and numerical solutions in Figures 4.47 and 4.49 which shows a much narrower frequency content in the numerical solutions, with a peak closer to the center of the experimental frequency range in the thick case. The influence of the boundary condition was then analysed by prescribing a lateral displacement varying linearly from the value δ at the top-left corner to zero at the top-right corner, in order to model a slip in the boundary condition. The resulting wrinkles are shown in Figure 4.50, where we observe a less regular behaviour in the numerical solution starting around the middle of the cross-section, as for the experimental curve, although the behaviour near the right side is less accurate. Note also in Figure 4.50 that the Fourier transform of the numerical and experimental solutions are now very similar.

Finally, it appears that our numerical procedure adequately captures the experimental behaviour of [5], taking into account the various experimental uncertainties.

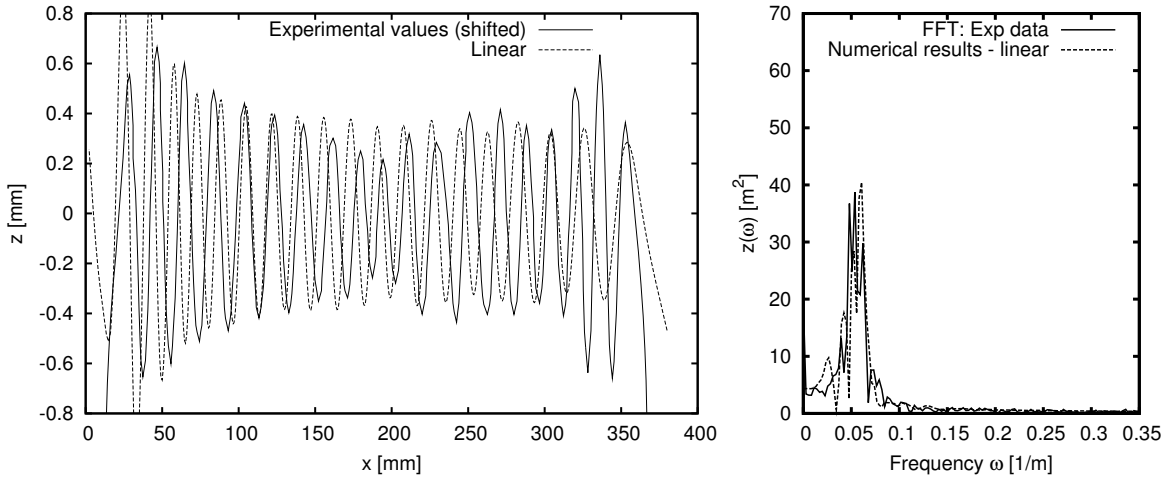

Figure 4.50: Effect of the linear constraint on the deformed shape of the physical membrane

Comparison with analytical estimates and numerical results

In [5] some analytical derivations are performed for the case considered, under various simplifying assumptions. In particular, the wrinkles half wave-length and half amplitude are then respectively estimated as

$$\lambda_{\text{an}} = \sqrt{\frac{\pi H t}{3(1-\nu^2)\gamma}}, \quad A_{\text{an}} = \sqrt{\frac{2Ht}{\pi} \cdot \sqrt{\frac{(1-\nu)\gamma}{3(1+\nu)}}}, \tag{4.194}$$

with H and L the height and width of the sheet, $\gamma = \delta/H$ the shear deformation. Substituting the above-given numerical values we find $\lambda_{\text{an}} = 14.4\,\text{mm}$ and $A_{\text{an}} = 0.36\,\text{mm}$. Results of the numerical solution are: $\lambda \approx 16\,\text{mm}$ and $A \approx 0.35\,\text{mm}$ when measuring near the center, which is in good agreement with the analytical values.

Numerical experiments were also performed in [5] using Abaqus. Three non-adapted meshes were tested, using so-called S4R5 shell elements. The first mesh element size was set slightly smaller than the wrinkle half-wavelength. The finer meshes were obtained by increasing the number of elements by approximately a factor of two or four. Figure 4.51 visualizes the resulting deformed solution, and it should be noticed in this Figure a peculiarity in the prescribed boundary conditions. Namely, that only translations along the x-direction were allowed on the two lateral sides. It is argued in [5] that these additional constraints may induce two extra oscillations, which are then subtracted from the counted number of wrinkles. In order to recall the existence of these extra oscillations, the values of [5] are explicitly list as "$n+2$" in Table 4.12. The converged values here reported – recall Table 4.11 – are intermediate between the converged values of Table 4.12 with and without taking into

account the additional two wrinkles.

The smaller oscillations observed in the experimental results near the top and bottom edges are much more adequately captured in our numerical solutions than in the Abaqus numerical results given in [5].

Table 4.12: Abaqus results (taken from [5], Table 4)

N. elements	$N_{wrinkles}$ Abaqus
3960	16+2
6950	19+2
13134	19+2

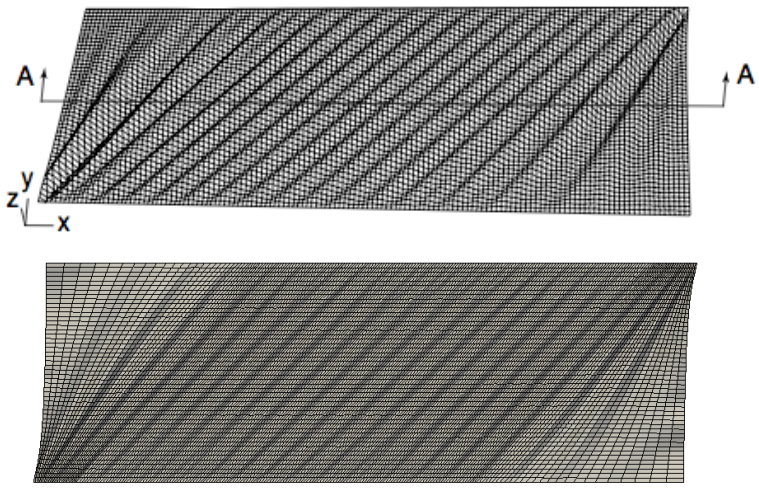

Figure 4.51: *Top:* Perspective view of the wrinkle pattern for the Abaqus result (taken from [5], Fig.6); *bottom:* wrinkle pattern for the MITC4 result; real displacements magnified by factor 2.5

4.3.4 Mesh, shape and material sensitivity in the wrinkling representation: evaluation for sail-type structure

Mesh sensitivity

A parametric grid sensitivity study was undertaken in order to assess the adequate grid fineness for accurately capturing the wrinkles. The purpose was also to verify whether the converging behaviour of the finite element solution is affected by the wrinkling development.

Two geometries and 14 meshes per geometry have been adopted for this mesh sensitivity analysis. In the first geometry, a Gennaker-like structure is analysed, and the geometry is described using a spherical sector of radius $R = 1000[mm]$, and of height and width cor-

responding to angles $\pi/2$ and $2\pi/5$, respectively. For symmetry reasons, it is considered only half of this geometry along the width direction; this reduced geometry is displayed in Figure 4.53. The second shape analysed has the same spherical part with a cylinder added underneath, in order to produce a spinnaker-like structure as displayed in Figure 4.57. The height of this cylinder is equal to the radius of the spherical component. In all the meshes the element size distribution was kept as homogeneous as possible. However, the meshes were designed with finer discretization in regions close to the corners, where wrinkling generation is expected. The characteristics of these meshes are reported in the Tables 4.13 and 4.14. For all the cases presented here, the nodes lying on the corners of the structure were simply supported (translations equal to zero), and a symmetry boundary condition was imposed on the whole central edge of the sail.

Table 4.13: Meshes specifications for the Gennaker mesh sensitivity analysis. Ne is the number of elements, Np the number of nodes and EpS the number of element per horizontal section

Mesh	m_2	m_3	m_5	m_{10}	m_{15}	m_{20}	m_{25}	m_{30}
Ne	49	130	406	1761	4066	7321	11526	16681
Np	67	158	405	1859	4214	7519	11774	16979
EpS	4	7	13	28	43	58	73	88
Mesh	m_{35}	m_{40}	m_{45}	m_{50}	m_{55}	m_{60}		
Ne	22786	29841	37846	46801	56706	67561		
Np	23134	30239	38294	47299	57254	68159		
EpS	103	118	133	148	163	178		

Two specific cross-sections were selected for their interest regarding the wrinkling pattern. First, as shown in Figure 4.52 the *Head* section is characterized by intersecting the deformed shape with a plane, the normal vector of which is tangent to the surface and directed along the bisector line, while the height of the cross-section is defined such that approximately half of the wrinkle length is intersected. The *Corner* cross-section is defined by intersecting the structure with a plane passing through a point Q located on the bottom edge at the crossing with the bisector line, see Figure 4.52. The plane is normal to a vector, the horizontal projection of which is tangent to the sail at the point Q, but vertically elevated at 45° upwards.

Figure 4.54 *left* shows the results in terms of displacement of selected points and Figure 4.54 *right* shows the number of wrinkles for the Gennaker geometry. Acceptable results

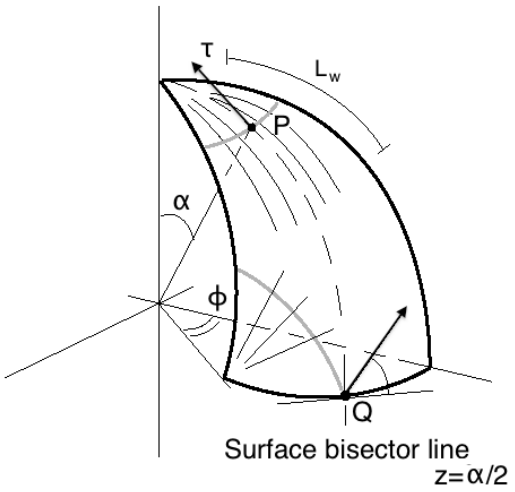

Figure 4.52: Definition used for identifying the *Head* and the *Corner* sections

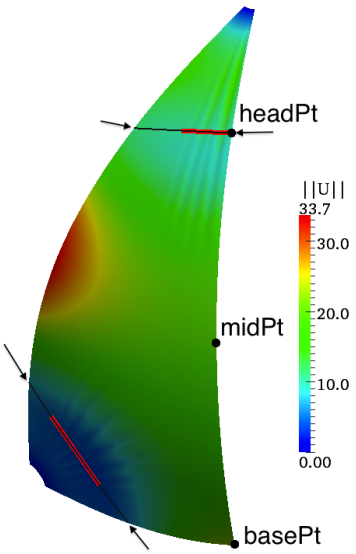

Figure 4.53: Gennaker geometry with *Head* and *Corner* cross-sections, with parts represented in Figures 4.55 *right* and 4.56 *right* highlighted in red

for the prediction of local wrinkling are obtained starting from the mesh m_{45}, which has about 20 elements per wrinkle in the *Head* section. This result is in line with that obtained in Section 4.3.3. Regarding the number of wrinkles captured with different meshes, it is interesting to observe the general behaviour of the curves, where discontinuities are observed when the mesh considered is able to capture new wrinkles of smaller dimensions. This is better seen in Figures 4.55-4.56, where deformed cross-sections are displayed for meshes of increasing accuracy. Note in particular in Figure 4.56 *right* how two small additional wrinkles are captured in the finest meshes, whereas the overall behaviour is well represented for coarser meshes.

Similar conclusions can be drawn in the case of the Spinnaker geometry, see Figure 4.58–

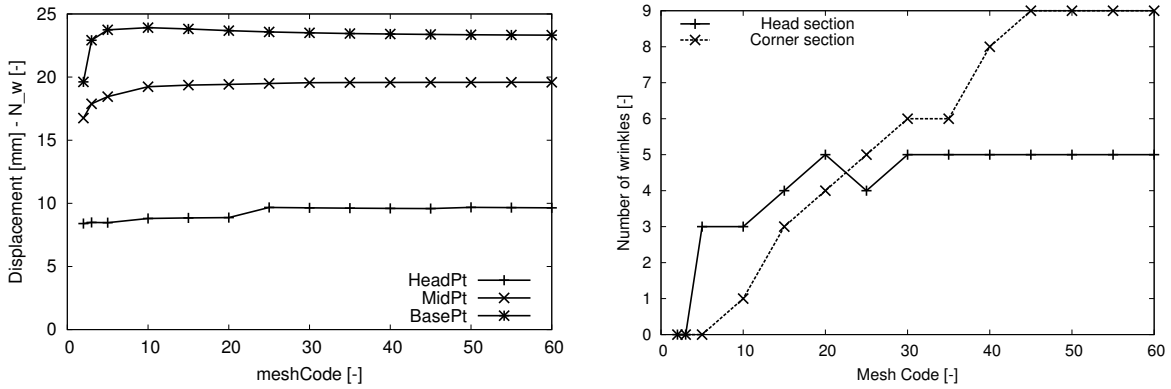

Figure 4.54: Gennaker shape – *left*: Mesh impact on point-wise displacements. *right*: Mesh sensitivity in the number of wrinkles

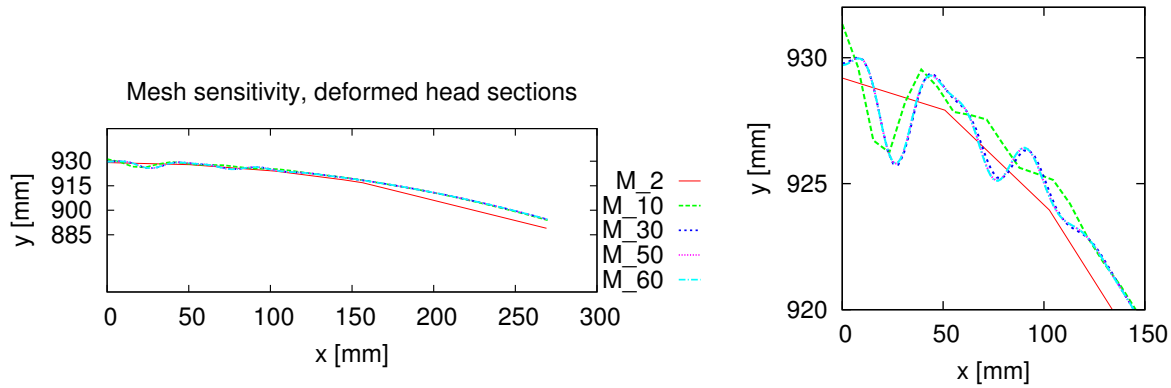

Figure 4.55: Gennaker shape mesh sensitivity – *Head* sections. *left*: Global view and *right*: Zoom on the wrinkled region

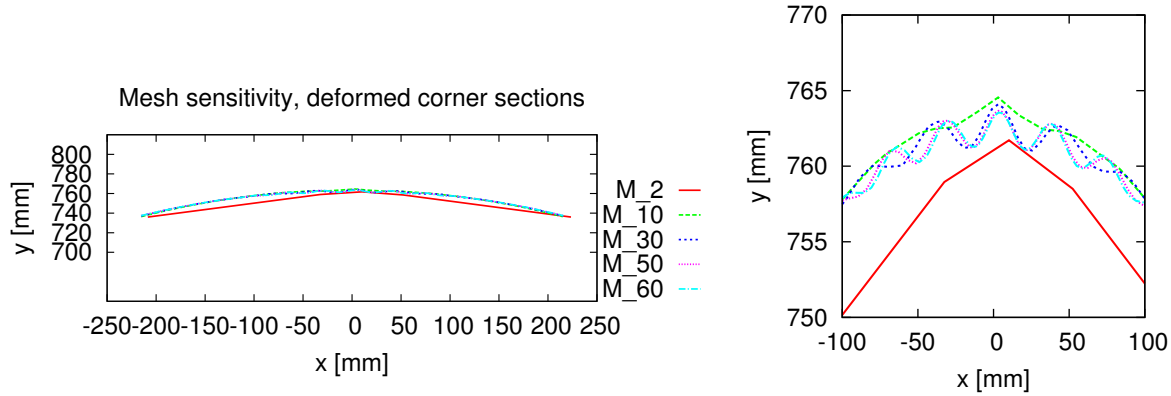

Figure 4.56: Gennaker shape mesh sensitivity – *Corner* sections. *left*: Global view and *right*: Zoom on the wrinkled region

4.60. In this case the overall displacements obtained are larger, since the sail is constrained at points farther away from each other, and developable surfaces – referring to the cylindrical part, here – tend to undergo larger motions. Regarding the wrinkling representation, it can

Table 4.14: Mesh specification for the Spinnaker mesh sensitivity analysis. Ne is the number of elements, Np the number of nodes and EpS the number of element per horizontal section

Mesh	m_3	m_5	m_{10}	m_{15}	m_{20}	m_{25}	m_{30}
Ne	24	104	513	1024	22203	3552	5133
Np	36	128	565	1283	2330	3687	5250
EpS	4	8	18	28	38	48	58
Mesh	m_{35}	m_{40}	m_{45}	m_{50}	m_{55}	m_{60}	
Ne	7072	9477	12848	16023	20088	23423	
Np	7262	9634	13105	16310	20410	23770	
EpS	68	78	88	98	108	118	

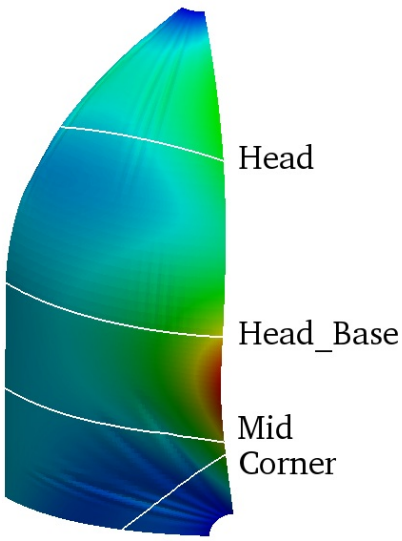

Figure 4.57: Spinnaker geometry with the trace of the sections used for the evaluations

be observed an adequate convergence with the sequence of meshes, except specifically in the *Head* cross-section. Although the curves in Figure 4.58 do not look well converged, some limited oscillations of the wrinkling count are due to the definition of the wrinkles recognition algorithm criterion, since in some cases the thresholds are reached or missed by a very small margin, while clear trends can be identified regarding the – hence approximate – number of wrinkles. In fact, this is the case for all sections except the *Head* section, which displays a high variability in the number of wrinkles. This is due to the progressive resolution of small amplitude wrinkles as the mesh becomes finer, see in particular Figure 4.60.

Figure 4.61 displays the details of the deformed pattern by plotting the distance to the

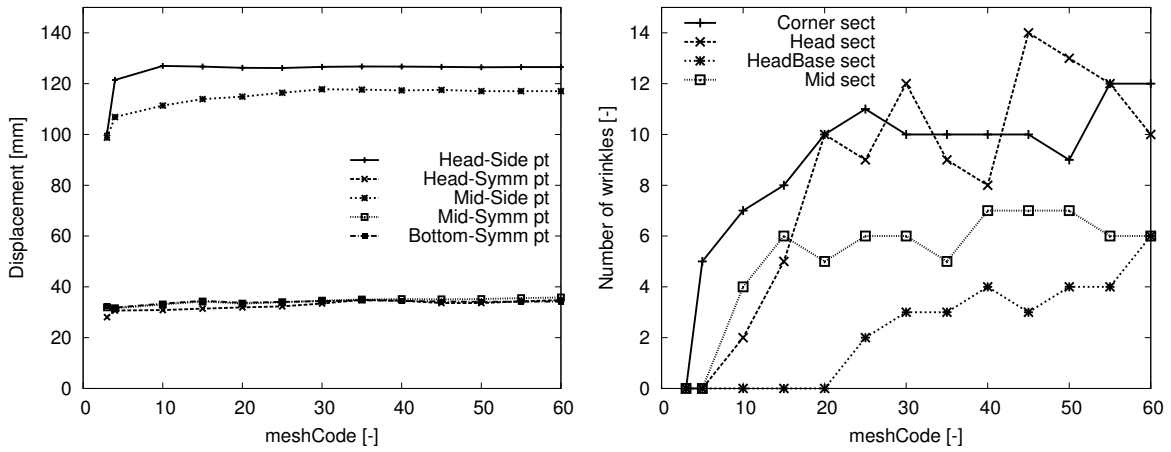

Figure 4.58: Spinnaker shape – *left*: Mesh impact on point-wise displacements. *right*: Mesh sensitivity in the number of wrinkles

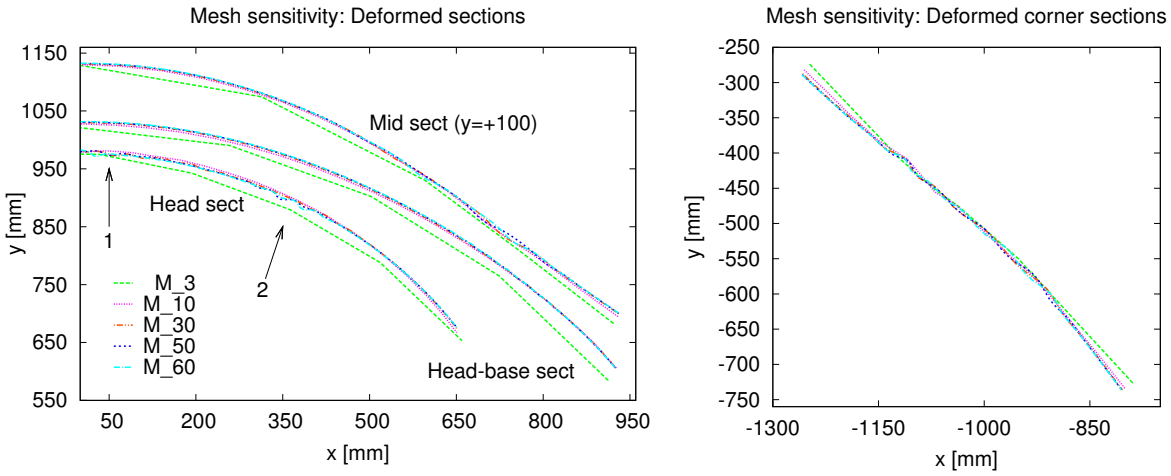

Figure 4.59: Spinnaker shape mesh sensitivity – *left*: *Head*, *Head-base* and *Mid* sections and *right*: *Corner* sections

regression curve against the arc-length coordinate, for two of the finest meshes already considered. The numerical solutions consistently identify two main groups of wrinkles, albeit that within each group the individual wrinkles are insufficiently resolved, with just a few nodes per wrinkle even for the finest mesh. This indicates a rather low physical stability – locally – in this configuration due to the shape considered. Moreover, as the wrinkling wavelength is consistently estimated with the three meshes, it can be conjectured that increasing the mesh by a factor 3–5 across the wrinkles would produce an accurate prediction of the phenomenon. Of course, refining the mesh uniformly and in all directions by such a factor would lead to inordinately expensive computations, hence the mesh adaptation should be performed locally and in a non-isotropic manner, which is out of the scope of our analysis. This phenomenon

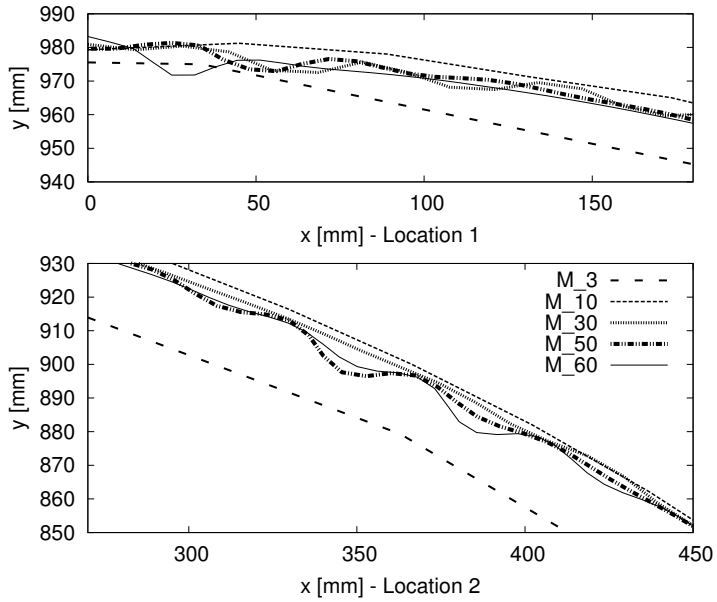

Figure 4.60: Spinnaker shape mesh sensitivity – Zoom on the wrinkles of the *Head* section, as specified by the arrows in Figure 4.59. *Top:* Region near the symmetry centerline. *Bottom:* Region near the half-side of the structure

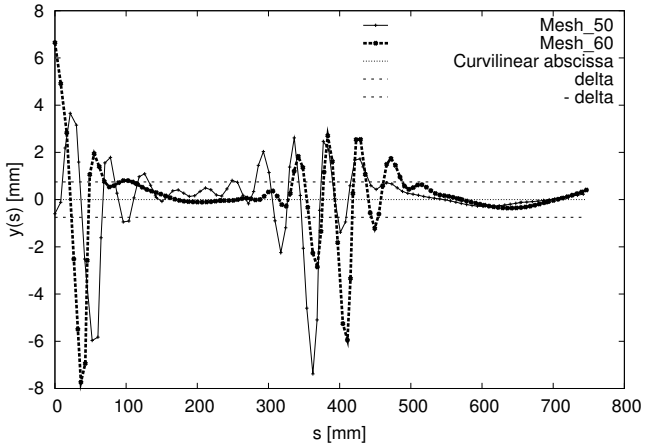

Figure 4.61: Spinnaker shape with $h/R = 1$: *Head* cross-section in arc-length representation for 2 fine meshes

is even more pronounced for Spinnaker shapes with a higher cylindrical body, as exemplified in Figure 4.62. In this case, some rather deep and rapidly oscillating wrinkles appear around the middle of the section, and here clearly much more refined meshes would be required to resolve these features, probably also with self-contact analysis involved.

Finally the conclusion that can be drawn is that in both the cases of the Gennaker and the Spinnaker, the mesh sensitivity analysis indicate that the wrinkling is a higher-order

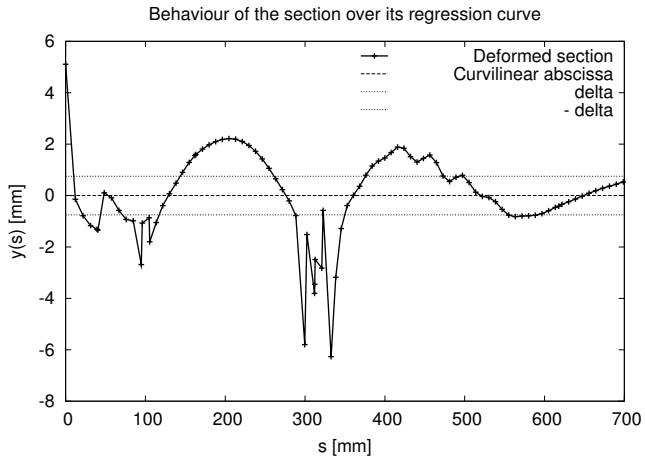

Figure 4.62: Spinnaker shape with $h/R = 1.5$: *Head* cross-section in arc-length representation for computational mesh

phenomenon, hence a relatively coarse mesh is able to represent the general behaviour of the sail, whereas a detailed wrinkling representation requires at least 20 elements per wrinkle.

Influence of material properties variations

A set of tests was carried out using the Gennaker geometry and nine different combinations of material properties, all of which are realistic for sail-type materials. The parametric changes concerned the Young modulus and the thickness. Starting with an initial value, both Young's modulus and thickness parameters were multiplied and divided by a factor two, thus defining the test grid reported in Table 4.15. Based on the results of the mesh sensitivity analysis, it was then decided to use the mesh referenced as 45 for the following evaluations, since this mesh provides good convergence properties of the solution, see Figures 4.54.

Table 4.15: Material test matrix (Analysis code number)

t [mm] / E [N/mm^2]	0.05	0.1	0.2
188	1	2	3
376	4	5	6
752	7	8	9

The same two probe *Head* and *Corner* cross-sections were considered as in Section 4.3.4. The deformed cross-sections are visualized in Figure 4.63, and the corresponding wrinkling indicators are plotted in Figure 4.64. Although no specific law can be identified regarding the

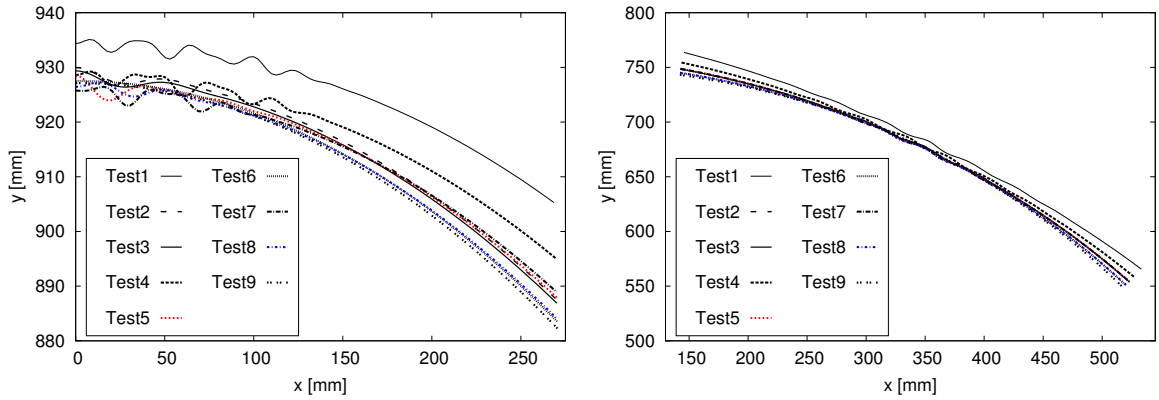

Figure 4.63: Parametric analysis for Gennaker shape – *left*: *Head* and *right*: *Corner* deformed sections for test cases referenced in Table 4.15

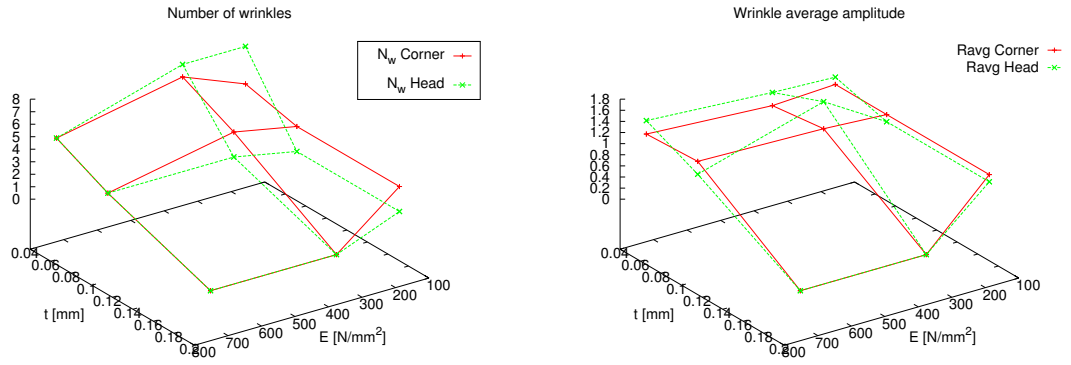

Figure 4.64: Parametric analysis for Gennaker shape – *left*: Number of wrinkles and *right*: Average amplitude of the wrinkles

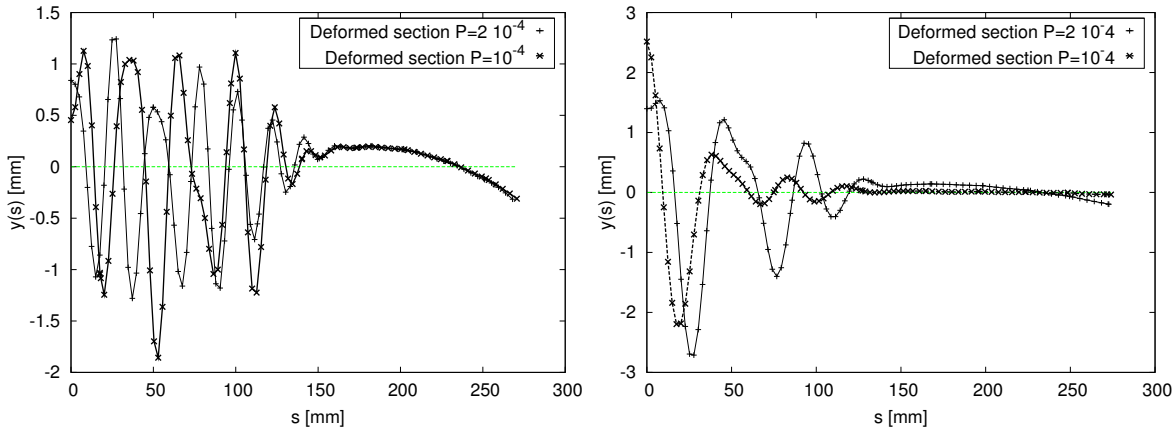

Figure 4.65: Influence of the load on the deformed Gennaker sections: homologous sections (cases 1 and 5) when doubling the load

dependency of these indicators with respect to the parameters considered, this study shows that our procedure can adequately capture the wrinkling behaviour for the whole parametric range of concern. Globally, the amplitude and the number of wrinkles are principally influenced by the thickness parameter, and as expected the thinner the material the larger the number and the amplitude of the wrinkles, for a given pressure load. By contrast, no clear general trend can be observed when varying Young's modulus.

A comparison can then be made when doubling the load. In this case the wrinkling pattern is not strongly affected, and similar features can be identified. This comparison is shown in Figure 4.65 for cases number 1 and 5, representative of the whole spectrum of analysed cases. The deformed sections preserve the same essential features, thus with a stronger dependency upon the material properties rather than the loading magnitude.

Influence of the geometry: Spherical shape with varying width

Table 4.16: Specifications of the analysed geometries

ϕ	$\pi/6$	$\pi/5$	$\pi/4$	$\pi/3$	$\pi/2$
EpS	75	90	111	150	225

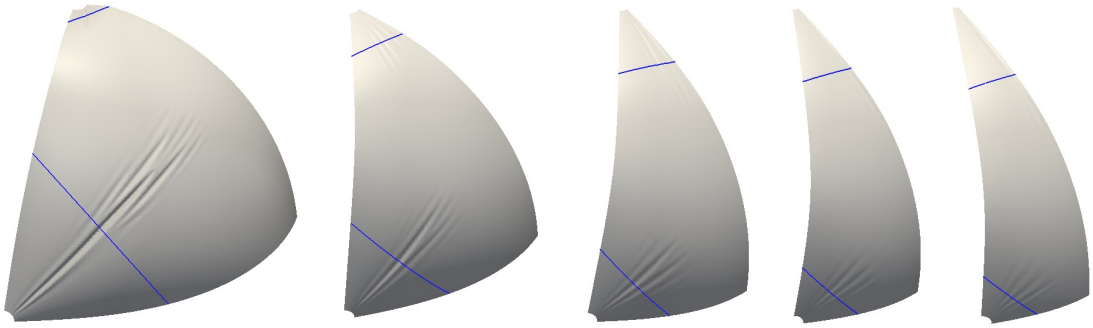

Figure 4.66: Five different analysed geometries (symmetry) with the trace of the sections used for the analysis

Five different spherical geometries were analysed for this investigation of the effect of the shape on wrinkling development. These geometries were derived from that already analysed in Section 4.3.4 by varying the half-width angle ϕ previously defined as $\pi/5$, see Figure 4.66. The mesh density was kept as constant as possible by preserving the ratio of number of element by width angle, which results in the number of elements per horizontal section EpS listed in Table 4.16. All physical quantities remained set as in Case 5 of Table 4.15.

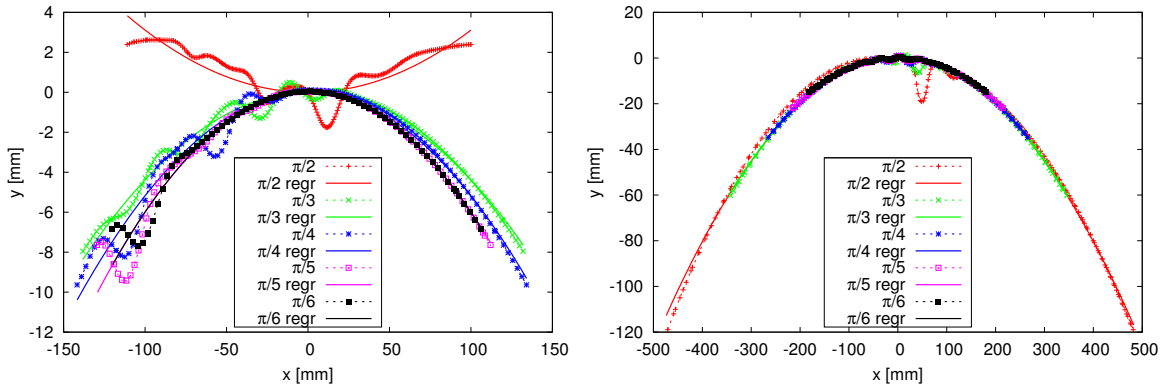

Figure 4.67: Gennaker shape with varying base angle – *left*: *Head* and *right*: *Corner* deformed sections

The resulting computed deformed *Head* cross-sections – as identified in Figure 4.52 – are shown in Figure 4.67, and the corresponding wrinkling indicators are given in Figure 4.68. All cross-sections have roughly similar extents, which is informative as regards the location of the wrinkles. More generally, the shapes of the deformed *Head* and *Corner* cross-sections – wrinkling included – are quite comparable for the various geometries, except for $\phi = \pi/2$ in the *Head* section for which the global curvature is inverted. This behaviour can be explained by observing that the extension of the wrinkles is in this case very small, hence the cross-section is located very near the attachment and the force transmission area associated with the wrinkles tends to pull the sail downwards.

In the *Corner* section, the number of wrinkles as well as the average wrinkle amplitude are largely influenced by the base angle. As expected, the wider the angle – i.e. the larger the structure – the higher the number and amplitude of wrinkles, see also Figure 4.66. Concerning the *Head* sections, the wrinkles present a more stable behaviour, both in terms of number and of amplitude.

Influence of the geometry: Spinnaker-like shapes with varying heights

Spinnaker-like shapes similar to that defined in Section 4.3.4 are considered in this section. Here, the parametric variation regards the height h of the cylindrical part with values $h/R = 1; 1.5; 2$, in addition to the previous case $h/R = 0.5$. All other quantities remain unchanged. Results are reported in terms of the deformed sections already shown in Figure 4.57, where the *Head-base* section is always defined as the junction of the spherical and cylindrical parts, and the so-called *Mid* section is taken at half the height of the cylindrical part.

Increasing the height of the cylindrical body the overall pattern formed by the displacements – namely, along the force application direction in the lower part of the structure, and

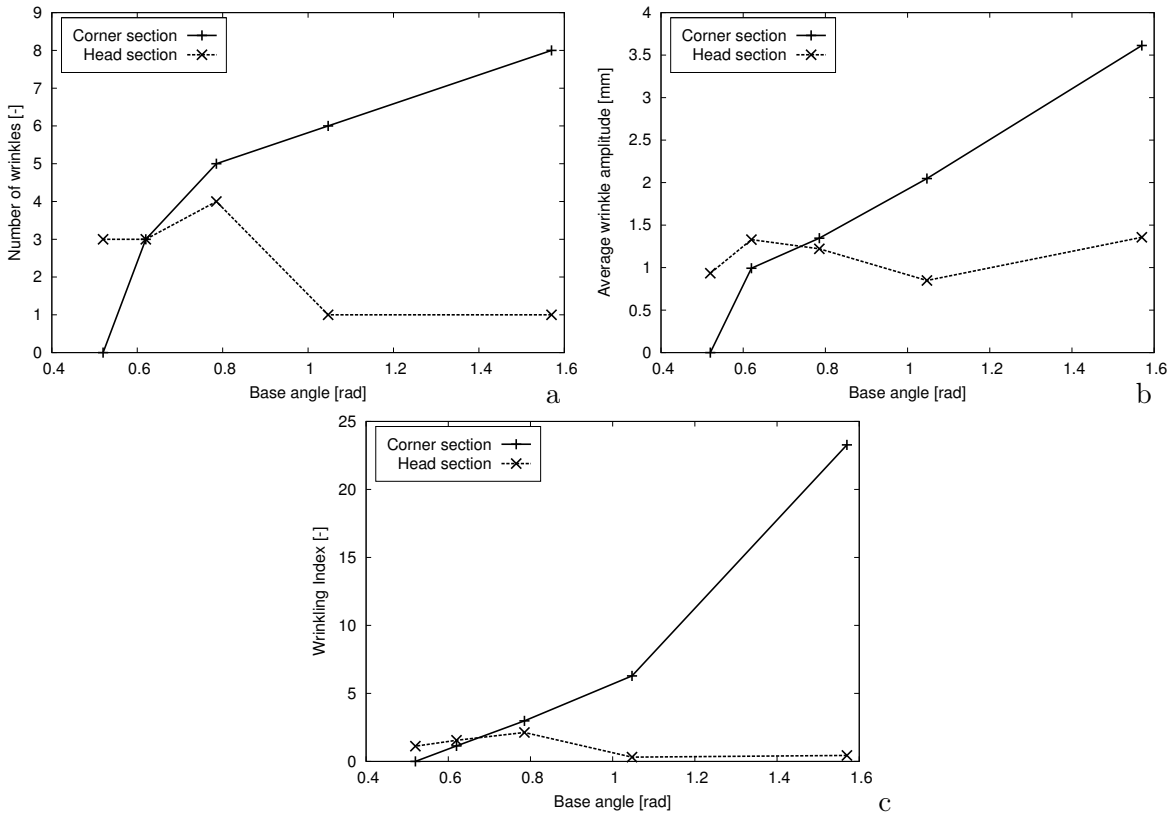

Figure 4.68: Gennaker shape with varying base angle – *a*: Number, *b*: Average amplitude and *c*: Wrinkling index of wrinkles for the *Head* and the *Corner* sections

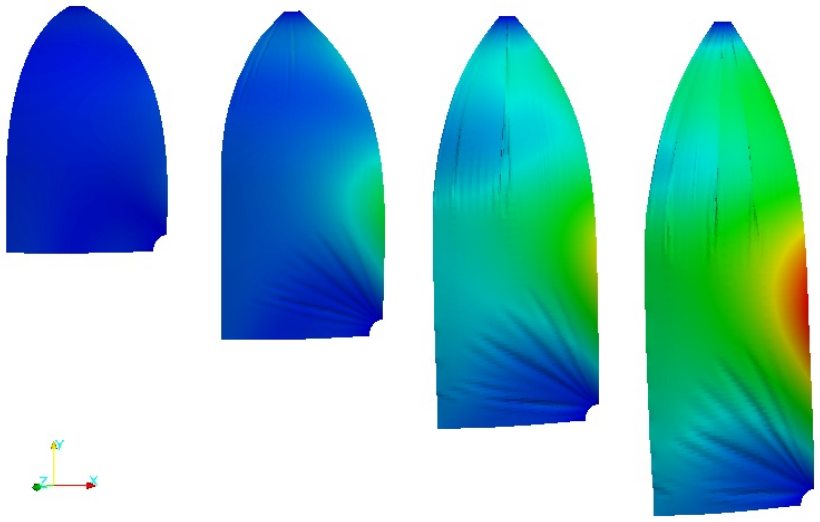

Figure 4.69: Spinnaker-like deformed shapes

in the opposite direction in the higher part – is more and more marked, see Figures 4.69 and 4.70. In addition, in the higher part the spherical shape progressively becomes flatter as the width decreases due to the distance to the lower boundary conditions, while sharp wrinkles

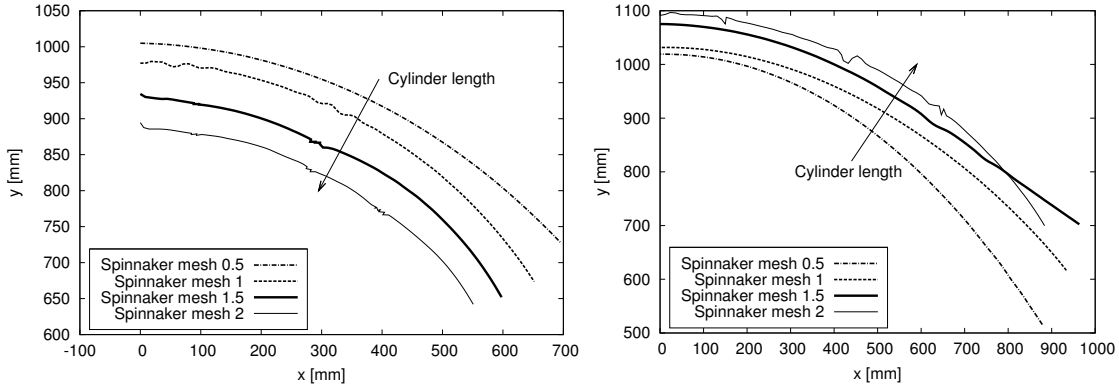

Figure 4.70: Spinnaker shape with varying cylinder length – *left*: *Head* and *right*: *Head-base* deformed sections

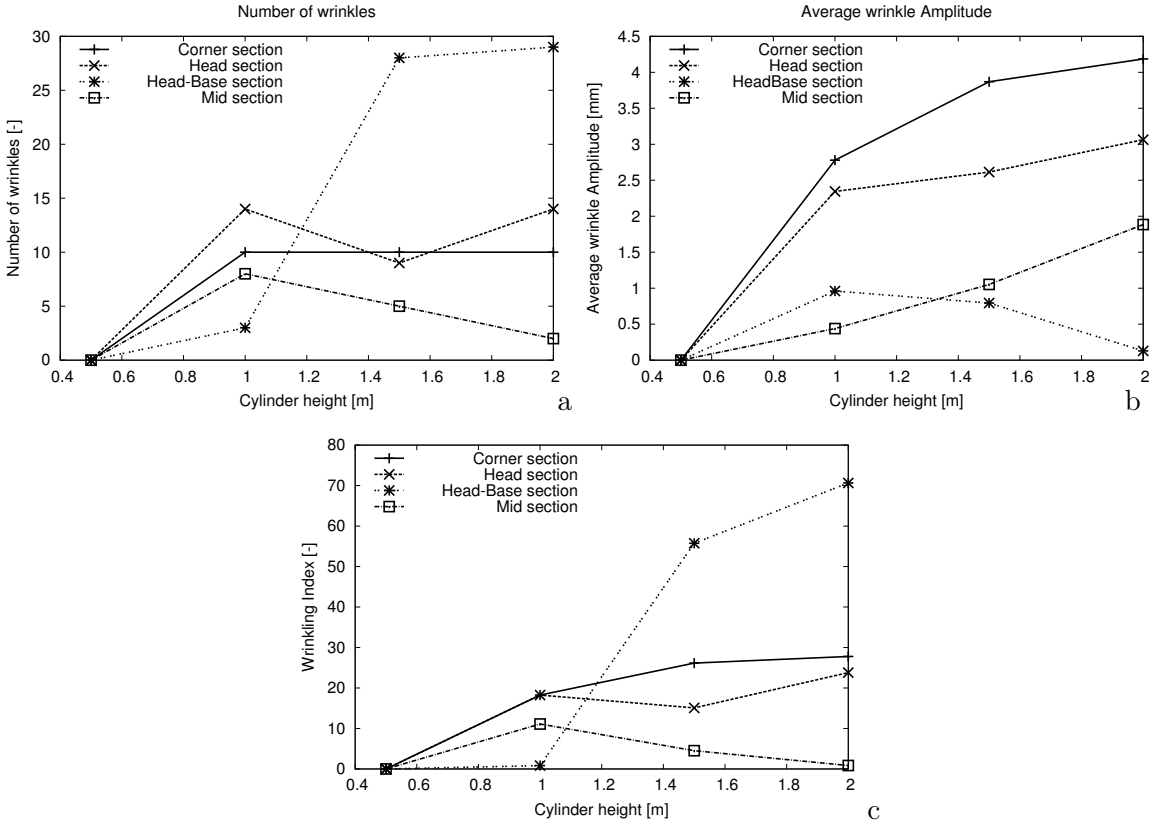

Figure 4.71: Spinnaker shape with varying cylinder length – *a*: Number, *b*: Average amplitude and *c*: Wrinkling Index of the identified wrinkles

appear and contribute to the overall width reduction, indeed. The wrinkling behaviour is analysed in more detail in Figure 4.71 which provides for each shape and section the number of wrinkles and the average wrinkle amplitude, recall Figure 4.22.

Analysing these indicators in conjunction with the deformed shapes visualized in Figure 4.69, the mean amplitude of the wrinkles increases with the height of the cylindrical part.

Only the *Head-Base* section constitutes an exception, which occurs because the wrinkling is so developed in this junction region that some wrinkles tend to roll-over, thus inducing very small amplitude oscillations. This reveals an area of rather low physical stability, in which the wrinkling is insufficiently captured by the mesh. The response in terms of the number of wrinkles – see Figure 4.71 *left* – tends to be more stable. Here also, the number of wrinkles for the *Head-Base* section constitutes an exception, as it rapidly increases then stabilizes around much higher values than in the other sections.

4.4 Summary

In this Chapter the simulation of the sail fabric was approached, and the use of the shell elements was proposed for increasing the accuracy of the calculations, especially for wrinkled configurations. The wrinkling can be observed on the sails and naturally appears in the numerical solution when using shell finite elements. The reasons for choosing the MITC shells were detailed, as for instance this formulation is particularly suitable for the analysis of thin structures.

The prediction performances of the method were demonstrated in several test cases involving sail-type devices and cable boundary conditions. Results obtained with the MITC shells and with the CST membranes were compared, and it was shown that the shell performs better in all cases.

Damping was analysed and discussed in the detail, because this was found to be a valuable strategy to increase the stability of the structural system in a natural way. Wrinkling corresponds in fact to a post-buckled configuration, reaching which requires to overcome some unstable states which might cause the divergence of the solution.

Once the stability of the system is assured, the method offers excellent prediction performances for wrinkled patterns. The method was shown to deal well with sail-type three dimensional configurations.

The calculations presented here give an insight on the prediction performances of the structural method. This will be used with no major modifications in Chapter 5 for the analysis of the fluid structure interactions.

Chapter 5

Fluid Structure Interactions

In the previous chapters the fluid and the structural dynamics have been detailed and examples have been reported of the prediction performances of the presented methods. The scope of this chapter is to discuss how to couple the computations: the fluid load is used to deform the structure, and the computed displacements are imposed to the structural interface in the fluid domain. Fluid Structure Interaction problems can then be seen as a three-field coupled problems: the fluid, the structure and the evolution of the structural interface in the fluid domain.

Several strategies are suitable for this kind of multi-field coupled problems, but two main families can be identified: the monolithic and the partitioned approaches.

In a monolithic approach the whole fluid-structure discrete system is solved in a single computer code; this leads to a very large system of non-linear equations to be solved simultaneously. Although the method is stable, this approach is not often employed because of the difficulties in the numerics and the high computational effort required. Moreover, a monolithic approach leads to computer codes which are generally not modular. Changing parts of the code, such as for example the fluid or the structural solver is a difficult task.

The partitioned approaches are the most common strategy adopted for solving multi fields problems. In such an approach several codes are coupled together, every code is in charge of a particular task and it communicates the relevant data at the interface with the other solvers. Each solver being in charge for one particular field, no requirement is imposed for the solution strategy within each domain: homogeneous data are required only at the interface. This type of approach has then great modularity because it easily allows swapping between existing sophisticated solvers.

Two main families of partitioned method can be then identified: the weak or explicit coupling [79], which allows fast but not necessarily stable solutions, and the strong or implicit

coupling schemes [115], unconditionally stable but computationally more expensive. A review of the methods, as well as the issues causing instability are discussed in Section 5.1.3 and 5.1.5.

Different strategies can be adopted for defining the motion of the structural interface in the fluid domain. Again, two main families can be identified: the first includes the Immersed Boundary [116], level set or ghost cell [93] method; the second is the Arbitrary Lagrangian Eulerian (ALE) method [11]. In the first type of approach the fluid equations are computed on a purely Eulerian grid, and the structure is identified as a boundary condition in terms of velocity or forces to be applied in specific locations, namely at the current position of the structure. This family of methods are particularly suited for large displacements and distortions of the structure. The drawback of such a method is that it is not generally possible to take into account the boundary layer development on the structural interface. In other words, the structure is represented with a *free-slip* condition. This assumption is generally acceptable for fully separated flows (see [81]) but its validity can be argued for flows around streamlined objects.

In the ALE approach the Eulerian grid follows the structural deformation of the structural interface, remains fixed on some computational boundaries of the computational domain and deforms in some arbitrary way within the fluid domain. Arbitrary refers to any mapping able to uniformly transfer the displacements of the structural interface into the domain: the fluid nodes will follow the structural motion on the structural boundary, will remain fixed in the locations far away from the body and the motion will be progressively mapped using a function of the distance from the body. for instance the most popular way to map the motion of the structure consists in using a Laplacian operator. In this particular framework, the fluid equations need to be modified for taking into account the mesh velocity, as it is discussed in Section 5.1.1. The advantage of this method is that the structural interface is represented as a wall, it is then possible to compute the boundary layer development using the normal treatment for walls in fixed domains. The main drawback of the ALE approach regards the quality of the mesh, which can easily be compromised if the structure is subjected to large distortions. Beyond some limits this can seriously compromise the quality of the results, and in the limit case singularities can be generated, thus causing divergence of the solution (see Section 5.2.7).

In this work a strongly coupled partitioned method with Laplacian mesh diffusion was chosen for coupling the Finite Volume fluid approach with the Finite Elements structural

method. The solvers used in this chapter are exactly the same as in the previous ones: OpenFOAM for the fluid part and Modulef (using MITC shell elements) for the structural part were only modified for allowing the communication of the relevant data. The fluid load calculated by OpenFOAM is transferred and opportunely used in the structural domain; the resulting displacements calculated by Modulef are transferred back for modifying the fluid domain. The communications being carried out using the Message Passing Interface (MPI), only minor modifications were made to the codes, primarily regarding the sub-cycling within the same time-step for allowing fixed point iterations.

As in the previous chapters, several test cases are used to show the capabilities of the method. The rigid motion is validated through reference results [12] for a 2D cylinder section oscillating in steady flow (Section 5.2.1). The case of the 2D cavity where an unsteady imposed velocity at the top induces the displacements of the structural interface is analysed in Section 5.2.2. Isolated fluid and structural analysis in a number of configurations are analysed before coupling the calculations. The case is extended to a 3D cavity with deformable bottom in Section 5.2.3. The case analysed in Section 5.2.4 is a channel flow, where a flexible appendage deforms under the effect of the flow. The validation section terminates with the case of a flexible appendix behind a rigid structure 5.2.5. In this case vortex shedding is generated, thus the case is entirely unsteady.

Some limitations of the adopted method are presented in Section 5.2.7 with reference to the case of the parachute canopy analysed from a fluid perspective in Section 3.3.3 and from a structural perspective in Section 4.3.2. In this case the excessive mesh distortions produce singularities in the solution, and cause the divergence of the coupled solver.

5.1 Fluid Structure Interaction theory

5.1.1 Derivation of the ALE equations

Lagrangian and Eulerian

Two domains are normally employed in continuum mechanics: the material domain $R_X \in \mathbb{R}^n$, and the spatial domain R_x. The Lagrangian perspective consists in following the material particles of the continuum during their motion as in figure 5.1. In a computational grid, the grid nodes remain connected to the same material points. The motion of the material points relates the material coordinates X with the spatial coordinates x and it is defined by

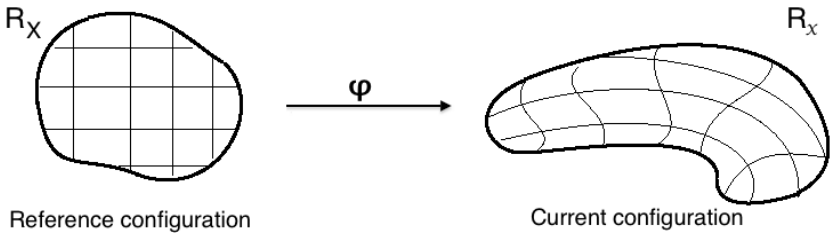

Figure 5.1: Lagrangian representation

a bijective function such that:

$$\begin{aligned} \varphi : R_X \times [t_0, t_{end}[&\rightarrow R_x \times [t_0, t_{end}[\\ (X,t) &\rightarrow \varphi(X,t) = (x,t) \end{aligned} \tag{5.1}$$

The Eulerian description is the most commonly used in fluid mechanics. In this case the computational grid is fixed while the continuum moves and deforms. Variables and functions are then defined in a fixed region of space. The material velocity v at a given mesh node corresponds to the velocity of the material point coincident at the considered time t with the considered node, and it is defined as $v = v(x,t)$. Since the Eulerian formulation dissociates the mesh nodes from the material particles, convective effects appear, as in Equation (12).

Because of the relative motion between the deforming material and the computational grid, Eulerian algorithms allow an easy treatment of complex material motion, but difficulties are found when deforming material interfaces or in presence of mobile boundaries. In this case in fact the calculation domain remains naturally fixed, thus interface tracking [93] or immersed boundary [116] techniques must be adopted.

Arbitrary Lagrangian Eulerian description

In the ALE description of motion, neither the material configuration R_X nor the spatial configuration R_x is taken as the reference. The referential configuration R_χ is used, where reference coordinates χ are introduced to identify the grid points. Three bijective maps are defined in order to transform the coordinate between reference systems. In addition to Equation (5.1), two new transformations are defined:

$$\begin{aligned} \mathbf{\Phi} : R_\chi \times [t_0, t_{end}[&\rightarrow R_x \times [t_0, t_{end}[\\ (\chi,t) &\rightarrow \mathbf{\Phi}(\chi,t) = (x,t) \end{aligned} \tag{5.2}$$

$$\begin{aligned} \mathbf{\Psi}^{-1} : R_X \times [t_0, t_{end}[&\rightarrow R_\chi \times [t_0, t_{end}[\\ (X,t) &\rightarrow \mathbf{\Psi}^{-1}(X,t) = (\chi,t) \end{aligned} \tag{5.3}$$

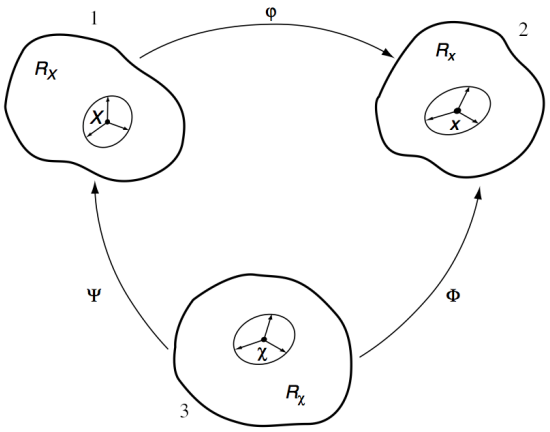

Figure 5.2: Reference domains and reference systems used in the ALE representation. From [11], Figure 4

where it has been presented the inverse of the last transformation for a matter of convenience in the following development.

The relative velocity between the material reference and the mesh is called *convective velocity* $\mathbf{c}$, and it is defined as (see Appendix C.1):

$$\mathbf{c} := \mathbf{v} - \hat{\mathbf{v}} = \frac{\partial x}{\partial \chi} \cdot \mathbf{w} \tag{5.4}$$

where $\mathbf{v}(\mathbf{X}, t) = \partial \mathbf{x}/\partial t|_x$ is the *material* velocity, $\hat{\mathbf{v}}(\chi, t) = \partial \mathbf{x}/\partial t|_\chi$ represents the mesh velocity and $\mathbf{w} = \partial \chi/\partial t|_X$ represents the particle velocity in referential domain.

The Navier-Stokes equations can then be reformulated by modifying the convective term (see Appendix C.2) as:

$$\rho \frac{\partial v}{\partial t} + \rho \left(v - \hat{v}\right) \nabla v = \rho f - \nabla p + \mu \Delta v \tag{5.5}$$

5.1.2 The equation of Fluid-Structure system

The equations for the fluid have been introduced in Section 3.1, and they have been reformulated for moving domains in Section 5.1.1. The equations of the structure have been introduced in Section 4.1. The basic equations of the fluid and the structure are here recalled and the coupling conditions are introduced; the whole set constitutes the governing equations for the coupled problem.

Consider the problem of an incompressible flow in $\Omega^F \times (0, T)$:

$$\begin{cases} \rho^F \frac{dv}{dt}|_\chi + \rho^F (v - \hat{v}) \cdot \nabla v - \mu \Delta v + \nabla p = \rho^F f^F \\ \nabla \cdot v = 0 \end{cases} \tag{5.6}$$

where the first is Equation (5.5) and the second is the continuity equation, see Appendix (A.2). Consider then the generic structural problem in the structural domain $\Omega^S \times (0, T)$:

$$\rho^S \frac{D\vec{x}}{Dt^2} - \nabla \cdot (\mathbf{F} \cdot \mathbf{S}(\vec{x})) = \rho^S \vec{b}^S \tag{5.7}$$

where $\mathbf{F}$ is the deformation gradient tensor and $\mathbf{S}$ the second Piola-Kirchoff stress tensor.

The fluid and the structural domain share one interface, here denoted as Γ, such as $\Gamma = \Omega^S \cap \Omega^F$. The coupling condition is expressed in kinematic and dynamic terms at the interface Γ, as the continuity of the displacement, the continuity of the velocity and the equivalence of the forces:

$$\vec{v}\,|_\Gamma = \dot{\tilde{X}}|_\Gamma \qquad ; \qquad \vec{d}\,|_\Gamma = \tilde{X}|_\Gamma \qquad ; \qquad \vec{f}^{\,F}|_\Gamma = -\vec{f}^{\,S}|_\Gamma \tag{5.8}$$

where $\vec{v}\,|_\Gamma$ is the fluid velocity, $\vec{d}\,|_\Gamma$ the mesh displacements and $\vec{f}^{\,F}|_\Gamma$ the traction force at the interface in the fluid domain; analogously $\dot{\tilde{X}}|_\Gamma$ is the velocity vector, $\tilde{X}|_\Gamma$ the displacements and $\vec{f}^{\,S}|_\Gamma$ the loading at the interface, but in the structural domain.

5.1.3 Coupling algorithms

Many different strategies can be adopted to discretize in time coupled Fluid Structure Interactions problems. In general however, three main families of algorithms can be identified, normally referred to as *explicit*, *semi-explicit* or *implicit*.

The characteristics of the *explicit* schemes are that one single solution is required for the fluid and the structure at every time step. This type of algorithm is in general computationally very efficient, but it is likely to encounter instabilities which might cause the divergence of the solution. Popular explicit schemes are the conventional serial staggered (CSS) [79], and they are based on the following steps:

1. Transfer the motion of the structure $\vec{X}_{n-1}$ to the fluid domain. The velocities will be linearly calculated as $\vec{X}_{n-1} - \vec{X}_{n-2}/\delta t$
2. Update the position of the moving mesh accordingly
3. Calculate fluid pressures p^n at the time n
4. Convert the fluid pressure in a Structural load and transfer to the structural domain
5. Calculate the motion of the structure $\vec{X}_n$

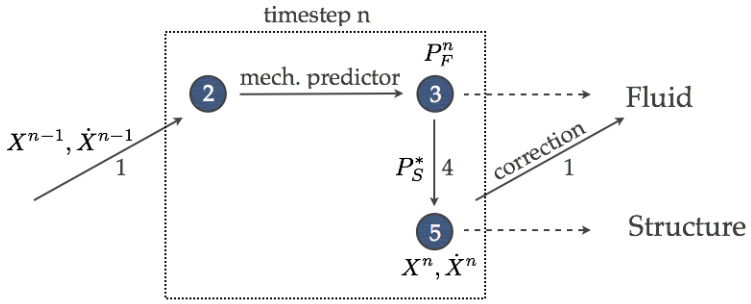

Figure 5.3: Schematic representation of the Conventional Serial Staggered coupling algorithm with a predictor-corrector type approach

6. Advance in time: $t = t^{n+1}$

Several different variations exist of this basic algorithm, where the differences are mainly represented by the data sent between the solvers. Although the basic algorithm does not necessarily respect the energy balance at the interface, it is possible to define improved conservative versions, such as the predictors-correctors CSS algorithms, Figure 5.3. In the setting proposed by [79] the displacements and the structural load is re-manipulated before it is sent to the other solver. As in Figure 5.3, at "1" the structure sends the displacement $\vec{X}^{n-1}$ to the fluid solver. At step "2" the fluid solver makes some sort of prediction of the displacements at the time-step $n+1$ and deforms the fluid domain accordingly. The pressures are then computed in this configuration and converted into the structural load P^* in step "3", where the superscript "*" indicates that this is the pressure obtained for the predicted displacements. A load vector can then be sent to the structural solver for calculating the new displacements $\vec{X}^{n+1}$ at step "4".

This family of algorithms, investigated in [79], are especially suitable for aero-elastic analysis – where for instance the density of the structure is much higher than the density of the fluid – but they might become unstable in particular configurations. As it was shown by Causin [80] and more recently by Forster [117], when coupling the incompressible fluid and the structural equations in an explicit "staggered" scheme an additional *artificial* term is generated, which acts as an additional mass on the fluid-structure interface and it is therefore called the "*Added mass*". It should be underlined that the term "*Added mass*" used here does not indicate the same physical concept traditionally used in CFD and in Naval Architecture. In this case the "*Added mass*" is an artificial effect due to the incompressibility which arises at the interface between the fluid and the structure when adopting staggered explicit "staggered" schemes. This additional term, the discrete derivation of which was shown by [117], is mainly

responsible for the insurgence of instability in the coupled analysis and it is mainly originated from the fact that – for explicit coupling – the fluid and the structure are not simultaneously solved (recall the meaning of P^*). The stability of the coupled system results then to be directly proportional to

- the time-step value Δt,
- the stiffness of the structure k^S,
- the thickness of the structure t^S,

and inversely proportional to

- the density ratio ρ^F/ρ^S,
- the characteristic size of the structure,
- the order of the numerical scheme,
- the viscosity of the fluid

It is relatively difficult to estimate if instability is likely to occur in the case of sail analysis, because on the one hand the thickness of the structure is very small ($\approx 0.1[mm]$) and the characteristic sizes are very large ($\approx 10[m]$); on the other hand the density ratio ($\approx 10^{-3}$) and the viscosity of the air ($\approx 10^{-5}$) are both relatively small.

In recent years several new advanced explicit algorithms have been formulated [118], [119] with very good performances in terms of stability, also for *critical* configurations. Their review and implementation is however well beyond the scopes of this thesis. Similar considerations can be done for the "*semi-implicit*" or "*semi-explicit*" algorithms. A review of the different available options can be found in [82].

In the *implicit* algorithms the equilibrium of the fluid-structure coupled system is verified at every time-step by means of fixed-point sub-iterations within the time-step until a convergence criterion is satisfied (see Section 5.1.5). The algorithm is then based upon the following steps:

1. Transfer the motion of the structure $\vec{X}_{n-1}$ to the fluid domain
2. Relax the displacements
3. Update the position of the moving mesh accordingly

4. Calculate fluid pressures p_k^n at the time n and the fluid structure iteration k

5. Convert the fluid pressure in a Structural load and transfer to the structural domain

6. Calculate the motion of the structure $\vec{X}_n^k$

7. Verify the convergence criterion. If this is not satisfied, return to point 2

8. Otherwise advance in time: $t = t^{n+1}$

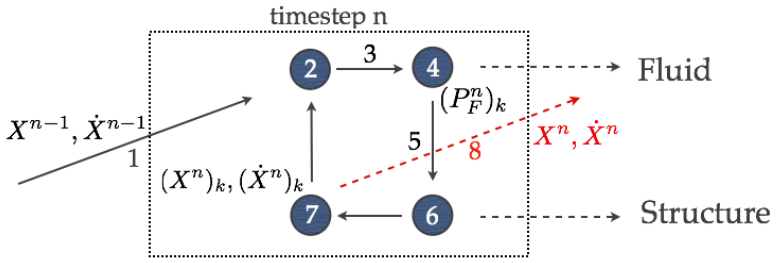

Figure 5.4: Schematic representation of the Implicit coupling algorithm

Several different variations of this basic algorithm exist, where differences mainly consist in the displacement relaxation strategy and the type of converged displacements sent from one time step to the next one. In general Aitken dynamic relaxation is used, where the displacements to be applied in the sub-iteration k are defined as (see [82]):

$$\vec{X}_{k+1} = \omega_k \, \vec{\tilde{X}}_{k+1} + (1 - \omega_k) \, \vec{X}_k \tag{5.9}$$

$$\omega_k = \frac{(\vec{X}_k - \vec{X}_{k-1}) \cdot (\vec{X}_k + \vec{\tilde{X}}_k - \vec{X}_{k-1} - \vec{\tilde{X}}_{k-1})}{\|\vec{X}_k + \vec{\tilde{X}}_k - \vec{X}_{k-1} - \vec{\tilde{X}}_{k-1}\|^2}, \; k > 1 \tag{5.10}$$

where $\vec{X}_k$ is the vector of the displacements to be applied in the fluid domain and $\vec{\tilde{X}}_k$ is the vector of the displacements calculated by the structural solver, both at the sub-iteration k. Of course, such a formulation can be used for $k > 1$, thus a fixed value arbitrarily small must be chosen for the first sub-iteration. The scheme is implemented as in Figure 5.5 *right*. A linear prediction for the displacements is performed for the last converged time step, such as: $\vec{X}_n^{predicted} = 2 \, \vec{X}_{n-1} - \vec{X}_{n-2}$. This prediction of the displacements, valid when the time-steps value Δt is constant, is applied into the fluid domain for calculating the first guess of the pressure for the iteration $k = 0$. A fixed "*well-chosen*" relaxation factor ω_k is then applied for iteration $k = 1$, and the calculation proceeds calculating the relaxation factor with Equation (5.10) in the following iterations.

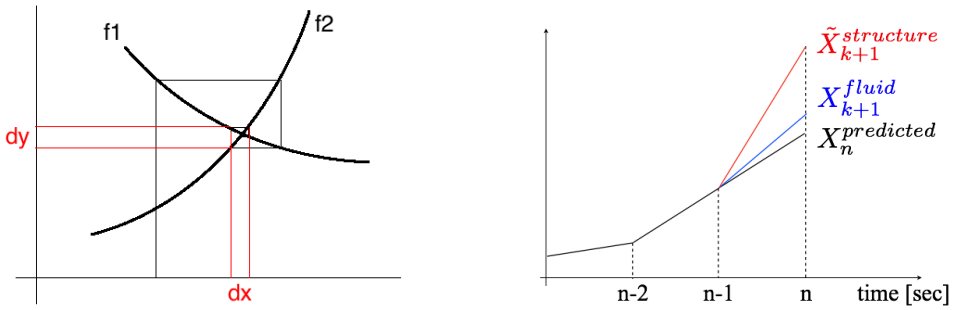

Figure 5.5: Schematic representation of scheme adopted for the FSI sub-iterations. *Left*: fixed point type convergence; *right* linear prediction and under-relaxation

The main advantage of the *implicit* coupling is that the algorithm is generally stable, because the equilibrium (and therefore the energy balance) at the interface is verified within every time-step. The main drawback of the *implicit* coupling algorithms is that they tend to be more computationally expensive, because the fluid and structure evaluations, which are computationally expensive, need to be repeated several times within one single time-step. Convergence it typically achieved in $6-10$ sub-iterations in the cases presented in the following (see Section 5.2).

In this thesis an *implicit* coupling with Aitken dynamic relaxation has been chosen for the FSI coupled analysis. The CSS *explicit* coupling is in fact non suitable for the kind of analysis this work aims to do. This clearly appears when observing the effect of a not fine enough convergence criterion (see Section 5.1.5, where the case presented in Chapter 5.2.4 is used to show some of the encountered stability issues). In the case of a purely explicit scheme no convergence criterion is imposed at all, thus situations such as in Figure 5.6 (or worse) are likely to be produced.

5.1.4 Stabilty of the coupled system: the added mass

The general equations of a coupled fluid-structure problem have been detailed in Section 5.1.2. As it was stated in the previous section, when coupling in a staggered scheme the incompressible fluid and the structural equations an additional *artificial* term is generated, which acts as an additional mass on the fluid-structure interface and it is therefore called the "*Added mass*". The discrete derivation of this additional term is shown in Appendix C.3 following the work of [117].

It can be shown that the condition for the coupled system to remain stable can be written

in the shape:

$$\frac{\rho^F V^F + a\,\Delta t\,k^F}{\rho^S L^s t^S + b\,\Delta t^2\,k^S}\,\underset{i}{max}\;\mu_i < C_{inst} \tag{5.11}$$

where ρ^F is the density, V^F a characteristic volume (then $m^F = \rho^F\,V^F$) and k^F is a characteristic stiffness value for the fluid; ρ^S is the density, L^S a characteristic length, t^S the thickness and k^S the characteristic stiffness for the structure. The terms $\underset{i}{max}\,\mu_i$ is the higher eigen-value of the added mass operator and essentially depends upon the problem's geometry. The value of the constants a, b and C_{inst} depends upon the adopted numerical scheme.

Equation 5.11 is explicative for several observations often done when attempting coupled analysis. In particular, it can be stated that the stability of the coupled system is proportional to :

- the density ratio ρ^F/ρ^S,
- the time-step value Δt,
- the stiffness of the structure k^S,
- the thickness of the structure t^S

the stability is then inversely proportional to the stiffness of the fluid, and therefore to its viscosity. Furthermore, the constants a, b and C_{inst} are a function of the particular discretization scheme. As it is shown in [117], in general increasing the order (and therefore the accuracy!) of the numerical scheme the stability condition results more restrictive: the coupled system is then more unstable.

The stability condition in Equation (5.11) mainly refers to the problem set-up, exception made for the time-step value and the numerical scheme. The instability therefore mainly derives by the definition of the physical problem, and it must not be considered as a purely numerical issue.

An additional note must be done regarding the time-step value. A higher bound for this value is constituted by the *Courant-Friedrichs-Lewy* (CFL) condition, which is a function of the characteristic size of the computational grid Δx and the velocity of the flow v:

$$\Delta t < \frac{\Delta x}{v} \tag{5.12}$$

in a coupled environment, the stability condition (5.11) determines a higher bound for the time-step value, qualitatively proportional to (see Appendix C.4):

$$\Delta t > C^* \frac{k^F m^F}{k^S\,\rho^S\,L^S\,t^S}\;\underset{i}{max}\,\mu_i \tag{5.13}$$

Table 5.1: Relaxed Dirichlet-Neumann fixed-point iterations scheme

usual setting	setting adopted in openFOAM
solve fluid:	solve solid:
$p_k = S^f(\gamma_k)$	$\tilde{\gamma}_{k+1} = S^s(p_k)$
solve solid:	apply relaxation:
$\tilde{\gamma}_{k+1} = S^s(p_k)$	$\gamma_{k+1} = \omega_k \tilde{\gamma}_{k+1} + (1-\omega_k)\gamma_k$
apply relaxation:	solve fluid:
$\gamma_{k+1} = \omega_k \tilde{\gamma}_{k+1} + (1-\omega_k)\gamma_k$	$p_{k+1} = S^f(\gamma_{k+1})$
$\gamma_k = S^s(S^f(\gamma_k))$	$p_k = S^f(S^s(p_k))$

with C^* a positive constant to be determined. For practical applications then the range of allowed time steps might be very restricted, or even empty. When this happens, the best strategy is to adapt the mesh size in order to make the CFL condition less restrictive. This indication is also coherent with the observations presented in Section 5.1.5

5.1.5 Additional notes

Note on the convergence criterion

In the particular OpenFOAM setting, the mesh motion must be applied before solving the fluid at every iteration. It is therefore convenient to adopt a scheme of the type: solve the structure, apply the displacements to the fluid domain, solve the fluid, check for convergence. This is equivalent to performing fixed-point iterations using the pressure as dependent variable, rather than the displacements, as shown in table 5.1. It is then natural to impose a convergence criterion on the pressure.

Furthermore, unlike the strong coupling (FE-FE; FV-FV) schemes, in a loose coupling (FV-FE) the only real guarantee of the conservation of the energy at the interface is represented by the fact that residuals remain very small. It seems then natural to add a convergence criterion on the displacements. The complete convergence criterion will then be composed by three conditions: minimum number of iterations (see section 5.1.3), convergence of the pressures, convergence of the displacements. An example is here reported, regarding the effect of a poor convergence criterion on the analysis, only considering the convergence of the displacements. Although the pressure signal is affected by a considerable noise (see figure 5.6

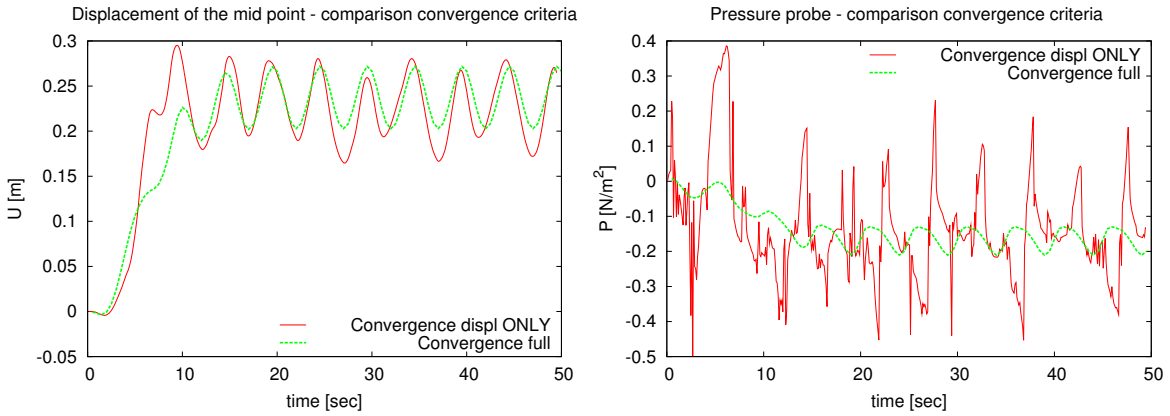

Figure 5.6: *Left*: When imposing a convergence criterion on the displacements only, an irregular displacement signal is found. On the *right* shows the lack of convergence of one pressure probe. When imposing a convergence criterion on both displacements and pressures the results are smooth and comparable with reference results (see section 5.2.2)

right), the point displacement probe (figure 5.6 *left*) results surprisingly smooth. The mean value is almost respected, but the amplitude of the oscillations do not stabilize on a constant band as in the case where the convergence criterion is based on both the displacements and the pressure. When adopting a correct convergence criterion the analysis results coherent and comparable with reference solutions published in the literature, see section 5.2.2

Note on the numerical diffusion: the effect of the numerical scheme and the time-step

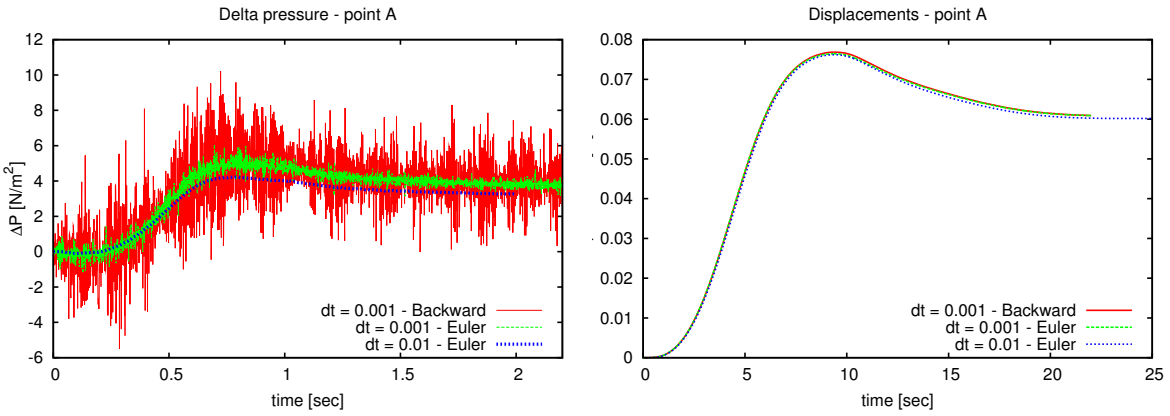

Figure 5.7: Pressure oscillations experienced in the response of the coupled computation. *Left*: Delta pressure signal and *right*: displacements for the test case presented in Section 5.2.4 when varying the scheme and the time-step value

It was stated in the previous section that the stability of the calculation is influenced by

time-step value and the order of the numerical scheme [117]. This leads to the non-intuitive conclusion that stability may be compromised when reducing the time step and increasing the order of the numerical scheme. Although in the present setting an implicit coupling is adopted, which is generally stable, some observations are reported regarding the test case analysed in Section 5.2.4, where a flexible interface deforms under the effect of uniform channel flow. In this case the mass density ratio is $\rho^F/\rho^S = 956/1500 = 0.63$. A time-step value $dt = 0.01$ produces a maximum Courant number $MaxCo = 0.1$. When adopting an Euler (first order) time marching scheme, results in terms of pressure and displacements (see Figure 5.7) are smooth and both coherent with the reference results reported in [13]. The time step value has then been reduced by a factor 10. Although this is a relatively high ratio, the resulting time-step ($\Delta t = 0.001$) is coherent with the values often adopted for analysis in the fluid domain, needed for verifying the CFL condition. In this case high frequency oscillations are produced, the amplitude of which can be estimated $\approx 25\%$ of the mean value. Increasing the order of the time marching scheme (second order backward) generates a further degradation of the results, the amplitude of the oscillation results in fact severely magnified. Although the oscillation of the pressure signal is non negligible, the calculated tip-node displacements are almost unchanged. This is not surprising, because the oscillating pressure signal has high frequency but a mean value which is comparable with the smooth case. The time constant of the structure is in fact much higher than that of the pressure signal, thus the structure acts then as a filter, which smooths the higher frequencies away.

The added mass effect can not be considered within the causes of the oscillations of the pressure because the calculation was performed with an implicit coupling algorithm, which is normally not affected by the added mass. In addition, similar behaviour has been experienced for the case where the displacements of the structural interface were imposed (sinusoidal law in space and time: $u = u(x,t)$), rather than calculated by an external structural solver, as it is done in the beginning of Section 5.2.2) . It can be concluded that the oscillation is completely generated within the fluid domain and it is not caused by a fluid structure coupling effect.

Two main factors must be starting such oscillations: the incompressibility and the singularity at the tip of the analysed configuration [120], which is typical of every cusp geometry or zero-thickness surface in the fluid domain. The singularity is propagated from the tip in the fluid domain, and its effect is more pronounced as the time-step value is reduced and the order of the time-marching scheme is increased. This seems then the effect of the numerical diffusion, which allows a natural smoothing and of course increases when using larger time-steps

and first order schemes.

When setting the case studies for fluid structure interaction analysis, it will be necessary to compromise in terms of the size of the computational grid. Finer grids produce in fact more accurate results, but they require smaller time-steps in order to satisfy the CFL condition, and this might cause oscillations as in Figure 5.7.

Note on the type of the values to be used for segregated FSI communications

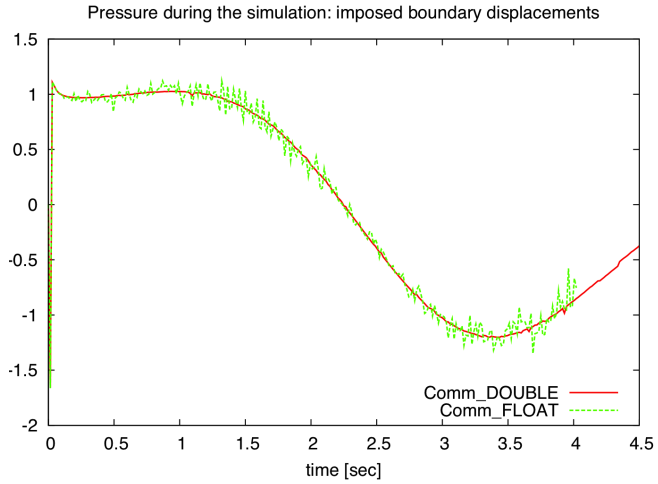

Figure 5.8: Exchanging data as single or double precision strongly affects the results. Pressure values are probed in the centre of the cavity (0.5,0.5)

Another note should be made about the type of values to be passed to the fluid solver. In the current setting in fact displacements are calculated by an external FORTRAN solver, while the fluid is calculated using the C++ OpenFOAM library. The communications between the solvers is assured by the communication library MPI. It was noted that double precision values must be passed; otherwise the truncation error introduces a significant noise in terms of fluid pressures. It is worth remarking that although the difference between a float and a double starts at the 7-*th* decimal place, the noise here identified in terms of pressure oscillates around the 10% of the correct value. This can be explained as the effect of the violation of the incompressibility condition. The comparison of the signals is shown in figure 5.8.

5.2 Numerical tests and validation

5.2.1 Oscillating Cylinder in stationary Fluid

The case of a bi-dimensional oscillating cylinder has been analysed by [12]. In the article the authors compare numerical and experimental results in terms of the induced velocity field. This case is therefore an ideal candidate for the validation of the ALE dynamic mesh motion techniques which have been implemented in environement OpenFOAM for the more general case of Fluid Structure Interactions analysis with deformable bodies.

Table 5.2: Adopted physical quantities

$D\,[m]$	$A\,[m]$	$\omega\,[Hz]$	$x(t)\,[m]$	Re	$\nu\,[m^2/s]$
1	0.7958	1.2566	$-A\,sin(\omega t)$	100	10^{-2}

Table 5.3: Number of elements for the mesh sensitivity analysis

$Mesh_1$	$Mesh_2$	$Mesh_3$	$Mesh_4$	$Mesh_5$	$Mesh_6$	$Mesh_7$
23868	41748	64428	149468	225348	279968	339388

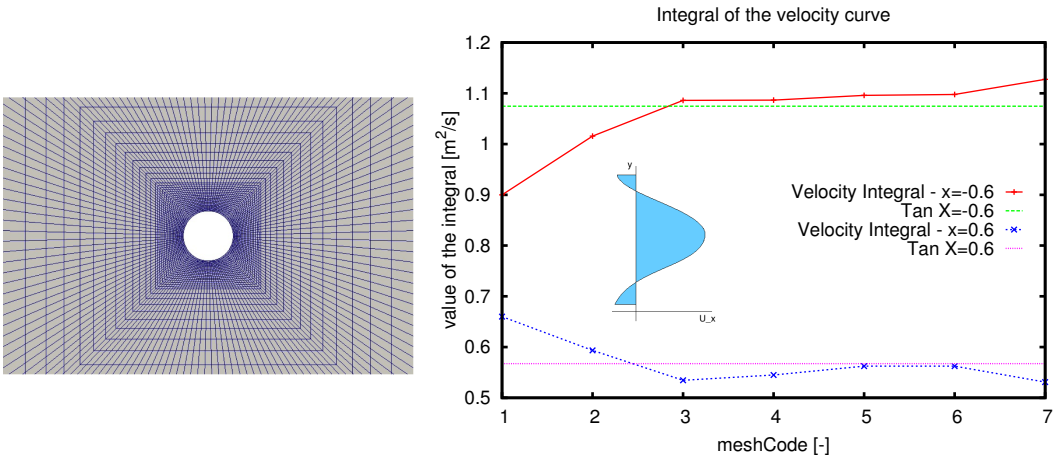

Figure 5.9: *Left*: Portion of the calculation domain close to the moving object (coarse mesh). *Right*: integral of the velocity profile ($x = \pm 0.6$) and reference value from [12]

The case setting are reported in table 5.2, and a portion of the calculation domain (coarse mesh) is shown in figure 5.9 *left*.

Seven meshes were analysed, the characteristics of which are reported in table 5.3. Four

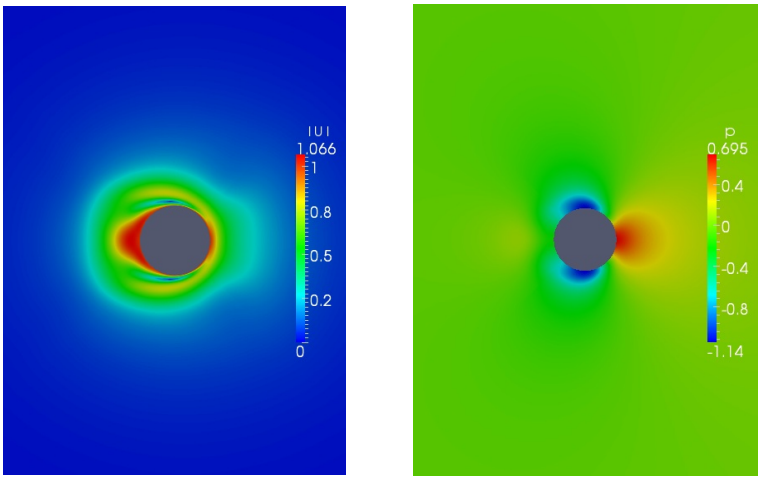

Figure 5.10: Velocity and pressure fields induced by the cylinder motions

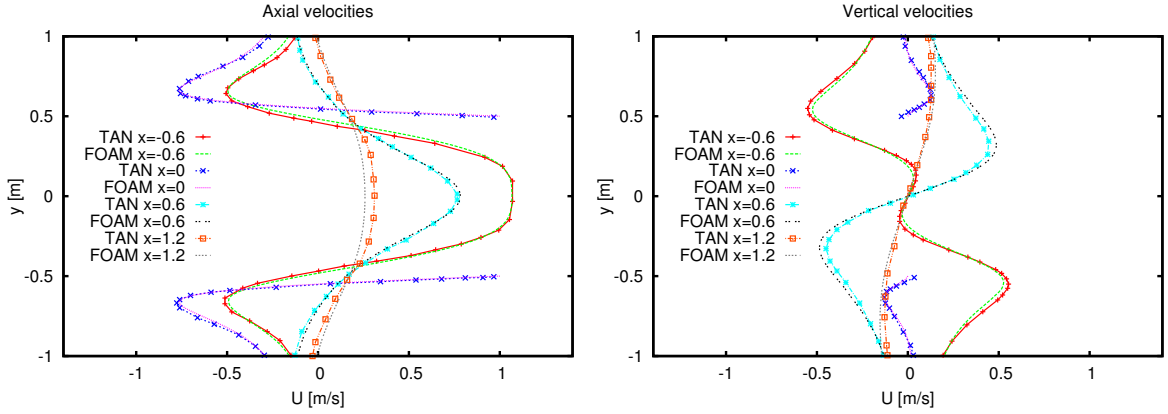

Figure 5.11: Horizontal and vertical velocity profiles measured at the locations: $x = -0.6; 0; 0.6; 1.2$ for the best result obtained with $Mesh_5$

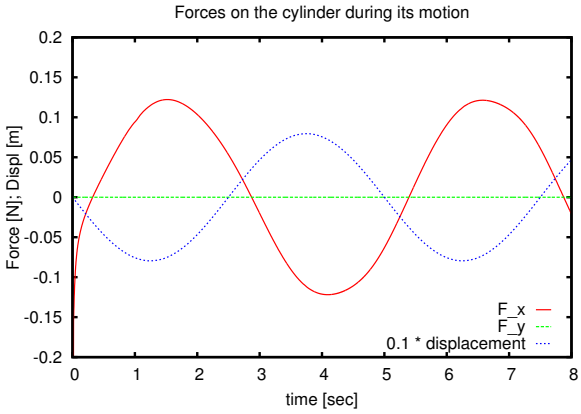

Figure 5.12: Forces acting on the cylinder versus time ($Mesh_5$)

locations have been used for the measure of the velocity profiles, following the reference results: $x = -0.6$; 0; 0.6 and 1.2. The measure is performed when the cylinder accomplished a complete cycle, viz 180°.

Figure 5.9 shows the mesh sensitivity in terms of the integral of the curves for $x = \pm 0.6$ shown in Figure 5.11. Of course the integral is calculated along the vertical direction: $\int u(y)dy$, as it is shown in the drawing in Figure 5.9. The best results are obtained with the mesh 5, the results presented in the following refer then to the analysis performed with this computational mesh. When further increasing the mesh, and in particular for Mesh 7, the quality of the solution starts to decrease. This must be the effect of the discretization error, which affects the results for this really fine – but not extreme – mesh. It can be guessed that such a sensibility to the discretization is due to accumulation of the error in the mesh motion algorithm.

The results obtained with the mesh 5 are in good general agreement with the reference solution (see figure 5.11). A higher scatter can be identified for for the axial velocity profile at $x = 1.2$ and the vertical velocity profile at $x = 0.6$. Such a difference is however largely within the acceptable error band arising between the numerical and the experimental results reported in [12]. Higher accuracy could eventually be achieved further increasing the domain size, which was set here at 9D in each direction.

An impression of the generated field, both in terms of velocity and pressures is reported in figure 5.10, while the pressure force induced on the cylinder during its motion is plotted in figure 5.12. The force signal has a sinusoidal behaviour with a phase shift of 0.35 [sec] with respect to the motion.

5.2.2 2D Cavity validation test case: fluid, structure and FSI

Fluid domain

This classic test, analysed by several authors [15, 13, 19, 16], is a typical benchmark for FSI. In this chapter the case will be carefully analysed. The case will be described, and some validation results for the fluid in a fixed domain and a constant velocity on the top wall will be presented. Prescribed displacements will then be assigned to the bottom wall. At last, full fluid structure interaction results will be presented and analysed. Some notes will be discussed on the sensitivity of the analysis to the errors and thus the convergence criterion to be adopted. Physical quantities are listed in Table 5.4. The case is laminar, since $Re = 10^2$. The case is initially analysed using a fixed domain, in order to validate the fluid calculation

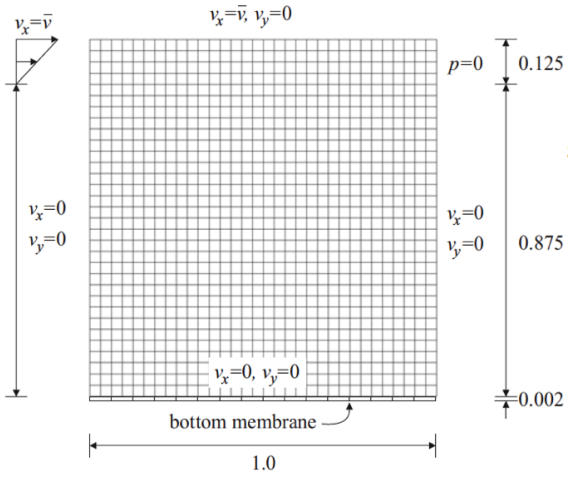

Figure 5.13: 2D cavity case setting. From [13], Sect 5.8.2

Table 5.4: Physical quantities for the analysed FSI case

ρ_f	ν_f	t_s	ρ_s	ν_s	E_s
$[Kg/m^3]$	$[m^2/s]$	$[m]$	$[Kg/m^3]$	$[-]$	$[N/m^2]$
1.0	0.01	0.002	500	0.0	250

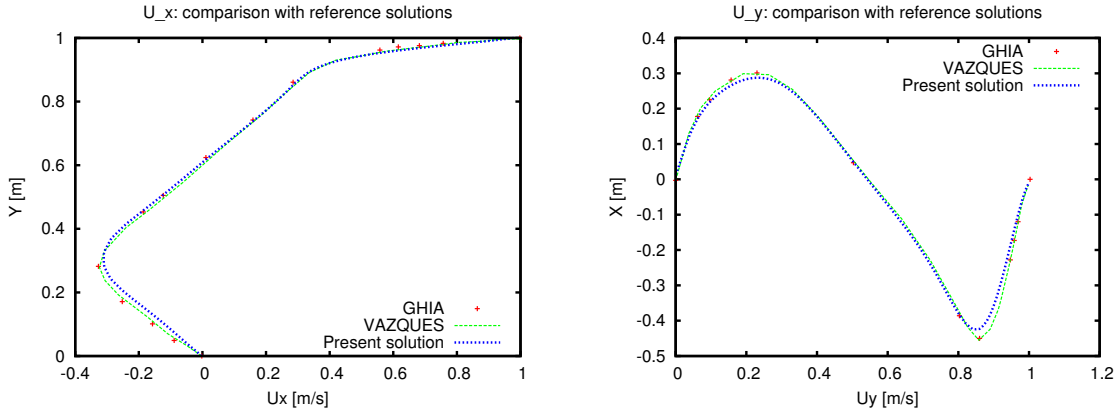

Figure 5.14: Comparison of the present solution (steady case and $U_{top} = const = 1[m/s]$)) with results from [14] and [13]. Results are extracted on the left on a vertical line (x=0.5); on the right on an horizontal line (y=0.5)

against the reference solution proposed by [13] and [14]. In order to be consistent with the settings of this reference case, some modifications are done with respect to the case setting shown in Figure 5.14 and Table 5.4. A constant velocity is in fact imposed on the higher wall, the value of which is 1 [m/s]. The fluid viscosity is set to 0.0025 [m^2/s^2], in order to realise a Reynolds number $Re = 400$. The boundary condition for the velocity has been imposed = 0

on the whole left wall.

Results are reported in Figure 5.14 in terms of velocity profile for the mid section of the cavity (x=0.5). The agreement with the reference solutions is very satisfactory.

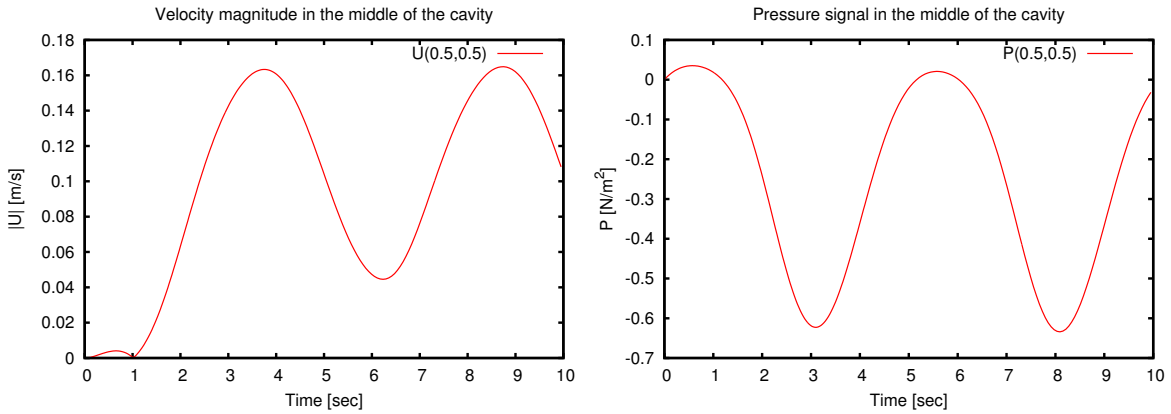

Figure 5.15: Velocity and pressure in the centre of the device versus the time. Unsteady inlet velocity ($u(t) = 1 - cos(2\pi t/5)$) and fixed domain

In a second analysis, unsteady velocity boundary conditions have been applied at the top surface. The fluid physical properties have been set as those in Table 5.4. The applied law for the velocity is defined as: $u(t) = 1 - cos(2\pi t/5)$, as in the FSI analysis proposed in [13]. The results are reported in terms of velocity and pressure induced on one point in the middle of the cavity ($x = 0.5$, $y = 0.5$) versus time in Figure 5.15.

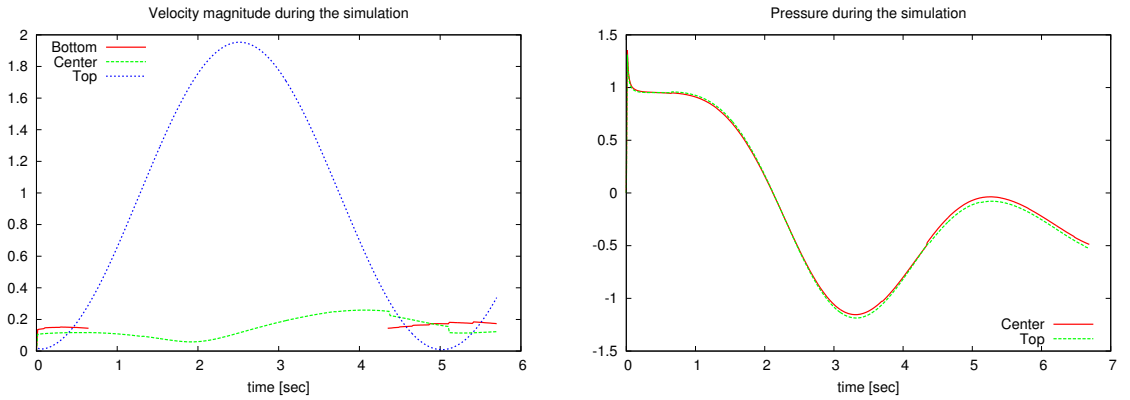

Figure 5.16: Velocity and pressure in two probe points in the centre (0.5,0.5) and the top (0.5,1) of the device versus time. Unsteady inlet velocity and prescribed motion of the domain's bottom. Compared to the previous solution with fixed bottom in Figure 5.15, the pressure peaks are doubled

Third step, the motion of the bottom has then been imposed using the law of the motion: $u_y = 0.25 \cdot sin(\pi x) \cdot sin(\pi t/5)$. The motion has then a sinusoidal shape in space and it evolves as a sine in time, is in agreement with the FSI solution reported in [13]. The boundary condition

for the velocity applied to this wall in the OpenFOAM setting passes from *fixed Value = 0* to *movingWallVelocity*. this condition imposes: $u = u_s$ on the considered boundary, with u_s the velocity of the wall. Results of this analysis are reported in Figure 5.16. Comparing these pressure signal with the previous analysis, the pressure peaks are now more than doubled ($-0.6\text{N/mm}^2 \rightarrow -1.3\text{N/mm}^2$) for the effect of the motion of the bottom.

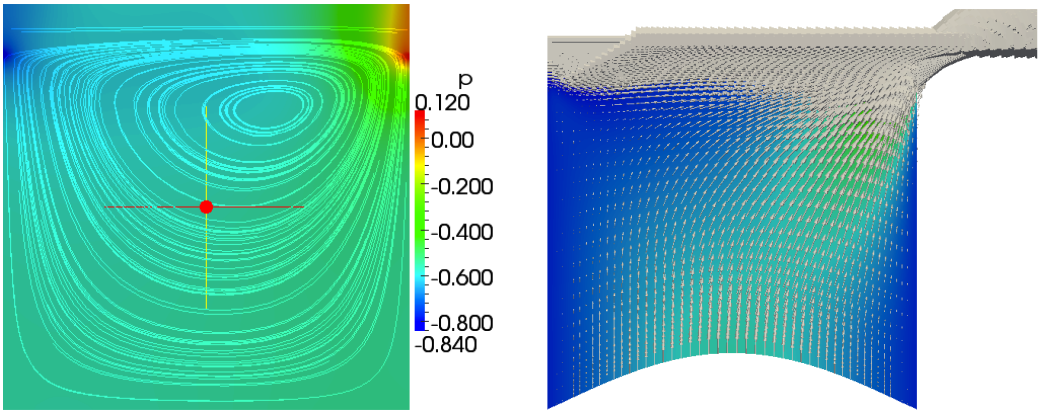

Figure 5.17: *Left*: screen shot of the pressure field and the streamlines for t=2.75 [sec] for the steady case; *right*: the velocity field (vertical component) with unsteady velocity on the top surface: $u(t) = 1-cos(2\pi t/5)$ and an imposed law of the motion for the bottom interface: $u_y = 0.25 \cdot sin(\pi x) \cdot sin(\pi t/5)$

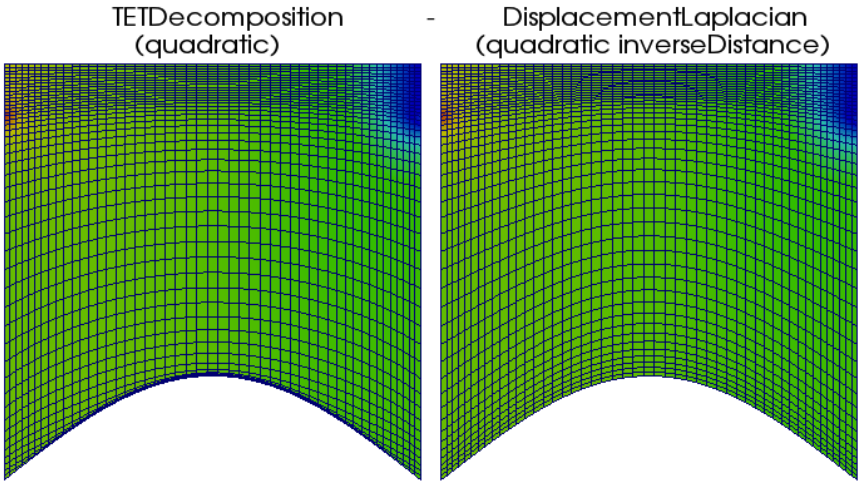

Figure 5.18: Cell quality is better preserved with the DisplacementLaplacian motion solver than with the LaplaceFaceDecomposition motion solver

A note should be here introduced, about the mesh motion strategy. Several algorithms are present in the OpenFOAM solver, but most currently the "laplaceFaceDecomposition" (also called TET) or the "displacementLaplacian" algorithm are used. Both algorithms are based on the same idea: the mesh motion is spread into the fluid domain with a Laplacian operator using the motion of the boundaries as boundary condition. However, the solution in terms

of mesh quality preservation can be rather different, as it is shown in Figure 5.18. Using the TET algorithm for this case clearly did not preserve the cell quality, thus the solution incurred in singularities and the analysis stopped. This did not happen for the same case using the DisplacementLaplacian motion solver. In the following it has then been chosen to use the DisplacementLaplacian motion solver for all analysis.

Structural domain

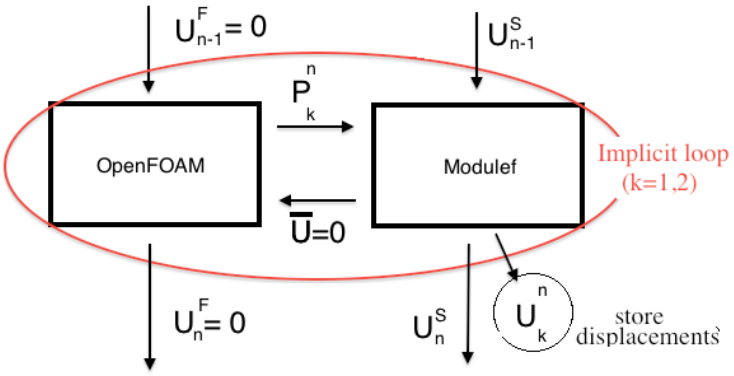

Figure 5.19: Decoupled scheme used for the debug of the FSI algorithm.

The FSI solver is here tested imposing ZERO displacements to the fluid domain at every time-step. With these setting the structural solver receives the pressures at the interface; although no feed back exists, the structure will deform under the effect of a cyclic fluid loading. Since the law of the velocity at the top is a sine, the structural problem reduces to an harmonic oscillator with sinusoidal applied force. A schematic diagram of the adopted strategy is shown in Figure 5.19.

Pressures calculated for both the cases of fixed fluid domain and fluid domain with imposed displacements have been analysed. In order to get convergence of the structural solver, both damping and sub-cycling are needed. The sub-cycling is introduced when the structural analysis do not converge in a given time-step and it is implemented using a bisection method. When convergence is not reached, the structural solver is reset to the configuration of the beginning of the time-step, the time step value is divided by two and two solutions are calculated prior to send the results (in terms of displacements) back to the fluid solver. Of course the sub cycling is not reduced to a factor two, but it allows multiple subdivisions, until a lower bound for the time-step value is reached.

Figure 5.20 reports the effect of the damping on the solution for the uncoupled structural

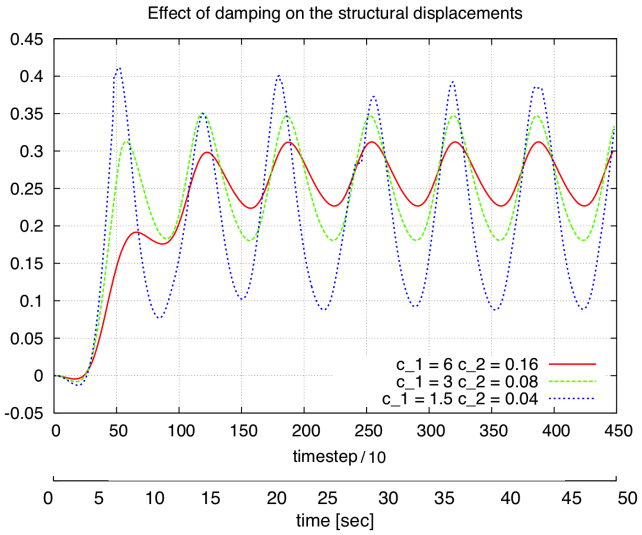

Figure 5.20: Structural displacements time history for the case where the fluid loading is applied to the structure. Unsteady top fluid velocity and fixed fluid domain (decoupled case, NO FSI). Effect of different damping values

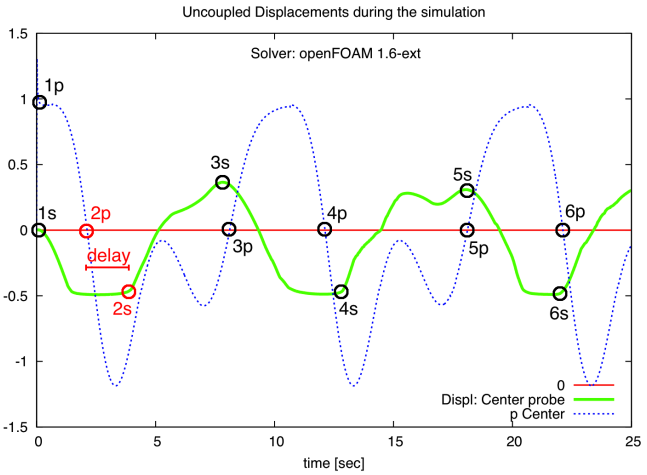

Figure 5.21: Structural deformation and pressure time history for the decoupled case where the fluid bottom moves with an imposed law of the motion

solution. In this case then the fluid pressure obtained with unsteady top velocity and fixed domain is sent to the structural solver and used as a loading condition. The effect of damping mainly affects the mean value and the amplitude of the solution, and it has a small effect only on the period of oscillation.

Figure 5.21 reports the results for the case when the pressure calculated in the fluid domain with imposed displacements of the bottom are transferred to the structural solver. In the figure some points have been underlined on the pressure (label: P) and the displacement (label: S) curve. These points represent the correspondence of the pressure and the displacements, or the points where the derivative of the displacement changes sign under the effect of a pressure sign inversion. A good correspondence is generally found. Only in the first load cycle (points 2, underlined in red) some shift is experienced by the structure, which remains in the same position for about 2 sec after the pressure has changed its sign. After this initial delay, the structure follows the fluid load.

Fluid Structure Interactions

Full fluid structure interactions analysis has been performed, using the implicit coupling scheme detailed in Section 5.1.3 and the case setting presented in Table 5.5.

Table 5.5: Analysis settings

Structural solver scheme	Fluid solver	Fluid Solver type	FSI coupling	Mesh motion diffusion
implicit mid-point rule	OpenFOAM 1.6-ext	Implicit-projection scheme	Implicit Aitken relaxation	displacement Laplacian
Time marching scheme (fluid)	dt	Max Courant n.	Tol displacements	Tol pressure
Backward	0.01	0.3	10^{-7}	10^{-2}
nCorrectors	nOuterCorrectors	nNonOrthogonal Correctors	C_1	C_2
3	2	2	0.75	0.02

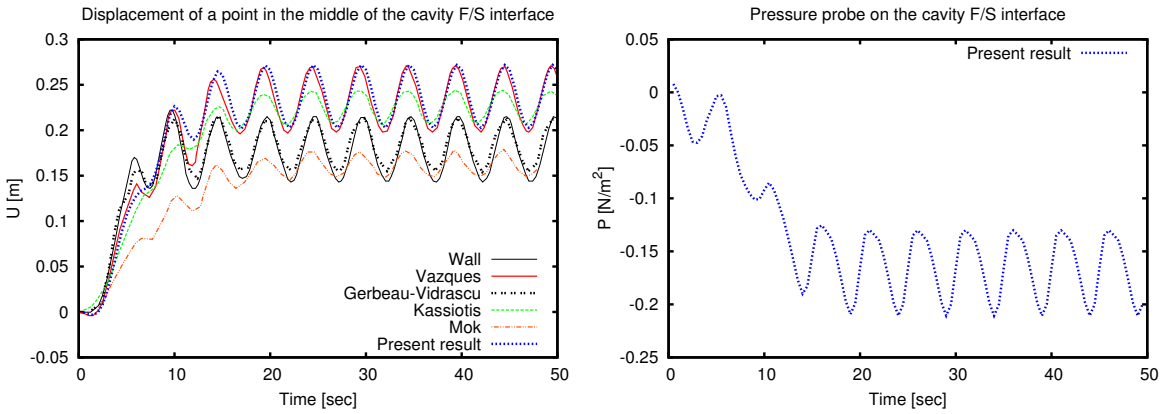

Figure 5.22: *Left*: FSI results obtained for the case of the 2D cavity and comparison with reference solutions from [15], [16], [17], [18] and [13] in terms of displacements. *Right*: pressure probe in the center of the moving interface. Such a probe is sampled extracting one value from the vector sent from fluid to the structural solver. Values are reported versus time

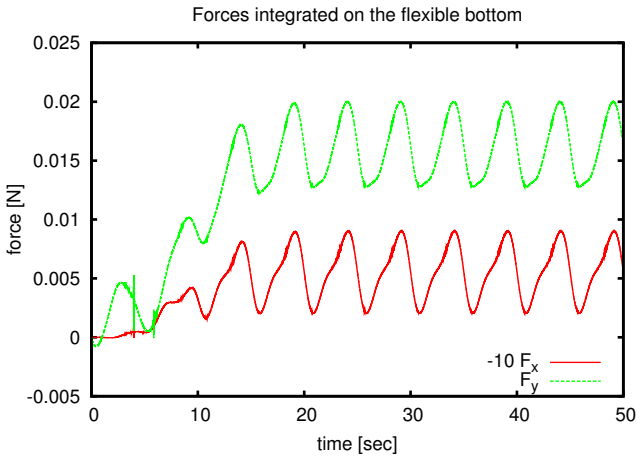

Figure 5.23: Forces integrated on the moving interface versus time. The x-component of the force is multiplied by a factor ($\beta = -10$) for visualization purposes. Some noise is visible on the plot, especially arising during the transient in the beginning of the simulation

The present solution is in good agreement with the solution presented in [13], but quite a large scatter can be identified with other reference solutions present in the literature. The source of these differences is not completely clear, but three main hypothesis can be attempted. First hypothesis, some inconsistency may arise in the choice of the boundary conditions. Unfortunately authors do not always clearly specify the set-up which has been adopted. The choice of the boundary conditions (especially in terms of pressure) has in fact a large impact on the force generation, as it was shown in [16]. A second source of uncertainty derives by the damping, which is not uniquely defined, and may cause variations in the solutions as in Figure 5.20. Third possible cause of the identified differences, the numerical scheme, which

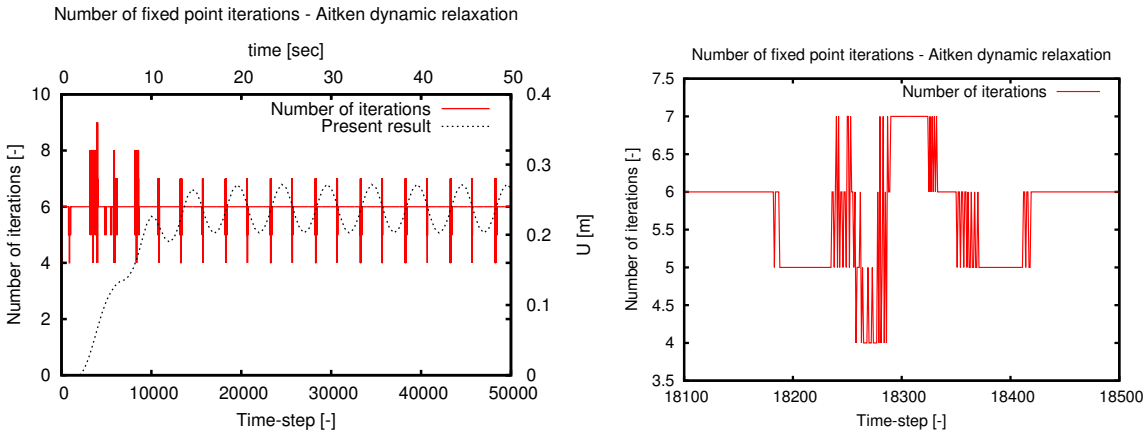

Figure 5.24: Number of iterations performed in every time step. The displacement curve is reported, and it appears how the number of iterations increases when the interface velocity attains its higher value. The number of iterations (4:6) is in general agreement with reference solutions declared in [13] and [15]. *Left*: whole time history; *right:* zoom on one peak

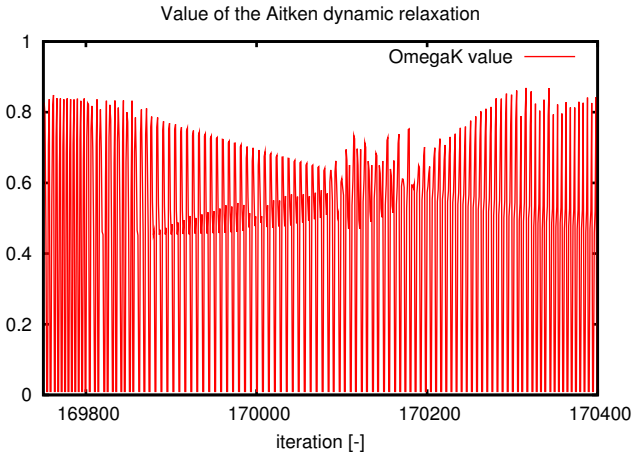

Figure 5.25: Value of the Aitken dynamic relaxation factor calculated during the calculation (zoom on one portion of the plot). This value is used from the second iteration, since in the first iteration a linear predictor is used. Therefore it is imposed = .01 for second iteration, and it typically takes values such as: 0.357 - 0.446 - 0.470 - 0.916 in the following iterations

can influence the solution, since not every scheme is equally dissipative.

Compared to the previous solutions with the fixed domain (Figure 5.15) or with the imposed displacements (Figure 5.15), the pressure remains here on much more smaller values: the pressure peaks passed from -0.6 [N/mm^2] or -1 [N/mm^2] to -0.2 [N/mm^2], results differ by a factor 3 or 5. Compared to the pressure plot, the force plot in Figure 5.23 shows some noise locally affecting the solution. Such noise does not show in figure 5.22 because it is a global and not a local phenomenon, or because in the analysis the pressure was sampled at a lower frequency than the force. Similar noise arising in FSI analysis is shown for example in

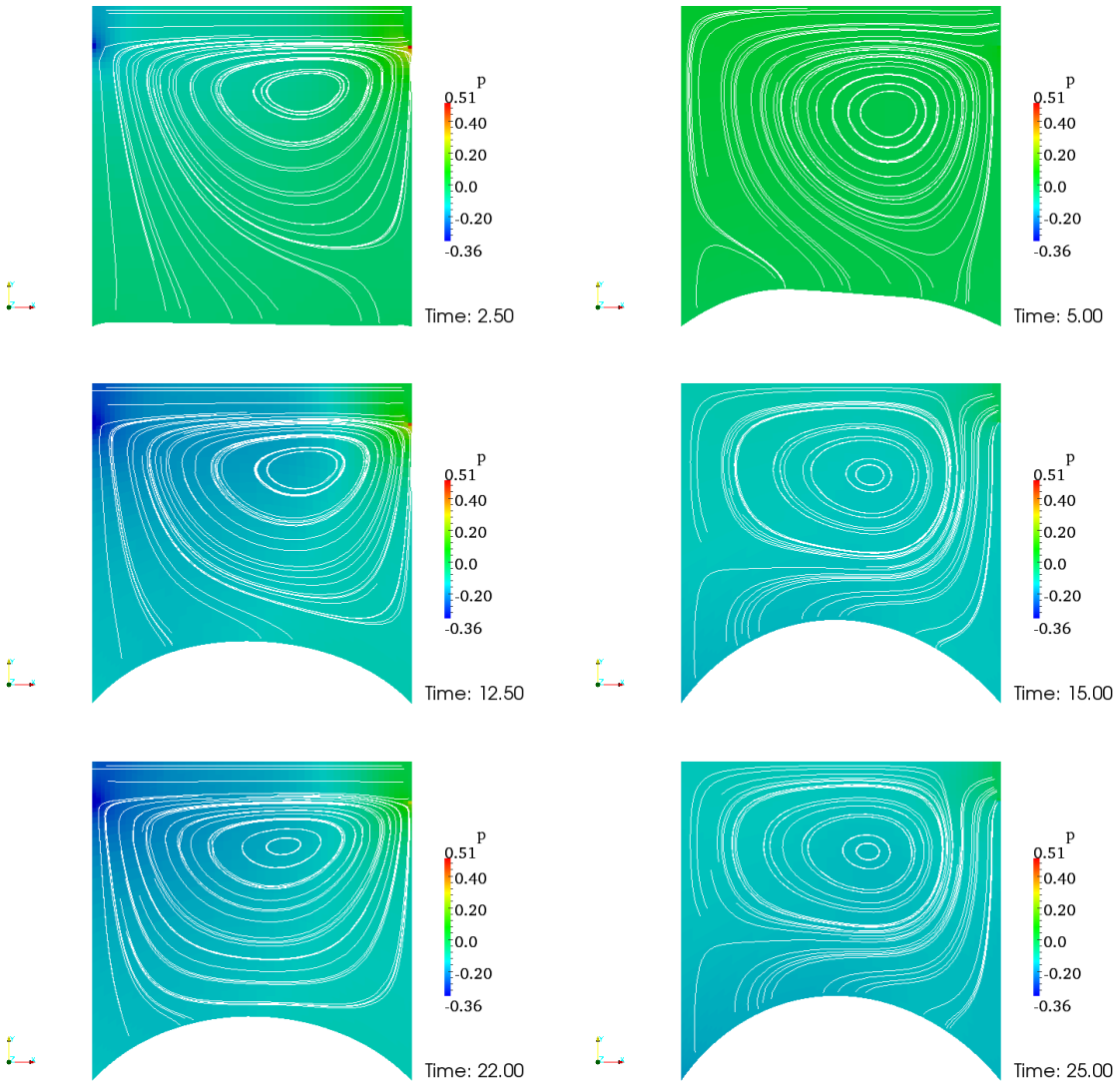

Figure 5.26: Screen shot in terms of fluid pressures and velocity streamlines for the FSI solution in different time-steps

[121], and it might be due to a lack of convergence within the time-step. Also it can be due to a convergence criterion which is not fine enough. It might be due to a limitation of the loose coupling scheme, which is by definition unable to perfectly match the coupling conditions at the interface, as stated in Section 5.1.5. Finally, recalling the plot in Figure 5.8, the noise might also be due to a truncation error. Although in this case the analysis was performed using double precision values, a truncation error always arises when performing numerical computations. This might produce the noise, the magnitude of which is however much more smaller that the one identified in Figure 5.8.

Most time-steps were resolved in 6 fluid structure iterations, however some peaks were

encountered in correspondence of the maximum velocity of the fluid structure interface. A zoom on one of this peaks, representative of all this kind of peaks, is represented in figure 5.19 *right*. It appears then that the number of iterations is initially reduced to five. This is not surprising, since in this zone the displacement is close to its mean value. Close to $y = \overline{y}$ the sin function is well approximated by a straight line (i.e: use a Maclaurin series), therefore the first order predictor is particularly accurate. After some time steps however some error must be accumulated, which requires more iterations to reach a converged solution.

This test case shows that the method is capable of reproducing Fluid Structure Interactions in large displacements, and it is thus suitable for the analysis of thin laminates such as sails in a fluid domain. A note should be done about the convergence criterion, which has been shown to be crucial for the correct representation of the coupled solution. This is detailed in Section 5.1.3 using the results presented in this Section.

5.2.3 3D Cavity validation test case

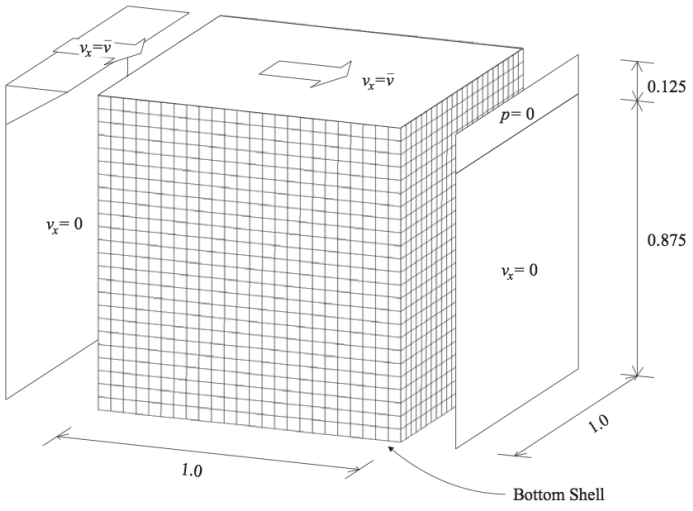

Figure 5.27: 3D cavity case setting. From [13], Sect 5.8.3

The test case shown here is the three-dimensional extension of the case reported in section 5.2.2. Results in terms of displacements for this case have been published by [13], [19]. Compared to the case analysed in Section 5.2.2, all quantities remain the same, but the domain is three dimensional and fully constrained between walls.

Eigen analysis was performed in order to check for the damping values to be applied. Such values are reported in Table 5.6, and an image of the eigen-vectors is reported in Figure 5.28.

Table 5.6: Results from the eigenvalue analysis

ω_n [Hz]	T_n [sec]	C_1	C_2
0.0081	777.7	0.008	123.8

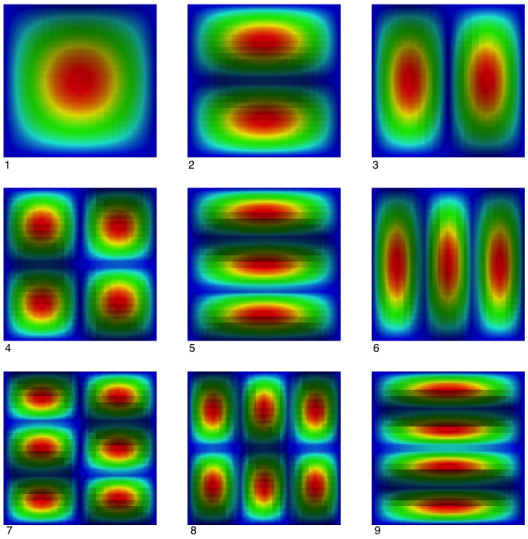

Figure 5.28: First nine eigen-vectors of the analysed structure

Seven analyses were performed using different damping values. This was done in order to check the dependency upon the damping, which was discussed in Section 4.1.9 and in Section 5.2.2. General good agreement was found between the reference results and the present solution, as it is shown in Figure 5.30. In this case the damping was tuned to be mainly viscous, and the global damping coefficient value in correspondence of the natural frequency value exceeds 90. The present solution is in general agreement with the reference solutions [13], [19] in terms of displacements; it tends however to oscillate with smaller amplitude and the response results slightly shifted on the right. This is indeed the effect of the high viscous damping applied, and similar behaviours can be identified in Figure 5.20. The force plot in Figure 5.30 *right* is obtained integrating the pressure on the structural interface for every time-step. The result is smooth and regular, and the signal presents the same frequency as the displacements curve in figure Figure 5.30 *left*. However, compared to the reference solution [19] the magnitude of the forces results here much higher. The reason for this is not completely clear, since the adopted setting in both analyses is consistent in terms of boundary conditions. Unfortunately, other reference solutions were not found in terms of forces.

Six different test were performed for investigating the effect of the damping coefficient value

on the response of the system. The results are reported in Figure 5.31. The main difference between the solutions is found in the displacement signal's amplitude, as it has already been identified in Section 5.2.2. Comparing the two types of damping however (viscous: Figure 5.31 *left* and visco-elastic: Figure 5.31 *right*), it appears that the solution is especially sensitive to the variations of the viscous damping. In this case in fact the damping tends to zero for the higher frequencies. Relatively high damping coefficient values (e.g. $c_1 = 0.15, c_2 = 0.005 \Rightarrow \xi \approx 9.25$) are then not enough for assuring a smooth evolution of the structural interface, and higher order harmonics appear on the displacement signal. The higher order modes are also visible in figure 5.32 *left*, where a screen shot of the solution for the mainly viscous damping values is reported and compared with a higher damped solution, on the *right*. A smooth evolution is assured when further increasing the damping. Of course, when adopting very large damping values a long transient with small oscillations is experienced.

A rather different situation arises when adopting a mainly visco-elastic damping. In this case the higher order frequencies are always damped, and the variation of the solution affects the amplitude of the evolution of the structural interface.

Figure 5.32 reports a cross section of the deformed structural interface at the same instant for different adopted damping coefficients. The damping variation affects the whole solution in terms of global deformation.

In terms of FSI iterations the damping has also a non-negligible influence: six iterations are generally required for the higher damping coefficients, while nine are required when adopting the lower damping. The general values reflect however what has been shown in Figure 5.24. The analysis is therefore computationally heavy: the whole simulation consisting of 40 seconds in physical time requires more than 12 hours on a double processor machine.

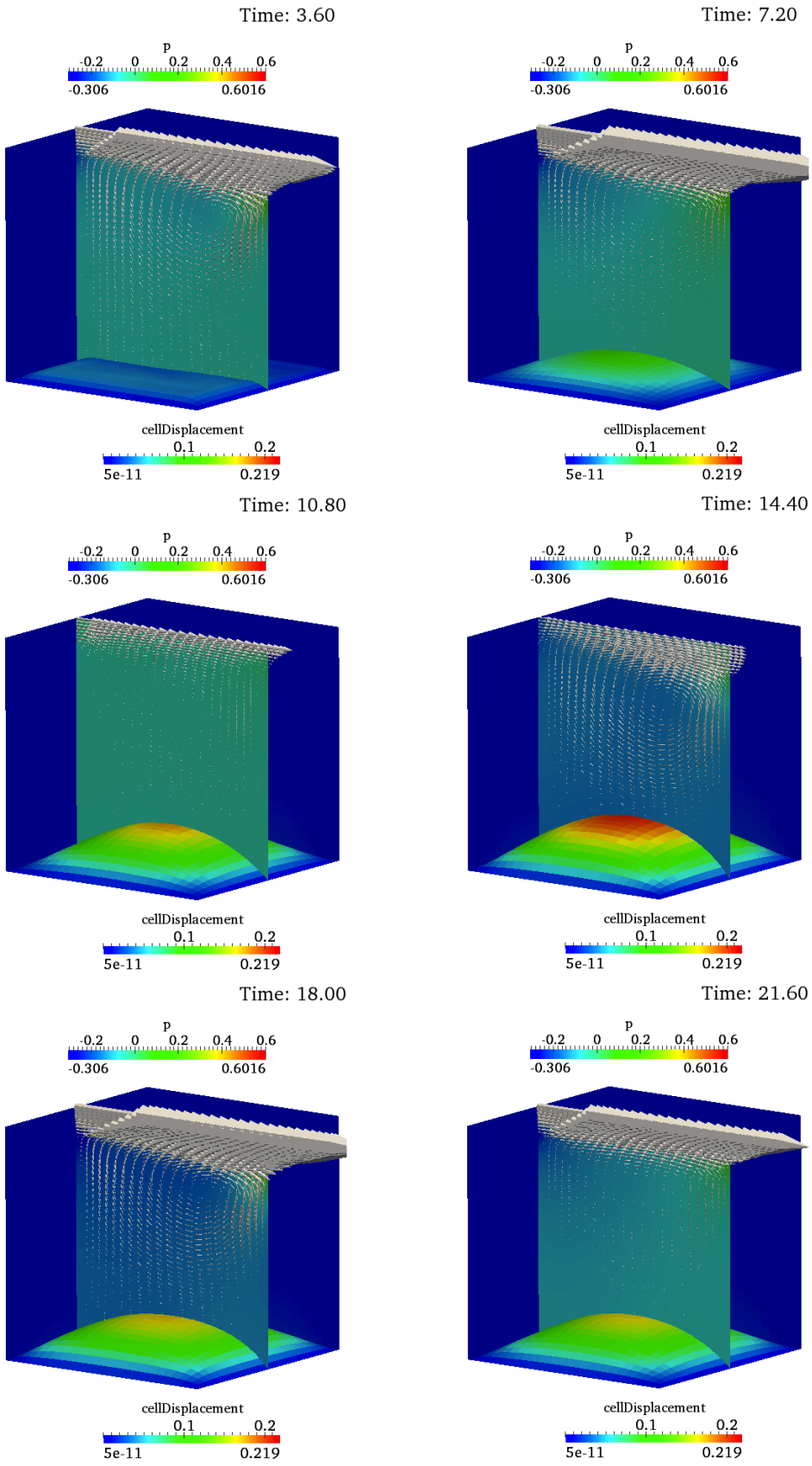

Figure 5.29: Various instants of the simulation using damping coefficients C_1=1.5; C_2=0.05

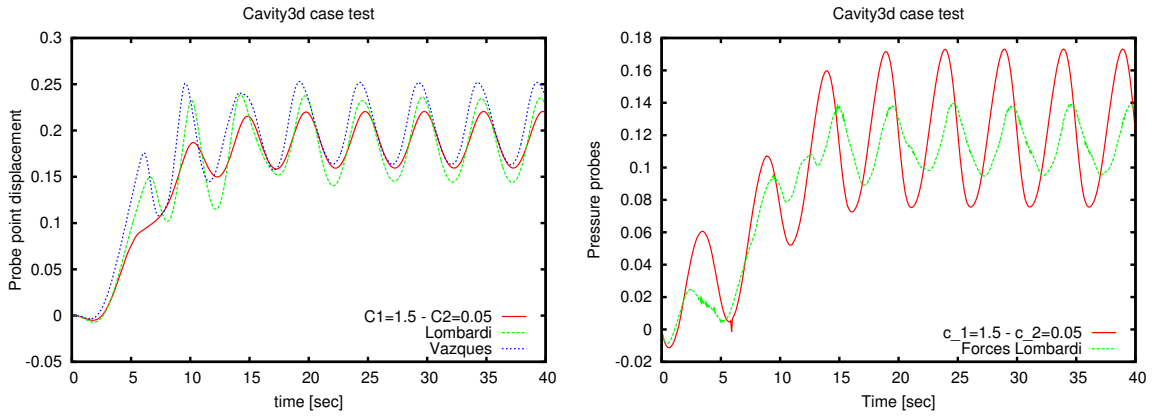

Figure 5.30: *Left*: Displacement of one point in the center of the structural interface. Damping: C_1=1.5; C_2=0.05. *Right*: force plot for the analysed case

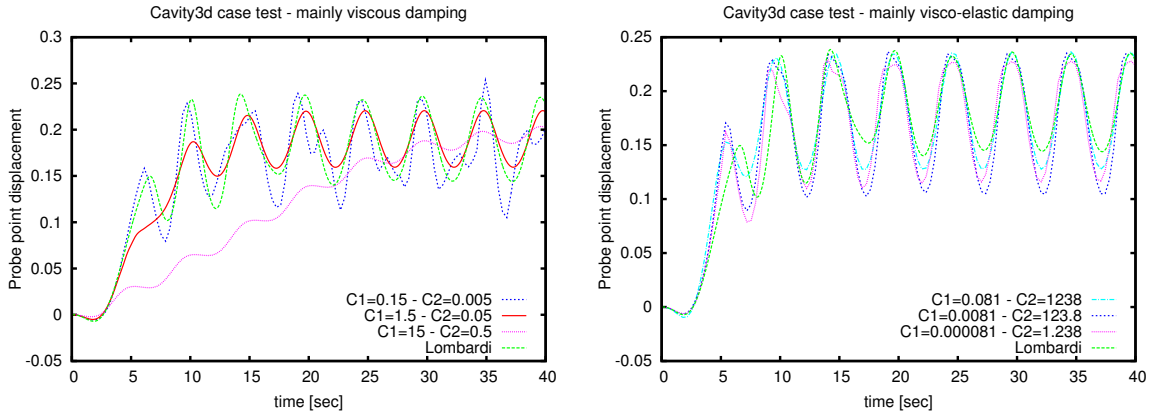

Figure 5.31: *Left*: Displacements of the point probe when using a mainly viscous damping. *Right*: mainly visco-elastic damping. In both case the reference solution [19] is reported

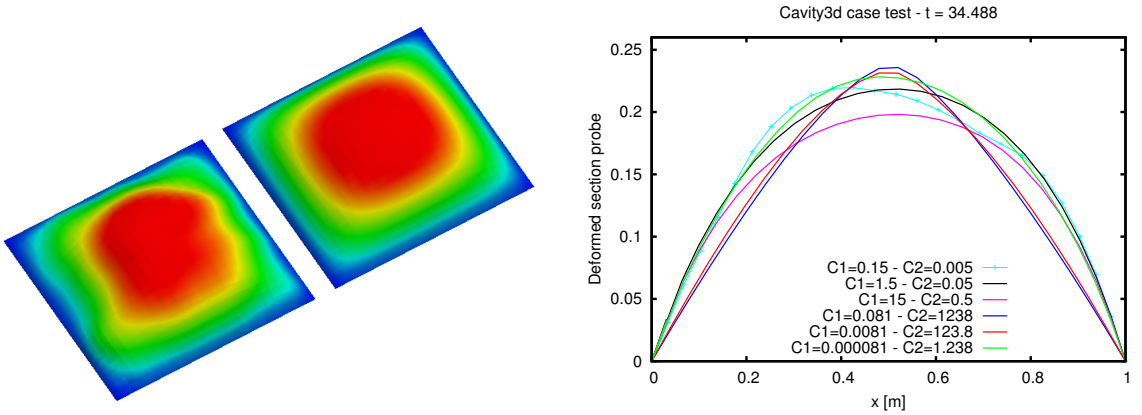

Figure 5.32: *Left*: screen shot of the configuration of the deformed interface at the same instant (t=34.488) for different damping coefficient values: $c_1 = 0.15; c_2 = 0.005$ and $c_1 = 1.5; c_2 = 0.05$. Higher modes appear on the deformed shape when adopting small values of viscous damping. *Right*: cross section of the structural interface showing the shape

5.2.4 2D Channel with Flexible Wall

The case of a channel with a flexible wall has been presented by [83] and [13], as represented in Figure 5.33. The test case was here repeated; some inconsistency must however be highlighted compared to the reference set-up: in the present case the structural interface is treated in the fluid domain as a zero thickness surface, while in the references the thickness is entirely represented in the fluid domain. It can be however argued that such an inconsistency is small because the thickness of the structure is small compared to its length ($t/L = 5 \cdot 10^{-3}/2.5 \cdot 10^{-1} = 2\%$).

A parabolic velocity profile was imposed at the inlet, going from 0 in $y = 0$ to $\overline{v}$ at the top of the domain $\overline{y} = 0.25$. A cosine function in time was imposed to the top velocity $\overline{v}$ in order to realize a smooth transient to reach the final steady state. Such a law in time was represented by the piecewise function:

$$\overline{v}(t) = \begin{cases} \frac{0.06067}{2}\left(1 - cos\left(\frac{\pi t}{10}\right)\right) & \text{if } t < 10 \\ 0.06067 & \text{otherwise} \end{cases} \tag{5.14}$$

On the other surfaces defining the calculation domain the velocity was imposed as in Table 5.10. No damping was applied to the structure. The two-dimensional domain was represented as one-cell thick three-dimensional domain, and it was discretized using 2700 hexahedra in the fluid domain, with 19 tetrahedra representing the structural interface. The physical quantities used for this case are reported in Table 5.7. The case is completely laminar, since the *Reynolds* number value is 100.

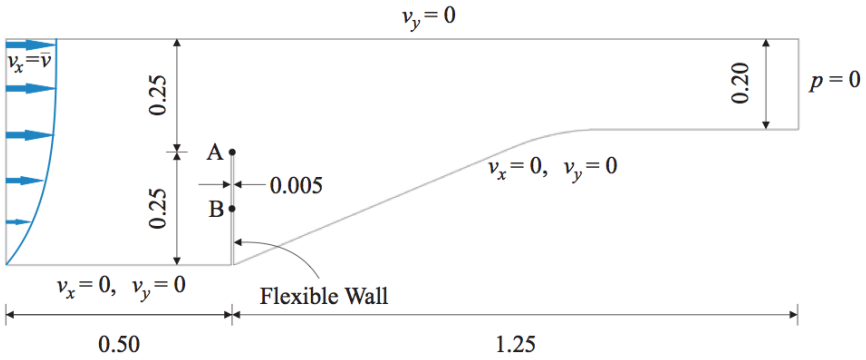

Figure 5.33: Case setting. From [13], Figure 5.18

A very good correlation is found between the results of this analysis and the reference results in terms of displacements: in particular the present analysis closely follows the results published by [83]. A higher scatter is found in terms of pressure probes, and in particular

Table 5.7: Physical quantities adopted for the case of the channel with flexible appendix

ρ_f $[Kg/m^3]$	ν_f $[m^2/s]$	t_s $[m]$	ρ_s $[Kg/m^3]$	ν_s $[-]$	E_s $[N/m^2]$	Re_L $[-]$	dt $[sec]$
956	0.145	0.005	1500	0.45	$2.3 \cdot 10^6$	100	0.01

Table 5.8: Boundary conditions applied for the channel with flexible appendix

	Inlet	Outlet	Top wall	Bottom wall	Struct. interface
U	$\overline{u}(y,t)$	Zero Gradient	Free slip	Wall function	movingWallVelocity
P	Zero Gradient	0	Zero Gradient	Zero Gradient	Zero Gradient

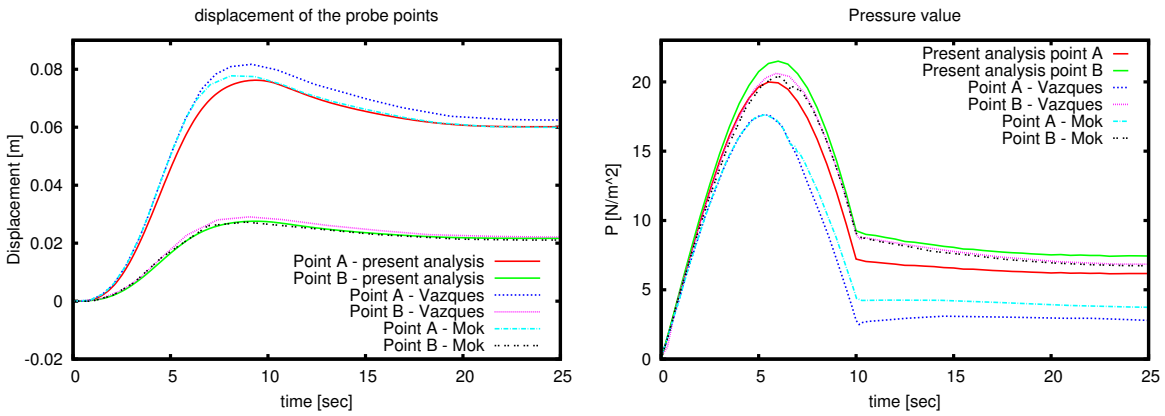

Figure 5.34: Comparison of the present results in terms of *left*: probes point displacement and *right*: probes point pressure

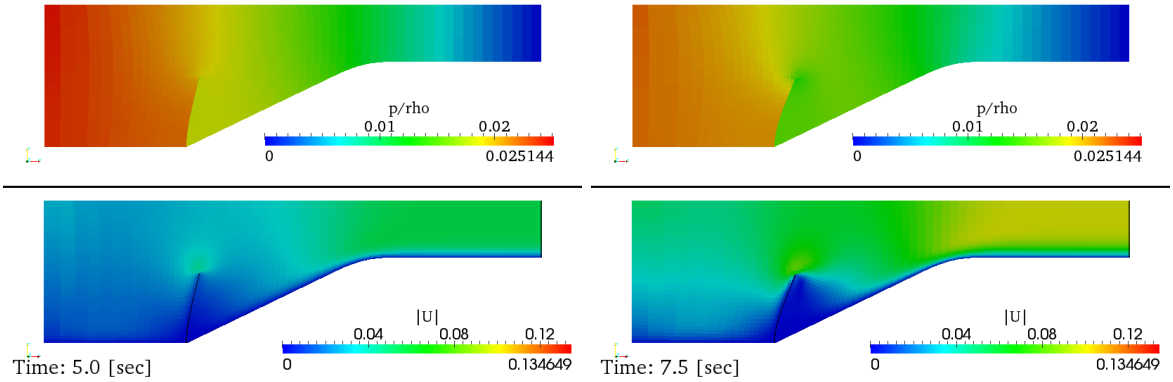

Figure 5.35: Schreen shot of the solution in terms of pressure and velocity. Time t = 5 ; 7.5 [sec]

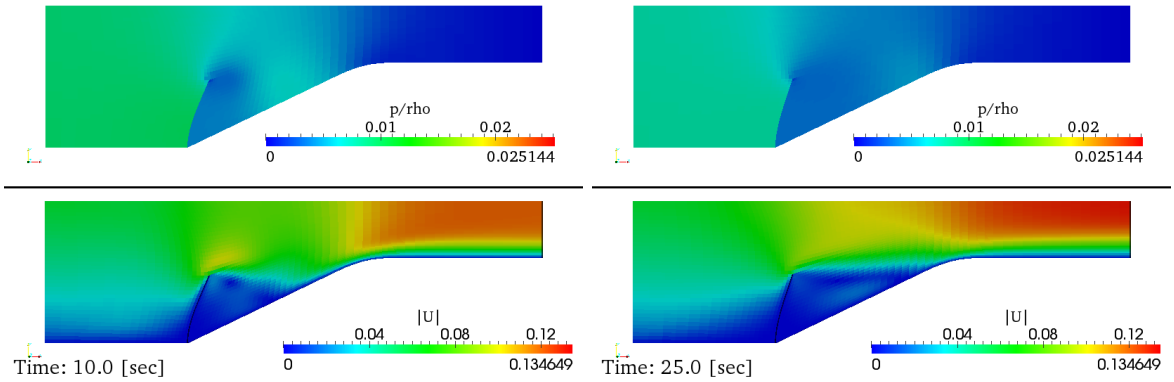

Figure 5.36: Screen shot of the solution in terms of pressure and velocity. Time t = 10 ; 25 [sec]

compared to the reference solutions the pressure results in the present case more uniformly distributed. The pressure at the point A takes in fact values very similar to the pressure measured at the point B, while this value is almost doubled for the reference solution (see Figure 5.34.

Various screen shots of the solution are reported in Figure 5.35 and 5.36 in terms of pressure and velocity fields. Figure 5.37 *left* reports the plot of the pressure forces integrated on the structural interface in time. Although the pressure signal in Figure 5.34 *left* looks smooth, some noise appears in terms of the global force signal. The origin of such a noise could be an excessive value of the convergence criterion, or it could be related to a lack of the numerical diffusion (See Section 5.1.5). Some comparable disturbance has also been identified in Section 5.2.2, Figure 5.23. Such a noise has however very limited amplitude but a rather high frequency, thus its effect on the structural deformation is absolutely negligible.

Figure 5.37 *right* reports the number of FSI iterations per time step required in the analysis for reaching convergence. The pressure signal has also been scaled and plotted in the graph. Good correlations can be observed between the applied load and the number of iterations required to reach the equilibrium.

5.2.5 2D Flag validation test case

The case of a channel flow with a flexible appendage has been proposed by [83], [13], [16]. The computational domain is represented in Figure 5.40. As in Section 5.2.4, an inconsistency must be underlined between the present analysis and the reference results used for validation purposes. In the present case in fact the structural interface is represented as a $zero-thickness$ surface in the fluid domain, whereas the thickness was entirely represented in the reference cases. Such an assumption was considered acceptable, the thickness being small

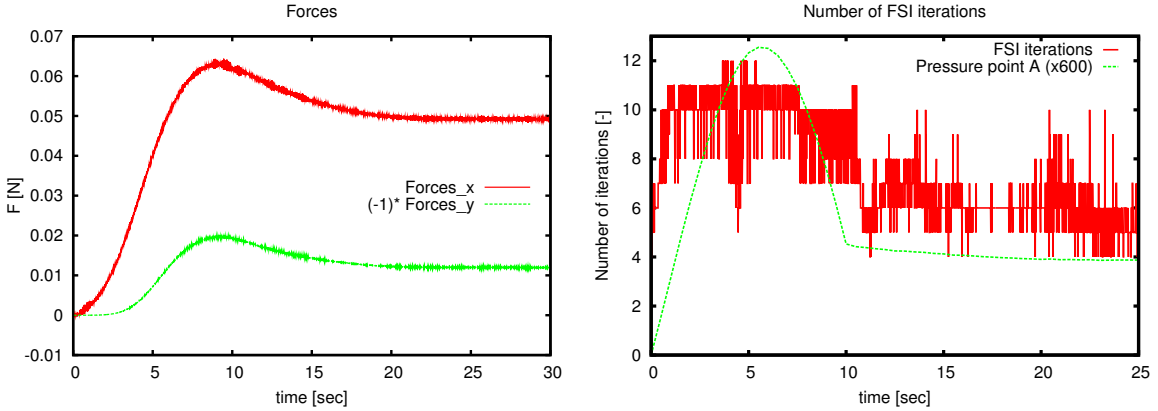

Figure 5.37: Channel with flexible appendix. *Left*: pressure forces integrated on the structural interface and *right*: number of iterations per time step. The pressure signal (opportunely scaled) is reported for comparison

compared to the longitudinal extension of the flexible appendage ($t/L = 6 \cdot 10^{-2}/4 = 1.5\%$).

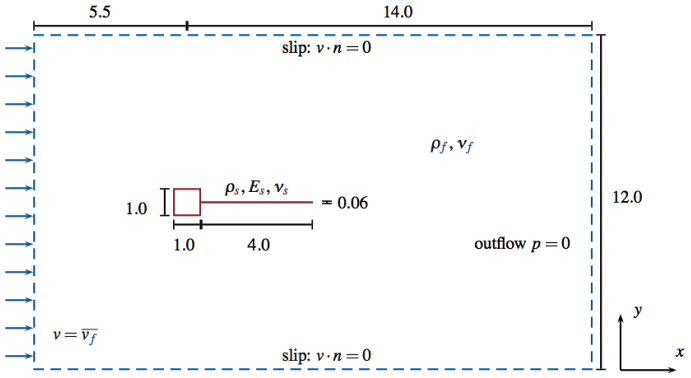

Figure 5.38: Channel flow with flexible appendage: computational domain. From [16], Figure 14

Compared to the previous test case in Section 5.2.4, in this case the *Reynolds* number is higher ($\approx$ 330). The flow exhibits then a transient behaviour (see also Section 3.4.1), where vortices are shed from the square bluff body and periodically excite the structure. The thickness and the material of the structure, reported in Table 5.9, are chosen so that the natural frequency is close to the frequency of the vortex shedding.

A fluid mesh with 7054 tetrahedra was employed, with 40 elements representing the structural interface (see Figure 5.42). This mesh was conformal to the one used by [16] and allowed a relatively fast solution. The whole coupled simulation (20[*sec*] physical time) takes about one night of computation on two processors, one of which was in charge for the fluid and one for the structure.

The case was initialised by running a purely fluid simulation for one [*sec*], thus obtaining

a steady but coherent fluid field with two main symmetric vortices, the center of which is located close to the tip of the structural interface, and two secondary vortices on each side, see Figure 5.39. Because of the symmetry of the field this configuration produces no transverse load, thus the coupled simulation begins smoothly and it is likely not to produce any shock or instability in the initial phase. After this phase, $6-9$ FSI Iteration per time-step were needed to reach convergence.

Table 5.9: Physical quantities adopted for the case of the channel with flexible appendage

ρ_f $[Kg/m^3]$	ν_f $[m^2/s]$	t_s $[m]$	ρ_s $[Kg/m^3]$	ν_s $[-]$	E_s $[N/m^2]$	Re_ℓ $[-]$	dt $[sec]$
$1.18 \cdot 10^{-3}$	$1.54 \cdot 10^{-1}$	0.06	0.1	0.35	$2.5 \cdot 10^6$	330	0.001

Table 5.10: Boundary conditions applied for the channel with flexible appendage

	Inlet	Outlet	bluff body	Struct. interface
U	(51.3, 0, 0)	Zero Gradient	Wall function	movingWallVelocity
P	Zero Gradient	0	Zero Gradient	Zero Gradient

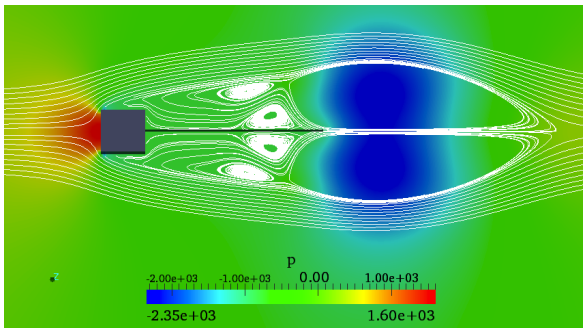

Figure 5.39: Channel flow with flexible appendage: screen shot for the initialised pressure field and streamlines ($t = 1\,[sec]$)

Results are reported in terms of the tip point displacements in Figure 5.43 with the results from [83], [13] and [16] for comparison. The tip point displacement is in fact representative of the whole displacement field: as it is shown in Figure 5.43 the structure mainly oscillates in the first mode, see also [83].

After an initial transient, the duration of which is 2 to 3 $[sec]$, all the solution converge

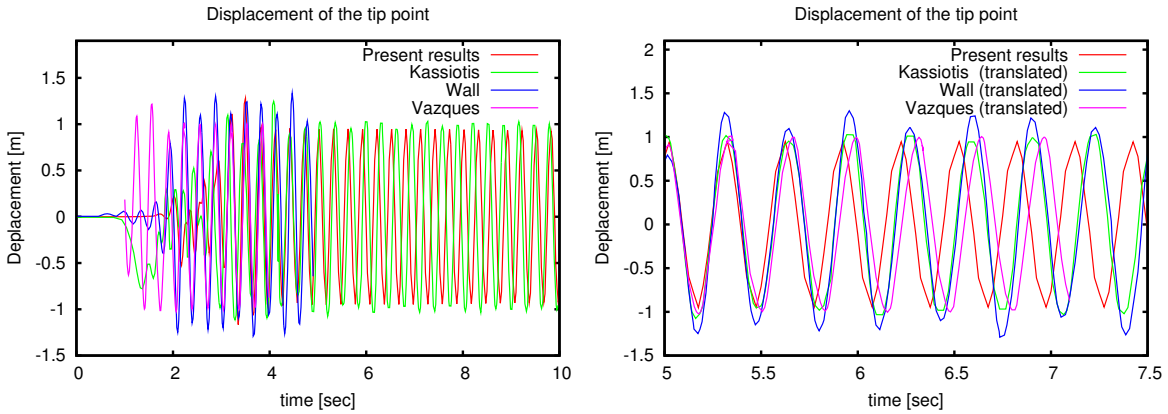

Figure 5.40: Channel flow with flexible appendage: horizontal displacement of the tip point. *Left*: present and reference results in the whole simulation. *Right*: zoom on the same data, with all the curves translated in order to get the same starting point for $t = 5\,[sec]$

on the same band of values ($\approx -1 \rightarrow 1$). The results for the present solution are relatively regular, and they lie particularly close to the solution reported by [16], which used the same fluid solver and computational mesh for the fluid domain. The other reference results lie in quite a large band, with harmonic oscillations which are not identified by the present solution and which are only partially identified by [16]. Similar considerations can be done in terms of the oscillation frequency, see Figure 5.40 *right*. In the Figure a part of the steady region is reported for the whole set of solutions, with curves translated such as the phase in the left part of the plot is comparable. The oscillation reproduced by the present solution results faster than the reference solutions; the resulting difference is however quite small. Note in particular that the distance between the present solution and the solution [16] is comparable with the difference between the solution [16] and [13].

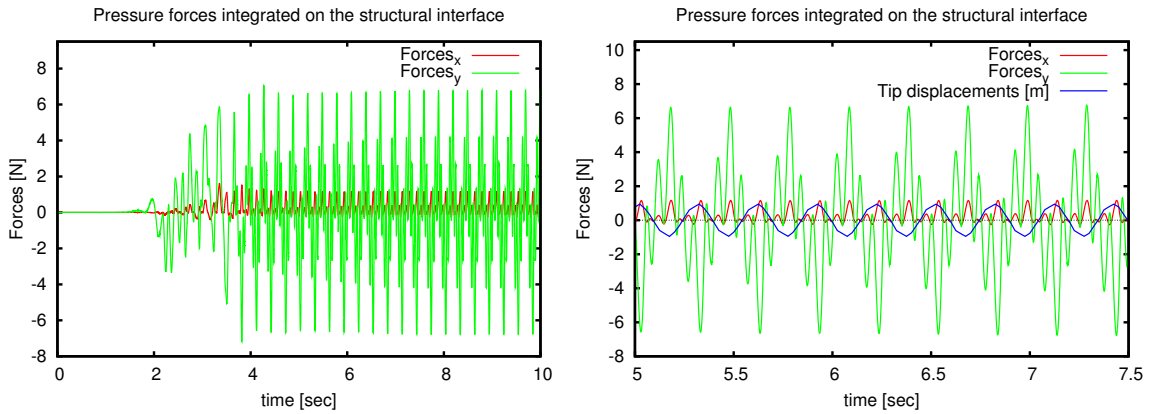

Figure 5.41: Channel flow with flexible appendage: pressure forces integrated on the structural interface. *Left*: whole simulation; *right*: zoom on a portion of the simulation ($5 \rightarrow 7.5\,[sec]$)

The force plot in Figure 5.41 shows a cyclic behaviour with three main peaks per cycle, due to the complex vortex formation shown in Figure 5.43. The phase of the force signal and the tip displacement are time-shifted of one cycle, for the effect of the relatively high inertia of the structure.

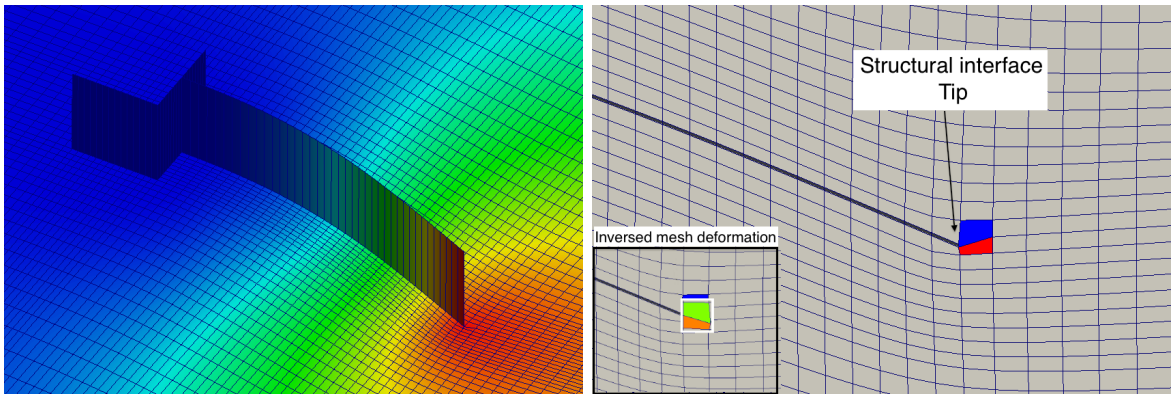

Figure 5.42: Channel flow with flexible appendage: *left*: Laplacian diffusion of the mesh motion. *Right*: detail of the deformed mesh at the tip of the structural interface, where the deformation of the mesh is subjected to distortions when the larger displacements are applied

The fluid mesh was deformed using a Laplacian operator, the role of which is to spread the displacements of the structural interface into the whole fluid domain. A diffusivity coefficient based on the inverse of the squared distance was adopted, because this strategy gives the better performance in terms of mesh quality conservation (see [122]). Figure 5.42 *left* shows the global mesh deformation for the higher displacements of the structural interface ($U_y \approx 1$). Although the mesh quality is generally well preserved, the elements close to the tip of the structural interface are subjected to distortions. This is probably caused by the singular point which represents the tip; in this point the mesh motion algorithm is unable to correctly detect the sign of the motion and inverts the displacement of the element. This has been represented in Figure 5.42 by inverting the region of the image close to the tip (see the smaller box in the bottom-left of the Figure). It appears that the calculated displacement of the first point connected to the tip of the structural interface moves in the wrong direction; whereas changing the sign of the motion preserves the tangency with the body.

5.2.6 Gennaker like Sail

A spherical surface is used to define a Gennaker-like sail, as shown in Figure 5.44. The principal dimensions of the structure and the applied physical quantities are reported in Table 5.12, and are the typical dimensions for a model-scale sail. The structure was designed using

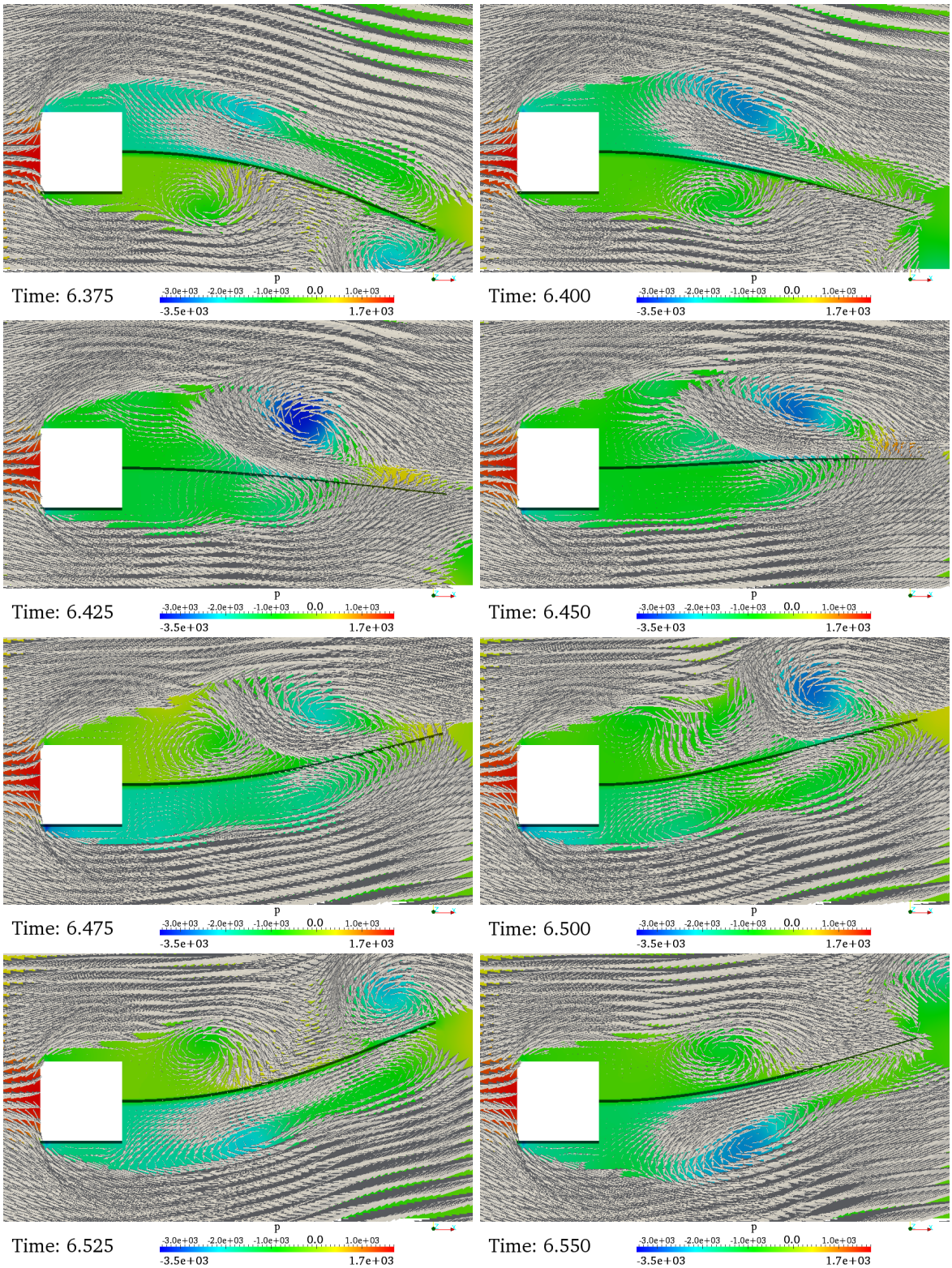

Figure 5.43: Channel flow with flexible appendage: Sequence of snaps shots for one complete cycle of the displacements of the flexible appendage

a sphere of radius 1 $[m]$, a horizontal span of 60°, a vertical span of 96° in correspondence of the leading edge and of 76° at the trailing edge. The sperical sector so defined was then rotated of $\pi/4°$ around the vertical axis and of $-\pi/5.2°$ around the x-axis. The geometry so defined is shown in Figure 5.44. The sail was constrained on two corners; a cable boundary condition was applied to the third corner, where the attachment point of the cable was set at the point (1, 0.93, -0.6). The distance between the fixed point and the attachment point on the sail is: vertical= $0.2\,m$, transversal= $0.02m$, axial= $0.93\,m$.

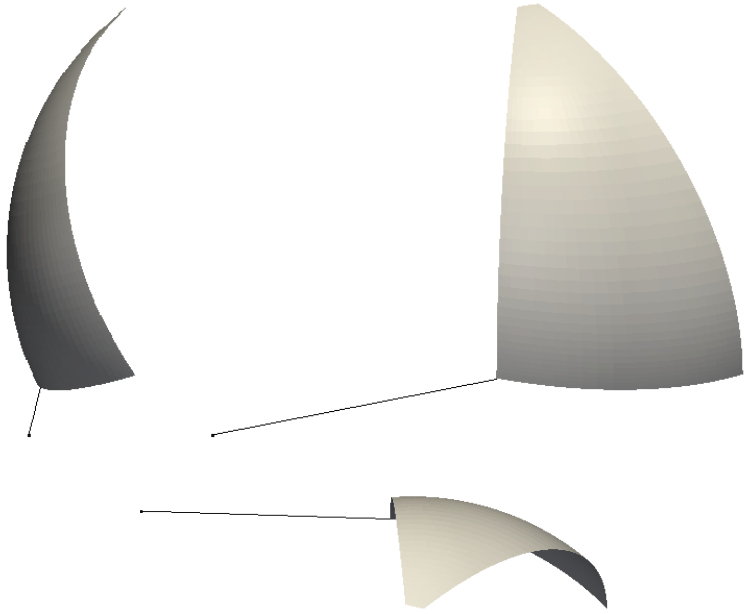

Figure 5.44: Geometry of the undeformed sail, obtained using a spherical sector of radius R.

Table 5.11: Geometry quantities used for the definition of the sail and the fluid domain

H	P	R	ℓ_{cable}	x_{domain}	y_{domain}	z_{domain}
$[m]$	$[m]$	$[m]$	$[m]$	$[m]$	$[m]$	$[m]$
1.2	0.8	1	0.94	6	5.5	2.7

Eigenanalysis was performed as in the previous chapters for identifying the Rayleigh damping coefficients and the mode shapes of the sail. Some of the first eigenvectors are reported in Figure 5.45; it is expected that the deformation of the sail will primarily involve the first mode, with higher modes propagating along the free edges of the sail. The damping constants, calculated in the standard way as in the previous chapters, resulted to be: $c_1 = 0.0084$ and $c_2 = 118.74$.

Table 5.12: Adopted physical quantities

ρ_s $[\frac{Kg}{mm^3}]$	t_s $[mm]$	E_s $[\frac{N}{mm^2}]$	ν_s $[-]$	ρ_F $[\frac{Kg}{m^3}]$	ν_F $[\frac{m^2}{s^2}]$	U_{inlet} $[m/s]$	Re $[-]$
$1.15e^{-6}$	.1	188	0.4	1.225	$1.15e^{-5}$	$(0.8, 1.2, 0)$	$0.9e^5$

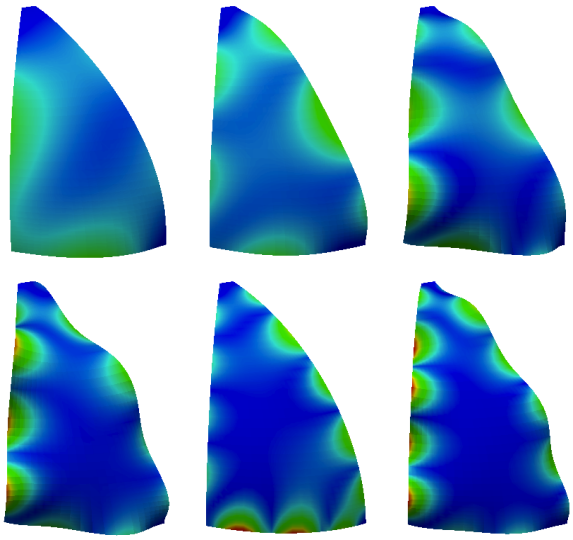

Figure 5.45: Eigenvectors 1, 3, 5, 7, 9 and 10 for the analysed configuration

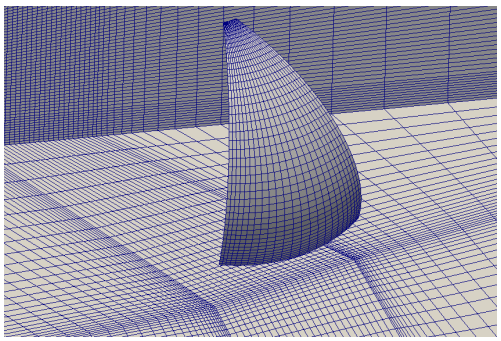

Figure 5.46: Fluid mesh adopted for the case of the Gennaker

A fluid mesh with 260-thousand Hexaedra was used, with thousand hexaedra constituting the structural interface, as it is shown in Figure 5.46. The element size in the region close to the wall was set to be coherent with the use of wall functions, therefore it was realised $y^+_{avg} > 30$. The mesh was designed in order to allow for some distortion of the fluid elements and for keeping the calculation time within reasonable limit.

The fluid field was initialised with constant velocity and the geometry of the sail was kept fixed, until when a steady state was reached after $7.5[sec]$, as in Figure 5.50, where

the coefficients are calculated using the projected area of the sail 1.13 $[m^2]$. As expected, a stationary flow is encountered, with local recirculation in the region close to device in the leeward side of the sail, as in Figure 5.47. Tip vortices are generated from the top and the bottom of the sail, as it is identified by the streamlines in Figure 5.48. The force coefficient plot for this initial phase in reported in Figure 5.50 *left*.

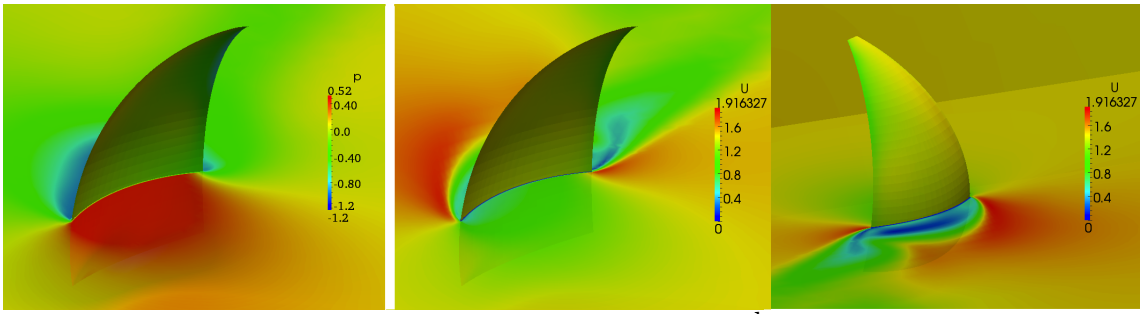

Figure 5.47: Initial fluid field in terms of: a pressure and b-c velocity horizontal cuts. The height of the section cut is approximately $\frac{1}{3}$ of the height of the entire device

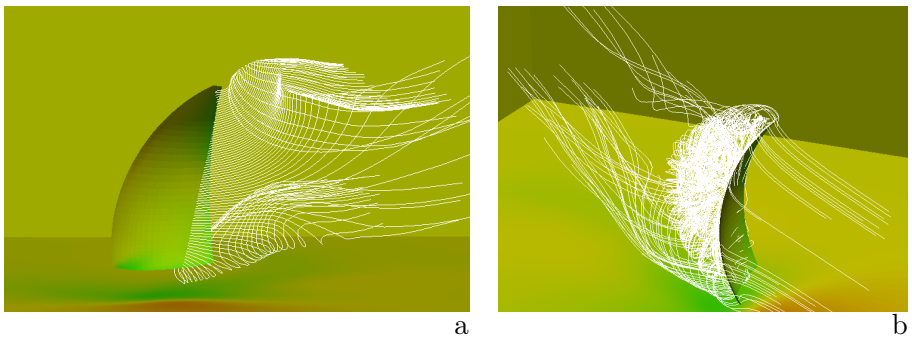

Figure 5.48: Initial fluid field in terms of streamlines view. The streamlines probed in the windward side (a) show a potential behaviour with two tip vortices. A local recirculation region is identified in the leeward part of the sail (b)

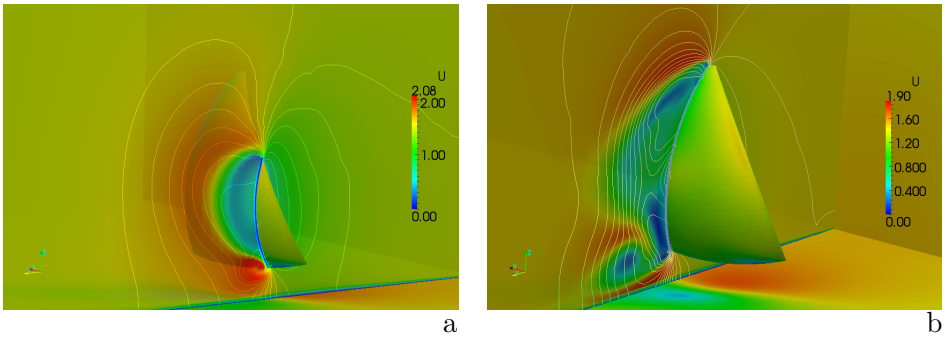

Figure 5.49: Initial fluid field: vertical section cuts close to the leading edge (a) and the trailing edge (b) of the sail in terms of velocity magnitude and contours

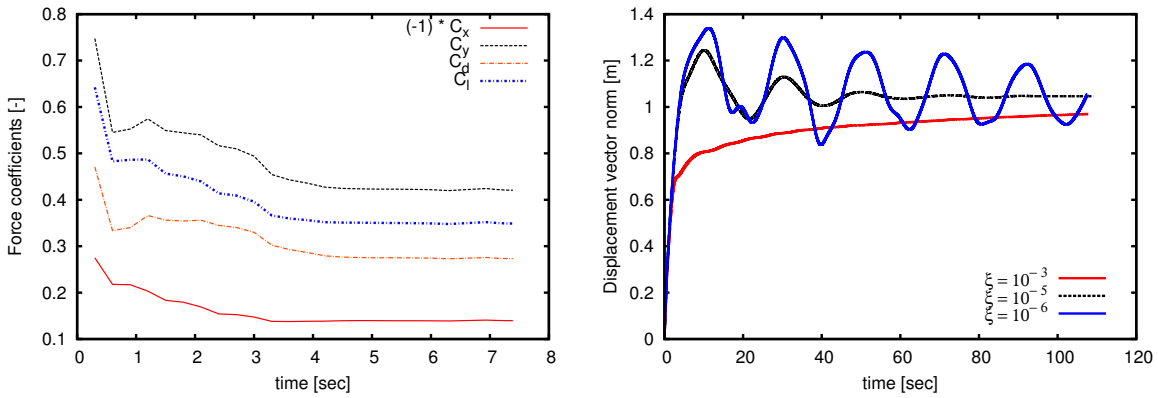

Figure 5.50: *Left*: force coefficients in the initialization phase with fixed geometry. *Right*: norm of the displacement vector for different values of the damping coefficient ξ

Fluid Structure Interaction analysis was performed using this fluid field as a starting point. No particular initialization was used for the structural model. The dynamic analysis with no artificial damping ($\xi = 0$) produced the divergence of the solution for the combined effect of the limited thickness and the instability induced by the cable boundary condition. It was found, however, that a very small damping ($\xi = 10^{-6}$) was sufficient to overcome the instability, with no remarkable effect on the general behaviour of the structure. Figure 5.50 *right* reports the displacement vector for different damping coefficient values. The results obtained using this damping value show however a continuous oscillation which seems rather um-physical. By experience it can be adduced that typically the inflation of a sail follows an "almost" critical damped path, with eventually one or two main oscillations before settling to a final steady value. In this sense the most realist path appears to be the one obtained using $\xi = 10^{-5}$. The results obtained with this damping value will be then discussed in the following.

Figure 5.51 reports the velocity and the pressure fields over a vertical section passing close to the trailing edge of the sail.

Although the deformation path follows mainly the first mode, some higher frequencies are excited for the smaller values of the damping. The evolution of the structure influences the main two vortices, which are reinforced because of the increase in the curvature of the sail. This is further confirmed by the pressure field, which is initially relatively smoothly distributed. In the final phase though two main lower pressure regions are generated, the centre of which is located on the higher third and the bottom of the sail.

As the sail is inflated, it follows a typical under-critical damping deformation path, which converges to the final value in the time of about one natural period ($\approx 20[sec]$). Although

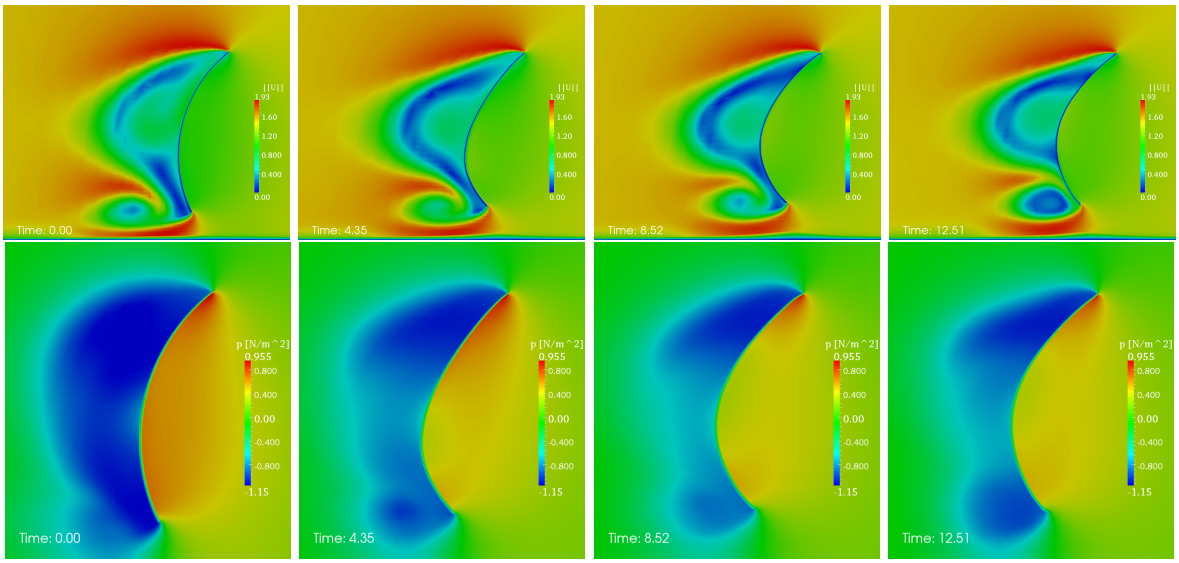

Figure 5.51: Vertical section cut in terms of *top*: velocity and *bottom*: pressure field, with the time evolution of the structural interface and of the main two vortices. From *left* to *right* the screen shot are captured for $t = 0; 4.35; 8.52$ and $12.51\,[sec]$

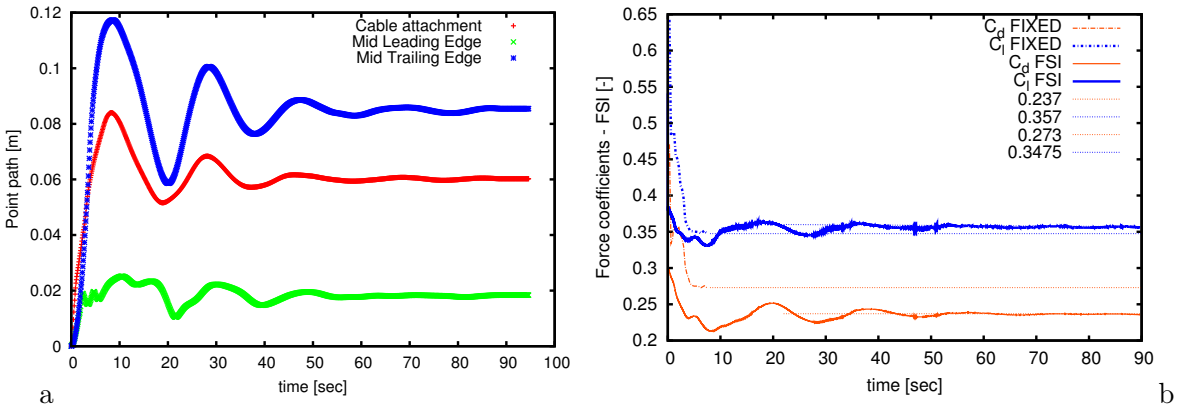

Figure 5.52: Time path of three probe points on the structural interface and lift/drag coefficients during the inflation process. The values obtained for the fixed geometry and already presented in Figure 5.50 are reported

this time constant appears relatively long, its value seems confirmed by the case with the Rayleigh damping set to zero, before the divergence of the solution. The evolution of the whole sail and the particular boundary condition is well represented by the three points path represented in Figure 5.52-*a*. The evolution of the cable attached point is relatively bounded, because of the boundary condition, constricting the displacement path on a spherical surface. Larger displacements arise on the trailing edge, as it can be seen also in Figure 5.54 both in terms of the global displacements and the deformation of some chosen sections.

The force plot is reported in Figure 5.52-*b*, where also the force obtained with the fixed

geometry and already reported in Figure 5.50 is reported for the comparison. The drag is reduced by 15% and the lift is increased by 3%. This behaviour is not surprising, and it can be easily explained observing the sections reported in Figure 5.54. As the sail is inflated, the structural deformation determines the sections of the sail to 'open', slightly changing the initial configuration, which results in this case to be initially over-trimmed.

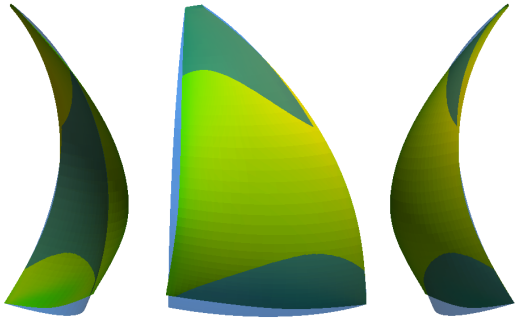

Figure 5.53: Design (blue) versus final flying shape (yellow). Back, side and front view

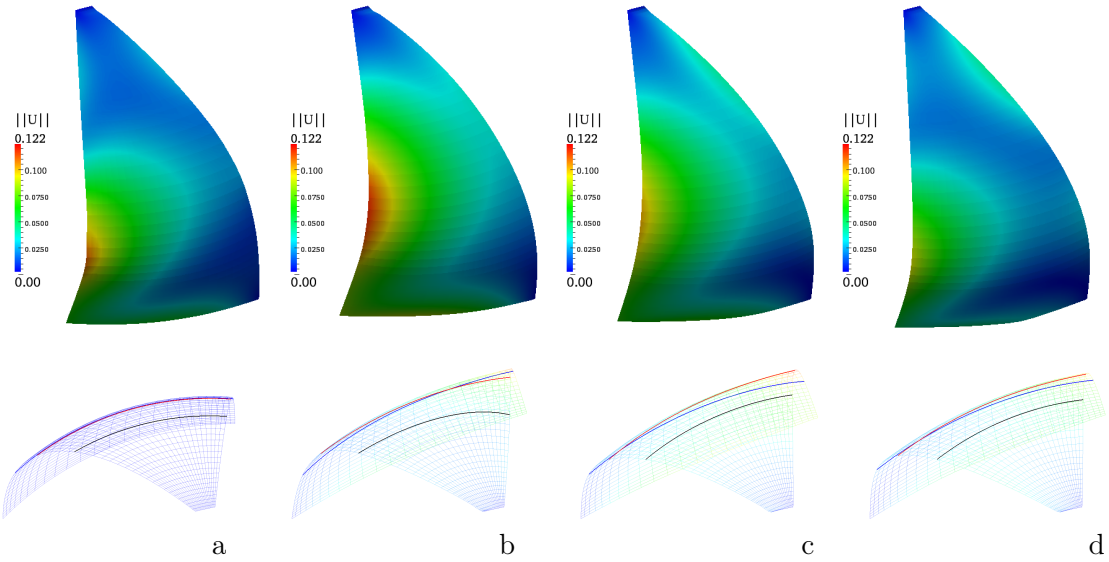

Figure 5.54: Evolution of the structural interface and of the section cuts highlighted in Figure 5.52.

The unsteady behaviour of the sail was reproduced, and the results are qualitatively coherent with experimental observations and the practise of sailing. The impact of the fluid-structure interaction effect was shown, and differences in the force generation were found to overcome 15 % in terms of the drag force.

Effect of the longitudinal position of the cable attachment point

This section investigates the effect of the longitudinal position of the attachment point of the cable: this corresponds to the effect of the lead car on a real sail-boat. Simulations were repeated with the previous settings for four configurations, where the transversal and vertical coordinates are constant and set as in the previous analysis: $y = 0.93$, $z = -0.6$, while four values of the longitudinal position of the cable attachment point were tested, namely $x = 0.5$, 1, 1.5, 2, as shown in Figure 5.55.

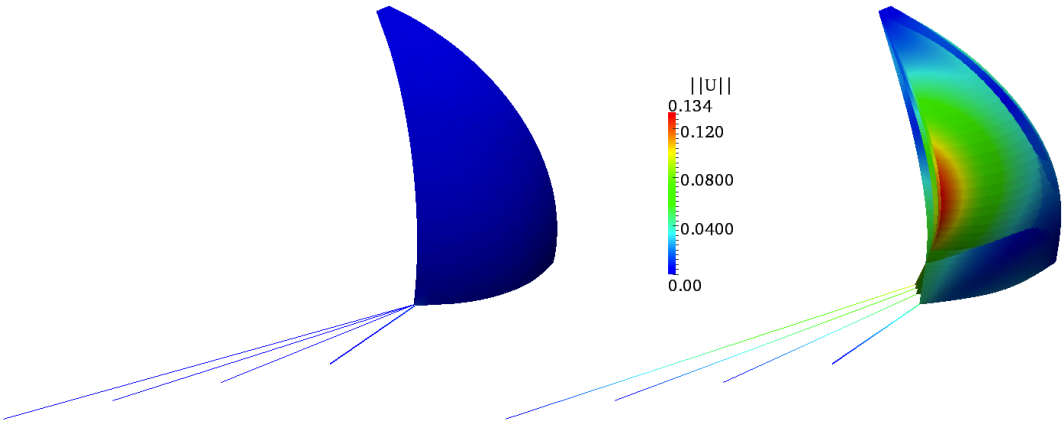

Figure 5.55: Four configurations adopted for the investigation of the effect of the length of the cable: design and final deformed shapes

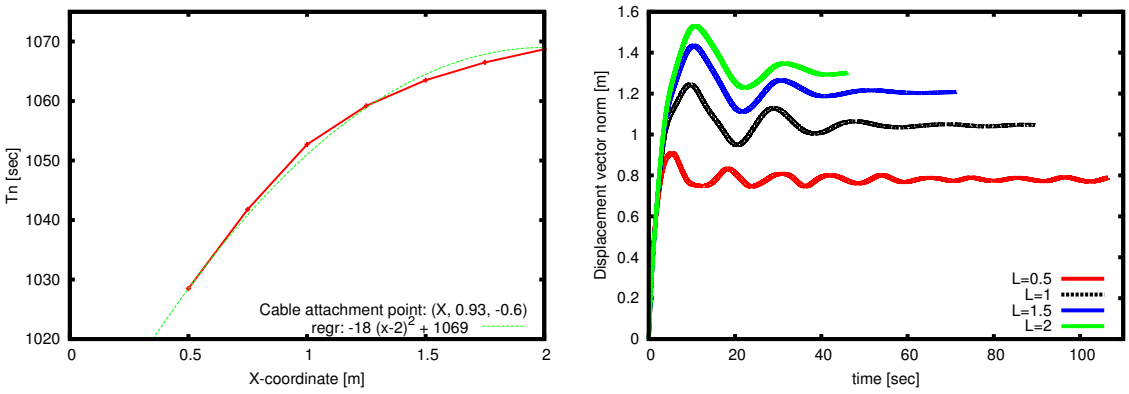

Figure 5.56: *Left*: Value of the natural frequency (linear calculation) as a function of the position of the attachment cable fixed point. *Right*:

Figure 5.56 *left* reports the value of the natural period for the linear structure; as the cable length increases the natural period becomes longer following a quadratic path. This is confirmed when observing the time evolution of the structure in terms of the norm of the displacements vector displayed in Figure 5.56 *right*. As the cable increases, the period of the

oscillations increases and the damping becomes more effective: the case with $X = 2$ settles on a steady path after two oscillations, while $X = 0.5$ produces numerous small oscillations, which are progressively damped at the end of the simulated time ($t = 106[sec]$). This behaviour can be explained observing that the damping coefficients were set for the case $X = 1$ and were left un-altered for the whole set of calculations. Because of the Rayleigh damping definition, the global damping coefficient ξ linearly increases with the natural period (see Section 4.1.9). Of course, as the length of the cable increases, the allowed displacements are also higher, as it is shown in Figure 5.56 *right*.

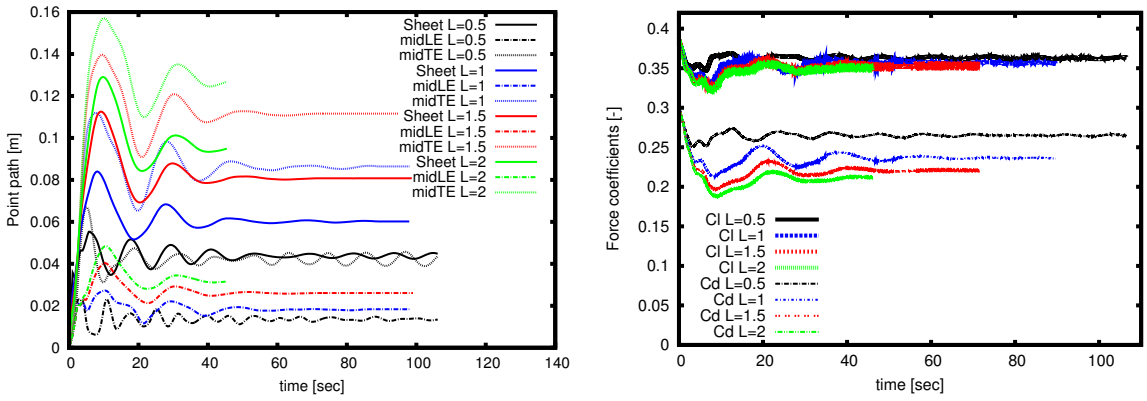

Figure 5.57: *Left*: point path (cable attachment, mid Leading Edge and mid trailing edge) and *Right*: value of the lift/drag coefficients versus time during the inflation of the sail.

The time path of selected points of the structure – namely on the cable's attachment point, on the mid of the leading, trailing edge – are shown in Figure5.57 *left*. The general behaviour of the four analysed configurations is similar to the behaviour discussed in Figure 5.56, thus this shows that the sail mainly deforms on the first mode; however a remarkable difference arises for the configuration with the shorter sheet. Unlike the other cases in fact, here the magnitude of the displacement of the sheet point is comparable with the magnitude of the displacement at the mid trailing edge point. This indicates that the trailing edge of the sail remains quite closed, and does not open as for the other cases, as it is confirmed by inspecting the section traces reported in Figure 5.58 *left*. This configuration is well know by sailors, who tend to advance the lead car when they want to close the trailing edge of the sail. By doing so in fact the action of the sheet is more vertical, thus increasing the tension on the trailing edge of the sail.

As the horizontal coordinate of the attachment point of the cable X increases, the lift coefficient remains relatively stable ($.353 - .364$, $\delta = 3\%$), whereas the larger variations are experienced by the drag coefficient ($0.21 - .265$, $\delta = 20.7\%$), see Figure 5.57. The lift is in fact

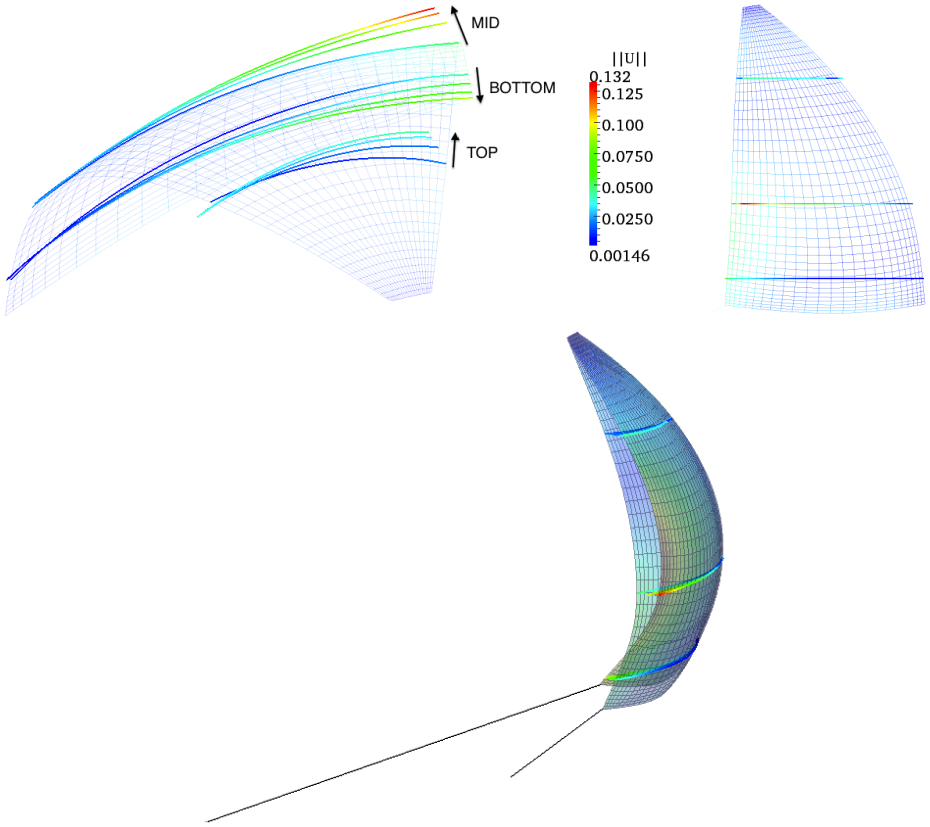

Figure 5.58: Section cuts on the sail: *left*: as the longitudinal position of the attachment point of the cable reduces the vertical component of the reaction force increases, slightly modifying the whole pattern of the sail. the deformed structural mesh corresponds to the case $X = 0.5$ *right*: the height of the section cuts; *bottom*: perspective view of the deformed sail with $X = 0.5$ and $X = 2$

primarily influenced by the leading edge, which remains almost unchanged on the whole sail, see Figure 5.58. The drag coefficient, on the other hand, shows to be primarily influenced by the configuration of the trailing edge, which is subjected to large variations. As X increases in fact the lower sections tend to close, while the sections in the rest of the sail tend to open, and the drag reduces. This indicates that the sail is not initially set into its optimal configuration.

5.2.7 The limitation of the technique: divergence in the case of the canopy caused by the excessive folding pattern.

In the previous Sections some FSI test cases have been analysed, which show the validity of the ALE method implemented in OpenFOAM for the coupled Fluid-Structure analysis. For the test cases which have been presented the topology of the structure remained however unchanged; in other words the deformation of the structural interface was constituted by a smooth mapping in space and time.

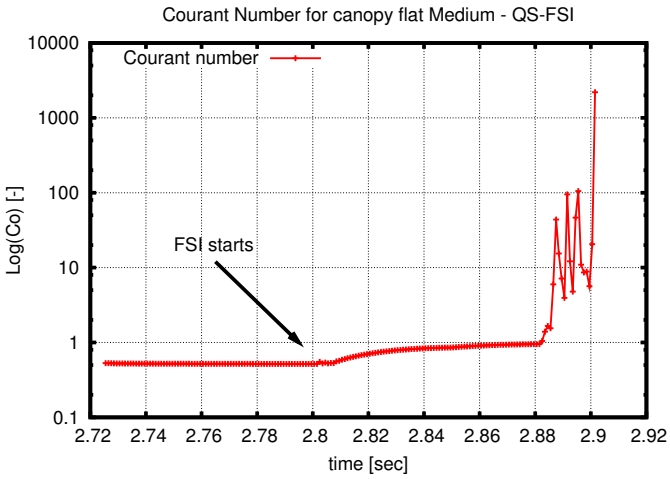

Figure 5.59: Courant number value during the simulation

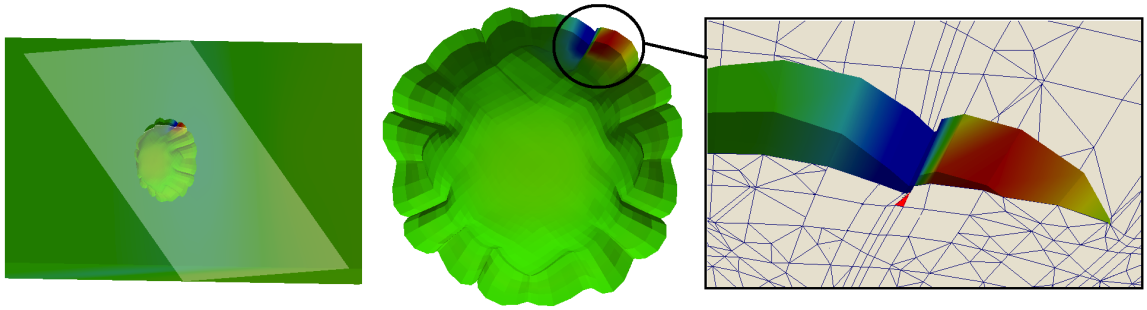

Figure 5.60: The fluid solution diverges because of the inversion of a volume cell. Triangular cells are the result of the graphic interpolation

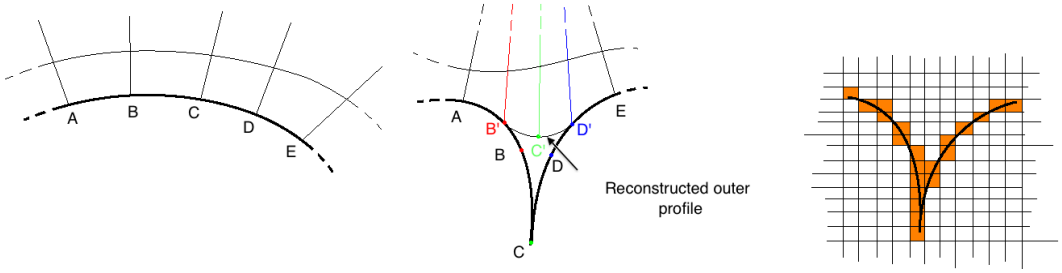

Figure 5.61: A possible way to treat the singularities represented by the wrinkles, on the *left*, is to use a smoothing, able to reconstruct the outer surface of the structure thus neglecting the singular region. On the *right*: a more practical way is to use a *ghost-cell* method

Scope of this section is to investigate the effect of topological changes, such as for instance the large wrinkles forming in the case of the parachute canopy, analysed in terms of the fluid dynamics in Section 3.3.3 and of structural mechanics in Section 4.3.2. Such folds are the effect of the initial shape of the structure – a developable surface – moving to a new deformed configuration which is namely non-developable (see in particular Figure 4.39 and 4.40).

The case was here tested in a FSI coupled environment, a series of screen shots of the solution are reported in Figure 5.62. As expected, the structural deformation begins under the effect of the fluid loading. Several folds are generated in correspondence of the cable's attachment points and the canopy assumes a rounded shape, as in Figure 4.42. However, after $2.9sec$ physical time the solution severely diverges, as it appears in terms of pressure in the fourth screen shot in Figure 5.62 and in terms of the Courant number in Figure 5.59.

The cause for this explosion of the solution is the singularity represented by the apex of the folds. Figure 5.60 reports a plot of the configuration of the canopy just before the explosion of the solution. It can be appreciated how the generated folds present a cusp in the apex, thus the volume elements result severely distorted in this region. In particular, the element highlighted in red in the right of the figure results negatively defined.

A volume element is negatively defined when one of the lines joining the node crosses one face. In this case the calculation of the element's volume results in a negative number, and the element is said to be negatively defined. Elements subjected to this type of distortions determine singularities in the solution, as it happens for instance in this case.

Several approaches might be adopted for the solution of problems of this kind. Re-meshing could contribute in some cases; however this might not be an effective strategy when self-contact arises on the surface of the structure. In this case a more radical topological change would be needed, able to reconstruct the outer pattern of the canopy, thus disconnecting the fluid elements from parts of the surface of the structural interface, as in Figure 5.61. In this case, when a deep wrinkle is recognized the internal nodes are moved on an external smooth surface, defined *ad-hoc*. The actual implementation of an algorithm capable of performing such a smoothing poses however several problems, from the automatic 3 dimensional recognition of the wrinkles, the definition of the smoothing and the transfer of the load from the reconstructed smoothed surface to actual configuration of the finite elements. Finally, there is no guarantee that such a method is conservative.

A more practical way to deal with such a problem is thus to prefer the ghost-cell method (see [81]) to the ALE method. With such an approach the fluid grid is not subjected to any deformation, and the deep folds can generate without problems, as in Figure 5.61 *right*. In this case the fluid grid is purely Eulerian, and the effect of the structure is represented as a boundary condition in terms of forces or velocity. The main problem is then the recognition of the position of the structure in the fluid grid; this is normally solved through the use of level set techniques [93].

Although the case presented here is a limit case, situations of this sort can be locally encountered when performing simulations on sail-type structures, see for instance Section 4.3.4. If this happens, the current analysis set-up in ALE framework is likely to diverge.

5.3 Summary

In this chapter the fluid and the structural calculations presented in the two previous chapters were coupled together. The Arbitrary Lagrangian Eulerian method was adopted, because this gives a conservative environment for the analysis of the fluid structure interaction analysis. It was chosen to use an implicit coupling algorithm assuring the stability of the scheme, although this is one of the most expensive options in terms of computational effort.

Several test cases were presented, the response calculated with the present method resulted coherent and comparable with previous analysis.

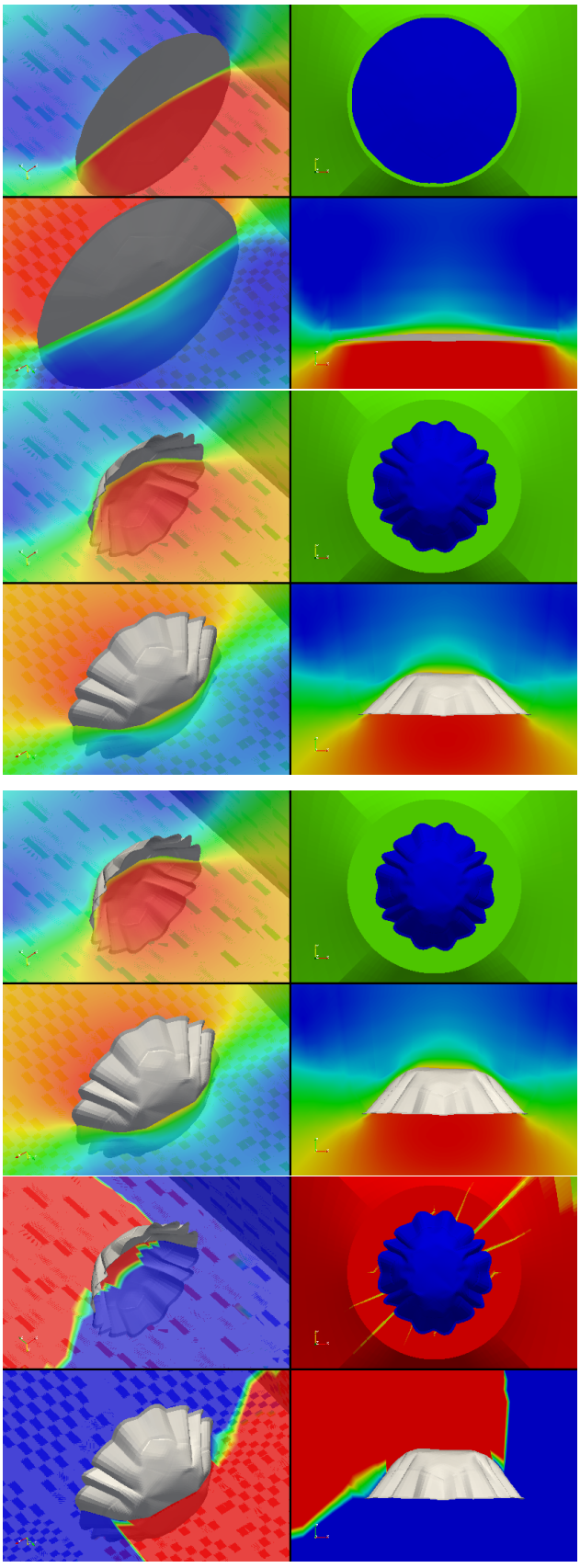

Figure 5.62: Pressure field during the coupled analysis. The deep folds generating on the surface of the structure determine the divergence of the solution

Chapter 6

Conclusions

6.1 Overview

The simulation of yacht downwind sails has been investigated with particular emphasis on the detailed simulation of the structural deformation, the flow development and the unsteady fluid-structure interaction analysis. In all these fields, the simulations have been critically approached and the most appropriate engineering techniques have been adopted.

Typical flow developing on downwind sails is turbulent, with a transitional zone in the beginning of the device, and separation arises for the effect of the curvature and the relatively high angle of attack. The combined effect of the particular flow regimes under analysis and the environment can produce unsteady flow conditions.

Downwind sails are highly deformable structures made of thin fabrics, the shape of which is influenced by the loading and the boundary conditions. When particular combinations of loading and boundary conditions arise the deformation of the fabric is affected by a buckling related phenomenon, called *wrinkling*, which determines out of plane oscillations on the deformed configuration. The extension of this phenomenon may affect large parts of the sail, thus slightly modifying the local stress/strain distribution in the structure.

The aim of this work was to develop a method able to produce a reliable analysis of the performances of the sails, both in terms of the fluid and the structural mechanics, and to couple such calculations in a conservative fluid-structure interactions framework. It was then chosen to couple an existing Finite Volume method with turbulence model (RANS) for the fluid dynamics analysis with shells finite elements for the analysis of the structural fabric deformation. The coupling was approached using an Arbitrary Lagrangian Eulerian (ALE) framework and an implicit algorithm.

The RANS approach was chosen for its relative computational efficiency: using methods with higher computing requirement could in fact result in a substantial increase of the com-

putational effort, especially when performing coupled fluid structure interactions analysis. Any future change in the solver can however be performed with ease, because the partitioned method allows great modularity.

Traditionally the structural analysis of sails has been approached using the membrane model. This model is based over the assumption that the structure is so thin that its bending stiffness can be neglected. The use of the membrane model may result in singularity of the (final steady) solution when particular combinations of stress and strain are encountered, typical for instance of the wrinkling, which is controlled by the bending stiffness. It was then chosen here to adopt the shell model, which considers all the deformation components and it is therefore suitable for the analysis of the wrinkled configurations typical of downwind sails. Elements of the MITC family have been chosen for their ability to treating structures with small thickness.

The ALE framework was adopted for the coupled fluid-structure interactions analysis because it is conservative and it guarantees no accuracy losses compared to similar analysis with fixed domains.

6.2 Contributions

The main contributions of this work to sail system flow analysis are presented here. They are divided in three main subjects, following the main structure of this work.

6.2.1 Fluid

The fluid dynamics has been analysed with the Finite Volume method and the turbulence has been resolved using the SST turbulence model. A complete review of the adopted methods has been detailed and – when possible – explanatory simplified examples have been presented. The prediction performances of the method have been discussed and numerous validation examples have been presented, both in terms of static and dynamic fluid analysis.

In terms of the stationary analysis, it was shown by means of experimental comparisons that the finite volume method with the SST turbulence model performs well in predicting the boundary layer development and adverse pressure gradient separation – once the right mesh have been set (see Section 3.3.1). The separation can also be geometrically induced, such as for instance by the presence of sharp edges. In this case (see Section 3.3.3) the mesh sensitivity is substantially reduced and the free shear flow results very well captured.

The principal effect of the presence of wrinkles on a 2D cross-section of boundary surfaces

– such as a wrinkled sail – consists in a substantial decrease of the lift/drag ratio compared to an equivalent smooth case; in computational terms the presence of the wrinkles reduce the requirements for mesh fineness, because the boundary layer thickness increases, and this determines a decrease in the effect of the wall on the outer flow (see Section 3.3.2). It results in fact that the flow splits in two regions, one of which is interested by local recirculation and one *potential* outer region. The pressures generated on the wrinkled surface oscillate around the value obtained for an equivalent smooth case.

Unsteady RANSE (U-RANS) techniques resulted generally able to adequately capture the behaviour of unsteady flows and the vortex shedding induced unsteadiness (see Section 3.4); the unsteadiness results to have a substantial impact on the performances of the sail, and it increases (+5%) the performances of drag devices such as a downwind sail.

6.2.2 Structure

The fabric was simulated using *shell* finite elements, for which all the components of the deformation (membrane, bending and shear) are directly reproduced. It is then possible to analyse post-buckled configurations such as the wrinkling without the need for additional *ad-hoc* models. The instability due to the very limited thickness ratio and to the wrinkling is overcome by the use of a dynamic scheme with *Rayleigh* damping, allowing to avoid divergence of the numerical analysis. Shell elements of the MITC family have been chosen, in order to avoid the numerical *locking*. A complete review of the methods and the modelling choices has been detailed, and the methods – including the MITC shell model – have been presented in a form which is intended to be particularly suitable for an implementation perspective. Where possible, the effects of the different modelling choices have been detailed with simple examples, and a number of validation test cases have been presented.

The choice of using *shell* finite element was motivated by the comparison with the CST membranes, which traditionally have been adopted in sail analysis, against experimental values (see Section 4.3.1). The shells behave remarkably better than the CST membranes and the differences are identified, which overcome 30% of the maximum displacement for all the analysed configurations, namely developable and non-developable surfaces.

Very accurate prediction performances have been obtained when analysing structure in large displacements, such as for instance a parachute canopy held with cables (see Section 4.3.2). Tests of this kind have been used for validating the accuracy of the adopted non-linear formulation when reproducing the deformation of a structure in large displacements. Despite

the very large difference between the initial and the final configurations, the comparison with experimental data is very satisfying.

The wrinkle development was successfully simulated with MITC shells. Using shells it is in fact possible to directly represents the wrinkles, thus overcoming the need for additional *ad-hoc* models to be superposed to membrane finite elements. The use of a dynamic framework (see Section 4.2.2) allows for a *natural* approach, where no particular initialisation is required. The wrinkling was analysed in terms of stability (see Section 4.1.10), and it was shown that it is possible to overcome such an instability by opportunely tuning the value of the damping coefficient. Neglecting to do so results in severe convergence issues, which may cause the divergence of the solution well before reaching a final equilibrated configuration. Remarkably accurate results have been obtained compared to experimental test cases using grids with about 20 elements per wrinkle. An enhanced wrinkling index was proposed, which allows to detect the general behaviour of a deformed section in terms of the wrinkling development (see Section 4.1.10). When extending the analysis to 3-dimensional sail-type geometries constituted by spherical (see Section 4.3.4, 4.3.4) and cylinder sectors (see Section 4.3.4), the overall deformed configuration and the wrinkling pattern result adequately captured for a number of shapes and material properties. For just a few geometries, however – corresponding to Spinnaker shapes with a long cylindrical body – some very fine and highly oscillating wrinkling behaviour was clearly detected, the complete resolution of which has been considered out of the scopes of this work.

6.2.3 Fluid-Structure Interactions

Fluid-structure interaction analysis was performed using an implicit coupling algorithm with Aitken dynamic relaxation in a fully unsteady ALE framework. This was chosen because it allows for moving or deforming interfaces without losses in terms of the accuracy compared to standard fixed-mesh computations. The implicit coupling was adopted because it guarantees the stability of the coupled calculation.

It was shown that the requirements in terms of the convergence criterion are critical for the adequate representation of the pressure signal: using a not-fine-enough convergence criterion may produce a considerable noise (see Section 5.1.5). This noise has however a limited effect on the displacements, because the structure is characterized by long time constants and is therefore only partially affected by high frequency loadings.

The numerical diffusion was shown to be beneficial (see Section 5.1.5), because it opposes

to the combined effect of the geometrical singularity at the tip of *zero-thickness* surfaces and the incompressibility, both responsible for the generation of oscillations in the pressure signal. The most direct implication is that using very fine grids does not necessarily produce more accurate coupled analysis, because this reduces the numerical dissipation in space and in time.

A non negligible source of noise was then found due to the numerical truncation error. Although this error is supposed to be small, differences can be identified when exchanging single or double precision values between the solvers, showing once again the sensitivity of the coupled analysis to any disturbance (see Section 5.1.5).

The coupled calculations were validated using a number of test cases, and good agreement was found with reference results published in the past, both for steady or unsteady configurations. The ALE mesh motions techniques were validated against reference results for an oscillating 2D cylinder section, and very satisfactory agreement was found (see Section 5.2.1).

The coupled response for a lid-driven cavity with flexible bottom was presented for both the 2D and the 3D case (see Sections 5.2.2 and 5.2.3). For these tests the answer in terms of the displacements was shown to be coherent with reference solutions available in the literature and obtained with different methods and schemes. Quite a large scatter was however identified between the reference solutions, for the effect of the numerical dissipation and also changes in the combinations of the boundary conditions. With the present method however it was shown that it is possible to match one or another solution by tuning the artificial damping term.

The case of flexible appendages immersed in external flows was investigated for both steady (see Section 5.2.4) and vortex shedding induced unsteady configurations (see Section 5.2.5). The structural interface was represented here as a zero-thickness surface, while the thickness was fully represented in the reference cases; despite this the results remained comparable, the thickness being small for the analysed cases ($1 - 3\%$ of the characteristic length). Such a geometrical representation is generally needed when analysing sails, the thickness of which is several orders of magnitude smaller than the other characteristic sizes. A drawback of such an approach is that a zero thickness surface determines the presence of (at least) a singular point, which might be one of the causes for the noise experienced in the pressure signal (see Section 5.1.5).

Finally, the case of a 3-dimensional Gennaker-type sail was analysed (see Section 5.2.7). The method previously validated is capable of reproducing the dynamic transient represented by the inflation process, and the simulation remained stable even for the relatively large

displacements to which the structural interface is subjected. The fluid damping shows in this case to be relatively high; a very limited amount of the Rayleigh damping is however necessary for overcoming instabilities deriving by the limited thickness and the boundary conditions, with two points simply supported and the third held with a cable. The final equilibrium configuration was found to be in agreement with the physics of the phenomena involved and the sail practise, and a substantial difference (lift: $+3\%$, drag: -15%) was found comparing the analysis performed with a fixed geometry or the coupled computations.

Developments of the methods here presented may in due course become part of the sail design and a valuable tool for helping the sail maker in the decision making and the optimization process.

6.3 Achievements

- Calculations for the prediction of the boundary layer over curved geometries with adverse pressure gradients in turbulent flows were validated against experimental results. The flow was resolved using the RANS method, and indications were derived in terms of the calculation grid requirements.

- The influence of wrinkles on cross-flow boundary layers and the effect on the force generation process was investigated. The conclusions are in line with what expected and coherent with conclusions of previous works. Wrinkles determine a substantial increase in the drag and decrease in the lift.

- Unsteady configurations have been investigated using the U-RANS method. Estimates have been derived of the effect of the unsteadiness in terms of the performances (lift, drag). It appears that the unsteadiness is beneficial in the force generation process, as it increases the performances of the device.

- Further investigations regarded the validation of the RANSE results for the specific case of a drag devices made of thin fabric. Excellent agreement was found and a low mesh sensitivity compared to other analyses. This was explained as the beneficial effect of having a geometrically induced separation point.

- A dynamic framework involving the non-linear Shell MITC4 finite elements and cables with Rayleigh damping was developed and tested.

- A methodology for setting the Rayleigh damping coefficients was proposed, and extensive investigation of the effects of these values was presented all through the thesis.

- The actual method was compared with the *state of the art* methods, previously adopted for sail structural analysis. The MITC shells finite elements resulted more accurate than the CST membranes for all the analysed configurations. The shells offer the possibility to analyse *wrinkled* configurations, for which the membrane model is inadequate.

- The structural method was employed and validated for a number of cases involving large displacements and cable boundary conditions

- The method was validated for wrinkled configurations, and investigations regarded the wrinkling development arising in different configurations of sail-type structures.

- A wrinkling index was proposed, to be used as a global measure of the wrinkling development on fabric structures

- A full unsteady and conservative Fluid Structure Interactions coupling environment was developed using the fluid and the structural codes previously validated

- The coupled calculations were validated using several reference test cases. Good agreement was found in all the analysed cases, which gives confidence on the performances of the method

- The coupled calculation was used for the analysis of sail-type configurations, and it was shown that the structural deformation has a non-negligible impact on the force generation process

6.4 Further research

Further research primarily regards the experimental validation for the transient calculations. It was in fact not possible to find publications reporting the design and the flying shape, or experimental measurements for the dynamic behaviour of a downwind sail.

From a fluid perspective, in the current research RANS techniques were used. LES techniques are however more and more adopted as the computational resources become available, because they generally offer higher prediction performances. No investigation was performed in this research about the separation or the laminar-to-turbulent transition, which might be

determinant for the correct prediction of the separation and slightly change the flow development, and thus the shape of the leading edge of the sail sections.

From a structural perspective, the future work should primarily investigate the effect of orhotropic constitutive relationships and the reinforcements on the corners of the sail. Of course, one key point is the use of more realistic design shapes.

The fluid-structure interaction routine is computationally expensive and for a matter of time the code was not modified to run in parallel. The application of an appropriate semi-explicit or an explicit coupling algorithm could then speed-up the calculation of one order of magnitude in some configurations. Also, a deeper investigation should be attempted for understanding the causes and the effects of the noise which affects the pressure signal when reducing the discretisation in time or space. This is of primary concern for analysis aiming to capture a detailed description of the flow.

Simulations should then be performed with induced unsteady boundary conditions for taking into account the effects of gusts or the boat's motions, and systematic series of simulations could be used for deriving general guidelines for design optimisation purposes.

Appendix A

Appendices to the Fluid Dynamic Chapter

A.1 The transport theorem (first form)

The transport equation states:

$$\frac{d}{dt}\int_{V(t)} F(x,t)\ dV = \int_{V(t)} \frac{dF}{dt}\ dV + \int_{S(t)} F\ v\ n\ dS \tag{A.1}$$

Proof. Defined a field $F(x,t)$ and applying the integration by part we obtain the mathematical identity, also called the transport theorem:

$$\frac{d}{dt}\int_{V(t)} F(x,t)dV = \int_{V(t)} \frac{dF}{dt}\ dV + \int_{V(t)} F\ \frac{d(dV)}{dt} \tag{A.2}$$

the last term of the equation can be reformulated as:

$$\frac{d(dV)}{dt} = \frac{d(dx_1dx_2dx_3)}{dt} = (\frac{dv_1}{dx_1} + \frac{dv_2}{dx_2} + \frac{dv_3}{dx_3}) \cdot dx_1dx_2dx_3 = \nabla \cdot \vec{v}\ dV \tag{A.3}$$

Equation (A.2) becomes then:

$$\frac{d}{dt}\int_{V(t)} F(x,t)\ dV = \int_{V(t)} \frac{dF}{dt}\ dV + \int_{V(t)} F\ \nabla \cdot \vec{v}\ dV \tag{A.4}$$

recalling the divergence theorem:

$$\int_{V(t_0)} \nabla \cdot (F\ \vec{v})\ dV = \int_{S(t_0)} F\ \vec{v} \cdot \vec{n}\ dS \tag{A.5}$$

Equation (A.4) becomes then:

$$\frac{d}{dt}\int_{V(t)} F(x,t)\ dV = \int_{V(t)} \frac{dF}{dt}\ dV + \int_{S(t)} F\ \vec{v} \cdot \vec{n}\ dS \tag{A.6}$$

□

A.2 The continuity equation

The continuity equation for incompressible flows reads:

$$\nabla \cdot \vec{v} = 0 \tag{A.7}$$

Proof. The mass conservation in the control volume dV reads:

$$\frac{d}{dt} \int_{V(t)} \rho \, dV = 0 \tag{A.8}$$

using equation (A.4) this can be reformulated as:

$$\int_{V(t)} \frac{\partial \rho}{\partial t} + \rho \nabla \cdot \vec{v} \, dV = 0 \tag{A.9}$$

and, this being valid for every control volume dV:

$$\frac{\partial \rho}{\partial t} + \rho \nabla \cdot \vec{v} = 0 \tag{A.10}$$

This is called the continuity equation. In the hypothesis of an incompressible fluid, valid for low speed aerodynamics, the density ρ can be considered constant. The time derivative then vanishes and the continuity equation further simplifies to the form:

$$\nabla \cdot \vec{v} = 0 \tag{A.11}$$

□

A.3 The transport theorem (second form)

If the transport theorem is reformulated for the quantity $\rho \, F(x,t)$, it becomes:

$$\frac{d}{dt} \int_{V(t)} \rho \, F(x,t) \, dV = \int_{V(t)} \rho \frac{dF}{dt} \, dV \tag{A.12}$$

Proof. applying as in appendix A.1 the derivation rule, we obtain:

$$\frac{d}{dt} \int_{V(t)} \rho \, F(x,t) \, dV = \int_{V(t)} \frac{d\rho}{dt} \, F(x,t) \, dV + \int_{V(t)} \rho \, \frac{dF}{dt} \, dV + \int_{V(t)} \rho \, F \, \frac{d(dV)}{dt} \tag{A.13}$$

This can be re-written, treating the last term as in equation (A.3) as:

$$= \int_{V(t)} \left[\frac{d\rho}{dt} F + \rho \frac{dF}{dt} + \rho F \nabla \cdot v \right] dV \tag{A.14}$$

The first and the last term vanish because of the continuity equation; the second form of the transport theorem results then:

$$\frac{d}{dt} \int_{V(t)} \rho F(x,t) dV = \int_{V(t)} \rho \frac{dF}{dt} dV \tag{A.15}$$

□

A.4 Demonstration of equation (3.14)

Proof.

$$\nabla \cdot \mathbf{T} = \Big(\frac{\partial}{\partial x_1}, \frac{\partial}{\partial x_2}, \frac{\partial}{\partial x_3}\Big) \cdot \begin{bmatrix} -p & & \\ & -p & \\ & & -p \end{bmatrix} = -\Big(\frac{\partial p}{\partial x_1}, \frac{\partial p}{\partial x_2}, \frac{\partial p}{\partial x_3}\Big) = -\nabla p \tag{A.16}$$

□

A.5 Demonstration of equation (3.17)

Proof.

$$\big(\nabla \mathbf{T}\big)_i = \frac{\partial T_{ij}}{\partial x_j} = \frac{\partial}{\partial x_j}[(-p + \lambda \nabla \cdot \vec{v})\delta_{ij} + 2\mu D_{ij}] = \frac{\partial}{\partial x_j}(-p + \lambda \nabla \cdot \vec{v}) + 2\mu \frac{\partial D_{ij}}{\partial x_j} = \tag{A.17}$$

$$= -\nabla p + \lambda \nabla(\nabla \cdot \vec{v}) + 2\mu \frac{\partial}{\partial x_j}\Big[\frac{1}{2}\Big(\frac{\partial v_i}{\partial x_j} + \frac{\partial v_j}{\partial x_i}\Big)\Big] = -\nabla p + \lambda \nabla(\nabla \cdot \vec{v}) + \mu\Big[\Delta v_i + \frac{\partial}{\partial x_i}\Big(\nabla \cdot \vec{v}\Big)\Big] \tag{A.18}$$

□

A.6 Correlations

It is shown here that the time average of the product of two fluctuating quantities Φ and Ψ :

$$\overline{\Phi\Psi} = \overline{(\Phi + \phi')(\Psi + \psi')} = \overline{\Phi\Psi + \Phi\psi' + \Psi\phi' + \phi'\psi'} = \overline{\Phi\Psi + \phi'\psi'} \tag{A.19}$$

where the mixed term $\Phi\psi'$, $\Psi\phi'$ are set to zero by the fact that the product of a mean quantity and a fluctuating quantity has zero mean. The term $\overline{\phi'\psi'}$ is not necessarily zero.

A.7 Demonstration of equation (3.24)

The derivation of RANS equation from the Navier-Stokes equations is here shown

Proof. Recalling equation (3.18) and rewriting the first term using equation (12). For the x-component of the velocity:

$$\rho\frac{\partial u}{\partial t} + \rho\ \overline{U}\cdot\nabla u = \rho f - \nabla p + \mu\Delta u \tag{A.20}$$

It is now possible to express the velocity under the RANS assumption as:

$$\rho\frac{\partial (u+u')}{\partial t} + \rho\ (u+u', v+v', w+w')\cdot\nabla(u+u') = \rho f - \nabla p + \mu\Delta(u+u') \tag{A.21}$$

developing, and operating the average with the correlation stated in appendix A.6:

$$\begin{aligned}\rho\overline{\frac{\partial u}{\partial t}} + \rho\overline{\frac{\partial u'}{\partial t}} + \rho\left(\overline{\frac{\partial(uu+u'u')}{\partial x}} + \overline{\frac{\partial(uv+u'v')}{\partial y}} + \overline{\frac{\partial(uw+u'w')}{\partial z}}\right) = \\ = \rho f - \nabla p + \mu\left(\overline{\frac{\partial^2 u}{\partial x^2}} + \overline{\frac{\partial^2 u'}{\partial x^2}} + \overline{\frac{\partial^2 u}{\partial y^2}} + \overline{\frac{\partial^2 u'}{\partial y^2}} + \overline{\frac{\partial^2 u}{\partial z^2}} + \overline{\frac{\partial^2 u'}{\partial z^2}}\right)\end{aligned} \tag{A.22}$$

since the derivative is a linear operator: $\overline{\frac{\partial F}{\partial t}} = \frac{\partial}{\partial t}\overline{F}$. Applying to the last equation, and remembering the RANS assumptions (equations (3.23)) it is then possible to derive the RANS equation:

$$\rho\overline{\frac{\partial u}{\partial t}} + \rho\left(\frac{\partial(\overline{u}\,\overline{u} + \overline{u'u'})}{\partial x} + \frac{\partial(\overline{u}\,\overline{v} + \overline{u'v'})}{\partial y} + \frac{\partial(\overline{u}\,\overline{w} + \overline{u'w'})}{\partial z}\right) = \rho f - \nabla p + \mu\left(\frac{\partial^2\overline{u}}{\partial x^2} + \frac{\partial^2\overline{u}}{\partial y^2} + \frac{\partial^2\overline{u}}{\partial z^2}\right) \tag{A.23}$$

rewriting:

$$\rho\left(\frac{\partial(\overline{u_j}\,\overline{u_i} + \overline{u_j'u_i'})}{\partial x_j}\right) = \rho f_i + \frac{\partial}{\partial x_j}\Big[-p\delta_{ij} + \mu\Big(\frac{\partial\ \overline{u_i}}{\partial x_j} + \frac{\partial\ \overline{u_j}}{\partial x_i}\Big)\Big] \tag{A.24}$$

□

A.8 Demonstration of equation (3.30)

Proof. The complete transport equation for the turbulent kinetic energy writes (see: [42]):

$$\frac{\partial k}{\partial t} + \overline{u}_j\frac{\partial k}{\partial x_j} = \tau_{ij}\ \frac{\partial\overline{u}_i}{\partial x_j} - \epsilon + \frac{\partial}{\partial x_j}\left[\nu\frac{\partial k}{\partial x_j} - \frac{1}{2}\ \overline{u_i'u_i'u_j'} - \frac{1}{\rho}\ \overline{p'u_j'}\right] \tag{A.25}$$

where:

$\frac{\partial k}{\partial t} + \overline{u}_j \frac{\partial k}{\partial x_j}$	material derivative of k
$\tau_{ij} \ \frac{\partial \overline{u}_i}{\partial x_j}$	production of k, the rate at which turbulent kinetic energy is generated from the mean flow
$\epsilon = \nu \overline{\frac{\partial u_i'}{\partial x_k} \frac{\partial u_i'}{\partial x_k}}$	dissipation of k per unit mass, the rate at which turbulent kinetic energy is converted into thermal energy through the action of viscosity
$\frac{\partial}{\partial x_j}\left[\nu \frac{\partial k}{\partial x_j}\right]$	Molecular diffusion of k, operated by the fluids natural molecular transport processes
$\frac{\partial}{\partial x_j}\left[\frac{1}{2} \ \overline{u_i' u_i' u_j'}\right]$	Turbulent transport of k, the rate at which turbulent kinetic energy is transported throughout the fluid by the turbulent fluctuations
$\frac{\partial}{\partial x_j}\left[\frac{1}{\rho} \ \overline{p' u_j'}\right]$	Pressure diffusion of k, which is the turbulent transport of k due to the correlation between velocity fluctuations and pressure fluctuations

In order to solve this transport equation, it is still necessary to model the unknown correlation of turbulent fluctuations that appear in the turbulent transport and pressure diffusion term. This is achieved using the gradient-diffusion approximation which states, for the generic variable Φ:

$$- u_j \Phi' \approx \frac{\nu_T}{\sigma_k} \frac{\partial \Phi}{\partial x_j} \tag{A.26}$$

with such approximation the turbulent transport term reads:

$$\frac{1}{2}\overline{u_i' u_i' u_j'} = \left[\overline{u_i'} \ \frac{1}{2} \ \overline{u_i' u_j'}\right] = \overline{u}_i' \ k = \nu_T \frac{\partial k}{\partial x_j} \tag{A.27}$$

Unfortunately is no equivalent approximation can be used for the pressure-diffusion term. Consequently it has become common practise to group this two terms together as:

$$\frac{1}{2}\overline{u_i' u_i' u_j'} + \frac{1}{\rho}\overline{p' u_j'} = -\frac{\nu_T}{\sigma_K} \frac{\partial k}{\partial x_j} \tag{A.28}$$

where σ_K is a closure coefficient calibrated experimentally for simple homogeneous flows. Using this approximation the k-equation reduces to

$$\frac{\partial k}{\partial t} + \overline{u}_i \frac{\partial k}{\partial x_j} = \tau_{ij} \ \frac{\partial \overline{u}_i}{\partial x_j} - \epsilon + \frac{\partial}{\partial x_j}\left[\left(\nu + \frac{\nu_T}{\sigma_K} \frac{\partial k}{\partial x_j}\right]\right. \tag{A.29}$$

□

A.9 One-dimensional Finite Volume discretization example

It is here reported a simple example of the use of the Finite Volume scheme for the solution of a convection-diffusion equation. For further details the reader should refer to [6], Ch.5.2. From Equation (3.40) a steady convection-diffusion equation can be derived eliminating the derivative and the source terms. In one dimension:

$$\frac{d}{dx}(\rho\phi u) = \frac{d}{dx}(\Gamma\nabla\phi) \tag{A.30}$$

and the continuity Equation (see appendix A.2) becomes:

$$\frac{d(\rho u)}{dx} = 0 \tag{A.31}$$

Integration of Equations (A.30) and (A.32) on the control volume shown in Figure A.1 gives:

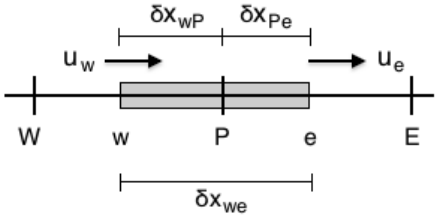

Figure A.1: One-dimensional control volume

$$\begin{aligned}(\rho u A\phi)_e - (\rho u A\phi)_w &= \left(\Gamma A\frac{\partial\phi}{\partial x}\right)_e - \left(\Gamma A\frac{\partial\phi}{\partial x}\right)_w \\ (\rho u A)_e - (\rho u A)_w &= 0\end{aligned} \tag{A.32}$$

Introducing the notation:

$$\begin{aligned}F_w = (\rho u)_w \quad , \qquad F_e = (\rho u)_e \\ D_w = \frac{\Gamma_w}{\delta x_{WP}} \quad , \qquad D_e = \frac{\Gamma_e}{\delta x_{PE}}\end{aligned} \tag{A.33}$$

where F represents the convective mass flux per unit area and D the diffusion conductance at cell faces. Equation (A.32) can now be written (using a first order scheme, and after dividing by the area A) as:

$$\begin{aligned}F_e\phi_e - F_w\phi_w &= D_e\,(\phi_E - \phi_P) - D_w\,(\phi_P - \phi_W) \\ F_e - F_w &= 0\end{aligned} \tag{A.34}$$

It was assumed here that the velocity field is known, and that therefore it is possible to calculate the values of F_e and F_w. Using a central differencing scheme, the transport property

ϕ can be written as:

$$\phi_e = (\phi_P + \phi_E)/2 \tag{A.35}$$

$$\phi_w = (\phi_W + \phi_P)/2 \tag{A.36}$$

Substituting in Equation (A.32) yields:

$$\frac{F_e}{2}\,(\phi_P + \phi_E) - \frac{F_w}{2}\,(\phi_W + \phi_P) = D_e\,(\phi_E - \phi_P) - D_w\,(\phi_P - \phi_W) \tag{A.37}$$

$$\Big[\Big(D_w - \frac{F_w}{2}\Big) + \Big(D_e - \frac{F_e}{2}\Big)\Big]\phi_P = \Big[\Big(D_w + \frac{F_w}{2}\Big)\phi_W + \Big(D_e - \frac{F_e}{2}\Big)\Big]\phi_E$$

$$\Big[\Big(D_w + \frac{F_w}{2}\Big) + \Big(D_e - \frac{F_e}{2}\Big) + (F_e - F_w)\Big]\phi_P = \Big[D_w + \frac{F_w}{2}\Big]\phi_W + \Big[D_e - \frac{F_e}{2}\Big]\phi_E \tag{A.38}$$

$$a_P\phi_P = a_W\phi_W + a_E\phi_E \tag{A.39}$$

where the coefficients a_P, a_W and a_E are substituted for the expressions in square brackets in Equation (A.38). This Equation can be applied to the one-dimensional domain represented in Figure A.2. For an internal node (node 2, 3, 4) it is then possible to write Equation (A.39). Border nodes (1, 5) must be further treated. Boundary conditions for node 1 are in fact that $\phi_w = \phi_W = \phi_A$; for node 5 $\phi_e = \phi_E = \phi_B$. Equation (A.34) can be written the for node 1 as:

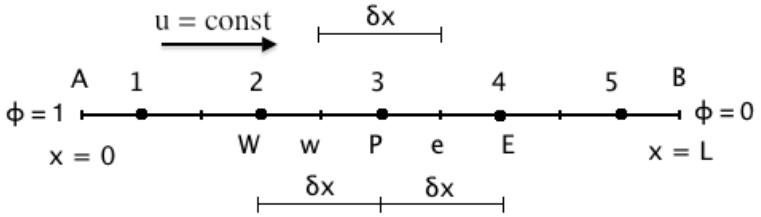

Figure A.2: One-dimensional domain

$$\frac{F_e}{2}\,(\phi_P + \phi_E) - F_A\,\phi_A = D_e\,(\phi_E - \phi_P) - D_A\,(\phi_P - \phi_A) \tag{A.40}$$

where the second term was not approximated since its value is known. Observing that $D_A = \frac{2\Gamma}{\delta x} = 2D$ and that $F_A = F$, this equation yields:

$$\Big(\frac{F_e}{2} + D_e + 2D\Big)\phi_P = \Big(-\frac{F_e}{2} + D_e\Big)\phi_e + (F + 2D)\phi_A \tag{A.41}$$

Similarly, by observing that $D_B = \frac{2\Gamma}{\delta x} = 2D$ and that $F_B = F$, the expression for the node 5 is:

$$\Big(-\frac{F_w}{2} + D_w + 2D\Big)\phi_P = \Big(-\frac{F_w}{2} + D_w\Big)\phi_w + (2D - F)\phi_B \tag{A.42}$$

The problem can then be generalised in a form similar to Equation (A.39) as:

$$a_P\phi_P = a_W\phi_W + a_E\phi_E + S_u \tag{A.43}$$

Table A.1: Dicretisation coefficients

Node	a_W	a_E	S_p	S_u
1	0	D-F/2	-(2D + F)	(2D + F)ϕ_A
2, 3, 4	D+ F/2	D-F/2	0	0
5	D+F/2	0	-(2D+F)	(2D + F)ϕ_B

where $a_P = a_W + a_E + F_e - F_w - S_p$ with the coefficients summarized in Table A.1:

It is then possible to express Equation (A.43) for all the considered elements. Setting then u=0.1 m/s, the convective mass flux per unit area $F = \rho$ u $= 0.1$ $[Kg/(m^2 s)]$, the diffusion conductance $D = \Gamma/\delta x = 0.5$ $[Kg/(m^2 s)]$, $\phi_A = 1$ and $\phi_B = 0$, this yield a system of Equation, the size of which is the number of elements, in the unknowns ϕ_i. Every element being connected with two side element, the system is sparse but non-symmetrical:

$$\begin{bmatrix} a_{11} & a_{12} & 0 & 0 & 0 \\ a_{21} & a_{22} & a_{23} & 0 & 0 \\ 0 & a_{32} & a_{33} & a_{34} & 0 \\ 0 & 0 & a_{43} & a_{44} & a_{45} \\ 0 & 0 & 0 & a_{54} & a_{55} \end{bmatrix} \cdot \begin{bmatrix} \phi_1 \\ \phi_2 \\ \phi_3 \\ \phi_4 \\ \phi_5 \end{bmatrix} = \begin{bmatrix} S_u \\ 0 \\ 0 \\ 0 \\ S_u \end{bmatrix} \tag{A.44}$$

A.10 Staggered grids

In the previous section the finite volume method was illustrated for the steady convection-diffusion of a scalar variable ϕ. When solving the momentum Equations (3.18) the situation is more complex because of problems associated with the pressure source terms. If velocities and pressures are stored at the same grid locations in fact, some unphysical situations can be computed, where the continuity is not respected. This problem is generally illustrated (see [20], Ch.6.8.2) with the example in Figure A.3: The velocity field in Figure A.3 respects the condition posed by the continuity Equation. It is therefore an admissible velocity field, even if it not continuous:

$$\nabla \cdot v = 0 \Rightarrow \frac{u_{i+1,j} - u_{i-1,j}}{2\Delta x} + \frac{v_{i,j+1} - v_{i,j-1}}{2\Delta y} = 0 \tag{A.45}$$

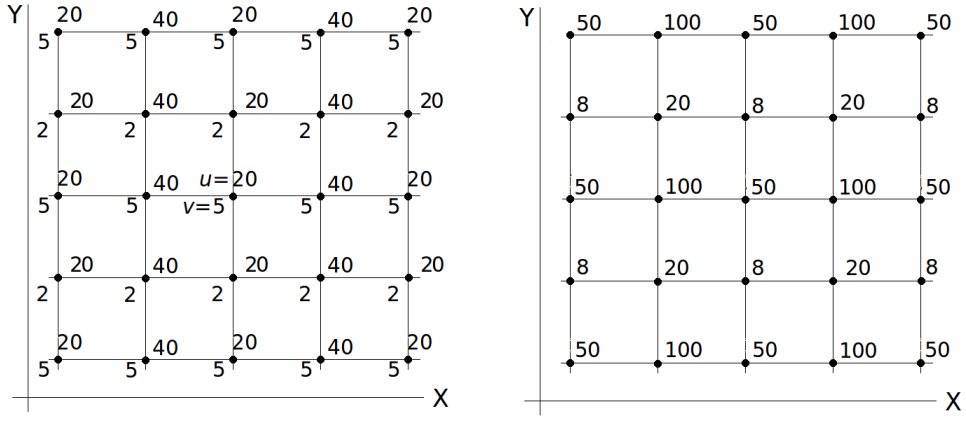

Figure A.3: Unphysical velocity (left) and pressure (right) distributions. From [20], Figures 6.13 and 6.14

Similar considerations can be made for the checkerboard pressure field represented in Figure A.3, where the discretized pressure gradient leads to the (unacceptable) result:

$$\frac{\partial p}{\partial x} = \frac{p_{i+1,j} - p_{i-1,j}}{2\Delta x} \Rightarrow 0 \tag{A.46}$$

$$\frac{\partial p}{\partial y} = \frac{p_{i,j+1} - p_{i,j-1}}{2\Delta y} \Rightarrow 0 \tag{A.47}$$

One of the techniques used for overcome this problem is the use of staggered grid, where new nodes are placed between the existing points and the characteristic quantities are interpolated over these points. In particular pressure and velocities are calculated at different points. Using the example of Figure A.4, pressures are calculated on the black points, by using the values interpolated on the white circles. Velocities use an inverse scheme, and they are interpolated on the white circles, using the values of the original black nodes.

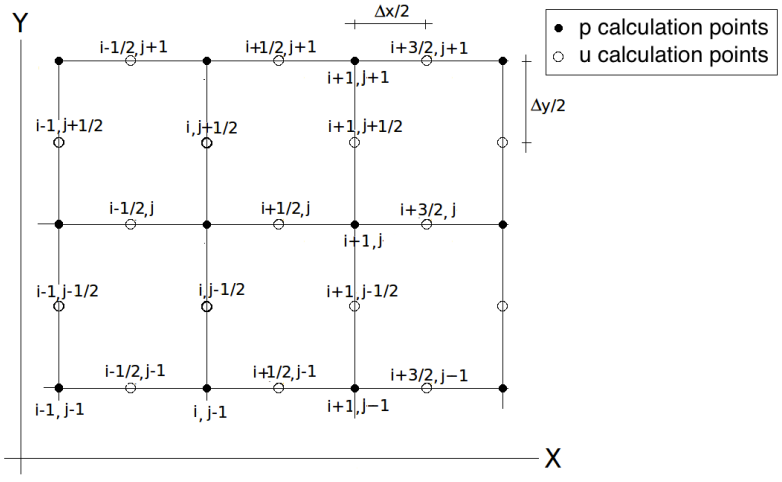

Figure A.4: Staggered grid interpolation. From [20], Figure 6.15

The use of such scheme leads then to the need of calculating velocities and pressures separately. This is the base idea of the pressure correction algorithms such as the SIMPLE and the PISO.

The use of staggered grids is not the only technique adopted for avoiding the calculation of unphysical fields. In the case of OpenFOAM, interpolations are performed using a *Rhie-Chow* collocated grid interpolation. All the basic idea remain unchanged, but the interpolations are performed using a different scheme. For a matter of clarity it was chosen here and in the following Sections to review the – basic of the – staggered grids only. Further details, concerning in particular the implementation of the *Rhie-Chow* scheme in OpenFOAM can be however found in [101].

A.11 Pressure-velocity coupling: SIMPLE and PISO

The SIMPLE (Semi Implicit Method for Pressure-Linked Equations) is an iterative algorithm based upon the following scheme:

- Guess field for pressure (p^*) and calculate the velocity components (u^*, v^*), normally from the previous iteration.

- Navier-Stokes Equations are solved in the pressure-correction formulation (see Equation (A.59)) using p = p^*. The unknowns are therefore reduced to the velocity components u^*, v^*

- Since the guess of the velocity field u^*, v^* is calculated with the pressure guess p^*, the continuity Equation is not necessarily satisfied. The residual is then used for calculating a pressure correction p' (Equation (A.66)), for calculating a new pressure field p^*

- Iterate until the pressure correction residual is smaller than a given tolerance

A 2-dimensional example (see [20], Ch.6.8.3 for further informations) is reported in the following. Consider Navier-Stokes Equations in conservative form (from Equation (3.18) applying Equation 0.5):

$$\frac{\partial(\rho u)}{\partial t} + \rho u \cdot \nabla u = -\nabla p + \mu \nabla^2 u \tag{A.48}$$

and consider the staggered grid in Figure A.5 Velocity and pressure for the grid point $i + 1/2$

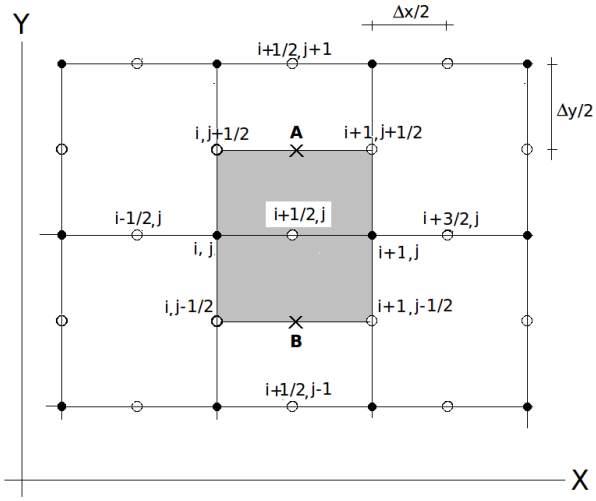

Figure A.5: Staggered grid interpolation

are defined using the auxiliary points A and B. Define then:

$$v_A = \frac{1}{2}\Big[v(i,j+\frac{1}{2}) + v(i+1,j+\frac{1}{2})\Big] \tag{A.49}$$

$$v_B = \frac{1}{2}\Big[v(i,j-\frac{1}{2}) + v(i+1,j-\frac{1}{2})\Big] \tag{A.50}$$

Navier Stokes Equations (first component) can then be discretised around the point $i+\frac{1}{2}$:

$$\frac{\partial(\rho u)}{\partial t} = \frac{1}{dt}\Big[(\rho u)^{n+1}_{i+\frac{1}{2},j} + (\rho u)^{n}_{i+\frac{1}{2},j}\Big] = < a > \tag{A.51}$$

$$\frac{\partial(\rho uu)}{\partial x} = \frac{(\rho uu)^n_{i+\frac{3}{2},j} - (\rho uu)^n_{i+\frac{1}{2},j}}{2\Delta x} = < b > \quad , \quad \frac{\partial(\rho uv)}{\partial y} = \frac{(\rho u_A v_A)^n - (\rho u_B v_B)^n}{2\Delta y} = < c > \tag{A.52}$$

$$\frac{\partial p}{\partial x} = \frac{(p)^n_{i+1,j} - (p)^n_{i,j}}{\Delta x} = < d > \tag{A.53}$$

$$\frac{\partial^2 u}{\partial x^2} = \frac{u^n_{i+\frac{3}{2},j} - u^n_{i+\frac{1}{2},j} + u^n_{i-\frac{1}{2},j}}{\Delta x^2} = < e > \quad , \quad \frac{\partial^2 u}{\partial y^2} = \frac{u^n_{i+\frac{1}{2},j+1} - u^n_{i+\frac{1}{2},j} + u^n_{i+\frac{1}{2},j-1}}{\Delta y^2} = < f > \tag{A.54}$$

and using the notation: $< A > = -[< b > + < c >] + \mu\ [< e > + < f >]$; $< B >$ calculated as $< A >$, but in the second direction, placed between nodes $_{i,j}$, $_{i+\frac{1}{2},j}$ and $_{i+\frac{1}{2},j}$, $_{i+1,j}$. Velocity values are interpolated using points C,D. Substituting Equations (A.51) into (A.54) in Equation (A.48), the 2-d Navier-Stokes equations can then be re-written in the discretised form:

$$\begin{cases} (\rho u)^{n+1}_{i+\frac{1}{2},j} = (\rho u)^n_{i+\frac{1}{2},j} + < A > dt - \frac{dt}{dx}(p_{i+1,j} - p_{i,j})^n \\ \\ (\rho v)^{n+1}_{i+\frac{1}{2},j} = (\rho v)^n_{i,j+\frac{1}{2}} + < B > dt - \frac{dt}{dx}(p_{i,+1j} - p_{i,j})^n \end{cases} \tag{A.55}$$

substituting the pressure guess $p*$ the equations will be solved for the intermediate velocity field $u*, v*$:

$$\begin{cases} (\rho u^*)^{n+1}_{i+\frac{1}{2},j} &= (\rho u^*)^n_{i+\frac{1}{2},j} + < A^* > dt - \frac{dt}{dx}(p^*_{i+1,j} - p^*_{i,j})^n \\ \\ (\rho v^*)^{n+1}_{i+\frac{1}{2},j} &= (\rho v^*)^n_{i,j+\frac{1}{2}} + < B^* > dt - \frac{dt}{dx}(p^*_{i,+1j} - p^*_{i,j})^n \end{cases} \tag{A.56}$$

The correction for p^* is calculated as follows. Subtracting Equation A.56 and A.55 (first component):

$$[\rho(u - u^*)]^{n+1}_{i+\frac{1}{2},j} = \rho[u - u^*]^n_{i+\frac{1}{2},j} + [< A > - < A^* >]dt - \frac{dt}{dx}(p_{i+1,j} - p^*_{i+1,j}) - (p_{i,j} - p^*_{i,j})^n \tag{A.57}$$

and introducing the notation:

$$\begin{aligned} u - u^* &= u' \\ < A > - < A^* > &= < A' > \\ p_{i+1,j} - p^*_{i+1,j} &= p'_{i+1,j} \\ p_{i,j} - p^*_{i,j} &= p'_{i,j} \end{aligned} \tag{A.58}$$

the Navier-Stokes Equations in terms of correction are written as:

$$\begin{cases} (\rho u')^{n+1}_{i+\frac{1}{2},j} &= (\rho u')^n_{i+\frac{1}{2},j} + < A' > dt - \frac{dt}{dx}(p'_{i+1,j} - p'_{i,j})^n \\ \\ (\rho v')^{n+1}_{i+\frac{1}{2},j} &= (\rho v')^n_{i,j+\frac{1}{2}} + < B' > dt - \frac{dt}{dx}(p'_{i,+1j} - p'_{i,j})^n \end{cases} \tag{A.59}$$

The pressure correction term is calculated by ensuring that velocity field satisfy the continuity Equation. The first step in the SIMPLE algorithm is to (arbitrarily) set: $< A' >= 0$, $< B' >= 0$, $(\rho u')^n = 0$, $(\rho v')^n = 0$. The fact that this choice is arbitrary is the reason of the word SEMI in the name of SIMPLE algorithm. This conditions are imposed, since it is true at convergence. Other schemes use different assumption, and they are then called Fully Implicit methods.

Modifying Equation (A.59) under these assumptions, and recalling the definition of u' Equation (A.58):

$$\begin{cases} (\rho u)^{n+1}_{i+\frac{1}{2},j} &= (\rho u^*)^{n+1}_{i+\frac{1}{2},j} - \frac{dt}{dx}(p'_{i+1,j} - p'_{i,j})^n \\ \\ (\rho v)^{n+1}_{i+\frac{1}{2},j} &= (\rho u^*)^{n+1}_{i+\frac{1}{2},j} - \frac{dt}{dx}(p'_{i,+1j} - p'_{i,j})^n \end{cases} \tag{A.60}$$

The continuity Equation (see appendix A.2), discretized around the point $_{i,j}$ is:

$$\frac{(\rho u)_{i+\frac{1}{2},j} - (\rho u)_{i-\frac{1}{2},j}}{\Delta x} + \frac{(\rho v)_{i+\frac{1}{2},j} - (\rho v)_{i-\frac{1}{2},j}}{\Delta x} = 0 \tag{A.61}$$

subsituting Equation (A.60) in Equation (A.61) leads to:

$$\begin{aligned} &\frac{(\rho u^*)^{n+1}_{i+\frac{1}{2},j} - \frac{\Delta t}{\Delta x}(p'_{i+1,j} - p'_{i,j})^n - (\rho u^*)^{n+1}_{i-\frac{1}{2},j} + \frac{\Delta t}{\Delta x}(p'_{i,j} - p'_{i-1,j})^n}{\Delta x} + \\ &\frac{(\rho v^*)^{n+1}_{i+\frac{1}{2},j} - \frac{\Delta t}{\Delta y}(p'_{i+1,j} - p'_{i,j})^n - (\rho v^*)^{n+1}_{i-\frac{1}{2},j} + \frac{\Delta t}{\Delta y}(p'_{i,j} - p'_{i-1,j})^n}{\Delta y} = 0 \end{aligned} \tag{A.62}$$

It is now possible to drop the $.^n$ index, since it is imposed that the continuity Equation is satisfied at the instant $*$, which is between ^{n} and $^{n+1}$. Equation (A.62) can then be reformulated as a function of pressure correction as:

$$\begin{aligned} p'_{i,j}\ 2\Big(\frac{\Delta t}{\Delta x^2} + \frac{\Delta t}{\Delta y^2}\Big) + p'_{i+1,j}\Big(-\frac{\Delta t}{\Delta x^2}\Big) + p'_{i-1,j}\Big(-\frac{\Delta t}{\Delta x^2}\Big) + p'_{i,j+1}\Big(-\frac{\Delta t}{\Delta y^2}\Big) \quad + \\ p'_{i,j-1}\Big(-\frac{\Delta t}{\Delta y^2}\Big) + \frac{1}{\Delta x}\Big[\rho u^*_{i+\frac{1}{2},j} - \rho u^*_{i-\frac{1}{2},j}\Big] + \frac{1}{\Delta y}\Big[\rho v^*_{i,j+\frac{1}{2}} - \rho v^*_{i,j-\frac{1}{2}}\Big] \quad = 0 \end{aligned} \tag{A.63}$$

rewriting in a more compact shape:

$$p'_{i,j}\ \mathbf{a} + p'_{i+1,j}\ \mathbf{b} + p'_{i-1,j}\ \mathbf{b} + p'_{i,j+1}\ \mathbf{c} + p'_{i,j-1}\ \mathbf{c} + \mathbf{d} = 0 \tag{A.64}$$

the pressure correction term d is then calculated as:

$$\mathbf{d} = -p'_{i,j}\ \mathbf{a} - (p'_{i+1,j} + p'_{i-1,j})\ \mathbf{b} - (p'_{i,j+1} + p'_{i,j-1})\ \mathbf{c} \tag{A.65}$$

this is in the form of an elliptic Equation (similar for example to the Poisson Equation), due to the formulation of **a** and **b** coefficients. It is then a diffusive Equation, the role of which is to diffuse in the domain the pressure correction. This is calculated as:

$$p^*_{i,j} = p_{i,j} + d \tag{A.66}$$

Often this pressure correction is too large to produce stable calculation, and under-relaxation techniques must be adopted in order to assure convergence.

The PISO (Pressure Implicit with Splitting operators) is a pressure-velocity calculation procedure involving one predictor step and two corrector steps. It can be seen as an extension of the SIMPLE algorithm, with an further corrector step. The details of these algorithms are omitted here, but for more details one may refer to [6].

A.12 Calculation of D in OpenFOAM

Included here is the C++ code for the calculation of the Normalised Invariant of the Deformation Tensor **D** implemented in environement OpenFOAM.

```
1
2  #   include "fvCFD.H"
3
4  int main(int argc, char *argv[])
5  {
6          #   include "setRootCase.H"
7          #   include "createTime.H"
8          #   include "createMesh.H"
9
10          volScalarField D
11          (
12            IOobject
13              (
14                "D",
15                runTime.timeName(),
16                mesh,
17                IOobject::READ_IF_PRESENT,
18                IOobject::AUTO_WRITE
19              ),
20            mesh
21          );
22
23         instantList timeDirs = timeSelector::select0(runTime, args);
24
25         forAll(timeDirs, timeI)
26         {
27                 runTime.setTime(timeDirs[timeI], timeI);
28
29                 Info<< "Time = " << runTime.timeName() << endl;
30                 Info<< "Reading field U\n" << endl;
31
32                 volVectorField U
33                 (
34                         IOobject
35                         (
36                                 "U",
37                                 runTime.timeName(),
```

```
38                                      mesh,
39                                      IOobject::MUST_READ,
40                                      IOobject::AUTO_WRITE
41                                  ),
42                                  mesh
43                              );
44
45                              volTensorField gradU = fvc::grad(U);
46
47                              volSymmTensorField S = 0.5*symm(gradU);  //symm part
48                              volTensorField W = 0.5*skew(gradU);  // anti-symmetric part
49
50                              volScalarField SS =  S&&S;
51                              volScalarField WW =  W&&W;
52
53                              volScalarField D
54                                (
55                                 IOobject
56                                 (
57                                  "D",
58                                  runTime.timeName(),
59                                  mesh,
60                                  IOobject::NO_READ,
61                                  IOobject::NO_WRITE
62                                  ),
63                                 ( SS - WW) / (WW + SS)
64                                 );
65
66                              D.write();
67                      }
68          return(0);
69      }
```

Listing A.1: Calculating the Normalised Invariant of the Deformation Tensor in OpenFOAM

Appendix B

Appendices to the Structural Chapter

B.1 Higher order tensors in the variant and covariant bases

The variant-contravariant representation for vectors was introduced in Chapter 4, section 4.1.2. For higher order tensors, mixed forms combining covariant and contravariant orders can be used. For example equation B.1 involves the contravariant-covariant components of the second order tensor $\vec{\vec{T}}$:

$$\mathbf{T} = \sum_{m=1}^{3}\sum_{n=1}^{3} T^{m}_{\cdot\ n}\ \vec{i}_m \otimes \vec{i}^n \tag{B.1}$$

The symbol "." is used to identify the order of the covariant and contravariant vectors in the decomposition considered. $T^{m}_{\cdot\ n}$ multiplies then before for the base-component $\vec{i}_m$ and then $\vec{i}^n$. In general in fact $T^{m}_{\cdot\ n} \neq T_{n}^{\cdot\ m}$.

With the notation here introduced, it is then possible to write a tensor in four different basis:

$$\begin{aligned}
\mathbf{T} &= \sum_{m=1}^{3}\sum_{n=1}^{3} T^{m}_{\cdot\ n}\ \vec{i}_m \otimes \vec{i}^n \\
\mathbf{T} &= \sum_{m=1}^{3}\sum_{n=1}^{3} T_{m}^{\cdot\ n}\ \vec{i}^m \otimes \vec{i}_n \\
\mathbf{T} &= \sum_{m=1}^{3}\sum_{n=1}^{3} T^{mn}\ \vec{i}_m \otimes \vec{i}_n \\
\mathbf{T} &= \sum_{m=1}^{3}\sum_{n=1}^{3} T_{mn}\ \vec{i}^m \otimes \vec{i}^n
\end{aligned} \tag{B.2}$$

The inverse of such composition is trivial, and directly derives from the application of Equation

4.2:

$$\begin{aligned} T^{m}_{\cdot\ n} &= (\vec{\vec{T}}\ \vec{i}_n) \cdot \vec{i}^{m} \\ T^{\cdot\ n}_{m} &= (\vec{\vec{T}}\ \vec{i}^{n}) \cdot \vec{i}_m \\ T^{mn} &= (\vec{\vec{T}}\ \vec{i}^{n}) \cdot \vec{i}^{m} \\ T_{mn} &= (\vec{\vec{T}}\ \vec{i}_n) \cdot \vec{i}_m \end{aligned} \tag{B.3}$$

Using Einstein notation makes the expressions lighter. In the expression of tensor components then equation B.1 becomes as in equation B.4. The letters m and n are then called *dummy* indexes - since they are repeated they involve a sum from 1 to 3:

$$\mathbf{T} = T^{m}_{\cdot\ n}\ \vec{i_m} \otimes \vec{i^n} \tag{B.4}$$

Combinations of contravariant and covariant indices in Einstein's notation can be very effectively used to compute the results of dot and double dot products. In this framework, notations becomes 'natural'. For example, for two vectors $\vec{u}$ and $\vec{v}$:

$$\vec{u} \cdot \vec{v} = (u^m\ \vec{i}_m) \cdot (v_n\ \vec{i}^n) = u^m v_n\ (\vec{i}_m \cdot \vec{i}^n) = u^m\ v_n\ \delta^m_n = u^m\ v_m \tag{B.5}$$

Similarly, for second-order tensors:

$$\vec{\vec{T}} \cdot \vec{\vec{U}} = U^{mk}\ T_{kn}\ \vec{i_m} \otimes \vec{i^n} = U^{m}_{\cdot\ k}\ T^{k}_{\cdot\ n}\ \vec{i_m} \otimes \vec{i^n} = U^{\cdot\ k}_{m}\ T_{kn}\ \vec{i^m} \otimes \vec{i^n} = ... \tag{B.6}$$

and:

$$\vec{\vec{T}} : \vec{\vec{U}} = U^{mk}\ T_{km} = U^{m}_{\cdot\ k} T^{k}_{\cdot\ m} = U^{\cdot\ k}_{m}\ T^{\cdot\ m}_{k} = U_{mk}\ T^{mk} \tag{B.7}$$

B.2 Demonstration of equation 4.18

Proof. by definition:

$$b_{\alpha\beta} = \vec{a}_3 \cdot \vec{a}_{\alpha,\beta}$$

and by construction:

$$\vec{a}_3 \cdot \vec{a}_\alpha = 0 \quad \Rightarrow \quad \partial_{\xi_\beta}(\vec{a}_3 \cdot \vec{a}_\alpha) = 0 \tag{B.8}$$

$$\vec{a}_{3,\beta}\, \vec{a}_\alpha + \vec{a}_3\, \vec{a}_{\alpha,\beta} = 0 \tag{B.9}$$

substituting the definition of $b_{\alpha\beta}$ then:

$$b_{\alpha\beta} = -\vec{a}_{3,\beta} \cdot \vec{a}_\alpha \tag{B.10}$$

□

B.3 Demonstration of equations 4.20

Proof. starting with the definition:

$$b^{\lambda}_{\alpha} = a^{\lambda\mu}\, b_{\mu\alpha} \tag{B.11}$$

this can be transformed using equation 4.18: $b_{\alpha\beta} = -\vec{a}_{3,\beta} \cdot \vec{a}_{\alpha}$ as:

$$a^{\lambda\mu}\, b_{\mu\alpha} = -a^{\lambda\mu} \cdot \vec{a}_{3,\alpha} \cdot \vec{a}_{\mu} \tag{B.12}$$

since then': $a^{\lambda\mu} \cdot \vec{a}_{\mu} = \vec{a}^{\lambda} \cdot \vec{a}^{\mu} \cdot \vec{a}_{\mu} = \vec{a}^{\lambda} \cdot \delta^{\mu}_{\mu} = \vec{a}^{\lambda}$:

$$-\, a^{\lambda\mu} \vec{a}_{3,\alpha} \cdot \vec{a}_{\mu} = -\vec{a}_{3,\alpha} \cdot \vec{a}^{\lambda} \tag{B.13}$$

Observing then that $\vec{a}^{\lambda} \cdot \vec{a}_3 = 0$, differentiating with respect to α:

$$\vec{a}^{\lambda}_{,\alpha} \cdot \vec{a}_3 = -\vec{a}^{\lambda} \cdot \vec{a}_{3,\alpha} \tag{B.14}$$

substituting in the last equation:

$$-\, \vec{a}_{3,\alpha} \cdot \vec{a}^{\lambda} = \vec{a}^{\lambda}_{,\alpha} \cdot \vec{a}_3 \tag{B.15}$$

□

B.4 Demonstration of equation 4.21

Proof. In general it is always possible to decompose a vector $\vec{r}$ on a covariant-contravariant basis (recall Equation 4.2) such as:

$$\vec{r} = (\vec{r} \cdot \vec{a}_1) \cdot \vec{a}^1 + (\vec{r} \cdot \vec{a}_2) \cdot \vec{a}^2 + (\vec{r} \cdot \vec{a}_3) \cdot \vec{a}^3 \tag{B.16}$$

or equivalently:

$$\vec{r} = (\vec{r}\,\vec{a}^1)\,\vec{a}_1 + (\vec{r}\,\vec{a}^2)\,\vec{a}_2 + (\vec{r}\,\vec{a}^3)\,\vec{a}_3 \tag{B.17}$$

in the shell framework: $\vec{a}_3 \cdot \vec{a}_3 = 1$, because the normal vector is normalised; thus:

$$(\vec{a}_3 \cdot \vec{a}_3)_{,\alpha} = 0 \quad \Rightarrow \quad \vec{a}_{3,\alpha} \cdot \vec{a}_3 = 0 \tag{B.18}$$

Rewriting $\vec{a}_3$ in the shape of (B.16):

$$\vec{a}_{3,\alpha} = (\vec{a}_{3,\alpha} \cdot \vec{a}_1) \cdot \vec{a}^1 + (\vec{a}_{3,\alpha} \cdot \vec{a}_2) \cdot \vec{a}^2 + \tag{B.19}$$

where the last term vanishes because of Equation (B.18). Rewriting then:

$$\vec{a}_{3,\alpha} = (\vec{a}_{3,\alpha} \cdot \vec{a}_{\lambda}) \cdot \vec{a}^{\lambda} \quad \lambda = 1,\, 2 \tag{B.20}$$

□

B.5 Derivation of the strain tensor

Recall the definition of the shell geometry in Equation 4.14. The initial reference configurations writes then:

$$\vec{x} = \vec{\varphi}(\xi^1, \xi^2) + \xi^3 \, \vec{a}_3(\xi^1, \xi^2) \tag{B.21}$$

where $||\vec{a}_3|| = 1$ and $\vec{a}_3 \cdot \vec{\vec{\nabla}}\phi = 0$. The current configuration is:

$$\vec{X} = \vec{\phi}(\xi^1, \xi^2) + \xi^3 \, \vec{A}_3(\xi^1, \xi^2) \tag{B.22}$$

with $||\vec{A}_3|| = 1$. The displacements can then be written as (see also Equation 4.31:

$$\vec{U} = \vec{X} - \vec{x} = \vec{\phi} - \vec{\varphi} + \xi^3(\vec{A}_3 - \vec{a}_3) \tag{B.23}$$

The strain tensor is generically defined as:

$$\mathbf{e} = \frac{1}{2}(\mathbf{F}^T\mathbf{F} - \mathbf{I}\,) = \frac{1}{2}\left(\frac{\partial \vec{X}}{\partial \xi^i}\frac{\partial \vec{X}}{\partial \xi^j} - \frac{\partial \vec{x}}{\partial \xi^i}\frac{\partial \vec{x}}{\partial \xi^j}\right) \tag{B.24}$$

using the definition for the covariant base vectors in Equation 4.29 then: $\vec{g}_i = \frac{\partial \vec{x}}{\partial \xi^i}$ and $\vec{G}_i = \frac{\partial \vec{X}}{\partial \xi^i}$ and the definition of the metric tensor for the initial and the current configurations: $g_{ij} = \vec{g}_i \cdot \vec{g}_j$ and $G_{ij} = \vec{G}_i \cdot \vec{G}_j$. Equation (B.24) rewrites:

$$e_{ij} = \frac{1}{2}(G_{ij} - g_{ij}) \tag{B.25}$$

and using the definition and (B.23),

$$\vec{G}_i = \frac{\partial \vec{X}}{\partial \xi^i} = \frac{\partial}{\partial \xi^i}(\vec{x} + \vec{U}) = \vec{g}_i + \vec{U}_{,i} \tag{B.26}$$

the strain tensor (B.24) then becomes:

$$\begin{aligned} e_{ij} &= \frac{1}{2}[\,(\vec{g}_i + \vec{U}_{,i})(\vec{g}_j + \vec{U}_{,j}) - g_{ij}\,] = \\ &= \frac{1}{2}[\,\vec{g}_i\vec{U}_{,j} + \vec{g}_j\vec{U}_{,i} + \vec{U}_{,i}\vec{U}_{,j}\,] \end{aligned} \tag{B.27}$$

where the first two term are the linear Green-Lagrange strain tensor, and the third is a non-linear term.

B.6 Demonstration of equation 4.22

Proof. Recalling equations (4.18) and (4.21), it is valid that:

$$-\vec{a}_{3,\alpha} \cdot \vec{a}_\lambda = b_{\lambda\alpha} \tag{B.28}$$

So, since:

$$\vec{a}_{\alpha,\beta} = \frac{\partial^2 \phi}{\partial \xi^\alpha \partial \xi^\beta} = \vec{a}_{\beta,\alpha} \tag{B.29}$$

it is possible to write:

$$\vec{a}_{3,\alpha} = -b_{\lambda\alpha}\vec{a}^\lambda = -b_{\alpha\lambda}\vec{a}^\lambda \tag{B.30}$$

rewriting now the term on the right hand side using the same decomposition as in Equation (B.16):

$$\begin{aligned} b_{\lambda\alpha}\vec{a}^\lambda &= b_{\lambda\alpha}(\vec{a}^1\vec{a}^\lambda\vec{a}_1 + \vec{a}^2\vec{a}^\lambda\vec{a}_2 + \vec{a}^3\vec{a}^\lambda\vec{a}_3) = \\ &= \vec{a}^{1\lambda}b_{\lambda\alpha}\vec{a}_1 + \vec{a}^{2\lambda}b_{\lambda\alpha}\vec{a}_2 + \vec{a}^{3\lambda}b_{\lambda\alpha}\vec{a}_3 = \qquad \text{(B.31)} \\ &= b^1_\alpha\vec{a}_1 + b^2_\alpha\vec{a}_2 + b^3_\alpha\vec{a}_3 = \qquad \text{(B.32)} \\ &= b^\lambda_\alpha\vec{a}_\lambda \qquad \text{(B.33)} \end{aligned}$$

Equation (B.30) becomes then:

$$\vec{a}_{3,\alpha} = -b_{\alpha\lambda}\vec{a}^\lambda = -b^\lambda_\alpha\vec{a}_\lambda \tag{B.34}$$

□

B.7 Demonstration of equation 4.30

Proof. Using the definition of $g_{\alpha\beta}$:

$$g_{\alpha\beta} = \vec{g}_\alpha \cdot \vec{g}_\beta \tag{B.35}$$

and using equation (4.29):

$$\begin{aligned} \vec{g}_\alpha &= \vec{a}_\alpha - \xi^3 b^\lambda_\alpha \vec{a}_\lambda \\ \vec{g}_\beta &= \vec{a}_\beta - \xi^3 b^\lambda_\beta \vec{a}_\lambda \end{aligned} \tag{B.36}$$

then:

$$g_{\alpha\beta} = \vec{a}_\alpha \cdot \vec{a}_\beta - \xi^3\, b^\mu_\beta\, \vec{a}_\mu\, \vec{a}_\alpha - \xi^3\, b^\lambda_\alpha\, \vec{a}_\lambda\, \vec{a}_\beta + (\xi^3)^2\, b^\lambda_\alpha\, b^\mu_\beta\, \vec{a}_\lambda \cdot \vec{a}_\mu \tag{B.37}$$

The first term is trivially transformed to $\vec{a}_\alpha \cdot \vec{a}_\beta = \vec{a}_{\alpha\beta}$. The second and the third terms need to be carefully treated. Recall the formulation of the term $b_{\alpha\beta} = -\vec{a}_{3,\beta} \cdot \vec{a}_\alpha$ in Equation (4.18) and define a new variable u, for the demonstration purposes:

$$\vec{u} = \vec{a}_{3,\beta} \tag{B.38}$$

Recall now the formulations for variant and contravariant basis, and in particular Equation (4.6)

$$b_{\lambda\beta} = -\vec{u} \cdot \vec{a}_\alpha = -u^\lambda \tag{B.39}$$

Recalling the definition of b_α^β in Equation (4.20):

$$b_\alpha^\lambda = a^{\alpha\lambda}\, b_{\lambda\beta} = -a^{\alpha\lambda} u^\lambda = -u_\alpha \tag{B.40}$$

where the last equality holds because of Equation (4.4). Applying now Equation (4.5) and successively recalling the definition of $\vec{u}$ in Equation (B.38):

$$b_\alpha^\lambda = -u_\alpha = -(\vec{u} \cdot \vec{a}^\alpha) = -\vec{\alpha}_{3,\beta} \cdot \vec{a}^\alpha \tag{B.41}$$

The second term in Equation (B.37) can now be rewritten using Equations (B.41) and (**??**) as:

$$b_\beta^\mu\, \vec{a}_\mu \cdot \vec{a}_\alpha = -u_\mu \vec{a}_\mu \cdot \vec{a}_\alpha = -\vec{u}^\alpha = b_{\alpha\beta} \tag{B.42}$$

where the last equality is obtained by applying Equation (B.39). With similar considerations it can be shown that the third term $b_\alpha^\lambda\, \vec{a}_\lambda\, \vec{a}_\beta$ produces the same result.

The last term is simply transformed using the result just obtained and recalling the definition for the third fundamental form $c_{\alpha\beta}$ in Equation (4.19):

$$b_\alpha^\lambda\, b_\beta^\mu\, \vec{a}_\lambda \cdot \vec{a}_\mu = b_\alpha^\lambda b_\lambda^\beta = c_{\alpha\beta} \tag{B.43}$$

Substituting in (B.37)

$$g_{\alpha\beta} = \vec{a}_{\alpha\beta} - 2\xi^3\, b_{\alpha\beta} + (\xi^3)^2 c_{\alpha\beta} \tag{B.44}$$

□

B.8 Calculating a regression curve of order *n*

Given a set of N points $P_i = (x_i, y_i)$, its regression of order p is a curve in the shape $y = \sum_{i=0}^{p} c_i\, x^i$, where the coefficients c_i are chosen in order to minimise the error defined as:

$$\epsilon(c_i) = \sum_{k=1}^{N} \Big(\sum_{i=0}^{p} c_i\, x_k^i - y_k \Big)^2 \tag{B.45}$$

Such minimization is achieved imposing the conditions:

$$\frac{\partial \epsilon}{\partial c_i} = 0 \quad \forall \quad i = 1, p \tag{B.46}$$

This lead to the system of $p+1$ equations in the $p+1$ unknowns c_i:

$$\begin{bmatrix} n & \sum_k x_k & \sum_k x_k^2 & \dots \\ \sum_k x_k & \sum_k x_k^2 & \sum_k x_k^3 & \dots \\ \sum_k x_k^2 & \sum_k x_k^3 & \sum_k x_k^4 & \dots \\ \dots & .. & \dots & \sum_k x_k^{2p} \end{bmatrix} \cdot \begin{bmatrix} c_0 \\ c_1 \\ c_2 \\ \dots \\ c_p \end{bmatrix} = \begin{bmatrix} \sum_i y_i \\ \sum_i x_i y_i \\ \sum_i x_i^2 y_i \\ \dots \\ \sum_i x_i^p y_i \end{bmatrix} \tag{B.47}$$

Inverting the matrix is then possible to find the coefficients c_i which define the regression.

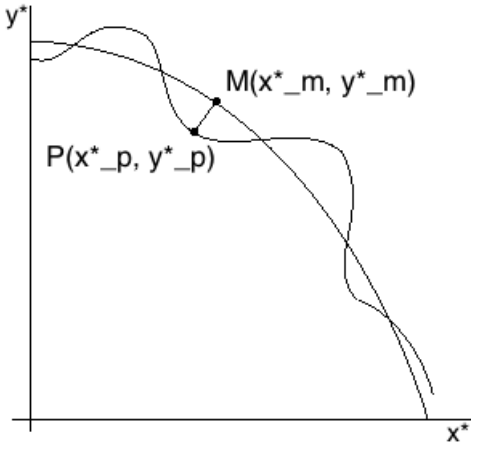

Figure B.1: Definition of the points on the deformed section and the regression parabola

The minimum distance of a point of the wrinkled section to the regression curve is then found solving another minimization problem. In this case the parameter to be minimized is the distance intercepting between the point M of the wrinkled section and the generic point P of the regression $y = \sum_{i=0}^{p} c_i\, x^i$ (see figure B.1). The (squared) distance between a point and the parabola: $D^2 = (x - x_p)^2 + (\sum_{i=0}^{p} c_i\, x^i - y_p)^2$, is minimised by imposing:

$$\frac{dD^2}{dx} = 0 \tag{B.48}$$

This condition leads to the equation of order $2p-1$:

$$x - x_p + \left(\sum_{i=0}^{p} c_i x^i - y_p \right) \left(\sum_{i=1}^{p} c_i x^{i-1} \right) = 0 \tag{B.49}$$

this condition in the unknown x is satisfied using a Newton algorithm, which recursively calculates:

$${}^{n+1}x = {}^{n}x + \frac{f({}^{n}x)}{f'({}^{n}x)} \tag{B.50}$$

where the derivative $f'({}^{n}x)$ is expressed as:

$$1 + \left(\sum_{i=1}^{p} c_i x^{i-1} \right) + \left(\sum_{i=0}^{p} c_i x^i - y_p \right) \left(\sum_{i=2}^{p} c_i x^{i-2} \right) \tag{B.51}$$

The increment in curvilinear abscissa is then numerically evaluated as the distance intercepting between the point M for the $i-th$ point and for the $i-1-th$ point. The curvilinear abscissa allows tracing the distance of the point set P_i on a straight line, thus the evaluation of the geometrical features of the wrinkled section is trivial.

Example

Table B.1: Results in terms of wave length and semi-amplitude

Lmin	Lavg	LMax	Rmin	Ravg	RMax	RfirstWr
18.818	25.160	44.627	0.152	0.638	1.358	0.895

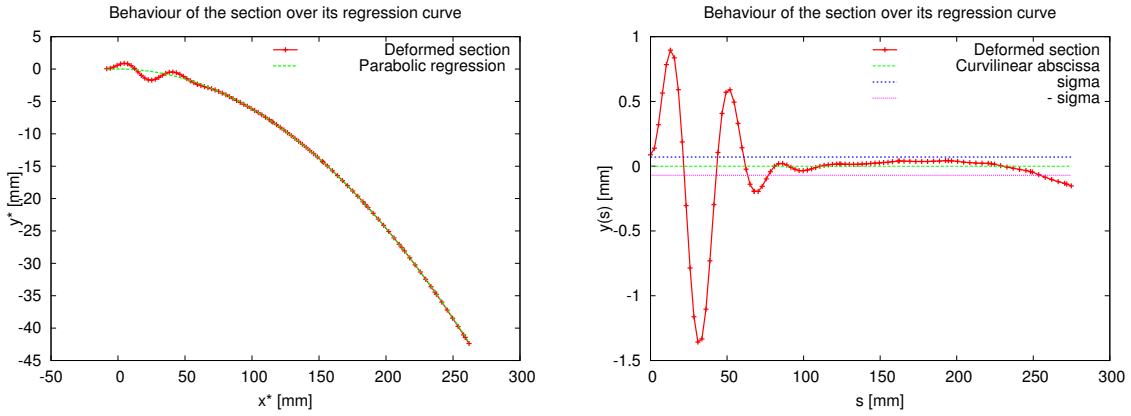

Figure B.2: Section curve and regression *left:* in the linear reference system x, y and *right* in the curvilinear reference system $s, y(s)$

An example is shown in figures B.2. The evaluation of the number of *Zero crossing* produced in this case the answer 7, and the number of wrinkle is 5. The wrinkles wave-length and semi-amplitude are reported in Table B.1.

B.9 Volume measures in curvilinear coordinates

Proof. An infinitesimal volume dV corresponding to the curvilinear coordinates differential: $(d\xi^1, d\xi^2, d\xi^3)$ is expressed as:

$$dV = |[\vec{g}_1, \vec{g}_2, \vec{g}_3]|\, d\xi^1 d\xi^2 d\xi^3 \tag{B.52}$$

where:

$$[\vec{g}_1, \vec{g}_2, \vec{g}_3] \overset{def.}{=} \vec{g_1} \cdot (\vec{g_2} \times \vec{g_3}) \tag{B.53}$$

$$\vec{g}_m = \frac{\partial \Phi}{\partial \xi^m} \tag{B.54}$$

Let $[\Phi_1, \Phi_2, \Phi_3]$ be the component in an orthonormal system of the chart $\vec{\Phi}$ defined in Section 4.1.1. Now:

$$g_{mn} = \vec{g}_m \cdot \vec{g}_n = \frac{\partial \Phi_p}{\partial \xi^m} \frac{\partial \Phi_p}{\partial \xi^n} \overset{def.}{=} G_{pm}\, G_{pn} = G^T G \tag{B.55}$$

G is then the matrix of the components of the covariant basis in orthonormal system. The determinant of the last equation can then be expressed as:

$$det(g_{mn}) = det(G^T G) = det(G)^2 \tag{B.56}$$

Now:

$$det(G) = det\left([G]_{3\times 3}\right) = det \begin{pmatrix} \frac{\partial \Phi_1}{\partial \xi^1} & \frac{\partial \Phi_1}{\partial \xi^2} & \frac{\partial \Phi_1}{\partial \xi^3} \\ \frac{\partial \Phi_2}{\partial \xi^1} & \frac{\partial \Phi_2}{\partial \xi^2} & \frac{\partial \Phi_2}{\partial \xi^3} \\ \frac{\partial \Phi_3}{\partial \xi^1} & \frac{\partial \Phi_3}{\partial \xi^2} & \frac{\partial \Phi_3}{\partial \xi^3} \end{pmatrix} \overset{def.}{=} \vec{g_1} \cdot (\vec{g_2} \times \vec{g_3}) \overset{def.}{=} [\vec{g}_1, \vec{g}_2, \vec{g}_3] \tag{B.57}$$

Therefore:

$$det(g_{mn}) = det(G)^2 = \left([\vec{g}_1, \vec{g}_2, \vec{g}_3]\right)^2 \tag{B.58}$$

and applying the square root:

$$\sqrt{det(g_{mn})} \overset{def.}{=} \sqrt{g} = \left|[\vec{g}_1, \vec{g}_2, \vec{g}_3]\right| \tag{B.59}$$

Equation B.52 can then be rewritten as:

$$dV = \sqrt{g}\; d\xi^1 d\xi^2 d\xi^3 \tag{B.60}$$

This result is valid for the continuum shell model represented by the chart $\vec{\Phi}$ in curvilinear coordinates. As shown in section 4.1.4 however, using the *Reissnles-Mindlin* kinematic assumption the shell is reduced to its midsurface and the thickness. It is then necessary to express the volume measures in terms of the midsurface, or to pass from the reference system constituted by the vectors $\vec{g}_m$ (see (4.1)) to the reference system build with the $\vec{a}_m$ (see (4.12)).

From Equation (4.13), and following the same notation used previously, it follows that:

$$\|\vec{a_1} \times \vec{a_2}\| = (\vec{a_1} \times \vec{a_2}) \cdot \vec{a}_3 \overset{def.}{=} [\vec{a}_1, \vec{a}_2, \vec{a}_3] \tag{B.61}$$

where, using Equations (4.29):

$$[\vec{a}_1, \vec{a}_2, \vec{a}_3] = (|[\vec{g}_1, \vec{g}_2, \vec{g}_3]|)_{\xi^3=0} \tag{B.62}$$

it is then possible (evaluating some more equations, which are here neglected but can be found in [4], Equations 2.155 to 2.160) to infer that Equation (B.60) can be modified as:

$$dV = \sqrt{a}\ d\xi^1 d\xi^2 d\xi^3 \tag{B.63}$$

□

B.10 Calculation of the covariant/contravariant metric tensor

The program listed below calculates the covariant and the contravariant components of the metric tensor. The input of the program is a file, the lines of which correspond to the components of three linearly independent base vectors. Once the vector components have been read, the program verify if they are linearly independent (det $\neq 0$) and it calculates the covariant components of the metric tensor g_{mn}. The contravariant components g^{mn} are then calculated inverting the matrix $\vec{\vec{g}}_{mn}$. The calculation of the inverse matrix is not detailed here, but it can be performed trivially for a 3x3 matrix. Here however a more generic solver was written, based on the Cholesky-Crout decomposition. With this method it is possible to calculate the triangularization of the matrix: the matrix $\mathbf{A}$ is transformed in the shape $\mathbf{L}\,\mathbf{L}^T$. The inverse of $\mathbf{A}$ will be then written as: $\mathbf{A}^{-1} = \mathbf{L}^{-1}\mathbf{L}^{-T}$, where the inverse of a triangular matrix is calculated by simply performing a series of products between its entries.

```
1
2   program VarContraVar
3
4     use dynalloc
5     implicit none
6
7     integer NF, Lfid, i, j,k
8     real i_(3,3), iA(3,3), val
9     real vec(3)
10    real g_mn(3,3), gAmn(3,3)
11    character*80 fid
12
13    print*, 'Please enter the file name...'
14    !read(*,*) fid
15    fid='BaseVectors'
```

```
16      Lfid=longg(fid)
17
18      NF=1
19      open(unit=NF,file=fid(1:Lfid))
20
21      !WARNING: VECTORS ARE STORED IN LINES!!
22      read(NF,*) i_(1,1), i_(1,2), i_(1,3)
23      read(NF,*) i_(2,1), i_(2,2), i_(2,3)
24      read(NF,*) i_(3,1), i_(3,2), i_(3,3)
25
26      print*,'==========================================='
27      print*, 'Entered CoVariant base vectors: '
28      do j=1,3
29         write(*,100) (i_(j,i),i=1,3)
30         print*, '--'
31      enddo
32      print*,'==========================================='
33
34      !verify if base vectors are linearly independent!
35      call det(i_,3,val)
36      if (val.eq.0)then
37         print*,'Error, vectors are not linearly independent!'
38      endif
39
40      !init the metric tensor...
41      do i=1,3
42         do j=1,3
43            g_mn(i,j)=0
44         enddo
45      enddo
46
47      print*, 'calculate the covariant components metric tensor...'
48      do i=1,3
49         g_mn(1,1)= g_mn(1,1)+i_(1,i)*i_(1,i)
50         g_mn(2,2)= g_mn(2,2)+i_(2,i)*i_(2,i)
51         g_mn(3,3)= g_mn(3,3)+i_(3,i)*i_(3,i)
52         g_mn(2,1)= g_mn(2,1)+i_(2,i)*i_(1,i)
53         g_mn(3,1)= g_mn(3,1)+i_(3,i)*i_(1,i)
54         g_mn(3,2)= g_mn(3,2)+i_(3,i)*i_(2,i)
55      enddo
56      g_mn(1,2)=g_mn(2,1)
```

```
57      g_mn(1,3)=g_mn(3,1)
58      g_mn(2,3)=g_mn(3,2)
59
60
61      print*, ' '
62      print*,'=================================='
63      print*, 'Covariant Metric Tensor g_mn... '
64      do i=1,3
65         write(*,100) (g_mn(j,i), j=1,3)
66      enddo
67      print*,'=================================='
68      print*, ' '
69
70      print*, ' Determinant of g_mn: '
71      call det(g_mn,3,val)
72      print*, val
73      print*, ' '
74
75      !gAmn = inv ( g_mn )
76      call inv(g_mn,3,gAmn)
77
78      print*, ' '
79      print*,'=================================='
80      print*, 'ContraVariant Metric Tensor gAmn... '
81      do i=1,3
82         write(*,100) (gAmn(j,i), j=1,3)
83      enddo
84      print*,'=================================='
85      print*, ' '
86
87      !contra-variant components:
88      !iAm= gAmn * i_n
89      call scopy(3*3,zero,0,iA,1)
90      do i=1,3
91         do j=1,3
92            do k=1,3
93               iA(j,i)=iA(j,i)+gAmn(j,k)*i_(k,i)
94            enddo
95         enddo
96      enddo
97      print*,'=================================='
```

```
98      print*, 'ContraVariant base vectors: '
99      do j=1,3
100        write(*,100) (iA(j,i),i=1,3)
101        print*,'--'
102     enddo
103     print*,'=========================================='
104     print*, ' '
105
106
107 100 format(3X,3(f5.2,2X))
108
109   end program VarContraVar
```

Listing B.1: The FORTRAN (main) code

Appendix C

Appendices to the Fluid Structure Interactions Chapter

C.1 The mesh velocity

Recall the transformations in (5.1), (5.2) and (5.3). The gradient of the mapping $\varphi(X,t)$ is defined as:

$$\frac{\partial \varphi(X,t)}{\partial(X,t)} = \begin{pmatrix} \frac{\partial(x,t)}{\partial X}\Big|_t & \frac{\partial(x,t)}{\partial t}\Big|_t \\ \frac{\partial(x,t)}{\partial X}\Big|_x & \frac{\partial(x,t)}{\partial t}\Big|_x \end{pmatrix} = \begin{pmatrix} \frac{\partial x}{\partial X} & \mathbf{v} \\ \mathbf{0} & 1 \end{pmatrix} \tag{C.1}$$

where $\frac{\partial \bullet}{\partial \bullet}\big|_B$ means 'holding the term B fixed'. It has then been defined the the mesh velocity $\mathbf{v}$. The last term takes a value of $\mathbf{1}$, because time is one-to-one mapped in every domain.

With similar considerations it it possible to identify the gradient of the transformations Φ as:

$$\frac{\partial \mathbf{\Phi}(\chi,t)}{\partial(\chi,t)} = \begin{pmatrix} \frac{\partial(x,t)}{\partial \chi}\Big|_t & \frac{\partial(x,t)}{\partial t}\Big|_t \\ \frac{\partial(x,t)}{\partial \chi}\Big|_x & \frac{\partial(x,t)}{\partial t}\Big|_x \end{pmatrix} = \begin{pmatrix} \frac{\partial x}{\partial \chi} & \hat{\mathbf{v}} \\ \mathbf{0} & 1 \end{pmatrix} \tag{C.2}$$

where the mesh velocity is now indicated as $\hat{\mathbf{v}}$. The gradient of the transformation Ψ^{-1} reads:

$$\frac{\partial \mathbf{\Psi^{-1}}(X,t)}{\partial(X,t)} = \begin{pmatrix} \frac{\partial(\chi,t)}{\partial X}\Big|_t & \frac{\partial(\chi,t)}{\partial t}\Big|_t \\ \frac{\partial(\chi,t)}{\partial X}\Big|_\chi & \frac{\partial(\chi,t)}{\partial t}\Big|_\chi \end{pmatrix} = \begin{pmatrix} \frac{\partial \chi}{\partial X} & \mathbf{w} \\ \mathbf{0} & 1 \end{pmatrix} \tag{C.3}$$

the velocity $\mathbf{w}$ can be interpreted as the particle velocity in the referential domain. It measures in fact the variation of the referential coordinate χ holding the material particle $\mathbf{X}$ fixed.

It is now possible to relates the gradients and find relations between the velocities $\mathbf{v}$, $\hat{\mathbf{v}}$ and $\mathbf{w}$. This is done using Figure 5.2 as a reference. Since it is possible to transform from

domain 1 to 2 or equivalently from 1 to 3 and from 3 to 2:

$$\begin{matrix} 1 \to 2 \\ \frac{\partial\,\varphi(X,t)}{\partial(X,t)} \end{matrix} = \begin{matrix} 3 \to 2 \\ \frac{\partial\,\Phi(\chi,t)}{\partial(\chi,t)} \end{matrix} \cdot \begin{matrix} 1 \to 3 \\ \frac{\partial\,\Psi^{-1}(X,t)}{\partial(X,t)} \end{matrix} \tag{C.4}$$

where the left hand side is described by equation C.1. The First term of the right hand side is described by equation C.2, and the last is described by equation C.3. Rewriting in matrix form then:

$$\begin{pmatrix} \frac{\partial x}{\partial X} & \mathbf{v} \\ \mathbf{0} & 1 \end{pmatrix} = \begin{pmatrix} \frac{\partial x}{\partial \chi} & \hat{\mathbf{v}} \\ \mathbf{0} & 1 \end{pmatrix} \cdot \begin{pmatrix} \frac{\partial \chi}{\partial X} & \mathbf{w} \\ \mathbf{0} & 1 \end{pmatrix} \tag{C.5}$$

which leads to the definition of the convective velocity $\mathbf{c}$. This is the relative velocity between the material and the mesh, and it is defined as:

$$\mathbf{c} := \mathbf{v} - \hat{\mathbf{v}} = \frac{\partial x}{\partial \chi} \cdot \mathbf{w} \tag{C.6}$$

C.2 ALE convective term

the fundamental ALE equations are formulated trough the use of opportune functions. Define then the functions in the three reference domains: $f(x,t)$, $f^*(\chi,t)$, $f^{**}(X,t)$, it is possible to compose with the transformations φ as:

$$f^{**}(X,t) = f(\varphi(X,t),t) \text{ ; or in a more compact notation: } f^{**} = f_o\varphi \tag{C.7}$$

the gradient of such expression (using the standard formulation for the derivative of composite functions) results:

$$\frac{\partial f^{**}(X,t)}{\partial(X,t)} = \frac{\partial}{\partial(X,t)} f(\varphi(X,t),t)\,\frac{\partial(x,t)}{\partial(x,t)} = \frac{\partial}{\partial(x,t)} f(x,t)\,\frac{\partial(\varphi(X,t))}{\partial(X,t)} \tag{C.8}$$

rewriting in matrix form:

$$\left(\frac{\partial f^{**}}{\partial X}, \frac{\partial f^{**}}{\partial t}\right) = \left(\frac{\partial f}{\partial x}, \frac{\partial f}{\partial t}\right) \begin{pmatrix} \frac{\partial x}{\partial X} & \mathbf{v} \\ \mathbf{0} & 1 \end{pmatrix} \tag{C.9}$$

this system generates two equations. The first being trivial it is here omitted; the second expresses the relation between the spatial and material derivative, as in equation 12:

$$\frac{\partial f^{**}}{\partial t} = \frac{\partial f}{\partial t} + \frac{\partial f}{\partial x} \cdot \mathbf{v} \quad \text{or:} \quad \frac{df}{dt} = \frac{\partial f}{\partial t} + \mathbf{v} \cdot \nabla f \tag{C.10}$$

Similarly it is possible to express equations for the transformation Ψ: $f^{**} = f^*{}_o\,\Psi^{-1}$. The convective velocity is then expressed as:

$$\frac{\partial f^{**}}{\partial t} = \frac{\partial f^*}{\partial t} + \frac{\partial f^*}{\partial \chi} \cdot \mathbf{w} \tag{C.11}$$

where, from equation 5.4 $\mathbf{w} = \mathbf{c}\ \partial\chi/\partial x$:

$$\frac{\partial f^{**}}{\partial t} = \frac{\partial f^{*}}{\partial t} + \frac{\partial f}{\partial x} \cdot \mathbf{c} \quad \text{or:} \quad \frac{\partial f}{\partial t}\Big|_X = \frac{\partial f}{\partial t}\Big|_\chi + \mathbf{c} \cdot \nabla f \tag{C.12}$$

such expression links the derivative in the material (Lagrangian) configuration X and the reference (ALE) configuration χ using the ALE convective term, where the relative velocity $\mathbf{c}$ is involved. In other words, the convective term needs now to take into account also for the grid velocity $\hat{\mathbf{v}}$. Navier-Stokes equations defined in equation 3.18 can now be reformulated in the ALE framework as:

$$\rho \frac{\partial v}{\partial t} + \rho \left(v - \hat{v}\right) \nabla v = \rho f - \nabla p + \mu \Delta v \tag{C.13}$$

where, compared to the original formulation of the Navier-Stokes equations, only the convective term is modified for taking into account the grid velocity $\hat{\mathbf{v}}$. The laplacian terms does not need modifications, because it involves a second derivative and is is therefore not affected by the relative velocity.

C.3 Derivation of the Added Mass discrete operator

The governing fluid equations (5.6) can be conveniently discretized (see [115]) in matrix form as:

$$\begin{cases} \mathbf{M}^F \cdot \dot{\mathbf{u}} + \mathbf{N}^F(\mathbf{u}) + \mathbf{G} \cdot \mathbf{p} = \mathbf{f}_\Gamma \\ \mathbf{G}^T \cdot \mathbf{u} = 0 \end{cases} \tag{C.14}$$

where $\mathbf{M}^F$ is the mass matrix, $\mathbf{N}^F(\mathbf{u})$ the internal force vector and $\mathbf{G}$ the discrete gradient operator of the fluid.

Assuming a linear framework, small motions, negligible changes of the relevant matrices in time, neglecting the fluid stiffness and assuming no structural damping, the coupled system can be written in matrix form by splitting into degrees of freedom I, interior to the fluid domain, and Γ, belonging to the interface, Equation (C.14) reads:

$$\begin{bmatrix} \mathbf{M}^F_{II} & \mathbf{M}^F_{I\Gamma} & \mathbf{G}_I \\ \mathbf{M}^F_{\Gamma I} & \mathbf{M}^F_{\Gamma\Gamma} & \mathbf{G}_\Gamma \\ \mathbf{G}^T_I & \mathbf{G}^T_\Gamma & 0 \end{bmatrix} \begin{bmatrix} \dot{\mathbf{u}}_I \\ \dot{\mathbf{u}}_\Gamma \\ \mathbf{p} \end{bmatrix} = \begin{bmatrix} 0 \\ \mathbf{f}_\Gamma \\ 0 \end{bmatrix} \tag{C.15}$$

With some basic algebra (entirely detailed in [115]) the interface coupling force $\mathbf{f}_\Gamma$ can be expressed in terms of the acceleration of the interface:

$$\begin{aligned}\mathbf{f}_\Gamma &= \{(\mathbf{M}^F_{\Gamma I}(\mathbf{M}^F_{II})^{-1}\mathbf{G}_I - \mathbf{G}_\Gamma)\big(\mathbf{G}_I^T(\mathbf{M}^F_{II})^{-1}\mathbf{G}_I\big)^{-1} \\ &\quad \times\big(\mathbf{G}_I^T(\mathbf{M}^F_{II})^{-1}\mathbf{M}^F_{I\Gamma} - \mathbf{G}_I^T\big) - \mathbf{M}^F_{\Gamma I}(\mathbf{M}^F_{II})^{-1}\mathbf{M}^F_{I\Gamma} + \mathbf{M}^F_{\Gamma\Gamma}\}\dot{\mathbf{u}}_\Gamma \qquad \text{(C.16)}\end{aligned}$$

the discrete operator in curly brackets has the dimension of a mass and is generally normalised by a characteristic fluid mass m^F, for instance a nodal mass matrix. This is why it is called *added mass* operator, and it reads then:

$$\begin{aligned}\mathscr{M}_A &=: \frac{1}{m^F}(\mathbf{M}^F_{\Gamma I}(\mathbf{M}^F_{II})^{-1}\mathbf{G}_I - \mathbf{G}_\Gamma)\big(\mathbf{G}_I^T(\mathbf{M}^F_{II})^{-1}\mathbf{G}_I\big)^{-1} \\ &\quad \times\big(\mathbf{G}_I^T(\mathbf{M}^F_{II})^{-1}\mathbf{M}^F_{I\Gamma} - \mathbf{G}_I^T\big) - \frac{1}{m^F}\mathbf{M}^F_{\Gamma I}(\mathbf{M}^F_{II})^{-1}\mathbf{M}^F_{I\Gamma} + \frac{1}{m^F}\mathbf{M}^F_{\Gamma\Gamma} \qquad \text{(C.17)}\end{aligned}$$

the fluid force at the interface Γ reads then:

$$\mathbf{f}_\Gamma = m^F\,\mathscr{M}_A\,\dot{\mathbf{u}}_\Gamma \qquad \text{(C.18)}$$

The structural system in Equation (5.7) can now be expressed as:

$$\mathbf{M}^S\,\ddot{\mathbf{X}} + \mathbf{K}(\mathbf{X}) = -\mathbf{f}_\Gamma \qquad \text{(C.19)}$$

where $\mathbf{M}^S$ is the mass matrix and $\mathbf{K}(\mathbf{X})^S$ is the stiffness operator of the structure. The right hand side is a vector which consists of the fluid forces only; all other contributions are neglected. In matrix form then:

$$\begin{bmatrix}\mathbf{M}^S_{II} & \mathbf{M}^S_{I\Gamma}\\ \mathbf{M}^S_{\Gamma I} & \mathbf{M}^S_{\Gamma\Gamma}\end{bmatrix}\begin{bmatrix}\ddot{\mathbf{d}}_I\\ \ddot{\mathbf{d}}_\Gamma\end{bmatrix} + \begin{bmatrix}\mathbf{K}^S_{II} & \mathbf{K}^S_{I\Gamma}\\ \mathbf{K}^S_{\Gamma I} & \mathbf{K}^S_{\Gamma\Gamma}\end{bmatrix}\begin{bmatrix}\mathbf{d}_I\\ \mathbf{d}_\Gamma\end{bmatrix} = \begin{bmatrix}0\\ -m^F\,\mathscr{M}_A\dot{\mathbf{u}}_\Gamma\end{bmatrix} \qquad \text{(C.20)}$$

where $\mathbf{K}^S$ is the stiffness matrix obtained by linearisation of the stiffness operator $\mathbf{K}(\mathbf{X})^S$. It appears then that the added mass operates as an additional mass on the interface degrees of freedom.

C.4 Derivation of the higher time-step bound of the stability condition

Recall the stability condition, with C_{inst} positive constant, (5.11):

$$\frac{m^F + a\,\Delta t\,k^F}{m^S + b\,\Delta t^2\,k^S}\,\max_i\,\mu_i < C_{inst}$$

this leads to the equivalent formulation:

$$(C_{inst}\, b\, k^S)\, \Delta t^2 - (a\, k^F \max_i\, \mu_i)\, \Delta t + (C_{inst}\, m^S - m^F \max_i\, \mu_i) > 0$$

this is a second order equation in the unknown Δt, and can be re-expressed in the more compact shape:

$$\mathbb{A}\, \Delta t^2 - \mathbb{B}\, \Delta t + \mathbb{C} > 0 \tag{C.21}$$

where the coefficients $\mathbb{A}$, $\mathbb{B}$ and $\mathbb{C}$ are proportional[1] to:

$$\mathbb{A} \quad \alpha \quad k^S \tag{C.22}$$

$$\mathbb{B} \quad \alpha \quad \max_i\, \mu_i;\ k^F \tag{C.23}$$

$$\mathbb{C} \quad \alpha \quad m^S \tag{C.24}$$

$$1/\alpha \quad m^F; \max_i\, \mu_i; \tag{C.25}$$

where all the terms are positive, in fact: all $\mu_i > 0$ (see [117], Remark 3.1), and all the stiffness and mass terms are positive by definition.

The determinant $\Delta = b^2 - 4ac$ of Equation (C.21) is therefore proportional to:

$$\Delta \quad \alpha \quad \max_i\, \mu_i\ ;\ k^F\ ;\ m^F \tag{C.26}$$

$$1/\alpha \quad k^S\ ;\ m^S \tag{C.27}$$

The time-step value therefore, evaluating only one solution of the second order equation (C.21) as: $\Delta t = -b + \sqrt{\Delta}/2a$, results also proportional to:

$$\Delta t \quad \alpha \quad \max_i\, \mu_i\ ;\ k^F\ ;\ m^F \tag{C.28}$$

$$1/\alpha \quad k^S\ ;\ m^S \tag{C.29}$$

or, defined an arbitrary positive constant C^*:

$$\Delta t > C^* \frac{k^F\ m^F \max_i \mu_i}{k^S\ m^S} \tag{C.30}$$

[1] Proportional must be here intended in a very weak sense: $A\ \alpha\ B$ if $\|A + B\| > \|A\|$ and vice-versa $A\ 1/\alpha\ B$ if $\|A + B\| < \|A\|$

C.5 Operating in the ALE framework in OpenFOAM

Using the ALE framework in the OpenFOAM framework is relatively straightforward, once the basics are understood. The following relates to the main modifications to be performed to the base code pimpleDyMFOAM implemented in in OpenFOAM version 1.6-ext.
Primarily some include are needed for the points/volumes interpolation. This is needed for making possible to directly assign the displacements of the points of the mesh:

```
#include "pointMesh.H"
#include "pointFields.H"
#include "volPointInterpolation.H"
```

Second step, it is necessary to find a reference to the location of pointDisplacement field. This is the memory address of the location where the values of the mesh point displacement vector is stored:

```
pointVectorField & PointDisplacement = const_cast<pointVectorField&>
                (mesh.objectRegistry::lookupObject<pointVectorField>
                ("pointDisplacement "));
```

Third, a reference to the structural interface and the relevant entries are found as:

```
IOdictionary couplingDict   //Search the Dict "CouplingDict" in constant
(
 IOobject
 (
  "CouplingDict",
  runTime.constant(),
  mesh,
  IOobject::MUST_READ,
  IOobject::NO_WRITE
 )
);

word sail = couplingDict.lookup(Wing) //search in  declared as 'coupling'
label fluidSideI = mesh.boundaryMesh().findPatchId(sail)
vectorField &pDisp=refCast<vectorField>
                (PointDisplacement.boundaryField()[fluidSideI]);
nFaces=mesh.boundaryMesh()[fluidPatchID].size();
```

Find the relevant size of the vector and declare a vectorField. This will store the pointDisplacements values (in my case they come from the structural solver)

```
int Psize= pDisp.size();
vectorField dispVals(Psize);
```

The pressures acting on the structural interface can be retrieved (see forces.C) and stored in a vector previously declared:

```
for(int ii=0; ii<nFaces; ii++){
        Press[ii]=double( sign[ii]*p.boundaryField()[fluidPatchID][ii]*rhoVal);
 }
```

The values of the point displacements of the structural interface, stored in the vectorField dispVals in the correct numbering, are assigned to the fluid domain with:

```
PointDisplacement.boundaryField()[ fluidSideI ] == dispVals;
```

The mesh is updated via the motionSolver specified in dynamicMeshDict (in this case it has been used the *dynamicMotionSolverFvMesh*) with:

```
mesh.update();
```

As stated in Section 5.1.5, in the OpenFOAM setting the mesh displacement must be applied before solving the the fluid.

C.6 Using MPI for code-to-code communications (C++ and Fortran)

In the present work a C++ finite volume library was coupled with a Fortran Finite Element code for performing Fluid Structure Interactions. The code-to-code coupling in a Multiple Program Multiple Data (MPMD) environment is not a trivial task, therefore the adopted setting is here reviewed. A deliberately simple tutorial code is reported, which shows the basics of the implemented communication strategy, rather than the actual complete Fluid Structure Interaction code. The framework detailed here is then suitable to be adopted for any other code-to-code coupling, using any language supporting the MPI library.

The type of communication which has been adopted here is based on the intercommunications, as in Figure C.1. Each piece of code lives in its own world, but it can communicate data with other solvers; the links used to send and receive the messages are created when the Master launches ("spawns") the Slaves.

The code is therefore executed by launching the master only; this will launch the slave(s) during the execution. In the tutorial, one array of data is initialised in the Master, passed to

the Slave, modified and sent back to the Master. The example is presented for one process to one process communication: every executable is executed in serial. However no major difficulty is encountered when modifying every code for Single Program Multiple Data (SPMD) communications, using therefore intra-communicators in the standard way.

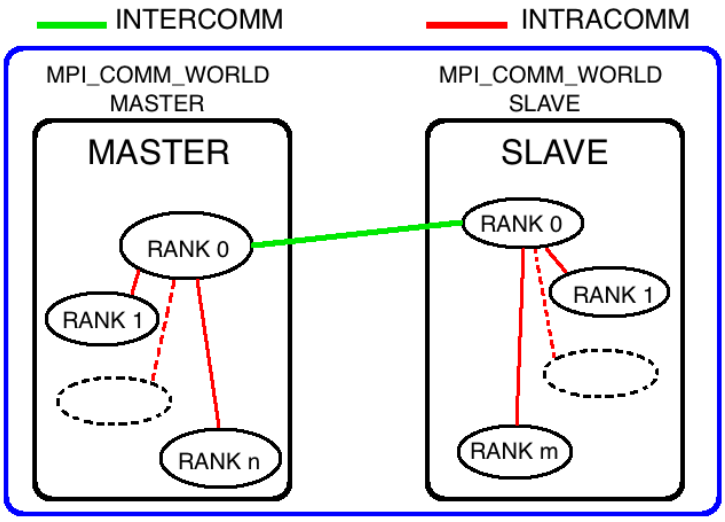

Figure C.1: Intercommunicators and intracommunicators

```
1
2  #include <iostream>
3  #include <stdio.h>
4  #include <stdlib.h>
5  #include <mpi.h>
6  using namespace std;
7
8  #define TAG_WORK 1
9  #define TAG_STOP 2
10
11 int main(int argc, char **argv)
12 {
13  int myrank, ntasks, ierr;
14  double data[10];
15  MPI_Status status;
16  int num_spawns = 1, master = 0;
17  MPI_Comm intercomm1;
18
19  // Initialize MPI
20  ierr = MPI_Init(&argc, &argv);
21
22  // Get the number of processes
```

```
23  ierr = MPI_Comm_size(MPI_COMM_WORLD, &ntasks);
24  if (ntasks>1)
25  {
26   printf("We must have ONE master \n");
27   exit(1);
28  }
29
30  // Get the individual process ID
31  ierr = MPI_Comm_rank(MPI_COMM_WORLD, &myrank);
32
33  // Spawn slave 1
34  ierr = MPI_Comm_spawn( "slave1",
35    MPI_ARGV_NULL, num_spawns, MPI_INFO_NULL, master,
36    MPI_COMM_WORLD, &intercomm1, MPI_ERRCODES_IGNORE );
37
38  if(ierr)
39   {
40     printf("Cannot execute slave1.sh \n");
41     exit(1);
42   }
43
44  //Init variables:
45  for (int i=0;i<10;i++){
46   data[i]=3.0;
47  }
48
49  for(int j=1;j<1000;j++)
50    {
51     //Send
52     for(int i=0;i<num_spawns;i++)
53      {
54        cout <<"Master sends "<<data[0]<<" to slave rank "<<i<<endl;
55        MPI_Send(&data,10,MPI_DOUBLE,i,TAG_WORK,intercomm1);
56      }
57
58     //Receive
59     for(int i=0;i<num_spawns;i++)
60      {
61        MPI_Recv(&data, 10, MPI_DOUBLE, i,MPI_ANY_TAG, intercomm1, &status);
62        cout<<"Master receives "<<data[0]<<" from slave rank "<<i<<endl;
63          }
```

```
64    }
65
66    //Send TAG_STOP to terminate the slaves
67    for(int i=0;i<num_spawns;i++)
68      {
69        MPI_Send(&data, 1, MPI_DOUBLE, i, TAG_STOP, intercomm1);
70      }
71
72     MPI_Comm_free(&intercomm1);
73     MPI_Finalize();
74     return 0;
75  }
```

Listing C.1: The C++ code for the Master

```
1
2       program slave
3
4       implicit none
5       include 'mpif.h'
6
7       integer :: i
8       integer myrank, ierr, taille, parentcomm, slavecomm
9       integer, dimension(MPI_STATUS_SIZE) :: state
10      double precision, dimension(:) :: montableau(10)
11
12      call MPI_Init(ierr)
13      call MPI_Comm_get_parent(parentcomm, ierr);
14      call MPI_Comm_dup(MPI_COMM_WORLD, slavecomm,ierr);
15      call MPI_Comm_size(slavecomm,taille,ierr);
16      call MPI_Comm_rank(slavecomm, myrank, ierr);
17
18      do while(1.eq.1)
19
20          call MPI_Recv(montableau,10,MPI_DOUBLE_PRECISION,0,MPI_ANY_TAG,
21     &                  parentcomm,state,ierr);
22          if (state(2).eq.2) then
23             exit
24          endif
25
26          do i=1,10
27             montableau(i) = montableau(i)+1.0
```

```
28          enddo
29
30          call MPI_Send(montableau,10, MPI_DOUBLE_PRECISION,0,3,
31       &              parentcomm,ierr)
32
33        enddo
34
35        call MPI_Finalize(ierr);
36        end program slave1
```

Listing C.2: The Fortran code for the Slave

```
1
2  CCC = /openMPI/bin/mpicxx
3  CCCFLAGS = -Wall -g
4  LDFLAGS = -lm
5
6  EXEC = master
7  OBJS = main.o
8
9  INCLUDES     =
10
11 .cpp.o:
12         $(CCC) $(CCCFLAGS)  $(INCLUDES) -c $<
13
14 $(EXEC): $(OBJS)
15         $(CCC)  $(CCCFLAGS) $(OBJS) $(LDFLAGS) -o $(EXEC)
```

Listing C.3: The C++ makefile

```
1
2  #Fortran OPTIONS
3  FFLAGS= -O
4  #Fortran compile object files
5  .DEFAULT: .f
6  .SUFFIXES:.f
7
8  .f.o: $*.f
9          /openMPI/bin/mpif90 -c -m64 $(FFLAGS) $*.f
10
11 #source file(s) name
12 OBJF= slave1.o
```

```
13 FEXE=slave1
14
15 all: $(OBJF) $(FEXE)
16 $(FEXE): $(OBJF)
17         /openMPI/bin/mpif90 -m64 $(OBJF) -o slave1
```

Listing C.4: The Fortran makefile

References

[1] D. Trimarchi and C. Rizzo, "A fem-matlab code for fluid-structure interaction coupling with application to sail aerodynamics of yachts," in *Proceedings of the 13th Congress of International Maritime Association of Mediterranean*, (Instanbul, Turkey), October 2009.

[2] D. Trimarchi, S. R. Turnock, D. Chapelle, and D. J. Taunton, "The use of shell elments to capture sail wrinkles, and their influence on aerodynamic loads," in *Proceedings of the Second International Conference in High Performance Sailing Yachts*, (Lorient, France), July 2010.

[3] D. Trimarchi, M. Vidrascu, D. Taunton, T. S.R., and D. Chapelle, "Wrinkle development analysis in thin sail-like structures using MITC shell finite elements," in preparation.

[4] D. Chapelle and K. J. Bathe, *The finite element analysis of shells: Fundamentals*. Berlin: Springer, 2001.

[5] Y. Wong and S. Pellegrino, "Wrinkled membranes: Experiments, analytical model and simulations," *Journal of Materials and Structures*, vol. 1, 2006.

[6] H. Versteeg and W. Malalasekera, *An introduction to computational fluid dynamics: the finite volume method*. Pearson Education Ltd., 2007.

[7] S. Song and J. Eaton, "Reynolds number effects on a turbulent boundary layer with separation, reattachment, and recovery," *Experiments in Fluids*, vol. 36, pp. 246–258, 2004.

[8] H. Johari and K. Desabrais, "Vortex shedding in the near wake of a parachute canopy," *Journal of Fluid Mechanics*, vol. 536, pp. 185–207, 2005.

[9] K. J. Desabrais, *Velocity field measurements in the near wake of a parachute canopy.* PhD thesis, Worchester Polytechnic Institute, Faculty of Mechanical Engineering, 2002.

[10] A. B. Phillips, S. R. Turnock, and M. Furlong, "Influence of turbulence closure models on the vortical flow field around a submarine body undergoing steady drift," *Journal of Marine Science and technology*, vol. 15, no. 3, pp. 201–217, 2010.

[11] J. Donea, A. Huerta, J. Ponthot, and A. Rodriguez-Ferran, "Arbitrary lagrangian eulerian methods," in *Encyclopedia of Computational Mechanics* (R. de Borst and T. J. Hughes, eds.), John Wiley & Sons, 2004.

[12] B. Uzonglu, M. Tan, and W. G. Price, "Low-reynolds-number flow around an oscillating circular cylinder using a cell viscous boundary element method," *International Journal for Numerical Methods in Engineering*, vol. 50, pp. 2317–2338, 2001.

[13] J. G. V. Vazquez, *Nonlinear Analysis of orthotropic membrane and shells structures including fluid-structure interaction.* PhD thesis, Departament de resistencia de materialsc i estructures a l'engineyeria, Universitat Politecnica de Catalunya, 2007.

[14] U. Ghia, K. N. Ghia, and C. T. Shin, "High-re solution for incompressible flow using the navier-stokes equations and the multigrid method," *Journal of Computational Physics*, vol. 48, pp. 387–411, 1982.

[15] D. Mok, W. Wall, and E. Ramm, "Accelerated iterative substructuring schemes for instationary fluid-structure interaction," *Computational Fluid and Solid Mechanics*, pp. 1325–1328, 2001.

[16] C. Kassiotis, A. Ibrahimbegovic, R. Niekamp, and H. G. Matthies, "Nonlinear fluid-structure interaction problem. part 1: implicit partitioned algorithm, nonlinear stability proof and validation examples," *Computational Mechanics*, vol. 47, pp. 305–323, 2011.

[17] J. F. Gerbeau and M. Vidrascu, "A quasi newton algorithm based on a reduced model for fluid structure interaction problems in blood flows," *Mathematical Modelling and Numerical Analysis*, vol. 37, p. 631 647, 2003.

[18] W. A. Wall, D. P. Mok, and E. Ramm, "Partitioned analysis approach of the transient coupled response of viscous fluids and flexible structures," in *Solids, structures and coupled problems in engineering, proceedings of the European Conference on Computational Mechanics*, 1999.

[19] M. Lombardi, A. Quarteroni, and N. Parolini, "Numerical simulation of sailing boats: dynamics, FSI and shape optimization," in *6th OpenFOAM workshop*, (Penn State University, USA), June 2011.

[20] J. Anderson, *Computational fluid dynamics: the basics with applications*. McGraw-Hill series in aeronautical and aerospace engineering, McGraw-Hill, 1995.

[21] S. Wilkinson, *Partially separated flow around masts and sails*. PhD thesis, University of Southampton, Fluid Structure Interactions department, 1984.

[22] M. Scarponi, *Including human performance in the dynamic model of a sailing yacht: a combined ship science-behavioural science approach towards a winning yacht-sailor combination*. PhD thesis, Universitá degli Studi di Perugia, Faculty of Mechanical Engineering, 2008.

[23] J. H. Milgram, "The analytical design of yacht sails," *Transactions SNAME*, vol. 76, pp. 118–160, 1968.

[24] M. Caponnetto, "The aerodynamic interference between two boats close-hauled," *International Shipbuilding Progress*, vol. 44, pp. 241–256, 1997.

[25] S. Collie, M. Gerritsen, and P. Jackson, "A review of turbulence modelling for use in sail flow analysis," tech. rep., University of Auckland, 2001.

[26] A. B. G. Querard and P. A. Wilson, "Aerodynamic of modern square head sails: a comparative study between wind-tunnel experiments and rans simulations," in *Proceedings of the modern Yacht*, (Southampton, UK), 2007.

[27] D. Boote and M. Caponnetto, "A numerical approach to the design of sailing yacht masts," in *Proceedings of 10th Chesapeake Sailing Yacht Simposium*, (Annapolis, Maryland, USA), 1991.

[28] T. Charvet, F. Hauville, and S. Huberson, "Numerical simulation of the flow over sails in real sailing conditions," *Journal of Wind Engineering and Industrial Aerodynamics*, vol. 63, no. 1-3, pp. 111–129, 1996.

[29] M. Hobbs, *Aeroelastic analysis of a Yacht Rig*. PhD thesis, University of Southampton, Fluid Structure Interactions department, 2000.

[30] T. Fukasawa and M. Katori, "Numerical approach to aeroelastic responses of three-dimensional flexible sails," in *Proceedings of 11th Chesapeake Sailing Yacht Simposium*, (Annapolis, Maryland, USA), 1993.

[31] Y. Roux, M. Durand, A. Leroyer, P. Queutey, M. Visonneau, J. Raymond, J.-M. Finot, F. Hauville, and A. Purwanto, "Strongly coupled VPP and ranse code for sailing yacht performance prediction," in *Proceedings of the third High Performance Yacht Design Conference* (T. R. I. of Naval Architects, ed.), (Auckland, New Zealand), december 2008.

[32] S. Malpede and A. Baraldi, "A fully integrated method for optimizing fiber-membrane sails," in *Proceedings of the third High Performance Yacht Design Conference* (T. R. I. of Naval Architects, ed.), (Auckland, New Zealand), december 2008.

[33] K. Graf and H. Renzsch, "RANSE investigations of downwind sails and integration into sailing yacht design processes," in *Proceedings of the second High Performance Yacht Design Conference* (T. R. I. of Naval Architects, ed.), (Auckland, New Zealand), december 2006.

[34] D. Greeley, K. Kirkman, A. Drew, and J. Cross-Whiter, "Scientific yacht design," in *Proceedings of the 9th Chesapeake Sailing Yacht Symposium*, (Annapolis, Maryland, USA), 1989.

[35] J. Pilate, "Development of a three-dimensional inverse sail design method," in *Proceedings of the third High Performance Yacht Design Conference* (T. R. I. of Naval Architects, ed.), (Auckland, New Zealand), december 2008.

[36] T. Speer, "Aerodynamics of teardrop wingmasts." Published on-line – http://www.tspeer.com, 1993.

[37] A. Veiga, *The analysis of partially separated flow on sails system using a sectional method.* PhD thesis, University of Southampton, Fluid Structure Interactions department, 2006.

[38] D. Coiro, F. Nicolosi, F. Scherillo, and M. Umberto, "Numerical and experimental aeroelastic analysis of sails," in *Proceedings of the first High Performance Yacht Design Conference* (T. R. I. of Naval Architects, ed.), (Auckland, New Zealand), december 2002.

[39] S. Turnock, *Prediction of ship rudder-propeller interaction using parallel computations and wind tunnel measurements.* PhD thesis, University of Southampton, Ship Science, 1993.

[40] G. Vernengo and S. Brizzolara, "Application of a vortex lattice method to the analysis of sail plans in upwind condition," in *Proceedings of the 13th Congress of International Maritime Association of Mediterranean*, (Instanbul, Turkey), October 2009.

[41] A. R. Claughton and I. M. C. Campbell, "Wind tunnel testing of sailing rigs," in *Proceedings of the international HISWA Simposium on yacht design and yacht construction*, (Amsterdam), pp. 89–106, November 1994.

[42] D. Wilcox, *Turbulence Modelling for CFD.* La Canãda, California: DCW industries inc., 1993.

[43] H. Miyata and Y. Lee, "Application of cfd simulation to the design of sails," *Journal of Marine Science and Technology*, vol. 4, pp. 162–172, 1999.

[44] S. Collie, M. Gerritsen, and M. O'Sullivan, "Numerical simulation of the turbulent flow past upwind yacht sails," tech. rep., University of Auckland, 2002.

[45] K. Graf and E. Wolf, "CFD investigations and design integration for IACC yachts," in *Proceedings of the first High Performance Yacht Design Conference* (T. R. I. of Naval Architects, ed.), (Auckland, New Zealand), december 2002.

[46] N. Parolini and A. Quarteroni, "Mathematical models and numerical simulations for the america's cup," tech. rep., Mox – Politecnico di Milano, 2004.

[47] B. Krebber and K. Hochkirch, "Numerical investigation on the effects of trim for a yacht rig," in *Proceedings of the second High Performance Yacht Design Conference* (T. R. I. of Naval Architects, ed.), (Auckland, New Zealand), december 2006.

[48] A. Schneider, A. Arnone, M. Savelli, A. Ballica, and P. Scutellaro, "On the use of cfd to assist with sail design," in *Proceedings of the 16th Chesapeake sailing Yacht Symposium*, (Annapolis, Maryland), 2003.

[49] V. Chapin, S. Jamme, and P. Chassaing, "Viscous computational fluid dynamics as a relevant decision-making tool for mast-sail aerodynamics," *Marine Technology*, vol. 42, pp. 1–10, 2005.

[50] J. Paton, P. Heppel, and H. Morvan, "Fluid structure interaction of yacht sail," in *Proceedings of the first International Conference in High Performance Sailing Yachts* (T. R. I. of Naval Architects, ed.), (Lorient, France), 2008.

[51] D. Trimarchi, S. R.Turnock, D. Chapelle, and D. J. Taunton, "Fluid-structure interactions of anisotropic thin composite materials for application to sail aerodynamics of a yacht in waves," in *Proceedings of the second Numerical Towing Tank Symposium*, (Cortona, Italy), 2009.

[52] J. Yoo and H. Kim, "Computational and experimental study on performance of sail of a sailing yacht," *Ocean Engineering*, vol. 33, pp. 1322–1342, 2006.

[53] C. Ciortan and C. Soares, "Computational study of sail performance in upwind condition," *Ocean Engineering*, vol. 34, pp. 2198–2206, 2007.

[54] Y. Masuyama, Y. Tahara, T. Fukasawa, and N. Maeda, "Database of sail shapes vs. sail performance and validation of numerical calculation for upwind condition," in *Proceedings of 18th Chesapeake Sailing Yacht Simposium*, (Annapolis, Maryland, USA), 2007.

[55] I. Viola, *Numerical and Experimental Flow Dynamics applied to Sailing Yacht Dynamics,*. PhD thesis, Politecnico di Milano, 2008.

[56] K. Hedges, P. Richards, and G. Mallinson, "Computer modelling of downwind sails," *Journal of Wind Engineering*, vol. 63, pp. 95–110, 1996.

[57] S. Collie, P. Jackson, M. Gerritsen, and J. Fallow, "Two-dimensional cfd-based parametric analysis of downwind sail designs," tech. rep., University of Auckland, 2001.

[58] H. Renzsch, O. Muller, and K. Graf, "Flexsail - a fluid structure interaction program for the investigation of spinnakers," in *Proceedings of the First International Conference in High Performance Sailing Yachts* (T. R. I. of Naval Architects, ed.), (Lorient, France), 2008.

[59] F. Durand, Mathieuand Hauville, P. Bot, B. Augier, Y. Roux, A. Leroyer, and M. Visonneau, "Unsteady numercal simulations of downwind sails," in *Proceedings of the first International Conference in High Performance Sailing Yachts* (T. R. I. of Naval Architects, ed.), (Lorient, France), pp. 57–63, july 2008.

[60] W. Lasher and P. Richards, "Validation of RANS simulations for international america's cup class spinnaker force coefficients in an atmospheric boundary layer," *Journal of Ship Research*, vol. 51, pp. 22–38, 2007.

[61] W. Lasher and J. Sonnenmeier, "An analysis of practical RANS simulations for spinnaker aerodynamics," *Journal Wind Engineering and Industrial Aerodynamics*, vol. 96, pp. 143–165, 2008.

[62] I. M. Viola and R. Ponzini, "A CFD investigation with high-resolution grids of downwind sail aerodynamics," in *Proceedings of the Developments in Marine CFD Conference*, (London, UK), March 2011.

[63] A. Wright and A. Claughton, "Offwind sail performance prediction and optimization," in *Proceedings of the Second International Conference in High Performance Sailing Yachts* (T. R. I. of Naval Architects, ed.), (Lorient, France), 2010.

[64] P. Atkinson, "On the structural response of a mast-sail system," in *Proceedings of the International conference on Computer-aided design for small craft - sail and power*, (Southampton, UK), 1988.

[65] O. Zienkiewicz and R. Taylor, *The Finite Element Method*. Burlington, USA: Butterworth Heinemann, 2000.

[66] F. Hauville, S. Mounoury, Y. Roux, and J. Astolfi, "Equilibre dynamique d'une structure idealement flexible dans un ecoulement : application a la deformation des voiles," in *Proceedings of the Journees AUM Brest*, (Brest), 2004. in French.

[67] F. Fantini, "Prestazioni di una vela. una metodologia di calcolo," 2004. in Italian.

[68] K. J. Bathe, *Finite Element Procedures in Engineering Analysis*. New Jersey: Prentice-Hall, 1996.

[69] J. Oden and T. Sato, "Finite strains and displacements of elastic membranes by the finite element method," *International Journal of Solid Structures*, vol. 3, pp. 471–488, 1967.

[70] J. Li and S. Chan, "An integrated analysis of membrane structures with flexible supporting frames," *Finite Elements in Analysis and Design*, vol. 40, pp. 529–540, 2004.

[71] B. Tabarrok and Z. Qin, "Nonlinear analysis of tension structures," *Computers and Structures*, vol. 45, pp. 973–984, 1961.

[72] P. Heppel, "Accuracy in sail simulation: Wrinkling and growing fast sails," tech. rep., 2002.

[73] M. Accorsi and J. Leonard, "Structural modeling of parachute dynamics," *AIAA Journal*, vol. 38, pp. 139–146, 2000.

[74] V. Arcaro, K. Klinka, and D. Gasparini, "Finite element analysis for geometrical shape minimization," *Journal of the International Association for Shell and Spatial Structures*, vol. 50, no. 2, 2009.

[75] H. Renzsch and K. Graf, "Fluid structure interaction simulation of spinnakers - getting closer to reality," in *Proceedings of the Second International Conference in High Performance Sailing Yachts* (T. R. I. of Naval Architects, ed.), (Lorient, France), 2010.

[76] S. Kang and S. Im, "Finite element analysis of dynamic response of wrinkling membranes," *Comput. Methods Appl. Mech. Engrg*, vol. 173, pp. 227–240, 1999.

[77] S. Turnock and A. Wright, "Directly coupled fluid structural model of a ship rudder behind a propeller," *Marine Structures*, vol. 13, no. 1, pp. 53–72, 2000.

[78] V. Chapin, N. De Carlan, and P. Heppel, "Design optimization of interacting sails through viscous CFD," in *Proceedings of the Second International Conference in High Performance Sailing Yachts*, (Lorient, France), July 2010.

[79] S. Piperno and C. Fahrat, "Partitioned procedures for the transient solution of coupled aeroelastic problems - part ii: energy transfer analysis and three-dimensional applications," *Comput. Methods Appl. Mech. Engrg*, vol. 190, p. 3147 3170, 1999.

[80] P. Causin, J. Gerbeau, and F. Nobile, "Added-mass effect in the design of partitioned algorithms for fluid-structure problems," *Computer Methods in Applied Mechanics and Engineering*, vol. 194, no. 42-44, pp. 4506–4527, 2005.

[81] K. Karagiozis, R. Kamakoti, F. Cirak, and C. Pantano, "A computational study of supersonic disk-gap-band parachutes using large-eddy simulation coupled to a structural membrane," *Journal of Fluids and Structures*, vol. 27, pp. 175–192, 2011.

[82] M. Fernández, Angel, "Coupling schemes for incompressible fluid-structure interaction: implicit, semi-implicit and explicit," *SeMa Journal*, vol. 55, pp. 59–108, June 2011.

[83] W. Wall and E. Ramm, "Fluid-structure interaction based upon a stabilized (ALE) finite element method," *Computational Mechanics*, 1998.

[84] M. Stein and J. Hedgeperth, "Analysis of partly wrinkled membranes," tech. rep., NASA, 1961.

[85] C. Wu and T. Canfield, "Wrinkling in finite plane-stress theory," *Quarterly of applied mathematics*, pp. 179 – 199, July 1981.

[86] R. Miller and J. Hedgeperth, "An algorithm for finite element anslisys of partly wrinkled membranes," *AIAA technical notes*, vol. 12, pp. 1761–1763, 1982.

[87] P. Contri and B. Shrefler, "A geometrically nonlinear finite element analysis of wrinkled membrane surfaces by a no-compression material model," *Communications in applied numerical methods*, vol. 4, pp. 5–15, 1988.

[88] K. Lu, M. Accorsi, and J. Leonard, "Finite element analysis of membrane wrinkling," *International Journal for Numerical methods in Engineering*, vol. 50, pp. 1017–1038, 2001.

[89] D. Roddeman, J. Drukker, O. C.W., and J. Janssen, "The wrinkling of thin membranes - part 1 - 2," *Transactions ASME*, vol. 54, pp. 884 – 892, 1987.

[90] M. Stanuszek, "Finite element analysis of large deformations of membranes with wrinkling," *Finite Elements in Analysis and Design*, vol. 39, pp. 599–618, 2001.

[91] E. Lee and Y. S., "Finite element analysis of wrinkling membrane structures with large deformations," *Finite Elements in Analysis and Design*, vol. 42, pp. 780–791, 2006.

[92] A. Tessler, D. Sleight, and J. Wang, "Nonlinear shell modelling of thin membranes with emphasis on structural wrinkling," tech. rep., American Institute of Aeronautics and Astronautics, 1961.

[93] F. Cirak and R. Radovitzky, "A lagrangian-eulerian shell-fluid coupling algorithm based on level sets," *Computers and Structures*, vol. 83, pp. 491–498, 2005.

[94] F. Cirak, M. Ortiz, and P. Schroder, "Fully c-1 conforming subdivision elements for finite deformation thin shell analysis," *Journal for Numerical method in Engineering*, vol. 51, pp. 813–833, 2001.

[95] F. Muttin, "A finite element for wrinkled curved elastic membranes, and its application to sails," *Communications in numerical methods in engineering*, vol. 12, pp. 775–785, 1996.

[96] J. Katz and A. Plotkin, *Low-speed aerodynamics*. Cambridge aerospace series, Cambridge University Press, 2001.

[97] J. Reddy, *An introduction to nonlinear finite element analysis*. Texas A & M University: Oxford University Press, 1993.

[98] T. Chung, *Computational Fluid Dynamics*. Computational Fluid Dynamics, Cambridge University Press, 2010.

[99] U. Piomelli and E. Balaras, "Wall-layer models for large-eddy simulations," *Annu. Rev. Fluid Mech.*, vol. 34, pp. 349–374, 2002.

[100] F. Menter, "Two-equation eddy-viscosity turbulence models for engineering applications," *AIAA journal*, vol. 32, pp. 1598–1605, 1994.

[101] F. P. Karrholm, *Numerical modelling in Diesel Spray Injection and Turbulence Interaction*. PhD thesis, Departement of Applied Mechanics, 2006.

[102] S. E. Belcher, T. M. J. Newley, and J. C. R. Hunt, "The drag on an undulating surface induced by the flow of a turbulent boundary layer," *Journal of fluid mechanics*, vol. 249, pp. 557–596, 1993.

[103] A. Molland, S. Turnock, and D. Hudson, *Ship Resistance and Propulsion: Practical Estimation of Ship Propulsive Power*. Ship Resistance and Propulsion: Practical Estimation of Ship Propulsive Power, Cambridge University Press, 2011.

[104] S. E. Belcher and J. C. R. Hunt, "Turbulent flow over hills and waves," *Annu. Rev. Fluid Mech.*, vol. 30, pp. 507–38, 1998.

[105] S. Taneda, "Visual observations of the flow past a sphere at reynolds numbers between 10^4 and 10^6," *Journal of Fluid Mechanics*, vol. 85, pp. 187–192, 1978.

[106] S. Hoerner, *Fluid-dynamic drag: practical information on aerodynamic drag and hydrodynamic resistance*. Hoerner Fluid Dynamics, 1965.

[107] C. D. Y. Xu, "Computation of force on a cylinder in a shear flow," *Journal of Fluids and Structures*, vol. 15, pp. 941–954, 2001.

[108] C. H. K. Williamson, "Vortex dynamics in the cylinder wake," *Annual Review of Fluid Mechanics*, vol. 28, pp. 477–539, 1996.

[109] R. Pattenden, S. Turnock, and X. Zhang, "Measurements of the flow over a low aspect-ratio cylinder mounted on a ground plane," *Experiments in Fluids*, vol. 39, pp. 10–21, 2005.

[110] H. Jasak and H. Weller, "Application of the finite volume method and unstructured meshes to linear elasticity," *International Journal for Numerical Methods in Engineering*, vol. 48, pp. 267–287, 2000.

[111] K. U. Bletzinger, "Structural optimization and form finding of light weight structures," *Computers and Structures*, vol. 79, pp. 2053–2062, 2001.

[112] C. Wang, H. Tan, X. Du, and Z. Wan, "wrinkling prediction of rectangular shell-membrane under transverse in-plane displacement," *Internationa journal of Solid and Structures*, vol. 44, pp. 6507–6516, 2007.

[113] P. L. Tallc and J. Mouro, "Structures en grands déplacements couplées á des fluides en mouvement," tech. rep., INRIA, 1996.

[114] P. Prukl, "The CST - an insidious survivor from the infancy of FEA," in *Proceedings of the 11th Symposium on Finite Element Methods in South Africa*, (Cape town, South Africa), 1992.

[115] U. Kuttler and W. A. Wall, "Fixed-point fluid structure-interaction solvers with dynamic relaxation," *Computational Mechanics*, vol. 43, no. 1, pp. 61–72, 2008.

[116] C. S. Peskin, "The immersed boundary method," *Acta Numerica*, pp. 1–39, 2002.

[117] C. Forster, W. Wall, and E. Ramm, "Artificial added mass instabilities in sequential staggered coupling of nonlinear structures and incompressible viscous flows," *Comput. Methods Appl. Mech. Engrg*, vol. 196, p. 1278âĂŞ1293, 2006.

[118] E. Burman and M. A. Fernandez, "Stabilization of explicit coupling in fluid-structure interaction involving fluid incompressibility," *Computer Methods in Applied Mechanics and Engineering*, vol. 198, no. 5-8, pp. 766 – 784, 2009.

[119] M. A. and Fernandez, "Incremental displacement-correction schemes for the explicit coupling of a thin structure with an incompressible fluid," *Comptes Rendus Mathematique*, vol. 349, no. 7-8, pp. 473 – 477, 2011.

[120] M. Dauge, "Stationary stokes and navier-stokes systems on two- or three-dimensional domains with corners," *SIAM J. Math. Anal.*, vol. 20, no. 1, pp. 74–97, 1989.

[121] D. P. Mok and W. A. Wall, "Partitioned analysis schemes for the transient interaction of incompressible flows and nonlinear flexible structures," in *Trends in Computational Structural Mechanics*, pp. 689–698, 2001.

[122] C. Kassiotis, "Which strategy to move the mesh in the computational fluid dynamic code openfoam," tech. rep., Ecole Normale Superieure de Cachan, 2008.

[123] M. Barnes, "Form finding and analysis of tension structures by dynamic relaxation," *International Journal of Space Structures*, vol. 14, no. 2, 1999.

[124] D. R. Chapman, "Computational aerodynamics development and outlook," *AIAA Journal*, vol. 17, no. 12, pp. 1293–1313, 1979.

[125] S. Hoerner and H. Borst, *Fluid-dynamic lift: practical information on aerodynamic and hydrodynamic lift*. L.A. Hoerner, 1985.

[126] J. Mosler and F. Cirak, "A variational formulation for finite deformation wrinkling analysis of inelastic membranes," *Comput. Methods Applied Mechanical Engineering*, vol. 198, pp. 2087–2098, 2009.

[127] F. Nobile, *Numerical Approximation of Fluid-Structure Interaction Problems with Application to Haemodynamics*. PhD thesis, Departament de Mathematiques, Ecole Polytechnique Federale de Lausanne, 2001.

[128] I. M. Viola, "Downwind sail aerodynamics: A cfd investigation with high grid resolution," *Ocean Engineering*, vol. 36, no. 12-13, pp. 974–984, 2009.

[129] D. Trimarchi, M. Vidrascu, D. Taunton, S. Turnock, and D. Chapelle, "Fluid structure interactions applied to downwind yacht sails," in *Proceedings of 10th Colloque National en Calcul des Structures* (U. of Monpellier, ed.), (Presq'île de Giens, France), 2011.